Universitat Autònoma de Barcelona

PhD Thesis

# Inkjet printing: a flexible manufacturing of functional ceramic coatings by Chemical Solution Deposition


**Marta Vilardell Navarro**


2014


**Supervised by:**

Dra. Susagna Ricart Miró

Dr. Xavier Granados García

**Tutored by:**

Dr. Ramón Yáñez López

PhD program in Materials Science

Chemistry Department - Science Faculty

ICMAB

CSIC

**Susagna Ricart Miró**, Científica Titular a l'Institut de Ciència de Materials de Barcelona, **Xavier Granados García**, Científic Titular a l'Institut de Ciència de Materials de Barcelona, i **Ramón Yáñez López**, Professor a la Universitat Autònoma de Barcelona

CERTIFIQUEN

que **Marta Vilardell Navarro**, Llicenciada en Química i Enginyeria de Materials, ha dut a terme sota la seva direcció el treball que porta per títol "Inkjet printing: a flexible manufacturing of functional ceramic coatings by Chemical Solution Deposition" i queda recollit en aquesta memòria per optar al Grau de Doctor.

I per a que així consti, signen el present certificat.

Dr. Susagna Ricart Miró  Dr. Xavier Granados García  Dr. Ramón Yáñez López

Llic. Marta Vilardell Navarro

Bellaterra, Març 2014

*Als meus pares*

*A la meva germana*

# Contents

# Acknowledgments

I would like to deeply thank the people and institutions that have made this thesis possible.

First of all, I give thanks to my supervisors Dr. Susagna Ricart and Dr. Xavier Granados for the opportunity given to me to realize this work, the freedom to focus this research, the shared discussions, and their confidence in me in many occasions. To Prof. Teresa Puig and Prof. Xavier Obradors for letting me being part of the *Superconducting Materials and Large Scale Nanoestructures* group. Thanks for supporting my attendance to a number of european and international meetings and courses.

I want to aknowledge the *Consejo Superior de Investigaciones Científicas (CSIC)* for the JAE fellowship and the financial support to visit an external laboratory. I also acknowledge the European projects (EFECTS FP7-NMP-2007-SMALL-1-205854, NESPA MRTN-CT-2006-035619, EUROTAPES FP7-NMP-Large-2011-280432, and the agreement contract with Zenergy Power GmbH), the Spanish Government (CONSOLIDER program CSD2007-00041, SENY MAT2011-28874-C02-01, SUPERCABLE) and the Generalitat de Catalunya (XARMAE, Pla de Recerca).

I also want to acknowledge the Zenergy Power GmbH team, now Deutsche Nanoschicht, for the nice collaboration we had during the first period of this research time, especially Dr. Michael Bäcker, Dr. Martina Falter and Dr. Jan Bennewitz.

I give thanks to Prof. I. Van Driessche, Prof. L. Calzada, Dr. J. Carrabina, Dr. A. Calleja and Dr. J. Ros for accepting being part of the jury of this thesis.

This work would have not been possible without the collaboration of a number of scientific experts in various fields:

I want to deeply thank A. Crespi, J. Esquius and X. Campos for the XRD sample measurements and their friendliness. Special thanks go to A. Crespi, for the disposition to answer my XRD questions; always available.

The experts in advanced physical measurements in our group, Dr. A. Palau and Dr. V. Rouco, for the transport measurements of my YBCO tracks and LSMO devices. Also, thank you very much for your patience and readiness to answer my physical doubts (... què faríem sense l'amic Kirschhoff?).

I am also very grateful to Dr. M. Coll and Dr. V.R. Vlad, my CSD-CZO-tape experts, for their help in many occasions, for their fine comments and suggestions.

Special thanks go to X. Sintas, for the time devoted to solve the electrical, optical and mechanical inkjet printing aspects, for the extensive discussions about engineering and inkjet deposition. To teach me that it is never too late to learn how to take a screwdriver.

Thank you very much, N. Romà and X. Palmer, for your willingness to teach me, when I arrived, how the laboratories worked at ICMAB and for your great support during this thesis.

Thanks a lot to Dr. E. Solano, for his help and support and the nice time spent in the synchrotron facilities.

Thanks to V. Rodríguez for the precursor solution preparation. B. Bozzo and S. Pérez are acknowledged for the magnetometry and profilometry measurements, respectively. I also want to acknowledge M. Simón and A. Gómez for the AFM measurements. Thanks a lot to J. Oró and A.E. Carrillo for the SEM measurements. E. León and E. Irisarri, thanks so much for the trainings and services in the cleaning room facilities.

I wish to acknowledge Prof. Isabel Van Driessche and the whole SCRiPTS Inorganic Chemistry group, from the University of Gent, for having me during a short 2 month stay at their laboratories, and for giving me full access to the printing equipment. Thanks to Jonas, Marcos, Melis, Nigel, Glenn, Kenny, Katrien, Vyshnavi, Klaartje and Petra for the pleasant atmosphere in the office and laboratories. I specially enjoyed the time spent in Gent. Thank you very much for the group activities, which made me feel as at home. I want to deeply thank Jonas, for his help during my stay, from scientific to non-scientific points of view.

I also owe thanks to my colleagues and friends at ICMAB and SUMAN group, which have been very supportive and helpful during this thesis: M. de Palau, A. Palau, M. Coll, P. Álvarez, N. Romà, M. Paradinas, E. Solano, R. Maynou, A. Llordés, M. Gibert, J. Zabaleta, J. Gázquez, R. Guzmán, V.R. Vlad, X. Palmer, M. Tristany, V. Rouco, J.C. González, X. Sintas, R. Luccas, P. Abellán, A. Carretero, C. F. Sánchez, C. Moreno, F. Martínez, C. Pop, A. Queraltó, V. Rodríguez, P. Cayado, F. Belarre, F. Vallès, B. Villarejo, L. Soler, R. Ayala, S. de Arriba, N. Mestres, A. Calleja and C. Oliveras.

Thanks a lot to Patrícia Álvarez for her organizational expertise.

Thanks to Neus Ballbé for sharing her skills in imaging and for designing the cover page of this thesis; ... per donar color a un MaR dE GoTeS.

Als companys de despatx, per l'excel · lent atmosfera a la sala de becaris durant aquests anys. Als que em van rebre: R. Luccas, K. Zalamova, B. Bozzo, A. Carretero, M. Romeu i F. Rigato. Als de més tard: V. Rouco, D. Pesquera, J.C. González, O. Vlasin, J. Malowney, C. Pop, M. Scigaj, P. Cayado, M. de la Mata i A. Genç. I als actuals: Roxy i X. Sintas.

No poden faltar en aquests agraïments la gent de fora de l'ICMAB, la Quimicanya i els del poble. Per l'amistat, per les infinites rialles, pel suport continu i ànims constants, per la complicitat, per l'ajuda quan ha calgut, per les converses, sortides, excursions, viatges, festimbolos, dancings i birres vàries. Per ser-hi. Moltes gràcies A. Serra, G. Toribio, A. Corominas, M. Estruga, N. Aparicio, R. Calzada, T. Figueras, N. Bardají, X. Vendrell, M. Rueda, A. Cruz, el petit Liam, E. Vargas, T. Grau, N. Ballbé, A. Domènech, N. Vilardell, A's Navarro, M. Pelegrí.

I per suposat, a la meva família, sempre tan a prop, sempre tan pendent, sempre aquí. Moltíssimes gràcies mare, moltíssimes gràcies pare, moltíssimes gràcies sister!

A tots i totes... mil gràcies, de veritat!

# Motivation

The unique and high value-added properties of functional ceramic oxides have triggered a significant number of emerging scientific fields leading to a wide spectrum of novel applications and devices. To fully exploit these developments, both the search for and implementation of low cost and scalable technologies are crucial if they are to have an impact in fields such as electronics, medicine and science, industrial processes, transport and power engineering. Various vacuum deposition techniques like pulsed laser deposition (PLD), chemical vapour deposition (CVD), sputtering, etc. have been used for up-scaled manufacturing of functional electroceramic epitaxial films [1, 2]. However, the intrinsic capital investment required has limited the production of these advanced materials. Chemical Solution Deposition (CSD) methodology [3, 4] has been proved to be a very efficient alternative for up-scaled and flexible production of functional ceramic oxides with lower costs than the conventional in situ physical deposition techniques. CSD has already been shown to be a successful methodology for the epitaxial growth of a broad scope of complex ceramic oxides with functional properties such as conductivity, pyroelectricity, piezoelectricity, ferroelectricity, ferromagnetism, magnetoresistance, semiconductivity and superconductivity [5–9]. Nevertheless, for many applications it is required to structure the films on specific shapes in order to make the development of methodologies which allow printing films on precise shapes worthwhile.

The implementation of CSD techniques in combination with Drop on Demand (DoD) inkjet printing technology [10–13] offers important advantages over standard deposition methodologies. Inkjet printing permits the scalability of functional electroceramic epitaxial films to large area manufacturing easily as a reel to reel deposition system. Introducing effective DoD systems [14–16] in the manufacturing process provides a more efficient way to homogeneously deposit the precursor solution on the substrate with film thickness control, among other processing advantages. Inkjet printing allows an accurate control of the deposition by controlling the dispensed solution volume and drop localization during the continuous process.

A notable difference with the common deposition CSD methodologies such as spin coating, dip coating, slot die techniques and other currently used full covering techniques such as PLD or CVD, inkjet printing offers the added value of permitting complex patterning in a single-pass deposition, avoiding post-treatment processes like scratching or laser scripting. This technology would simplify the device manufacturing process in a fully customized production. Furthermore, it is a flexible technology which permits the easy switching of the deposited material and the pattern during the process. Particularly, inkjet printing technique requires a careful control of ink physicochemical properties (mainly viscosity, surface tension and density) [17–19] which determine drop formation process [14], flow dynamics between drops and fluid behaviour onto the substrate [20, 21].

Over the past few years, inkjet printing has been implemented in a broad range of

modern applications [22], however, its integration in functional oxide materials has been scarcely found [23–25]. Throughout this dissertation, we have implemented the appropriate jetting system in order to produce functional ceramic oxide coatings and patterns by depositing self-made inks. Hence, the novelty of the work shown is twofold since it deals with the use of CSD methodology combined with DoD inkjet printing technology for the up-scaling manufacturing of functional ceramic oxides. In particular, in the present thesis we undertake the challenge of exploring three functional ceramic oxides: the $YBa_2Cu_3O_{7-x}$ (YBCO) high-critical temperature superconductor [26], the mixed-valence manganite oxide $La_{0.7}Sr_{0.3}MnO_3$ (LSMO) [27] and the fluorite oxide $Ce_{0.9}Zr_{0.1}O_{2-x}$ (CZO) [28], either in coatings or pattern configurations. The potential properties that high temperature superconductors (HTS) have generated in cuprate materials have led to significant efforts to develop them in long lengths and of sufficient quality to bring them onto the market. Second generation HTS coated conductors (CC's) [29], based on $(RE)Ba_2Cu_3O_{7-x}$ ((RE)BCO, being RE a rare earth: Y, Sm, Nd and Gd) are rapidly becoming the most desirable type of HTS wire for power, medical and magnet applications due to both their wide temperature and magnetic field working ranges. The need for high quality kilometer-length wires requires biaxial textured growth of the superconducting coating on a set of ceramic buffer layers over metallic substrates. This would achieve an adequate bed for the epitaxial growth of the superconducting layer with the corresponding added complexity. Despite being commercially available, a great deal of work is being done all over the world to improve their quality, scalability and production capacity. Effective patterning of HTS tracks for low AC losses multifilamentary coated conductors is also demonstrated by using YBCO precursor inks with selected physicochemical properties. Moreover, the complex mixed-valence manganese oxides (manganites) $(RE_{1-x}AE_x)MnO_3$, with RE a trivalent rare-earth ion (in our case, La) and AE a divalent alkaline earth ion (Sr, in this study) exhibits the colossal magnetoresistance (CMR) effect and a high degree of spin polarization, which make them very common in electron-spin based electronics, to mention but a few applications [30]. Finally, $Ce_{0.9}Zr_{0.1}O_{2-x}$ has been demonstrated as a good buffer layer for CC's due to its low mismatch with the YBCO superconducting layer.

In summary, we have optimized a scalable and cost-effective printing methodology, which will be demonstrated to yield superconducting, magnetoresistive and other types of coatings and patterns. Also, efforts have been made to tailor the physicochemical properties of the inks concerning drop formation and substrate wetting. In addition, we have also explored these coatings and patterns in depth, performing a complete characterization in terms of morphology, microestructure, magnetic and superconducting properties.

# 1. Introduction

This brief introduction aims to provide a very general overview of the relevance and general applications of functional ceramic oxides and put emphasis on the combination of Drop on Demand (DoD) inkjet printing technology with Chemical Solution Deposition (CSD) methodology for long-length manufacturing of functional ceramic oxides. In addition, the main features of the different ceramic oxides dealt in this thesis as well as their crystalline structure will be stressed. Finally, an outline of the thesis is given.

## 1.1. Functional ceramic oxides

Functional ceramic oxides have incited much research and have been brought onto the market due to their **singular and distinctive properties**. Metallicity, semiconductivity, piezoelectricity, pyroelectricity, ferromagnetism, ionic conductivity, thermoelectricity, superconductivity, ferroelectricity and magnetoresistance are some examples of the large variety of functionalities of ceramic oxide systems [5–9, 31]. This broad range of **properties** and **applications** has opened up enormous possibilities for the integration of these functional ceramics into standard electronics with more efficient devices. They are present in a wide gallery of modern devices such as solar cells [32], polymer displays [16, 33], biosensors [34], electronic devices [35, 36], non-volatile magnetic random access memories [37], spin-based devices [38], etc. Applications from environmental fields, energy generation and storage, medicine, industry, as well as catalysis, transport and information technology are other areas where functional ceramic oxides could be present. Besides, the appeal of functional ceramic oxides has been increased by the possibility to obtain these complex oxides in long lengths by combining CSD methodology [3,4,39] with inkjet printing technology [10,13,40], which drastically reduces the costs of the whole manufacturing process.

For next generation applications, abundant studies are being conducted around the world to untangle the structure-properties-function relationships of these advanced materials, which in the last few years, have led to numerous new behaviours including enhanced colossal magnetoresistance (CMR) [41], improper ferroelectricity, enhancement of ionic conductivity and memristance. In practical terms, to take advantage of such new properties, a thorough understanding needs to be gained of the interrelated triangle relationship. New **advances in characterization techniques** have enabled a deeper study of the structure of these materials. Besides macroscopic characterization techniques like Superconducting Quantum Interference Device (SQUID), magneto-optical Kerr effect (MOKE), more local techniques are crucial in order to try to unravel the physical phenomena that is taking place within these materials. The great advance in X-ray magnetic

circular dichroism (XMCD), or in Scanning Probe Microscopies (SPM) for instance may help to access to their internal structure [42, 43].

Numerous techniques exist for functional oxide deposition, which include physical vacuum techniques and chemical methodologies. Chemical Vapour Deposition (CVD), sputtering, Pulsed Laser Deposition (PLD) have been demonstrated as powerful methodologies for large-scale production of functional ceramic oxides [1, 2]. However, these techniques require sophisticated vacuum control and an extremely pure environment, which raise the price of the manufacturing process. Moreover, using these capital-intensive vaccum based techniques, patterns must be drawn by using additive approaches like scratching or photolithographic techniques. Solution-based deposition techniques are a tempting alternative to physical deposition methodologies. Indeed, inkjet printing, Chemical Bath Deposition, electrochemical deposition, electroless deposition techniques, spray coating, dip coating, meniscus coating, curtain coating, slide coating, doctor blading, die coating are all examples of solution based methodologies which can be used for up-scaling manufacturing of functional oxides [32]. Although most of the mentioned techniques can be adapted for patterning by using external physical or chemical masks, there are simpler specific techniques to produce patterns such as inkjet printing, screen printing, flexography, gravure printing, aerosol spray, stamp printing or dip pen lithography.

## 1.2. Chemical Solution Deposition (CSD): Metalorganic Decomposition Route (MOD)

Chemical Solution Deposition (CSD) is already an established methodology to obtain functional ceramic oxides for an extended range of disciplines [3, 4, 39, 44]. It has been settled as a powerful methodology for achieving materials such as bulk ceramics [45], coatings [23], porous solids [46] or nanoparticles [47–54] with high performances. Moreover, the CSD approach has been demonstrated as an efficient alternative methodology for up-scaled and flexible functional ceramic oxide manufacturing as processing conditions are much closer to ambient conditions. Other advantages of the CSD methodology are the high degree of control over the composition of the functional oxide by controlling the stoichiometry of the ceramic oxide precursor solution [55], which may open the possibility to deposit a huge range of materials and compositions.

Essentially, the CSD approach includes three basic steps:

1. **Precursor solution preparation**: selected precursor salts are dissolved in appropriate solvent(s) in the stoichiometric ratio that yields to the desired final ceramic oxide composition. In the case of, for instance, multielement compositions, the volatility of an element or the precipitation before deposition may produce slight deviations in the exact stoichiometry, which may require compositional corrections. Furthermore, on some occasions, additives (e.g. surfactants, monomers, polymers, chemical stabilizers) are introduced to the ink formulation for improved solution stability or for an ink rheological or wetting control.
2. **Precursor solution deposition**: in the second step, the as-prepared precursor solution is deposited onto the substrate. Conventional procedures to deposit solutions

are spin coating, dip coating, inkjet printing, slot die, among others. As the main goal of this thesis, we have used the inkjet printing technology to deposit all the samples studied.

3. **Thermal treatment:** in the last stage a thermal treatment is performed in order to obtain the ceramic oxide in the desired phase. Two approaches are usually employed: in the first approach, the as-deposited film is subjected to a first thermal treatment, typically at low temperatures (300-400°C) and in oxidizing atmospheres for decomposition of the organic matter. This first thermal treatment, called from now on, pyrolysis process, leads to a mixture of amorphous and nanopolycrystalline intermediate phases which subsequently, in a posterior thermal treatment at higher temperatures (700-800°C), crystallize into the desired ceramic oxide phase. Occasionally, the crystallized film may be post-annealed for microestructure readjustements. In the second approach, the organics removal (pyrolysis process) and oxide crystallization are carried out in the same processing step. The process is performed at temperatures sufficiently high to induce crystallization of the ceramic oxide.

An schematic illustration showing how films and patterns are obtained by CSD route is found in Fig. 1.1. More specific synthesis process conditions for the growth of each of the ceramic oxide relevant for this work will be given later in chapter 3.

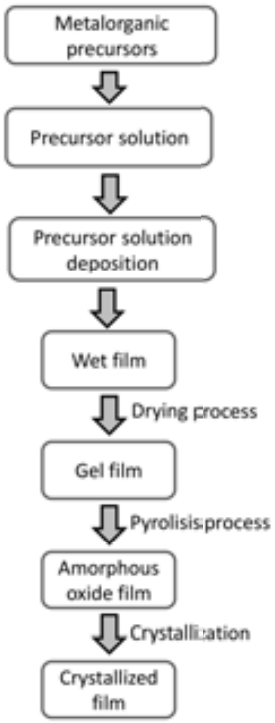


**Figure 1.1.:** Schematic representation of Chemical Solution Deposition (CSD) methodology. The process may be repeated as many times as necessary to achieve the desired coating thickness. Adapted from [3].

For optimum implementation of the CSD technique, several considerations in relation to precursor solution chemistry, substrate and processing parameters should be considered. In deciding the selection of effective precursor salts, various factors should be taken into

account. These precursors should have an appropriate solubility in the chosen solvent(s) to obtain stable solutions and should not leave undesirable residues after decomposition. In addition to metallorganic precursor properties, rheological and wetting ink properties (i.e. viscosity, surface tension and density) and their behaviour with the substrate should be controlled in order to achieve a uniform covering of the surface of the substrate. Besides, the determination of a proper thermal treatment is absolutely necessary in order to avoid cracks and any alteration in the film homogeneity during thermal treatment.

The comprehension of thermodynamical and kinetic aspects and the large number of parameters and interrelationships that take part in the CSD processing steps are decisive to control the final properties and microestructure of coatings. Although many advances have been made in recent years regarding processing control and tuning of properties through manipulation of deposition parameters, there is still room for greater knowledge, control and optimization of the various processes involved.

Particularly, the **Metalorganic Decomposition Route (MOD)** route [44] is a simple route to obtain functional ceramic oxide films. The basic approach consists of simply dissolving the chosen metalorganic compounds in a usual solvent in the adequate ratios to obtain the final ceramic stoichiometry, then deposit the solution onto the substrate and finally apply the adequate thermal treatments of pyrolysis and crystallization processes to obtain the ceramic oxide in the desired phase. Metalorganic compounds are a good choice as precursor salts since their solubility in polar organic solvents is adequate and, furthermore, they do not leave residues after thermal decomposition [56]. However, this solution-synthesis route possesses some limitations. The use of large organic ligands as starting metalorganic precursor salts may produce film cracking due to the weight loss and shrinkage that occurs during thermal decomposition. To surround this, metallic short chain carboxylates with the low content of organic counterpart (e.g. acetates, propionates and acetylacetonates) are usually employed in the MOD route. Finally, film porosity and the complexity to control the structural evolution throughout the whole process are important issues associated with this methodology.

## 1.3. Inkjet printing technology

Nowadays, interest in functional oxides has been heightened by the possibility to obtain these complex oxides by the CSD methodology in combination with other deposition technologies to produce them in long lengths, which drastically reduce the costs of the whole process. As previously mentioned, spin coating, dip coating or inkjet printing are examples of current CSD techniques used to obtain functional ceramic oxides coatings and patterns. In the first process, the scalability to large scale manufacturing is highly limited, while the main drawback of dip coating are the changes in the concentration and rheological properties of solutions during deposition. The *numerous printing processes*, the *gallery of materials* that can be formulated as inks, as well as the possibility to *deposit according to patterns* and its achievable *industrial scalability* are some key features that make inkjet printing technology [10, 12, 13, 22, 40] such an appealing technique in many applications. In the framework of this report, besides the basic scientific interest in the study of inkjet printing technology, we also investigated the possible implementation of

this technology with CSD from a more technological point of view. The following chapter will provide a general overview of the main characteristics and types of inkjet technology with special emphasis given to the various factors that constitute the overall inkjet printing process; from the ink to the printhead and the substrate. Among these aspects, representative inkjet applications [32,34,35,57,58] are also introduced in the next chapter.

Taking advantage of inkjet printing versatility, various functional ceramic oxides have been obtained throughout this research. In particular, $YBa_2Cu_3O_{7-x}$ (YBCO) [26], $La_{0.7}Sr_{0.3}MnO_3$ (LSMO) [27] and $Ce_{0.9}Zr_{0.1}O_{2-x}$ (CZO) [59] films and patterns have been prepared by means of CSD-MOD route in combination with inkjet printing methodology. Their capabilities to be exploited in an outspread range of applications make them highly attractive materials. In the next section, we will briefly review the main properties of YBCO, LSMO and CZO functional ceramic oxides.

## 1.4. High $T_c$ superconductors (HTS): superconductivity phenomenon

Superconductivity [60], discovered in mercury by K. Onnes in 1911, refers to the phenomenon in which certain materials display zero electrical resistance and expulse the interior magnetic field when they are cooled below a characteristic *critical temperature* $T_c$. This means that those materials are able to transport current without dissipation. The fully diamagnetic behaviour, called Meissner effect [60], is achieved through the generation of screening supercurrents. Superconducting materials can be classified as *low temperature superconductors* (LTS) and *high temperature superconductors* (HTS) [60]. However, from the applications point of view, materials with high $T_c$ are desirable. In this understanding, among HTS, copper-based superconductors (known as cuprates) are the most promising for power applications since they can operate at high fields with liquid nitrogen cryogenics (77K).

The YBCO compound, with $T_c \sim 92K$, was discovered in 1987 [61]. As a *type II superconductor*, it is found in Meissner state for magnetic fields below the critical field $H_{c1}$. Fig. 1.2 shows an schematic representation of the magnetic phase diagram of a type II superconductor.

For $H > H_{c1}$, unlike type I superconductors, the magnetic field penetrates into the material as tubes of quantized magnetic flux, called vortices [62]. This $H > H_{c1}$ region is known as the *mixed state* region and is delimited by two critical fields, $H_{c1}$ and $H_{c2}$, as shown in Fig. 1.2. Vortices are formed by a normal core of radius $\xi$, which is called the coherence length, surrounded by circulating Cooper pairs which penetrate a distance $\lambda$, the penetration depth, from the center of the vortex into the superconductor. These flowing currents generate a flux quantum in each vortex, so the magnetic flux inside the material is quantized. The presence of such vortices guarantees the existence of a large number of normal-superconductor interfaces in these type II superconductors. From $H_{c1}$ to $H_{c2}$, the number of vortices introduced in the superconducting material progressively increases. At the upper magnetic field $H_{c2}$, vortex overlap, and the magnetic field penetrates homogeneously through the material. In this situation, all superconducting properties are

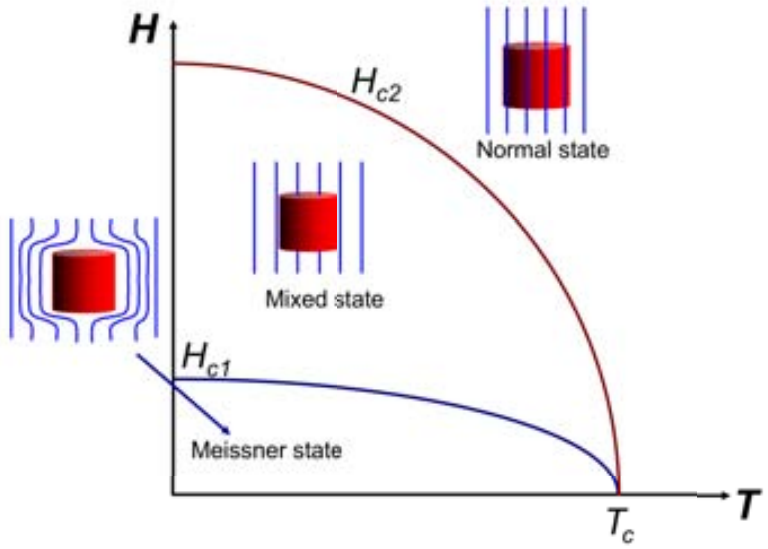


**Figure 1.2.:** Magnetic phase diagram for a type II superconductor.

lost and therefore, the transition to normal state occurs. It is important to remark that the ability to transport zero resistance current in the mixed state is limited by the vortex motion induced by the interaction between the flowing current and magnetic field in the vortex.

When a current $J$ circulates through a superconducting material in the mixed state, a Lorentz-like force $F_L$ per unit volume [62], $F_L = J\text{x}B$ acts on the vortices inducing their motion. When vortices start to move, due to the non-superconducting nature of the vortice core, there is *dissipation of energy* associated to the electric field $E = v\text{x}B$, where $v$ is the local velocity of the flux lines, and the material is not longer able to transport current at zero electrical resistance. Then, it exists a maximum current density that can circulate through the material without dissipation. This is termed *critical current density* and is symbolized as $J_c$. In contrast to $T_c$ and $H_c$, which are intrinsic properties, $J_c$ is a property associated to the nanostructure of the material. To avoid dissipation, vortices must be pinned in the material (i.e. $v$=0). It has been demonstrated that current-capabilities of coated conductors (CC's) [4] are fully enhanced if nanometric-sized defects of dimensions similar to the core of the vortice are present in the superconducting matrix to act as vortex pinning centers [29]. Dislocations, strain fields, twin boundaries, non-superconducting secondary phases, oxygen vacancies, etc. are effective *crystalline defects* to immobilize such vortices. In fact, at this time, research in YBCO superconducting films is basically focused on improving their performance by means of nanostructuring processes [63, 64].

The effectiveness of the pinning centers is indicated by the *pinning force* $F_P$. In other words, $J_c$ is defined as the current that produces a Lorentz-like force $F_L$ equal to the average pinning force $F_P$ exerted by the defects on the vortices, i.e. $F_P = J_c\text{x}B$. When the Lorentz force $F_L$ overcomes the pinning force $F_P$, vortices are no longer anchored and dissipation occurs. In other words, when $J$ exceeds $J_c$, the material adopts a loss energy state, still within the superconducting state (i.e. below $H_{c2}(T)$ in Fig. 1.2). In the

II-type superconductors $H-T$ diagram, it is possible to define the *irreversibility line*, which separates a region where the material, despite being in the superconductor state (kept until $H_{c2}$), shows a substantial electrical resistance ($J_c = 0$) from an area in which the resistance is zero ($J_c \neq 0$) and the defects present in the material act as effective vortex pinning centers. Therefore, the technological applicability of HTS superconductors is restricted below this irreversibility line, which is substantially more relevant than $H_{c2}$. Among HTS, and although it is not the material with the highest critical temperature, the YBCO compound exhibits the highest irreversibility line at 77K displayed so far [65], thus becoming the best candidate for high magnetic field and high temperature applications (i.e. magnets, motors, fault current limiters, MAGLEVS, magnetic separators, transmission cables, generators, transformers, MRI's, accelerators, etc.) [26].

### 1.4.1. $YBa_2Cu_3O_{7-x}$ crystal structure

$YBa_2Cu_3O_{7-x}$ is a cuprate superconductor of high critical temperature, $T_c \sim 92K$ [61]. Its unit cell, schematized in Fig. 1.3, is based on a triple perovskite $ABO_3$ stacked vertically along the c-axis: a central $YCuO_3$ perovskite with two adjacent $BaCuO_3$ perovskites and some oxygen vacancies. Such oxygen deficiency implies that $Cu$ ions are present with mixed oxidation states: $Cu^{+2}$ and $Cu^{+3}$. Each unit-cell has two $CuO_2$ planes which contain the mobile charge carriers across the superconducting current flows. These planes are separated by $CuO$ *chains* which act as *charge reservoirs* providing the density carriers to the *superconducting* $CuO_2$ *planes* [66, 67].

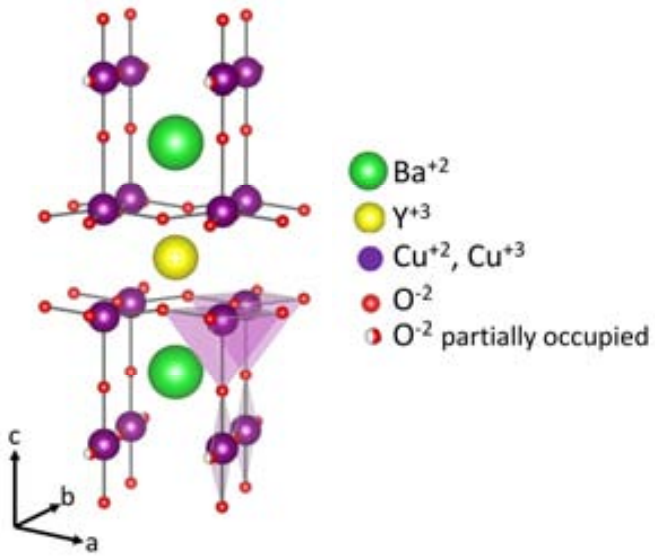


**Figure 1.3.:** Crystalline structure of the orthorombic superconducting $YBa_2Cu_3O_{7-x}$ phase for x<0.65 [68].

The oxygen sites in the $Y$ plane ($z = 1/2$) are never occupied, whereas the occupancy and distribution of oxygens on the basal $CuO_2$ plane ($z = 0$) give rise to two different crystalline structures: *tetragonal* or *orthorombic*. In the tetragonal phase, i.e. $0.65 < x < 1$, the oxygens are randomly located over the four possible sites in the basal plane.

This phase exhibits a *non-superconducting* behaviour. In contrast, in the orthorombic lattice, i.e. $0 < x < 0.65$, the oxygens are fully ordered along *b-axis* in 1D-chains. This distribution corresponds to the *superconducting phase* (see Fig. 1.3). The maximum critical temperature $T_c \sim 92K$ is achieved when x$\sim$ 0.06. For $x > 0.06$, the material is overdoped and $T_c$ drops [69]. For this oxygen doping, almost all the oxygen positions along the $b$ axis are occupied. In this sense, the optimum oxygen stoichiometry is achieved by tuning the processing conditions (basically temperature and oxygen partial pressure).

YBCO lattice parameters of both tetragonal and orthorombic phases are shown in Tab. 1.1:

| | Tetragonal ($x = 1$) | Orthorombic ($x \sim 0.1$) |
|---|---|---|
| a (Å) | 3.865 | 3.823 |
| b (Å) | 3.865 | 3.886 |
| c (Å) | 11.852 | 11.684 |

**Table 1.1.:** YBCO cell parameters in the tetragonal and orthorombic phases.

Due to its layered structure and the confined localization of carriers in the superconducting $CuO_2$ planes, YBCO shows a large anisotropy, which means that its properties differ greatly along $c$-axis and $ab$ planes. In particular, superconductivity along the $c$ axis is 7 times smaller than in the $ab$ planes, which implies that a good alignament of $ab$ planes with a very low misorientation between grains is absolutely essential for an easy current to flow and, therefore, for optimal superconducting performances [70]. In this way, a biaxial texture is a critical issue when YBCO coatings with high performances are required.

### 1.4.2. Second Generation (2G) Coated Conductors (CC's)

The capacity to transport currents without energy dissipation makes superconducting materials remarkably engaging. Losses reduction that derive from the use of HTS leads to an increase of reliability and efficiency in the generation, transmission and distribution of the electrical energy reducing, at the same time, the impact of power delivery on the environment. To achieve the full potential of HTS superconductors, relevant scientific and technological barriers must be overcome: they must show high performances with reduced manufacturing costs.

The first YBCO superconductors fabricated exhibited very low $J_c$ values (around $1 \cdot 10^{-3}$- $1 \cdot 10^{-4} MA/cm^2$ at $77K$ and self field), various orders of magnitude below practical values. The transport current in these materials was strongly limited by the angle between grain boundaries, which has been demonstrated that high angle ($\alpha > 2°$) grain boundaries become real barriers to current flow [71, 72]. The high anisotropy shown in the transport properties ($J_c \| c$ axis $<<$ $J_c \| ab$ planes) requires of the YBCO $ab$ planes being parallel aligned across the surface of the substrate.

Therefore, to reach competitive superconducting performances, is crucial that YBCO grains are highly biaxially aligned, featuring a kilometer-length single crystal [73]. So, the introduction in the manufacturing process of a template which induce texture is

absolutely crucial. This condition was first achieved by the deposition of epitaxial YBCO films [74] on (00l)-oriented single-crystal substrates (e.g. $SrTiO_3$(STO), $LaAlO_3$ (LAO), MgO), leading to $J_c$ values of the order of $1MA/cm^2$ at 77K and self field. At present, performances of YBCO films lead to $J_c$ values at $77K$ as high as $3-6MA/cm^2$. The selection of the single-crystal substrate is dictated by both the film/substrate and thermal expansion coefficient mismatches and the chemical compatibility between them.

However, HTS are ceramic compounds, and therefore, are brittle and difficult to handle and process. In this sense, a substrate which transmits them enough strenght and flexibility is definitively required. Besides, the challenge is to achieve cost-effective long length YBCO conductors using high throughput deposition processes, to compete with the conventional copper devices. To surmount all these limitations, a substrate technology behind YBCO coated conductors (CC's) has been developed. The real success appeared with the discovery of the so-called *second generation of conductors* (2G), or *coated conductors* (CC's) [75–77] based on (RE)$Ba_2Cu_3O_{7-x}$((RE)BCO, being RE a rare earth: Y, Sm, Nd and Gd). CC's are based on a multilayer architecture (e.g. epitaxial *buffer layer*/epitaxial YBCO layer/protective layer) deposited onto metallic substrates, as shown in Fig. 1.4.

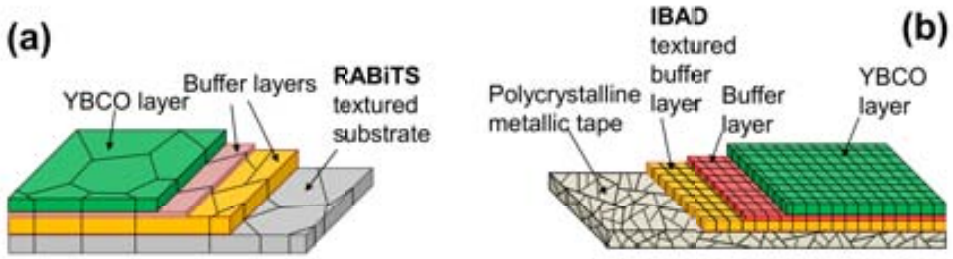


**Figure 1.4.:** Coated Conductors (CC's) architecture. (a) RABiTS and (b) IBAD approach.

Nowadays, there are two principal approaches for achieving long length textured coated conductors. One substrate technology is called Rolling Assisted Biaxial Textured Substrates (RABiTS) [75,78], and the other is based on the Ion Beam Assisted Deposition (IBAD) technology [79]. In the RABiTS procedure, the metallic substrate is textured by special thermomechanical treatments, which provides an adequate template for the deposition of the subsequent buffer layers and YBCO coating. In the IBAD approach, an energetic ion beam irradiates the substrate during the deposition of the textured buffer layer over a non-textured metallic tape. Currently, various companies are developing and comercializing long length biaxially textured coated conductors. SuperPower and American Superconductors are some examples of such companies. In the architecture used by SuperPower, both the YBCO layer and buffer layers are grown by vacuum techniques, whereas in the American Superconductors architecture, the YBCO layer is obtained via CSD. Performances displayed by these CC's are similar to those achieved by epitaxial YBCO films grown on single crystals. However, it should be taken into account that the metallic substrate has an inherent granularity on a microscopic scale, which is inherited by the YBCO layer in the final structure. The strong dependence of $J_c$ on grain misorientation and the percolative character of the electrical conduction require a continuous improvement of the texture quality of metallic substrates and buffer layers. However, up

to now, grain misorientations in the range of 2° have been achieved, which do not limit the superconducting current flow anymore. The overcoming of the grain boundary problem permitted the reproducible fabrication of HTS. The next challenges are to surmount the vortex pinning problem, i.e. how to create efficient non-superconducting centers (type, concentration and dimensions) to pin the vortices of moving and the achievement of cost-effective and high-performance CC's, depositing both YBCO and buffer layers by means of scalable deposition processes. Hence, the implementation of CSD in combination of inkjet printing technology offers enormous possibilities to deposit long length CC's and, in general, long length functional oxides.

## 1.5. Mixed-valence manganites

The next section is intended to give a general overview of the relevance of mixed-valence manganites, *manganites* from now on, summarizing their main properties and structure, with special emphasis to the strontium-doped-lanthanum-manganite $La_{1-x}Sr_xMnO_3$ (LSMO), one of the compounds studied in this thesis. For a profound analysis of the state of the art in the field, the reader is directed to the many reviews that cover this area [27, 41, 80–82].

Mixed-valence manganese oxides with a perovskite structure belong to the strongly correlated electronic systems of general formula $A_{1-x}B_xMnO_3$; where $A$ is a trivalent rare earth cation ($La, Pr, Nd, Sm$) or $Bi$, and $B$ is a divalent alkaline earth cation ($Ca, Sr, Ba,$ or $Pb$). The discovery of a simultaneous ferromagnetic and metallic behaviour in the mixed compounds $LaMnO_3 - BMnO_3$, with $B = Ca$,$Sr, Ba$, by Jonker and Van Santen [83] dates from 1950. This behaviour was explained yet in the context of the Double Exchange model (DE) by Zener [84], Anderson and Hasegawa [85] and de Gennes [86]. However, it was not till the 90's when it was discovered that the application of a magnetic field induces a large change in the electrical resistance of $La_{0.67}Ca_{0.33}MnO_3$ thin films, in the vicinity of their Curie temperature $T_C$ ($\sim 360K$; for x $\sim$ 0.3) [81], which is known as *Colossal magnetoresistance* (CMR) [27, 41, 81, 87]. CMR is an intrinsic phenomenon to manganites generally observed close to $T_C$. The physics behind this phenomenon have raised many fundamental questions [82], nevertheless, its combination with the *metal-insulator transition*, above room temperature, have opened up a broad range of technological opportunities in magnetic sensors, magnetoresistive random access memories, spin-injection devices, solid electrolytes in fuel cells and resistive memories to mention but a few applications.

Another interesting property of manganites is their high degree of *spin polarization* [88, 89]. Manganites are among the few compounds that exhibit half-metallicity as was demonstrated by Park et al [88], which makes these compounds especially interesting for spin-based electronics [38]. These properties may be modified by tuning the biaxial strain of LSMO films, modifying the external pressure [90], changing type and concentration of dopant and also by adjusting the oxygen stoichiometry [91].

However, not all the phenomena shown in manganites might be explained by the above-mentioned DE model. Electron-lattice interactions, Jahn-Teller distortions [41], charge/orbital ordering, or the antiferromagnetic superexchange, are all crucial aspects for

the understanding of the physics of manganites. Certainly, these interactions, matchings and the huge variety of chemical and physical properties of manganites give rise to the large richness, complexity and applications of this kind of systems [27, 41, 92].

Furthermore, the study of the LSMO system is specially engaging due to its good lattice mismatch $\epsilon = \frac{a_{film} - a_{substrate}}{a_{substrate}} \cdot 100$ [93] with YBCO ($\epsilon \sim 0.5\%$), which may be a candidate to be a buffer layer for the growth of epitaxial superconducting YBCO coated conductors [26].

### 1.5.1. $La_{0.7}Sr_{0.3}MnO_3$ crystal structure

Fig. 1.5 illustrates the perovskite unit-cell, $ABO_3$, where $A$ is the trivalent $La$ ion or the divalent $Sr$ ion, in the ratio determined by the doping parameter $x$; $B$ is the $Mn$ ion, with average valence $3 + x$, and $O$ is the oxygen anion. The manganese ions locate at the center of oxygen octahedra. Although the ideal perovskite belongs to the $Pm\bar{3}m$ cubic symmetry, many of the compounds with the perovskite-type structure display lower symmetries. This is the case of manganites, which general adopt either rhombohedral or orthorombic structures. For the LSMO case, is usual to describe its rhomboedrical structure in terms of pseudo-cubic notation, which simplifies the treatment of the structure [41, 94]. In this pseudo-cubic description, LSMO shows a lattice parameter $a \sim 3.873$Å and an angle $\sim 90.26°$ [95], which implies a very slight deviation from the perfect cubic symmetry. The average cation radius $R_A$ critically influences the tilting and rotations of the oxygen octahedra, with a strong impact on the $Mn - O - Mn$ bond angle. Such bond angle will dictate the transport and magnetic properties of manganites [41].

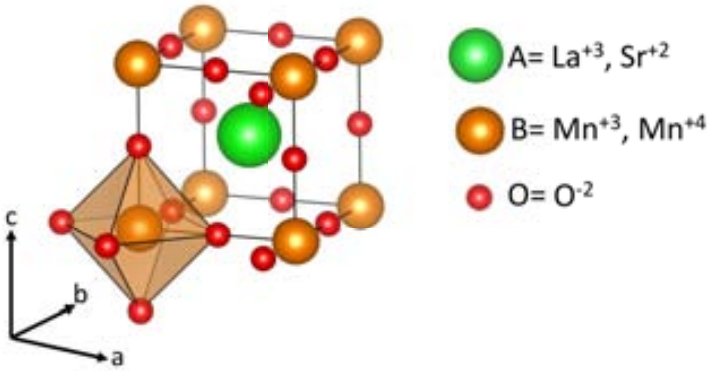


**Figure 1.5.:** Unit cell of the $La_{0.7}Sr_{0.3}MnO_3$ perovskite structure.

## 1.6. $CeO_2$

$CeO_2$ has been extensively accepted for its use in catalysis [96], gas sensing [97], ultraviolet filtration [98], energy storage systems [99] and as a polishing agent [100]. It is also an important component in many devices like in microelectronic [101] and silicon structures [102] and is a good candidate to be used as a buffer layer in the manufacturing of coated conductors due to its low lattice mismatch with the superconducting YBCO layer

($\varepsilon = 0.52\%$) [59, 103]. However, in addition to be a good cap layer, $CeO_2$ is also a good oxygen conductor which means that it is needed to control the thickness of $CeO_2$ films in multi-structures to protect the underlying film from oxidation and chemical reactions. Regarding this point, inkjet printing plays an important role due to the possibility to control the deposited ink volume. It was demonstrated [104] that the use of Zr-doped $CeO_2$ buffer layers increase the mobility of the system enabling an easier reconstruction of the layer surface [105, 106]. Within this work, doped $CeO_2$ buffer layers have been deposited by inkjet printing as underlying buffer layers for coated conductors.

### 1.6.1. $Ce_{0.9}Zr_{0.1}O_{2-x}$ crystal structure

$Ce_{0.9}Zr_{0.1}O_{2-x}$ displays a cubic fluorite structure $AO_2$ where $A$ is the trivalent $Ce$ ion or the divalent $Zr$ at ambient conditions (Fig. 1.6). The unit cell of fluorite is shown below. The fluoride ions are shown in yellow and the calcium ions in grey.

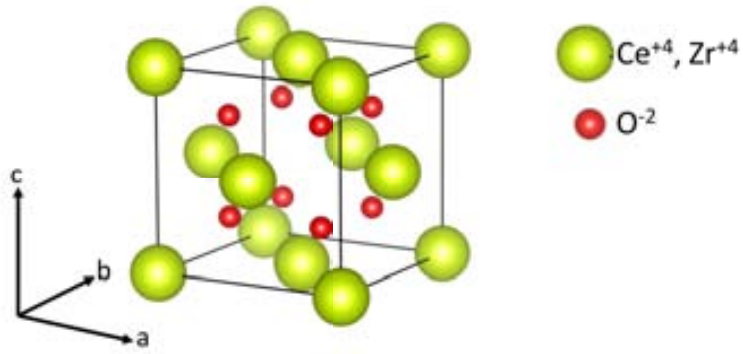


**Figure 1.6.:** Unit cell of the $Ce_{0.9}Zr_{0.1}O_2$ structure.

## 1.7. Outline of the report

The interest in functional ceramic coatings and patterns based on low cost and flexible manufacturing has been heightened by the effectiveness shown by the possibility of implementing effective drop on demand systems in the manufacturing process, which allows a more efficient way to to apply the precursor solution homogeneously onto the substrate, thus, enabling control of thickness of the ceramic coating, by controlling the drop size and the pitch of the printing pattern, among other manufacturing advantages such as control of solvent evaporation.

This dissertation is divided into seven main chapters. After a *motivation* section, *Chapter 1* is devoted to describe the relevance of functional ceramic oxides, including an overview of the broad range of applications where they are involved. The main properties of the functional ceramic oxides studied throughout this work are also briefly depicted in this introductory chapter. Basics of the inkjet printing technology, with emphasis to the different inkjet techniques, together with the main actors that play a crucial role in the overall inkjet printing process, are presented in *Chapter 2*. In *Chapter 3*, we give an

overview of the experimental procedures used for obtaining the various functional oxide precursor solutions object of this work. The characterization of the inks, as well as the inkjet printing devices employed for the deposition process and the thermal treatments performed to obtain the ceramic oxides, are described as well. The effect of the jetting parameters and the influence of the relevant ink physicochemical properties on the drop formation process and their influence on drop characteristics are extensively discussed in *Chapter 4*. *Chapters 5 and 6* examine the ink behaviour on the substrate, with the detailed experimental sequences followed to obtain YBCO and LSMO layers and patterns with their deep characterization from phase structural, textural, microstructural and physical point of view. *Chapter 7* provides the preliminary results obtained in the upscaling of the inkjet printing technology in combination with the CSD methodology to further technological development to longer lengths. The main conclusions of the work are collected in the *General Conclusions*. An *appendix* at the end of the manuscript gathers a glossary on fluid dynamics and the main issues on wetting phenomenon.

# 2. Inkjet printing technology

As mentioned in the motivation, the aim of this research is to implement a suitable technology for the manufacturing of functional ceramic oxides in long lengths. However, if the mass production of inkjet-produced coatings and patterns is to be realized, a fundamental understanding of inkjet printing technologies [10, 13, 22, 40, 107, 108], including how fluid properties and printing parameters affect deposition quality, are key challenges to comprehend the results obtained throughout this work. In addition to the main inkjet printing technologies, the relevant actors that play a significant role in the whole inkjet printing process, the ink requirements for a successful inkjet printing, as well as an overview of drop formation dynamics and some fundamentals of the ink-substrate interaction are adressed and described. At the end of the chapter, a selection of application examples is provided, illustrating the huge potentiality of such technology.

## 2.1. Main features of inkjet printing technology

The main characteristics of inkjet printing technology are highlighted in the following lines. Inkjet printing permits the scalability of functional ceramic oxides in a continuous reel to reel system. Besides, notable advantages of this technology include the versatility to switch on the flight the deposited material and the pattern design. Functional inks, waxes, polymers or nanoparticles are examples of the diversity of materials that might be printed as coatings, lines, arrays, arrays of arrays, drawings or even multistructures allowing to cover a plethora of compositions and configurations. Inkjet printing technology also enables to work in a broad range of substrates and rates, which reflects the high integration of the printing technologies into a wide scope of production scales.

In addition, the high repeatability of drop ejection mechanism allows us to control in a precise manner the deposited volume, in the picoliter range, and the localization of drops. The accurate drop volume control enables to tune film thickness and favours the complementary printing of large areas with delicate patterns [23, 109]. In contrast to the common deposition methodologies, inkjet printing permits the complex patterning in a single-pass deposition [23, 25, 110], which suppose an extra benefit from the standard screen printing, photolithography and mechanical approaches.

Furthermore, by using a closed ink reservoir, this methodology ensures a tight control of ink composition and rheological properties during deposition process. Moreover, as a non-contact method, the fluid can not be contaminated by the substrate. As will be mentioned in later sections, inkjet printing is highly sensitive to the physicochemical properties of the ink [17, 18]. It means that a high degree of control over the ink characteristics must be accurately tailored to control jetting reliability and drop formation (i.e.

drop volume and drop speed) [15, 111, 112], spreading on the substrate [20, 21, 113, 114], and connectivity between drops to, at the end, constrain the morphology of the final dried solid [19, 115, 116]. In this regard, ink essential parameters such as viscosity, surface tension, density, evaporation rate of the solvent, drop characteristics like drop volume and drop speed and the contact angle which makes the ink with the substrate must be strictly met and adjusted.

## 2.2. Types of inkjet printing technologies

Inkjet printing technologies can be divided into two main categories: ***Drop on Demand* (DoD) *inkjet printing*** and ***Continuous Inkjet printing (CIJ)*** briefly traced out in the picture below (Fig. 2.1) [10, 117–119].

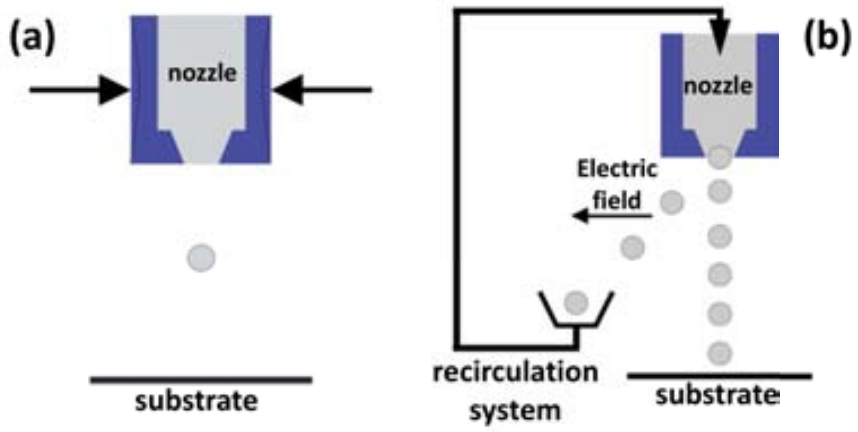


**Figure 2.1.:** Schematic comparison between (a) Drop on Demand and (b) continuous inkjet printing technologies.

Drop on demand inkjet printing systems may, in turn, be classified into three types, termed thermal inkjet printing [120], piezoelectric inkjet printing [12, 121, 122] and electromagnetic valve inkjet printing [123] processes (Fig. 2.2).

### 2.2.1. Continuous mode inkjet printing technology

The phenomena of drop formation from a stream of liquid flowing out from an orifice was noticed in 1833 by Savart [124] and then described mathematically by Rayleigh [125, 126] and Weber [127]. Lord Kelvin patented in 1867 [128, 129] the syphon recorder, which recorded telegraph signals as a continuous trace on paper using an inkjet nozzle deflected by a magnetic coil. The first commercial devices were introduced in 1951 by Siemens [130].

In continuous inkjet technology [131–134], a high-pressure pump directs the fluid from a reservoir to a nozzle, producing a continuous stream of ink drops via the Rayleigh-Plateau instability [125]. The vibration of a piezoelectric crystal creates an acoustic wave causing the stream of liquid to break into droplets at regular intervals. The drops break

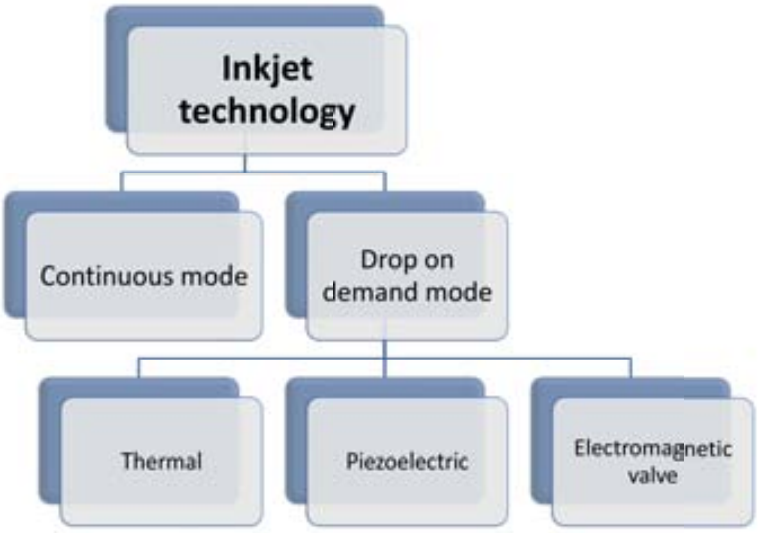


**Figure 2.2.:** Tree of inkjet technology showing the main categories which may be classified inkjet printing procedures.

off from the jet in the presence of an electrostatic field, referred to as the charging field, and thus they acquire an electrostatic charge. Then, the charged drops are directed by another electrostatic field, the deflection field, to either the substrate or redirected to the catcher for re-use. The more highly charged droplets are deflected to a greater extent. Commonly, this type of system is referred as 'continuous' because drops are produced continuously. There are extensive documents reviewing theoretical and experimental analysis of continuous mode printers, with special emphasis to the perturbance growth on the jet that leads to drop formation [123, 135, 136].

The major advantages of this technology are the very high velocity of the ink droplets which allows for a relatively long distance between the printhead and the substrate, and the very high drop ejection frequency (in the 80-100$KHz$ range) which might be convenient in high duty cycle applications. Another advantage is the freedom from nozzle clogging as the jet is working continuously, being less restrictive for high vapour pressure solvents.

Continuous inkjet printheads are faster than DoD printheads but they exhibit some disadvantges in contrast to DoD type printheads. The main disadvantage is that the characteristic ink recycling of this process may result in contamination and variation of the ink concentration and physicochemical properties due to its exposure to the environment. Another disadvantage is that, as drops are directed to the desired position by the deflection field, an electrically conducting fluid is required, which imposes some restrictions on ink formulation. Also, in this technology, only a small fraction of the droplets is used to print, the majority is being recycled, requiring the availability of a large volume of ink. Continuous inkjet printers are currently used in the industrial market, principally for product labelling of food and medicines.

## 2.2.2. Drop-on-demand (DoD) mode inkjet printing technology

In Drop-on-demand (DoD) inkjet systems, drops are only generated when required. DoD inkjet printing allows more flexibility with ink and system design and more control over drop positioning, and so it is the preferred technique for high-resolution graphics and materials deposition. DoD inkjet systems do not have fluid recirculation requirement, and this make their use as a general ink dispensing technology more straightforward than continuous mode technology. It is also much more convenient to implement for development work with small ink volumes while remaining scalable. As mentioned before, the three most common DoD means of generating a droplet are thermal, piezoelectric and electromagnetic valves.

### 2.2.2.1. Thermal inkjet printing

Thermal printheads [120, 137, 138] possess a resistor element inside each nozzle. To eject a drop from the nozzle, a current pulse passes through the resistor which causes a rapid vaporization of the ink, forming a bubble. As the bubble grows, the pressure inside the nozzle increases and the ink momentarily contained by the surface tension as a meniscus, bulges from the nozzle. When the bubble begins to collapse, the ink still in the channel between the nozzle and the bubble starts to move towards the collapsing bubble, causing a volumetric contraction of the ink at the nozzle which results in the separation of the bulging ink from the nozzle as a drop. The pressure then decreases within the system and the nozzle becomes refilled with ink. The acceleration of the ink out of the nozzle while the bubble is growing provides the momentum and velocity for propelling the drop towards the substrate. This is the most common technique for desktop inkjet printers (as produced by Canon and Hewlett-Packard, for instance), but imposes severe restrictions to fluids that may be vaporized without igniting the fluid. The inks used must have a volatile component to form the vapour bubble, otherwise droplet ejection cannot occur. The relatively large temperatures that are locally achieved in the chamber (∼200-300 °C) limit the range of materials that can be used in this kind of inkjet printers. For instance, high-vapour pressure inks or inks based on biomaterials are not advisable to use in this kind of printheads due to their possible degradation with the temperature [139]. There is also another technology used in this kind of inkjet printing based on the thermal deformation of a MEMS (MEMJET) [140].

For materials deposition, the electromagnetic and piezoelectric approaches are therefore strongly favoured.

### 2.2.2.2. Piezoelectric inkjet printing

Piezoelectric droplet formation is the other DoD technique used in domestic inkjet printers (from Epson and Hewlett Packard) and in most industrial inkjet printheads (Konika Minolta IJ Technologies, Xaar, Microfab Technologies, Microdrop Technologies, Ricoh Print Systems, Seiko Instruments, Xennia, Toshiba TEC, Trident Industrial Inkjet). In this kind of inkjet printing process, a piezoelectric actuator is the responsible to generate the drops [11, 12, 112, 141]. The operating system can be basically explained as

follows: the application of an electric field across the piezoelement causes a change on its shape. This deformation gives to mainly two variants on this approach. From one hand, the deformation of the piezoelectric material induces liquid column oscillations which break the fluid stream into droplets due to the activation of *acoustic resonances* in the system. From another side, the deformation of the piezoelement reduces the internal volume of the chamber, thus increasing the pressure and causing the ejection of a droplet through the orifice. Piezoelectric inkjet technology is favoured over thermal printing in many applications as it does not require the high T needed for thermal bubble printing. Pressure/meniscus control is also important to ensure that a droplet forms and leaves the printhead: piezoelectric printheads typically operates under a small negative pressure which stabilizes the meniscus. The drop volume depends on the diameter of the nozzle through the ink is ejected, the drive waveform, and the physicochemical properties of the ink, but is usually in the $pL$ range.

#### 2.2.2.3. Electromagnetic inkjet printing

This inkjet technology is also known as valve-jet technology. In this kind of inkjet technique, a chamber with a nozzle at one end is occupied by a plunger assembly, with a component to seal against the nozzle at one end and a magnetic core at the other. Pressurized ink is introduced, and a solenoid is used to open the valve by displacing the plunger when a drop is required. In this case, the amount of ejected liquid, in the $nL$ or $\mu L$ range, is controlled by means of the nozzle diameter, the time for which the valve is kept open (i.e. the *valve opening time* $\tau$*)*, the amount of power applied to the coil (i.e. the *valve opening voltage)* and the *pressure* placed upon the ink (see sec. 4.9.3.2).

## 2.3. Getting started in deposition

### 2.3.1. The inkjet printing toolbox

The key parameters that need to be evaluated as a whole to determine the inkjet printability are shown in next Fig. 2.3:

Important questions such as:

- What ink is going to jet?
- What is the substrate?
- What pattern is going to print?
- What throughput is needed for the specific printing application?
- What is the pattern feature size?

will determine the printhead and the ink to be used. Also, they will advise about the printer system that would be recommended to employ and therefore the adequate ink physicochemical properties.

In the next sections are outlined the different actors that play a significant role in the inkjet printing roadmap: the ink, the printhead and, finally, the substrate.

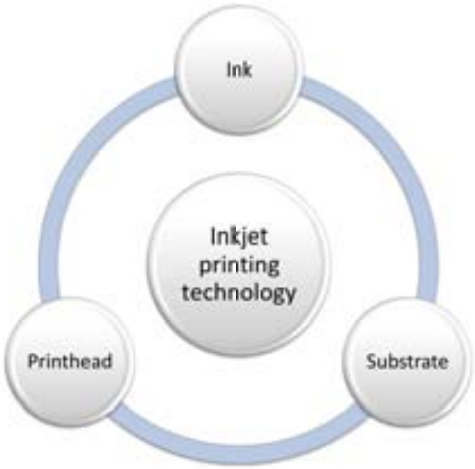


**Figure 2.3.:** Fundamental aspects of the inkjet printing technology.

## 2.4. The ink: design, requirements and types

Ink formulation is one of the most important points to go deeply into the inkjet printing process. Specially, the overall inkjet technology demands a meticulous scrutiny of the relevant physicochemical properties of the ink [17,18] cause they determine essential processes like drop ejection and drop spreading processes, as well the interaction when drops come into contact between them and with the substrate. It should again be emphasized that a stringent control over the ink chemistry and processing are needed tasks to achieve scalable and low-cost materials with optimum characteristics, although sometimes, due to the demanding requirements of inkjet inks, such adjustements are a hard and complex procedure. Concerning that, ink viscosity, surface tension, density, contact angle, evaporation rate of the solvent, drop volume and drop speed must be strictly met and adjusted [116].

The ink requirements for a successful inkjet printing, as well as the ink properties which affect inkjet performance and some typical ink problems are briefly emphasized in the next sections.

The main function of the ink is to place the functional molecules on a substrate. Basically, the ingredients of an ink might be described as follows:

- Functional material: the functional molecules, which may be as diverse as a metalorganic precursor for a superconducting ceramic or a conductive polymer for plastic electronics, a UV curable monomer for achieving a three-dimensional structure, a living cell for building an organ or even a colorant for the common graphic arts.
- Carrier solvent(s): of special importance is the choice of the carrier solvent (e.g. water, organic solvents, cross-linkable monomers). Mainly, the solvent determines

the boiling point and polarity of the ink, which dictate the drying mechanism. Also, the ink viscosity and the surface tension are influenced by the solvent and the types of additives. Furthermore, the solubility of the other ink components in the selected solvent and their effect on the other parts of the printer device (i.e. corrosion effects) is of great relevance.

- Other additives (surfactant and wetting agent(s), dispersants, binder(s), rheology modifier(s), humectant(s), photoinitiator(s), etc.). Rheological and wetting modifiers may also be simple molecules, monomers or polymers, which allow the control of the viscosity and/or the surface tension of the ink to enhance the jetting stability and/or the wetting behaviour onto the substrate.

Therefore, from the point of view of designing new inks, the formulator must take into consideration the effect and role of each ink component on the overall process, from the storage in the lab shelf and inside the reservoir in the printer setup, through the jetting process itself to their behaviour after impingement on the substrate, and finally, but not less important, their effects on the health and environment.

### 2.4.1. Types of inkjet inks

The selection of the various components of the ink is done according to the printing technology and the final function of the printed coating or pattern. Usually, inkjet inks are divided according to the nature of the solvent carrier in: water based inks (the main component of the liquid is water), solvent based inks (the liquid is composed of one or various organic solvents) and reactive inks (the main component may undergo into a polymerization reaction after ejection through the nozzle) such as UV inks which polymerize by UV radiation [142].

### 2.4.2. Ink requirements

In terms of inkjet printing applicability, and for a successful deposition, the standard solutions used for spin and dip coating in our research group were adapted for the inkjet deposition in different aspects. Thus, as essential characteristics the ink to be printed should accomplish are:

- Inks should be formulated to meet the specifications of viscosity and surface tension required from the manufacturer.
- Inks should be easy to handle with the suitable printheads and to modify their composition after additive tailoring to achieve the desired jetting performance.
- Inks should be compatible with the materials used in the printer setup.
- For a constant and reproducible drop ejection process, inks must have well controlled fluid properties (viscosity, surface tension, density, concentration) and this characteristics must remain constant over a prolonged period of time.
- Solutes and other additives present in the ink must be soluble and do not precipitate during the lifetime of the ink (i.e. ink homogeneity).

- During the ejection process, an adequate balance between the evaporation rate of the solvent(s) and the additives should be found in order to prevent partial or total nozzle clogging. On the other hand, a fast drying property is desired to achieve a good print quality of the coating or pattern onto the substrate.

As mentioned before, the ink should meet specific physicochemical requirements, which depends on its intended final application. In this understanding, each printer has a specific working window of surface tension and viscosity which enables a proper jetting. For example, general fluid property requirements for a fluid to be used in a piezoelectric printhead usually are within a viscosity range of $0.5mPa \cdot s$ - $40mPa \cdot s$ and between $20mN/m$ and $70mN/m$ for surface tension [143]. Some fluids with properties outside these ranges may be dispensed using this kind of inkjet devices, but with increased difficulty that usually or by a decrease in the final pattern or coating performance.

## 2.4.3. Ink properties influencing inkjet performance

Viscosity, $\eta$, surface tension, $\gamma$, and density, $\rho$, of the ink are the most important properties that affect fluid performance. The description of each property is given in the appendix, while the effects of each one on the inkjet printing process are shortly reviewed below.

### 2.4.3.1. Ink viscosity effects on inkjet printing

Viscosity plays a big role in stabilizing the elongating drop by eliminating the residual drop oscillations after the fluid detaches from the nozzle. Viscosity acts to dampen the instabilities that lead to satellite formation. If the ink is too viscous, then a large pressure is needed to generate a droplet due to viscous dissipation. However, if the viscosity is too low, the presence of satellites with the main drop will alter the final resolution of the printed feature. There is a need to find a trade-off between the volatility and the viscosity of the ink. Usually, high molecular weight and polar solvents have higher viscosities, but at the same time, they have associated lower vapour pressures which means that evaporate more slowly. This fact may affect the time spreading over the substrate. Contrarily, low viscosity inks usually are constitued of low molecular weight and low polar solvents and therefore, they have higher vapour pressures, which evaporate quickly. If the evaporation is too fast, the partial or total clogging of the nozzle may occur due to the precipitation of some precursor at the orifice.

Increasing the ink viscosity also causes an increase in the driving voltage required to create a drop of a fixed velocity. A deep study presenting the effects of ink viscosity on the drop formation is displayed in chapter 4.

### 2.4.3.2. Ink surface tension effects on inkjet printing

Surface tension controls the shape of the drop and is the driving force behind drop separation. The surface tension affects the wetting of ink supply systems, internal components of the printhead and the nozzle plate. This can have a significant effect on printing

reliability because of its effects on meniscus control. Surface tension has a small effect on the driving voltage requirements for a specific device. As surface tension increases, the drive voltage required to achieve the same drop velocity raises. Special attention should be taken with low surface tension inks, in which air suction is easily observed if high drop speeds are achieved.

#### 2.4.3.3. Ink density effects on inkjet printing

An increase in the fluid density requires more energy for expelling a drop of the same size because the kinetic energy is larger. Also, when density increases, the resonance frequency in the channel diminishes. Modifications in the fluid density implies variations in the acoustic speed of the fluid, affecting the actuation optimum pulse width of the waveform (see sec. 4.9.2.2) and the amplitude requirements.

#### 2.4.3.4. Ink vapour pressure effects on inkjet printing

High-vapour pressure inks favour the accumulation of dried solute at the nozzle during the progressive solvent evaporation, making more difficult to have a stable, reproducible and reliable drop jetting process.

### 2.4.4. Governing equations of fluid dynamics

The motion of a fluid of uniform density, $\rho$, and viscosity, $\eta$, is governed by the Navier-Stokes equations [144]. The Navier-Stokes equations are a set of two differential equations that describes the evolution in time of the interface shape and the flow fields along moving surfaces.

The ***rst Navier-Stokes equation*** specifies how the velocity field of the fluid, $u$, changes over time. It accounts for the motion of the fluid through space, along with any internal and external forces acting on it:

$$\frac{u}{t} = -(\quad \cdot u)\, u - \frac{1}{\rho}\quad p + \eta\quad {}^2u + F$$

The terms of the previous equation may be described as follows:

$\frac{u}{t}$ is the derivative of velocity with respect to time.

$-(\quad \cdot u)\, u$ is the convection term: this term originates because of the conservation of the momentum.

$-\frac{1}{}\quad p$ is the pressure term: this term englobes the forces generated by the pressure differences within the fluid, being $\rho$ the density of the fluid and $p$ the pressure.

$\eta\quad {}^2u$ is the viscosity term: in viscous fluids, friction forces cause the velocity of the fluid to move towards the vicinity. The variable $\eta$ is the viscosity of the fluid.

$F$ is the external force term: any external forces such as gravity or contact forces with objects are included in this variable.

In order to reduce the complexity of the problem, general assumptions are usual to impose to the fluid and the ejection system. One of them is that the fluid is assumed to be incompressible. The incompressibility constraint implies that the amount of fluid flowing into the liquid chamber must be equal to the amount of liquid flowing out. This presumption emanates the ***second Navier-Stokes equation*** given by:

$$\cdot u = 0$$

where $u$ is again the velocity field of the fluid.

### 2.4.5. Jettability: key parameters governing fluid dynamics

If the physicochemical fluid properties that govern fluid dynamics, such as density, surface tension and viscosity are included into independent dimensionless parameters, the mathematical analysis becomes more plain. There are four forces acting on the fluid that are typically important in inkjet printing [14, 17]:

- Gravity force: $\rho l^3 g$
- Inertia: $\rho l^2 v^2$
- Surface tension: $\gamma l$
- Viscous force: $\eta l v$

Where $\rho$ is the density, $\gamma$ is the surface tension and $\eta$ is the viscosity of the fluid, $l$ is a characteristic length (usually the nozzle diameter), $v$ is the velocity of a body of liquid and $g$ is the acceleration due to gravity.

The non-dimensionalization of the Navier-Stokes equations gives rise to the independent well-known dimensionless groups. They are:

- The ***Reynolds number (Re)***, which shows the ratio of inertial to viscous forces:

$$Re = \frac{lv}{}$$

- The ***Weber number (We)***, is the balance between inertial and capillary forces:

$$We = \frac{lv^2}{}$$

- The ***Bond number (Bo)*** measures the relative importance between gravitational and capillary forces:

$$Bo = \frac{gl^2}{}$$

- Another number in common use is the ***Ohnesorge number (Oh)***, which rates the viscous to capillary and inertial forces:

$$Oh = \frac{}{\overline{\overline{l}}}$$

But in the inkjet printing field, the ***inverse of the Oh number (Z)*** is currently found, it is a characteristic dimensionless number independent of droplet velocity which rates the inertial and surface forces with viscosity:

$$Z = (Oh)^{-1} = \frac{\overline{l}}{}$$

Therefore, as will be presented in chapter 4, drop formation behaviour may be evaluated by only three independent control parameters: the Ohnesorge number (Oh), the pulse width and the pulse amplitude of the excitation waveform. Fromm [17] predicted that stable drop formation in DoD systems is permitted only when $Z>2$, and for a given pressure pulse, the droplet volume will increase with increasing the value of the $Z$ number [10, 15]. This was later completed for Reis and Derby, who determined that stable drop generation occurs between $1<Z<10$, being the upper limit defined by satellites formation [145], while the lower bound is restricted by the great importance that viscous forces become at high $Z$ numbers. Recently, Jang et al. [18] redefined the printable range as $4<Z<14$ in the same way that we have demonstrated that is possible to produce single stable droplets in regions where $Z$ is significatively larger than 14 by tuning the excitation on harmonics of the liquid fundamental mode [23].

### 2.4.6. Diagnosing typical ink problems

The primary cause of inkjet printing problems is due to the ink drying on the orifice causing a solid block that plugs the nozzle. This problem derives to a major concern in ink design known as the *first drop problem*", where drop size, mass and drop speed differ between the first ejected drop and the subsequents [146, 147]. These issues make absolutely important to define a well-established nozzle cleaning procedure after each use of the printhead. Various flushings with series of solvents of different polarity are performed every time the ink is removed from the printhead.

## 2.5. The printhead

The second actor in the inkjet printing process is the printhead itself (Fig. 2.4).

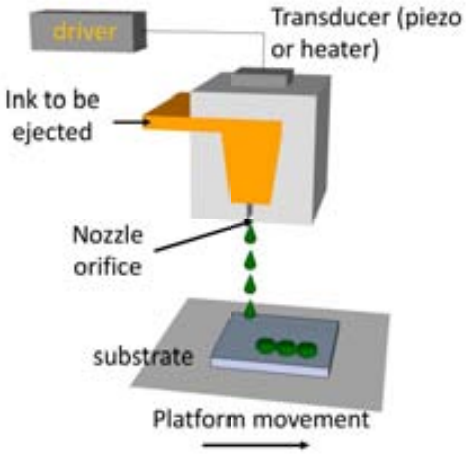


**Figure 2.4.:** Schematic representation of a piezo or thermal printhead.

There are many types of printheads (e.g. thermal, piezo, etc.), however, most of the time was devoted to piezo heads. For this reason, only some aspects regarding to piezoelectric devices will be presented. As mentioned in sec. 2.2.2.2, the actuation of the piezoactuator produces the oscillation of the liquid column which causes the breakup of the liquid thread into drops. The excitation of the piezoelectric printhead is performed by applying an electrical signal during a certain period of time. For this purpose, an actuation waveform is designed which is characterized mainly by means of two parameters: its **amplitude** and its **width**, as any oscillatory wave. There are many actuating waveforms that can be created and designed (from unipolar, through bipolar and sinusoidal waveforms). Some examples are displayed in next Fig. 2.5.

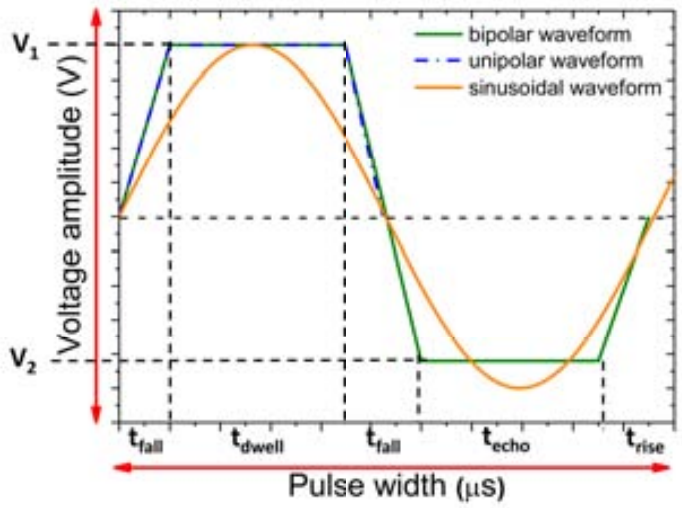


**Figure 2.5.:** Sketch of some examples of piezoelectric driving waveforms and their typical characteristics.

More complex and a myriad of other waveforms are well documented in patents and published in the general bibliography. As will be discussed in chapter 4, the actuating

waveform has a strong influence on the droplet ejection process, controlling and determining both the volume and the velocity of the fired drops.

### 2.5.1. Drop formation

Parameters for drop formation optimization are the width and amplitude of the driving waveform, the nozzle shape (through its impact on the acoustic impedance) and the ink physicochemical properties (see chapter 4). Optical inspection of drop behaviour in flight is essential at the development stage and for each new ink formulation in order to optimize the printing parameters and verify the performance of the ink. Next Fig. 2.6 exhibits an example of drop formation optimization using as an ink a LSMO precursor solution.

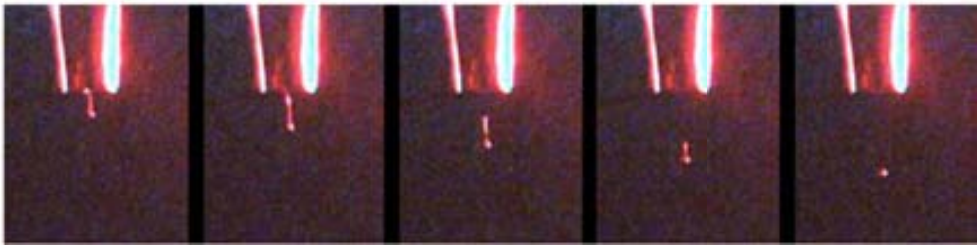

**Figure 2.6.:** Drop formation sequence of a 0.3M LSMO precursor solution. The solution was printed by using a piezohead with a nozzle orifice of $60\mu m$ with voltage amplitude $V_1 = +25V$; $V_2 = -20V$; corresponding times $t_{rise} \sim 3\mu s$; $t_{dwell} \sim 11\mu s$; $t_{fall} \sim 3\mu s$; $t_{echo} \sim 11\mu s$; $t_{final\,rise} \sim 2\mu s$ and frequency $f = 100Hz$.

### 2.5.2. Drop and line pitch, rastering mode and printing matrices

***Drop pitch*** ($\Delta x$) and ***line pitch*** ($\triangle y$) are relevant parameters in inkjet printing which will appear many times throughout this work. They describe the distance between the center of two drops in x and y directions, respectively. Drop and line pitch can be measured in linear units ($\mu m$ or $mm$) or as a rate, for instance in dots per inch ($dpi$) with a larger number meaning higher resolution.

All the printing experiments were performed using the *rastering mode*, represented in Fig. 2.7, which basically consists on covering each row and column of the whole surface to be printed. In our case, the printhead is stationary and the substrate moves at a constant speed. The printing procedure starts at the upper left corner of the substrate. First, the XY stage covers the whole row from left to right. When the first row is completed, then the stage displaces the line pitch $\Delta y$ down and the printing of the second line starts from right to left. The process is repeated until the $n^{th}$ printed line covers the entire surface.

For printing continuous coatings, the platform movement and the drop ejection were not synchronized. From one hand, the drop frequency (i.e. the number of drops per second) is selected. On the other hand, the platform moves at a constant speed, $10mm/s$, therefore, by dividing the speed of the platform by the drop frequency, the drop pitch is, therefore, directly established. However, for printing patterns, the movement of the platform and drop triggering were synchronized (e.g. droply synchronized). At each $\Delta x$, a

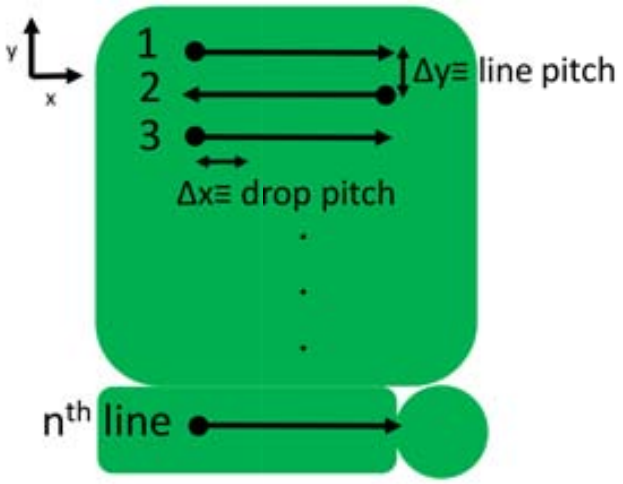


**Figure 2.7.:** Schematic representation in what consists the rastering mode. Our prints begin at the upper left corner, continues till the upper right edge, then goes down and to the left border and proceed on the right until the whole surface is printed.

drop is launched based on the corresponding pixel of a pre-loaded bitmap image, and once the end of the line is reached, the platform displaces a line pitch $\Delta y$. By defining the drop pitch in both x and y directions, it is established the *printing matrix*. Throughout this work, most of the experiments were performed using squared matrices, unless otherwise specified. Then, $\triangle x = \triangle y$ and only drop pitch will be given.

## 2.6. The substrate

The substrate is the last but not the less important element which take a fundamental part in the whole inkjet process. An essential point in the inkjet manufacturing technology is the process by which consecutive drops interact between them and with the solid substrate to form the final deposit. In this regard, the selection of the substrate, the impingement of the ink drops onto it, as well as the interaction and connectivity between them and with the substrate are critical aspects that will determine the dot quality and therefore will restrict the final morphology and performances of coatings and patterns.

### 2.6.1. The behaviour of a drop onto a solid substrate

To control the feature size of the inkjetted design, a basic understanding of the processes that take part during drop impact, spreading, fusion and solidification processes as a function of ink and substrate properties and drive waveform parameters is of great relevance. Those relationships are especially important, since they establish ink design and printing relationships that determine the limits over which well-defined structures can be printed.

#### 2.6.1.1. Drop impact, spreading and fusion

In spite of more than 100 years of research since the work of Worthington [148], the complex phenomenon of drop impact and spreading is still far from being fully understood and continues being studied both theoretically and experimentally [14, 113]. From an inkjet point of view, it is important to evaluate the fluid dynamics and control the behaviour of drops onto the substrate, from the moment when they impact onto the substrate in liquid form to the instant when the final pattern morphology is attained. In the first instance, it is relevant to control the location where drops land and ensure that they remain there. Secondly, it is necessary to identify and control the interactions that occur between drops and with the substrate prior to solidification. Given that the time scale for evaporation is much larger than the deposition time between two drops, they still remain in a liquid state once they impinge and merge onto the substrate.

#### 2.6.1.2. Phenomenology

Schiaffino and Sonin [149] proposed that the process of a droplet hitting a substrate with a certain velocity might be generally divided into three stages:

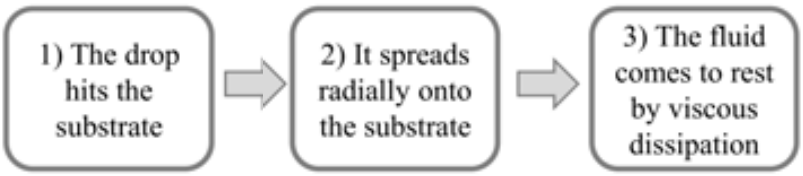


**Figure 2.8.:** General phenomenology of drop impact process. The whole process lasts less than few hundreds of ms.

First, the drop hits the substrate, then it spreads onto it until in a last step, the drop reaches the equilibrium state (see the process schematized in Fig. 2.8). In next sections, an insight into the phenomenology that take part during the drop impact and spreading processes will therefore be outlined.

#### 2.6.1.3. Drop impact onto the substrate

In the first stage, the droplet makes contact with the substrate. The result of drop impingement depends on the impact speed, the drop size, the direction of the drop relative to the substrate, the ink physicochemical properties (e.g.$\rho$,$\gamma$,$\eta$), the particular substrate-ink interaction [150] and by the intrinsic parameters of the substrate such as wettability and roughness. Depending on such variables, the splashing phenomenon may occur [21]. Usually, this splashing event may be observed in droplets with $We$ numbers from 100 to 1000 [113].

#### 2.6.1.4. Drop spreading and equilibrium

Later, as the film expands, liquid travels radially outwards. At this stage, the contact angle $\theta$ that makes the ink with the substrate and the surface energy of the substrate (see Appendix) are indispensable parameters to be considered. The final spreading may be controlled by the freezing of the contact line, which has a large influence on the final solid shape of the droplet as we will review later. In the final step, depending on the contact angle and the $We$ and $Re$ numbers, the film spreads and/or undergoes a succession of spreading and receding events until the contact line is arrested and a final contact angle is reached [114]. After drop impingement onto the substrate, the contact angle changes from the advancing to the receding contact angle (see Appendix). The receding speed depends largely on the impact velocity, the viscosity and surface tension of the ink and the substrate-ink interaction. When the drop impact speed and the surface tension of the ink increase, then the contact line retraction increases. At the end, the fluid comes to rest after a serie of inertial oscillations that are dampened by viscous dissipation.

In the initial period of the process, the spreading is driven by the kinetic energy of the impacting drop where drop diameter $b$ increases very fast [10,19,21,118,151,152]. In this first stage, the kinetic energy is dissipated and partly converted into surface energy as the drop is deformed. After the initial rapid spreading, $b$ is almost constant for a period of time. Spontaneous spreading then begins, and the variation of $b$ with time is well fitted by a power-law relationship as shown in Fig. 2.9. Finally, when the equilibrium is reached, $b$ remains constant. At this stage, the drop can be modelled to obtain the

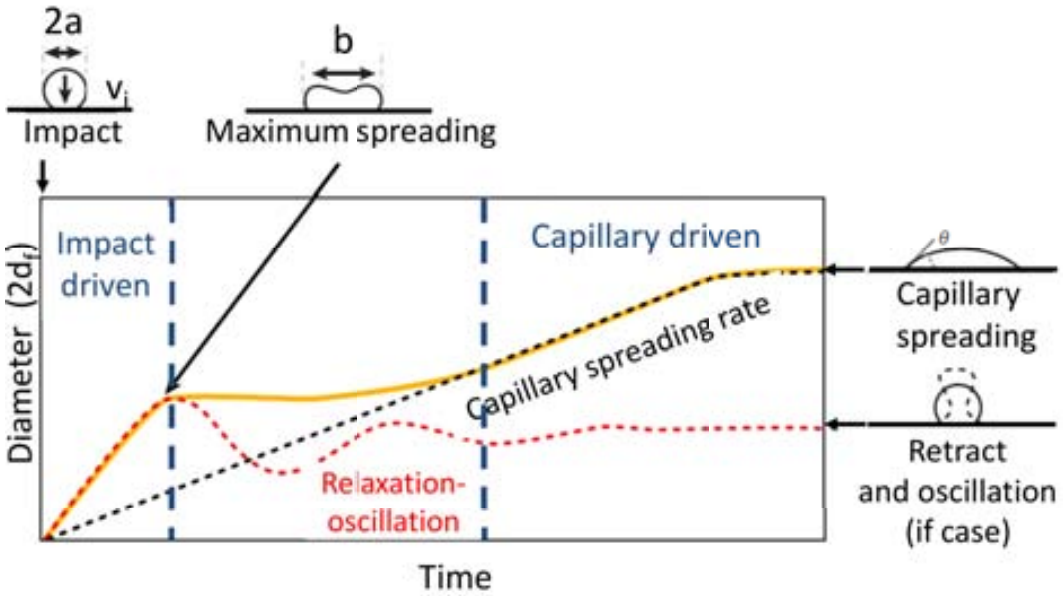


**Figure 2.9.:** Schematic illustration of the sequence of events that occurs after drop impingement onto the substrate. $\theta$ is the contact angle, $2a$ is the initial droplet diameter before impact, $b$ is the drop diameter at maximum spreading, and $v_i$ is the drop velocity at impact. In orange, it is displayed the drop diameter $b$ trend during the different stages of drop impact and spreading and finally when the equilibrium is reached. Adapted from [10].

maximum spreading of the drop [153] ($\xi_f$; $\xi_f = \frac{b}{2a}$; where $b$ is the drop radius onto the substrate and $a$ is the drop radius in flight). The final equilibrium spreading ratio is primarily determined by solid-liquid interactions and varies slightly with drop impact speed. Measuring and predicting the drop radius after impact provide a quantitative value of the pizel size [154–163].

#### 2.6.1.5. Adjustement of wetting properties

In some cases, it is absolutely demanding to tune solution properties in order to increase or decrease the wetting properties, according to the final printing application. For instance, additives are usually introduced in the ink formulation to increase the contact angle $\theta$ with the substrate to make patterns or more defined drawings or patterns. Or, in the case of printing complete layers, the functionalization of the substrate of the surface (e.g. plasma treatment [164], deposition of a very thin layer of a monomer) or the application of a primer onto the substrate are conventional substrate treatment to increase the wetting properties and therefore, favour the obtention of full coatings during printing.

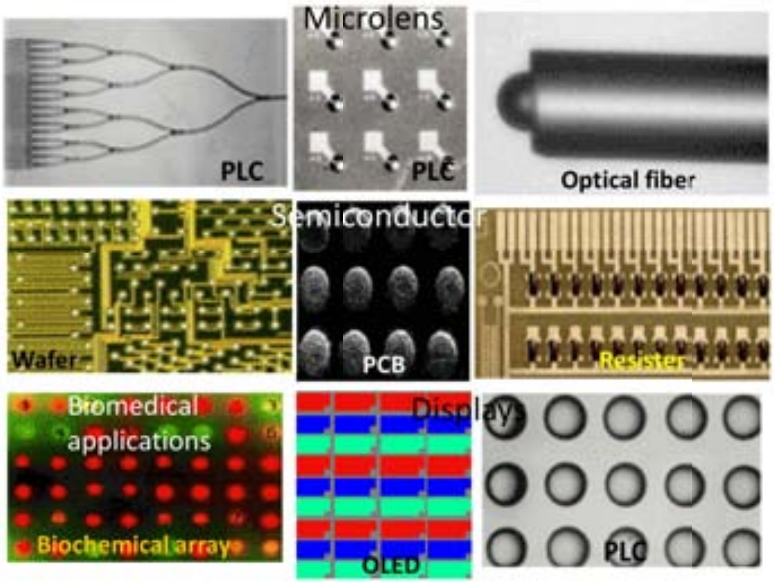


**Figure 2.10.:** Some examples of the broad range of applications and fields in which inkjet printing technology is gaining influence.

## 2.7. Applications

Over the past few years, inkjet printing has been implemented in an broad range of new applications [22] such as organic light emitting diodes (O-LEDs) [165], solar cells [32,166], electronic devices [35,36,167–170], polymer displays [16,33,57,58,171,172], rapid prototyping [173,174], biochemical arrays [175], ceramic component manufacture [176,177], biotechnology [34], organic semiconductors [31,178], etc. but there have been few reports of functional oxide coatings, particularly of superconductors [23,25,179–181] where biaxial texture and quality of grain boundaries are of great relevance. Figure

Fig. 2.10 displays the broad gallery of sectors and applications that inkjet printing has reached in the last years.

# 3. Experimental methodologies

This chapter will introduce the experimental procedures employed in the present work. Firstly, it will be described the experimental protocols carried out in the synthesis of the precursor inks and their characterization. The methodologies used for viscosity, surface tension and contact angle measurements will be briefly depicted. Secondly, the experimental inkjet devices used for functional oxide deposition are also presented as well as the precursor decomposition thermal treatments to the final crystalline phases. The thermal treatments performed to the substrates and the experimental techniques used to characterize the morphology, the structure and the magnetic and superconducting properties of the resultant films will be also shown.

## 3.1. Precursor solution preparation

In order to form functional patterns and layers, appropriate solutions of ceramic precursors have been prepared. As mentioned before, throughout this report, various functional ceramic oxides have been deposited, including $YBa_2Cu_3O_{7-x}$ (YBCO), $La_{0.7}Sr_{0.3}MnO_3$ (LSMO) and $Ce_{0.9}Zr_{0.1}O_{2-x}$ (CZO). According to the final application, these solutions have been properly tuned with some rheological and wetting modifiers in order to improve the jetting stability and the wetting behaviour on the substrate.

### 3.1.1. $YBa_2Cu_3O_{7-x}$ precursor solutions

The Metalorganic Decomposition (MOD) Route was used to prepare YBCO films shortly after the discovery of HTS. Y,Ba,Cu-carboxylate salts (e.g. acetates) were firstly used as YBCO chemical precursors, but the poor performances of the resultant YBCO films evidenced carbon contamination, primarily in the form of $BaCO_3$. Gupta et al. [44] offered a possible solution to this problem. They found that replacing the traditional acetate organic ligand with the fluorinated one (trifluoroacetate, TFA) caused the formation of metal fluorides (e.g. $BaF_2$ instead of $BaCO_3$.) upon decomposition. Such metal fluorides were further decomposed in humid atmosphere via HF removal, leading to the conversion to the metal oxides, and ultimately to YBCO. Moreover, $BaF_2$ decomposition was achieved by the water content in the gas flow, making possible then, a fine tuning of the film growth rate through the water pressure parameter. Several modifications of the MOD-TFA route have been reported [182–184] and currently YBCO films with comparable performances to the in situ approaches are obtained [4, 44, 182, 184].

The YBCO precursor solutions used for YBCO coatings are based on the standard YBCO-TFA precursor solution which has been optimized by members of our research

group at ICMAB [184]. This solution was used to obtain the YBCO films displayed along this work and is also the initial point for YBCO patterning purposes. It basically consists of metal-trifluoroacetates salts, i.e. $Y(TFA)_3$, $Ba(TFA)_2$ and $Cu(TFA)_2$ dissolved in ethanol. The molar concentration of the TFA salts was 0.25M, 0.50M and 0.75M which lead to the desired stoichiometric ratio of 1:2:3.

Historically in the group, the synthesis of the metal-trifluoroacetates salts was carried out by means of the reaction from commercial YBCO powder. The choice of starting from the commercial YBCO powder instead of the isolated TFA salts was related to the better reproducibility achieved. The lack of stoichiometry and the water contamination (>2% in weight), which lead to long purification steps, were the main drawbacks when starting from the separated salts [28]. In this section, it will be described both procedures. First, the synthesis of the TFA salts from YBCO commercial powder, which the most films and patterns along this thesis have been obtained, and then, from the isolated metallic salts.

#### 3.1.1.1. YBCO precursor solution from reaction of commercial YBCO powder

In order to form functional YBCO ceramic coatings and YBCO tracks, YBCO-TFA precursor solutions were prepared using ethanol as solvent.

The standard YBCO-TFA precursor solution is based on the chemical reaction of YBCO powder (yttrium barium copper oxide, Solvay) with an excess of trifluoroacetic anhydride (TFAA, Aldrich, 99%), a small amount of trifluoroacetic acid as a catalyst (10% volume, TFAH, Aldrich, 99%) and freshly distilled acetone as solvent (PA, Panreac) in an inert atmosphere. The mixture was heated at 50°C for 72h. Afterwards, the resulting solution was evaporated in vacuum and the residue was dissolved in absolute ethanol (DC, Panreac) till the final volume and desired concentration. The resulting solution was kept in a sealed vial under Ar atmosphere [184]. The sum of metals concentration ranges from 0.5M to 1.5M, although the 0.5M is our standard YBCO precursor ink for inkjet printing. It was achieved by simply diluting with ethanol the initial YBCO-TFA ethanol based precursor solution. Mention that throughout this research, the concentration specified for YBCO precursor solutions, both for films and patterns, refers to the concentration of sum of metals.

For YBCO patterning, we have employed a 0.5M YBCO-TFA/ethanol solution (sum of metals concentration) with the addition of a 5% w/w of 1,3-propanediol (Sigma Aldrich).

#### 3.1.1.2. YBCO precursor solution from separated salts

Yttrium and copper trifluoroacetate salts were prepared starting from commercial metallic trifluoroacetate salts (Alfa-Aesar and Aldrich). Barium trifluoroacetate was prepared by dissolving $BaCO_3$ (99%, Panreac) in trifluoroacetic acid using a standard procedure. In order to remove the waters of crystallization of $Ba(TFA)_2 \cdot xH_2O$ and $Cu(TFA)_2 \cdot xH_2O$, a drying procedure was carried out using a thermostatic vacuum dryer (Vacuo-Temp, from Selecta) operating at $10^{-2} mm$ Hg and T~85°C. We assumed that the salts were dehydrated when their weights (analytical scale) were found to be constant. Furthermore, in the case of $Cu(TFA)_2$, the change of colour from blue (hydrated) to green

(dehydrated) was a clear signal to identify the end of the drying process. The isolated TFA-salts were then dissolved, in the appropriate ratio, in anhydrous ethanol (Sigma Aldrich). After filtration through syringe filters (Teflon membrane, with a pore size of $0.2\mu m$), the volume was brought to the volume which gives the final total ion concentration. A 1.5M total metal concentration is commonly prepared. For inkjet printing purposes, the standard 1.5M solution is diluted to the final concentration, usually 0.5M (total metal concentration).

## 3.1.2. $La_{0.7}Sr_{0.3}MnO_3$ precursor solutions

### 3.1.2.1. LSMO propionate precursor solution

The metallic propionates, $La(CH_3CH_2COO)_3$, $Sr(CH_3CH_2COO)_2$ and $Mn(CH_3CH_2COO)_2$ were obtained by reaction of the corresponding acetates in propionic acid (Sigma Aldrich). Then, they were dried in vacum for 12h at 90°C. Afterwards, adequate amounts to obtain the desired metal stoichiometry, $La_{0.7}Sr_{0.3}MnO_3$ were weighted in order to get the final volume and desired concentration. For LSMO films, usually $10mL$ solutions of concentration of 0.03M (in Mn) were prepared with propionic acid as a solvent. These solutions remain stable and clear for almost one month storage.

### 3.1.2.2. LSMO acetate precursor solution

A more environmental friendly LSMO precursor ink was prepared based on the metallic acetates, $La(CH_3COO)_3$, $Sr(CH_3COO)_2$ and $Mn(CH_3COO)_2$. First, under vigorous agitation, the three metal acetates, in the stoichiometric amounts, were separately dissolved in mili-Q water (conductivity $\sim 17.7 M\Omega/cm$). Due to the poor stability of this solution, the metallic acetates were stabilized with chelating agents. In this understanding, the Sr and La acetates were dissolved in mili-Q water containing an excess of glycine (Sigma Aldrich) and the Mn acetate was dissolved in mili-Q water with an excess of ethylenediaminetetraacetic acid (EDTA, Sigma Aldrich). After two hours of stirring, the three independent solutions containing each one the metallic acetate and its stabilizing agent were mixed all together. The resultant solution was left under constant and intense agitation 1.5h. After this time, a solution containing EtOH/$H_2O$ (90:10 v/v) and polyethyleneglycol (PEG, MW=20000g/mol; Sigma Aldrich) was added to obtain the desired concentration and to control the rheological and wetting properties. The final solution was stirring up during 12h and finally filtered with syringe filters of $0.2\mu m$ of porous diameter. Solution concentrations in Mn up to 0.1M have been obtained, although, for LSMO inkjetted films, the concentration in Mn ranged from 0.01M to 0.04M (in Mn). It is worth to remark that those solutions tend to oxidize in contact with air, therefore, they must be kept hermetically sealed under argon atmosphere in a dark place. In this conditions, LSMO acetate based precursor solutions were stable for a month.

For LSMO patterning purposes, it was used an acetate based LSMO precursor solution with some modifications. By taking benefit of the stability of the propionate based LSMO precursor solution and the more environmental chemistry of the acetate based LSMO precursor ink, for LSMO patterns it was prepared a new and alternative ink

formulation. The metallic acetates, $La(CH_3COO)_3$, $Sr(CH_3COO)_2$ and $Mn(CH_3COO)_2$, were dissolved in mili-Q water as in the previous formulation, however, without chelate addition, the final concentration is achieved with a mixture of isopropanol and propionic acid 34:1 (v/v). The final solvent relation is 65:34:1 in volume. Hermetically sealed and in proper conditions of light and temperature, 0.05M solutions (in Mn) are stable for more than six months, which opens the possibility to be upscaled.

### 3.1.3. $Ce_{0.9}Zr_{0.1}O_{2-x}$ precursor solution

#### 3.1.3.1. CZO propionate precursor solution

CZO precursor solution was prepared by dissolving, first, a certain quantity of zirconium (IV)-2,4 pentanedionate $Zr(CH_3COCH{=}COCH_3)_4 \cdot xH_2O$ (Alfa Aesar) in propionic acid (Sigma Aldrich), at room temperature in adequate amounts according to the stoichiometric relationship [28]. Then, it is added the cerium (III) acetylacetonate hydrate $Ce(CH_3COCHCOCH_3)_3 \cdot xH_2O$ (Sigma Aldrich), also at $RT$. The solution at this point becomes between orange and yellow. After the addition of both precursor salts, the solution is heated at 40-50°C during 2h adopting, finally, a strong yellow colour. After filtration through a syringe filter, (PTFE membrane, with pore size of $0.2\mu m$), the volume was brought to the final concentration. Precursors solutions of 0.075M and 0.15M (total metal concentration) were prepared remaining stable no more than three weeks.

## 3.2. Precursor solution characterization

Due to the great relevance that play ink properties in determining essential processes in inkjet printing such as drop formation, drop spreading and wetting; after ink preparation and before deposition, the physicochemical parameters of all the inks were routinely analyzed. The properties to control are mainly viscosity, surface tension, contact angle, density, metal concentration, water content and pH. This deep study permits to carry out a quality control as well as determine if the as-prepared inks are found to be jettable with our inkjet printheads.

### 3.2.1. Metal concentration and water content determination

The sum of metals concentration of the YBCO precursor solutions was verified by standard chemical redox titrations for yttrium and copper analysis. For barium determination, a gravimetric procedure was performed. These analyses are crucial in order to assess the metal stoichiometry of solutions in order to readjust eventual non-stoichiometries by addition of the required metallic salt.

Water content of the solutions was examined by Karl-Fischer titration [185].

## 3.2.2. Density measurement

The density of solutions was obtained by weighting in an analytical balance $1mL$ of solution for three times.

## 3.2.3. Viscosity measurement

Instruments which measure the viscous flow behaviour of fluids are described as viscometers and, if they can also measure the viscoelastic properties of fluids are called rheometers.

### 3.2.3.1. Measuring principle

The rheometer we use to measure the viscosity is a HAAKE RheosStress RS600 (Thermo Electro, GmbH) equipped with a low inertia torque motor. The drive shaft of the motor is centered by an air bearing which ensures a virtually frictionless transmission of the applied torque to the sample. The deformation of the sample is detected with a digital encoder processing 512 million impulses per revolution. Available geometries for the sensor systems include coaxial cylinders, cone and plate and parallel-plates. One might imagine that the different sensor systems result from bending the flat plates shown in Fig. A.1.

Two modes are available in the existing rheometers:

1. The torque is measured at certain pre-set rotational speed: this mode is called *controlled rate method, CR*".
2. The rotational speed or deformation is measured at certain pre-set torque value: this is thermed *controlled stress method, CS* .

In rheometers operating in accordance with the *CR principle*, a speed (angular velocity) is pre-set which causes a shear rate in the sensor system filled with the sample. The torque required for achieving and maintaining the desired shear rate is related to the ***viscosity*** parameter. *CS-rheometers* are designed to operate according to the reversed principle. In this mode, a torque (shear stress) is pre-set and the resulting deformation, i.e. the resulting angular velocity (shear rate), is measured.

The relevant operational differences between both modes are summarized in the next Tab. 3.1:

| Mode | Input | Measurement | Result |
|---|---|---|---|
| CR-mode | shear rate $\dot{\gamma}$ | shear stress $\tau$ | shear stress $\tau$= f (shear rate $\dot{\gamma}$) |
| CS-mode | shear stress $\tau$ | deformation $\gamma$ | log deformation $\gamma$= f (log shear stress $\dot{\gamma}$) |

**Table 3.1.:** Summary of operational modes in conventional rotational rheometers.

The shear rate $\dot{\gamma}$ is proportional to the rotational movement (angular velocity $\Omega$) and to the geometrical shear factor $M_{factor}$: $M_{factor} = \Omega \cdot \dot{\gamma}$, so high angular velocities $\Omega$

mean high shear stresses. Besides, high $M_{factor}$ values stand for very small $h$ gaps. The angular velocity $\Omega$ results from the following equation $\Omega = \frac{2 \cdot \pi \cdot n}{60}$, where the rotor speed is $n$. The shear stress $\tau$ is proportional to the torque $M_d$ and to a characteristic geometry factor, which is identified as a shear stress factor $A_{factor}$: $\tau = M_d \cdot A_{factor}$. Then, high $M_d$ torques mean also high shear stresses. Large values of $A_{factor}$ stand for small sensors. The factor $A$ is calculated as described in next equation: $A_{factor} = \frac{2}{\pi R^3}$.

From the available sensor systems, in our case, for all the viscosity measurements, we have used a two parallel-plate configuration which allows measuring the viscosity at high shear rates (86000 $s^{-1}$) to approach the experimental conditions at the nozzle. Characteristic parameters of that system are the radius of the plate $R$ and the variable gap $h$ between the stationary and the movable plates (see Fig. 3.1).

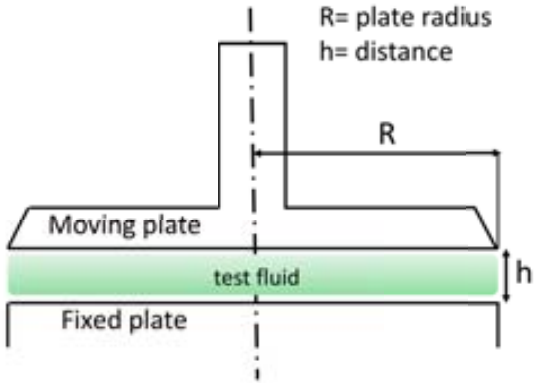


**Figure 3.1.:** Two-parallel system used as sensor system in our viscosity measurements.

The $M_{factor}$ is calculated as follows: $M_{factor} = \frac{R}{h}$ where again $R$ is the plate radius and $h$ is the distance or gap between the fixed and the movable plate. Particularly, the sensor we employed for viscosity measurements was a PP60 sensor system with $R = (30 \pm 0.006)$ $mm$, $A_{factor}$= $(23580 \pm 23.58)\frac{Pa}{N \cdot m}$ and $M_{factor} = 30s^{-1}$. The viscosity is then obtained by using the expression: $\eta = \frac{A_{factor} \cdot M_d}{M_{factor} \cdot \Omega}$.

Viscosity measurements were performed along this work at room temperature.

#### 3.2.3.2. Common sources of errors in viscosity measurements

Usual errors in viscosity measurements may come from the instrument, the sample's handling and the sample itself. For instance, common errors may be derived from the motor which generates the torque, the speed display or the test temperature settings. Every time the sensor system is inserted in the motor shaft, a zero setting should be performed. Once it is done, is advisable do not remove the sensor. Also, some innaccuracy related problems of sample's handling may exist. Regarding sample filling, we must take all necessary precautions to avoid trapped air between plates and minimize as much as possible the solvent loss in order to reduce errors in viscosity measurements. We should pay attention to the friction heating that is produced at high shear rates which may produce an appreciable increase of sample's temperature. Control of the temperature of

the sample during the test is mandatory since the viscosity shows a strong dependence with temperature.

### 3.2.4. Surface tension measurement

The measurement of surface tension in liquid-vapour and liquid-liquid systems becomes a relatively easy task, however, when the system involves solid surfaces, the determination of surface tension becomes more complex. There are numerous methods for measuring surface tension [186–189] that we will not discuss here. In this section, only different experimental techniques to determine $\gamma$ will be briefly mentioned. These include:

- The Wilhelmy plate technique: in which the force vertically acting on the plate by the liquid meniscus when the plate makes contact with the liquid is detected.
- The du Noüy ring method: in this technique, the maximum force to detach the liquid membrane from a ring or loop of wire that is hung parallel to the liquid surface is registered.
- The capillary rise or depression technique: in which the height of a liquid column in a capillary is measured after being dipped into the tested liquid.
- The maximum bubble-pressure method: this method is based on measuring the maximum pressure to force a gas bubble out of a capillary into a liquid
- The drop volume or weight method: in this method, the weight or volume of a drop falling from a capillary is measured.
- The micropippette technique: the interfacial tension is calculated from the minimum pressure at which the drop extends a hemispherical protrusion into the pippette.
- The *pendant drop method*: it is based on the idea that the shape of a pendant drop is determined by the balance between surface/interfacial tensions and an external force, such as gravity. One such tecnhique is the *ADSA (Axisymmetric Drop Shape Analysis)*, which determine the liquid/fluid interfacial tensions from the shape of axisymmetric menisci due to gravitational force. As is the methodology used throughout this work to determine the surface tension of the inks and the contact angle with the substrate, it will be shortly reviewed below.

#### 3.2.4.1. ADSA procedure

The basis for the determination of the contact angle and surface tension is the image of the drop on the surface or the drop hanging from a syringe needle, respectively.

The ADSA (Axysimmetric Drop Shape Analysis) technique [190–192] for the sessile and pendant drop measurements accomplish the contact angle and surface tension determination by finding the best fitting of the theoretical drop profile to the real one [193]. Theoretically, the equilibrium shape of a liquid drop can be numerically determined by solving the Laplace equation of capillarity together with proper boundary conditions. Then, ADSA software creates an objective function, which represents the discrepancy between the theoretical calculated Laplacian curve and the physical observed drop profile.

By considering the contact angle and surface tension adjustable parameters, ADSA minimizes the objective function numerically using the Newton-Raphson method. Once the best fit of the Laplacian curve to the real drop shape is found, the corresponding contact angle and surface tension are the true values. The various existing methods for calculating the contact angle and surface tension differ in the mathematical model used for analyzing the drop shape. The tangent, the circle fitting method and the Young-Laplace methods are some examples for contact angle and surface tension calculation. The best fit curve is identified by finding the minimum deviation of the experimental drop profile from the theoretical one. This function is computed by summing the squares of the normal distances between the calculated curve and the experimental points. Therefore, the theoretical Laplacian curve which minimizes the objective function is used to calculate the contact angle and surface tension. When using ADSA, is important to acquire good quality images so that the accuracy of selecting coordinate points along the experimental drop profile can be guaranteed. Fig. 3.2 shows the views of two drops taken by the DSA100 equipment. ADSA technique was used to determine the contact angle. In this technique, a high-resolution camera is mounted on a microscope and drops are illuminated from the side. The contour line of the drop and the baseline result from the positions of the maximum contrast. The video signal of the sessile drop is transmitted to an image processor, which digitize the image. Finally, data computation is performed in order to determine the surface tension and contact angle values. Meaningful differences of the contact angle values are only considered above 10°. We are not able to solve differences for smaller values, saying in practice that the solution completely wets the substrate.

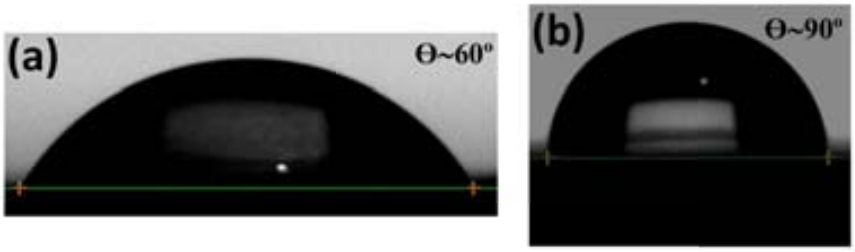


**Figure 3.2.:** Two examples of distilled water drops onto Ni metallic tape taken by the DSA100 equipment. In these case, ADSA (Axysimmetric Drop Shape Analysis) technique was used to determine the contact angle. In this case, the different contact angle comes from the different surface treatment submitted to these samples.

Through all this research, surface tension data was obtained by the evaluation of the video images of a pendant drop using the ADSA technique (sec. 3.2.4.1) and the DSA100 equipment (KRÜSS, GmbH) [194]. To summarize, if a drop of liquid is hanging from a syringe needle, then it will assume a characteristic shape and size from which the surface tension can be determined (Fig. 3.3). A requirement is that the drop is in hydromechanical equilibrium. When in hydromechanical equilibrium, the force of gravity acting on the drop and depending on its particular shape, corresponds to the Laplace pressure, which is given by the curvature of the drop contour at this point. After carrying out a numerical integration method, the theoretical drop profile is calculated. When the theoretical drop profile corresponds to the measured one, then the surface tension can

be calculated. Next Fig. 3.3 shows an image of a drop hanging from a needle and its numerical processing to determine the surface tension of the ink.

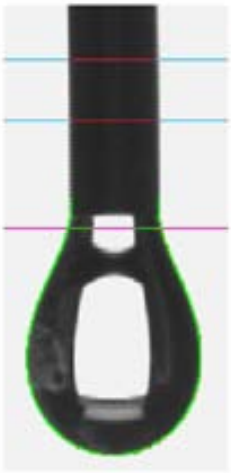

**Figure 3.3.:** Image of a drop hanging from a needle and its numerical processing to determine the value of the surface tension.

### 3.2.5. Contact angle measurement: characterization of the wettability of solid surfaces

Due to the great importance of contact angle measurements to study wetting phenomena, much effort has been devoted in the last decades to develop accurate methods for contact angle determination [195]. There are a variety of simple and inexpensive techniques for measuring contact angles [196], which will be briefly outlined in this section. For a deep description, the reader is directed to explore the myriad of reviews existing in the literature. For contact angle determination, the most common techniques [197–199], already described in the previous section, include:

- The Wilhelmy plate method
- Interference microscopy
- The capillary rising method
- The tilting plate method
- The captive bubble method
- The *sessile drop method*

The high sensitivity of contact angle measurements becomes at the same time both a problem and a challenge [200] and their accuracy can be strongly affected by the quality of the solid surface, the surface state, the temperature as well as the atmosphere at which the measurement is performed, and the deposited drop volume.

Throughout this work, contact angle and surface tension measurements were extracted from analysis of the images of $2\mu L$ digitized sessile drops photogtaphs, performed by means of a DSA100 equipment (KRÜSS, GmbH) by using the ADSA technique [196, 201, 202].

## 3.3. Precursor solution deposition

### 3.3.1. Description of inkjet printing devices

Throughout this research, inkjet printing was carried out using three kinds of different printing set-ups.

The system most employed was a proprietary mechanical system which incorporates **two single nozzle printheads**: a commercial piezoelectric actuated dispenser (Microfab Technologies, MJ-AB-01-60) with a $60\mu m$ nozzle diameter and an electromagnetic one with a $90\mu m$ nozzle diameter (Domino) (see Fig. 3.5a). Since the most part of this thesis was developed using the piezoelectric printhead, we find appropriate to show a zoom-in of Fig. 3.5a in order to have an in-depth view of this PZT printhead (Fig. 3.5b). For this $60\mu m$ nozzle diameter piezoelectric printhead, the drop volume was tailored by adjusting the compensation pressure, modifying the pulse width and amplitude of the piezoactuator waveform, and also by tuning the physicochemical ink properties such as the viscosity and the surface tension. In all the experiments presented throughout this work with this piezoelectric printhead, drop volume ranged between $10pL$ and $100pL$. In the same way, drop volume in the electromagnetic printhead was tuned by adjusting the opening voltage of the electrovalve, the aperture time of such valve and the ink pressure. Drop volumes obtained by the electromagnetic printhead oscillate from $10nL$ to $60nL$. Both printheads are stationary during printing. They were mounted onto a computer-controlled XY movable stage where the substrate is placed with a positioning repeatability of $2\mu m$. In all the studies described in this manuscript, the substrate platform moved at $10mm/s$. The gap (i.e. the distance between the nozzle and the surface of the substrate) should be set large enough to obtain the spherical like shaped drop after recoiling of the liquid thread and also before impacting on the surface. However, in order to avoid perturbations of drop trajectory, this gap should be set as short as possible. During the printing experiments, it was set at about $1.5mm$. Of special importance is the ability of this printer system to work in a controlled atmosphere when humidity sensible inks are required to print. All the printings were performed at 22°C and below 15% of relative humidity. Moreover, to prevent the fluid from dripping from the nozzle under the influence of gravity, a small negative pressure with a venturi system is applied, assuring that the pressure in the ink reservoir is slightly lower than ambient pressure.

Our printer includes a *stroboscopic visualization system* based on a LED which flashes at the same frequency that drops are generated, and a digital camera, which works in bright field mode (see next Fig. 3.4):

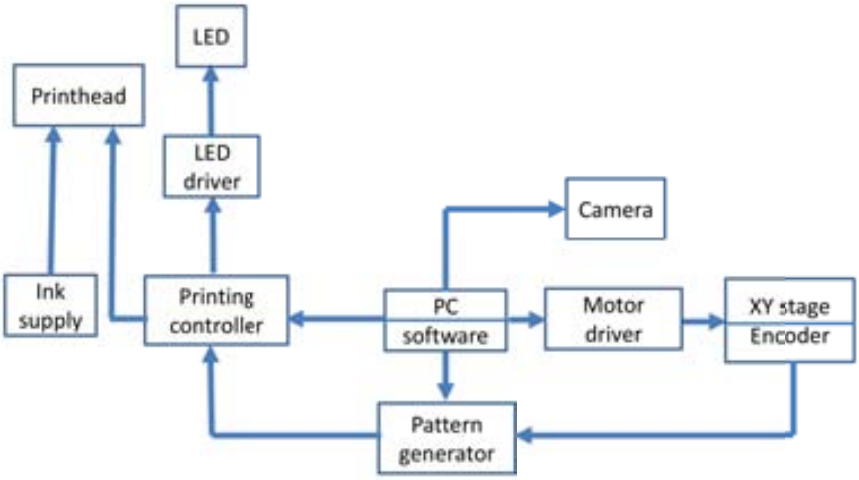


**Figure 3.4.:** Schematic representation of our proprietary inkjet system.

The strobe signal was generated by using the drop ejection trigger signal as a reference. The operator observes the stability of the drop shape and drop size by superimposing some tens of single events in an individual frame, freezing the position of the micron sized-drop. In addition, this enables to follow the drop formation and emission processes by adjusting the strobe delay time with a resolution of $1\mu s$ [152, 203]. The presence or not of blurry images allows us to monitor the repeatability and reproducibility of drop formation process. The whole drop process, from drop formation to drop impingement on the substrate was registered in the computer by a 1.3Mpixel commercial camera with an objective of $22mm$ focal length and a frame rate of $25fps$.

In the course of this thesis, a two-month stage in the University of Ghent (Department of Inorganic and Physical Chemistry) was performed to learn about multinozzle printer operation. In that laboratory, one of the inkjet devices they dispose is the commercial **Dimatix Materials Printer 2800** (DMP-2800, Fujifilm Dimatix Inc. [204])(see Fig. 3.5c). The DMP printer is equipped with disposable cartridges able to dispense droplets with nominal drop volumes between 1 and $10pL$. In our case, $10pL$ piezo cartridges with a capacity of $1.5ml$ were utilized. Each single-use cartridge has 16 nozzles linearly spaced at $254\mu m$ (Fig. 3.5d). In this system, the jetting process is achieved by applying an electrical pulse, defined by a jetting waveform, to piezo actuators located on the walls of the pumping chamber. The Dimatix Materials Printer has also a waveform editor and an integrated drop watcher system to allow waveform optimisation for its 16-nozzle cartridge and previously verify the nozzle jetting, consistency and reliability of drop formation. The printer operates by moving the printhead assembly across a platen. The temperature of the vacuum platform, which secures the substrate in place, may be adjusted up to 60°C. This system allows us to change different parameters: number of nozzles, drop spacing, substrate and cartridge temperatures, firing frequency and waveform design. Small variations from the standard DMP waveform were applied to print our functional ceramic oxides precursor inks.

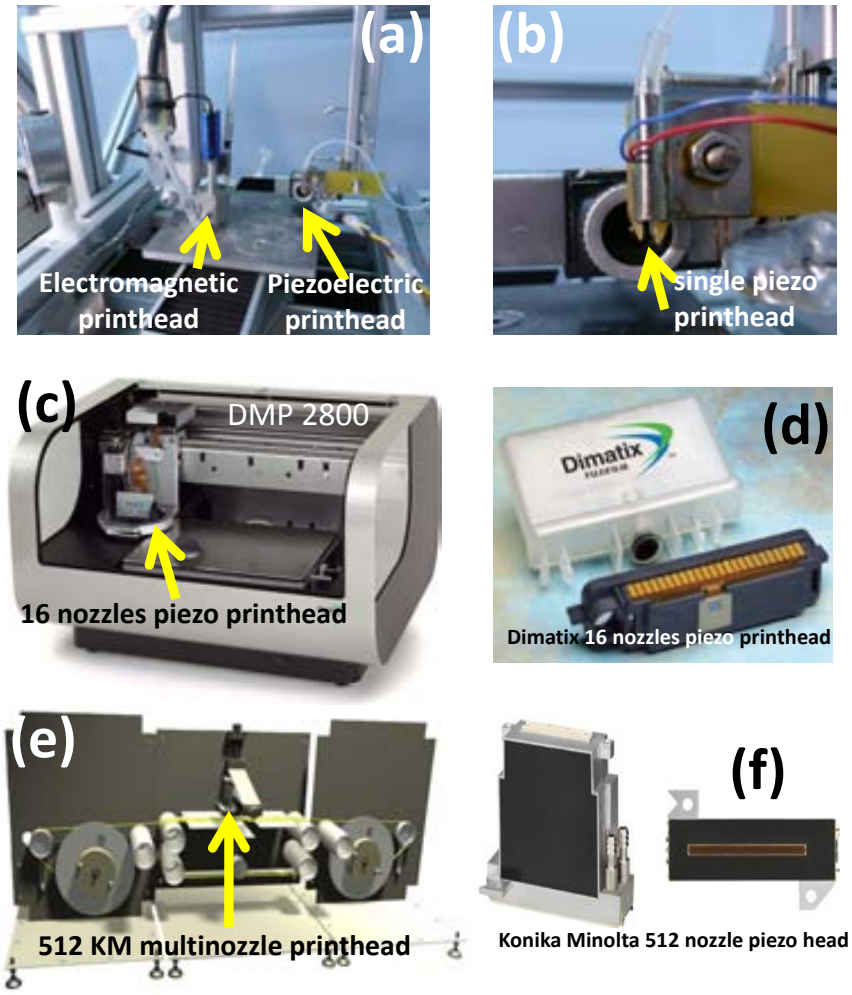


**Figure 3.5.:** Inkjet printing set-ups employed throughout this thesis. (a) Proprietary system with a commercial Microfab printhead of $60\mu m$ nozzle diameter and an electromagnetic one of $90\mu m$ of nozzle diameter. (b) Zoom-in of the $60\mu m$ nozzle diameter Microfab dispenser. (c) Dimatix Materials printer DMP-2800. (d) Replaceable Dimatix piezo cartridge with 16 nozzles. (e) Render of the reel to reel system in which is integrated the Konika Minolta 512 nozzle piezohead. (f) Views of the Konika Minolta 512 nozzle piezo printhead.

Finally, the third printer system employed is integrated in a **continuous reel to reel system** (Fig. 3.5e), composed of a feed reel that provides the substrate to be printed and a take up reel which holds it once the whole printing and thermal processes have finished. In this system, the printing process is performed by means of a **Konika Minolta (KM) 512 nozzle piezo printhead** (Fig. 3.5f) [205], where drops are ejected after the deformation of the small ink chambers made of piezoelectric material. The 512 nozzles, divided into two rows of 256 nozzles may be independently enabled or disabled. In our case, the KM512 printhead belongs to the M serie, which corresponds to a unit drop volume of $14pL$.

## 3.4. Substrates and thermal treatments

After inkjet deposition, samples were submitted to a heat treatment in order to obtain the ceramic oxides in the desired phase. Then, in next sections we describe, first, the thermal treatments of single-crystals substrates prior to deposition and, secondly, the experimental thermal processing followed for the YBCO, LSMO and CZO coatings and patterns.

### 3.4.1. Substrate treatment

The substrate is the first template for epitaxial growth and, consequently, they are an essential component to grow high quality structures with excellent properties. Extended efforts are deployed in the last time to study substrates' surfaces and to improve surface quality [206]. It is highly important to select the substrate in agreement with the characteristics and goals of the whole system. Global issues to consider regarding substrate selection include chemical compatibility with the structure to be deposited on top, thermal expansion, lattice mismatch and surface quality, among others. Throughout this thesis, deposition was performed on square shaped (5x5)$mm^2$ and (10x10)$mm^2$ $LaAlO_3$ [207, 208], $SrTiO_3$ [209, 210] single crystal substrates and commercial metallic tapes. Single crystal substrates were purchased from CrysTec (Germany, GmbH). In order to remove impurities and to reconstruct the surface terminations [209], the substrate's surface of the as-received single crystals was treated.

First, they were ultrasonicated in acetone and methanol during $5min$, then dried under a flow of nitrogen and finally treated up to 900 °C in constant oxygen flow, regulated by a mass flow, during 5h. The corresponding thermal profile is sketched in Fig. 3.6.

Through these treatments, substrate's surface rearranges, either by diffusion or desorption of atoms, till it achieves the surface structure energetically more favourable. For our (001) surfaces, the equilibrium structure exhibits atomically flat terraces separated by steps of height (n+1/2)$a$, where $a$ is the lattice parameter and n=1/2, 1, 3/2, 2,...The presence of steps is due to the miscut angle $\theta_m$. There is always a misalignment from the (001) plane in the cut of the single crystal, $\theta_m$∼typically of 0.1-0.2°. As a result, when (001) surfaces rearrange they show a stair-like morphology. Treated STO and LAO surfaces exhibit atomically flat terraces separated by one unit-cell high steps.

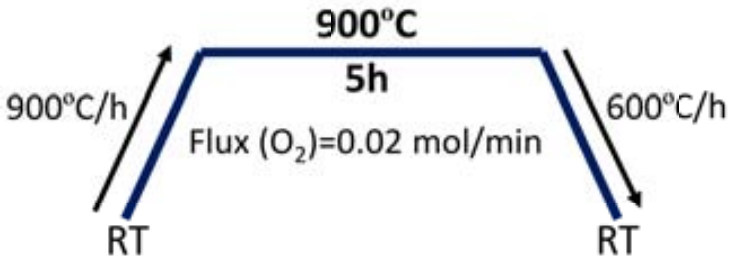


**Figure 3.6.:** Profile of the heat treatment used for surface conditioning of single crystal substrates. Prior to inkjet deposition, all the single crystal-substrates wer subjected to this thermal treatment.

Metallic tapes and other polycrystalline substrates (quartz, alumina, etc.) were cleaned without ultrasonication with acetone and methanol and dried with compressed nitrogen, but no thermal treatment was performed for this kind of substrates.

## 3.4.2. $YBa_2Cu_3O_{7-x}$ thermal processing

To obtain the desired YBCO phase, three thermal stages were performed called pyrolysis, growth and oxygenation processes.

### 3.4.2.1. Pyrolysis, growth and oxygenation

Three consecutive thermal treatments, called pyrolysis, growth and oxygenation processes were performed for YBCO formation.

The goal of the ***pyrolysis step*** is to remove the excess of solvent and decompose the organic matter, generating the amorphous or nanocrystalline metallic precursors. Consequently, due to the decomposition of the organic matter, a large fraction of precursor volume is eliminated during this process leading to a strong film shrinkage. Tensile stress relaxation arisen in this shrinkage process may lead to films with cracks or other kind of defects [211]. For this reason, a rigid control of processing parameters is essential in order to avoid these inhomogeneities. It is important to remark, as well, that any impurity (i.e. dust speck) on the surface of the substrate or on the as-deposited film will be detrimental on the homogeneity of the as-pyrolyzed film.

The pyrolysis process consists of slowly heating the sample up to 310°C in humid oxygen atmosphere (2% $H_2O$ in $O_2$). The reason to add water vapour to the oxygen flow is to prevent the sublimation of $Cu(TFA)_2$ by its hydro-stabilization [212]. Regions marked in blue in Fig. 3.7 means that the flowing gas is humid, otherwise, regions are drawn in green. The flow of humid oxygen gas was injected into the tubular furnace once the temperature reached 100°C to avoid the absorption of water in the gel film. Humid gas flow was obtained by injecting dry oxygen into flasks containing deionized water by using dispersion tubes. After $30min$ at 310°C, the sample was then cooled down in dry oxygen atmosphere.

The second heating step, the ***growth process***, in which the pyrolyzed film is heated at high T to crystallize in the tetragonal phase of YBCO, consists of a heating treatment in humid nitrogen gas mixed with $200ppm$ oxygen at 810°C during $3h$ (first part of the profile in Fig. 3.8). The wet atmosphere is required to decompose the $BaF_2$ from the pyrolysis into BaO and HF, being the latter evacuated by the gas flow. As descomposition of $BaF_2$ from pyrolysis proceeds, YBCO nucleation takes place at substrate interface. Thus, YBCO growth rate depends on water pressure, oxygen pressure, rate of gas flow and growth temperature.

This second heating process is followed by the third one, the ***oxygenation process***, which starts at 600°C with a subsequent plateau at 450°C for 3.5h under dry oxygen atmosphere (second part of the profile in Fig. 3.8) to finally convert the tetragonal YBCO phase into the superconducting orthorhombic YBCO phase. The whole thermal profile

followed for the YBCO samples obtained throughout this work is presented in Fig. 3.8 [5].

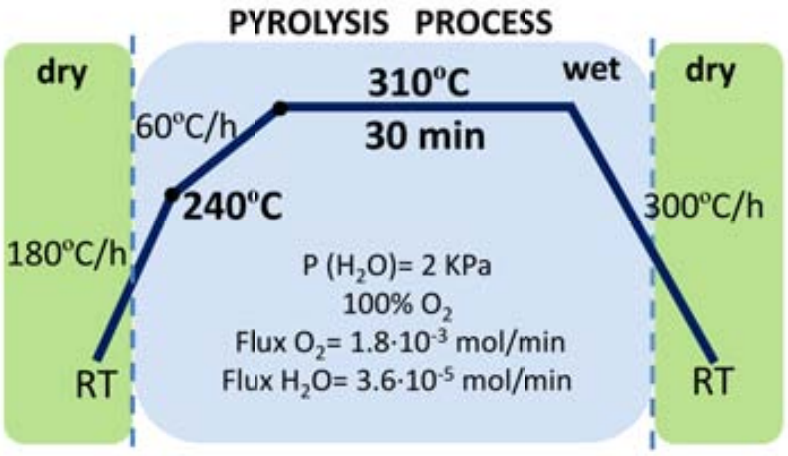


**Figure 3.7.:** Temperature heating profile used in pyrolysis of MOD-TFA YBCO coatings.

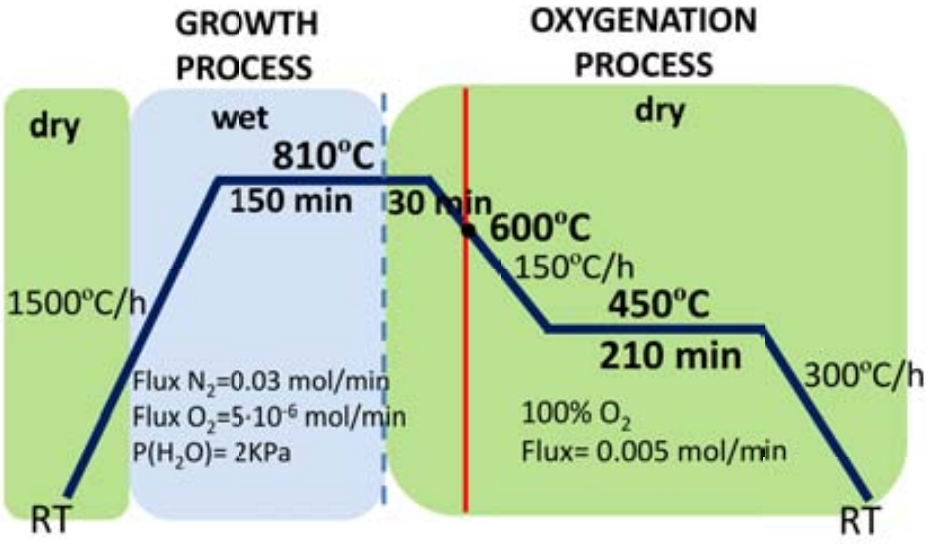


**Figure 3.8.:** Schematic representation of MOD-TFA YBCO growth and oxygenation processes.

### 3.4.3. $La_{0.7}Sr_{0.3}MnO_3$ thermal processing

For LSMO layers, the thermal treatment followed is sketched in Fig. 3.9. The samples were heated in air up to 900°C and maintained at this temperature during 5h.

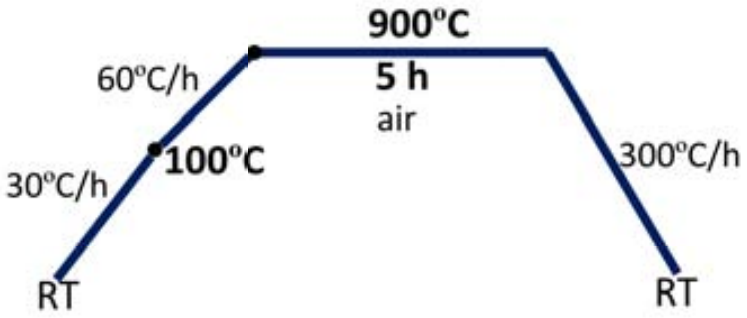


**Figure 3.9.:** Temperature heating profile used for LSMO films.

For LSMO patterns, the thermal treatment was slightly simplified (Fig. 3.10). They were also heated in air up to 900°C during 5h and then cooled down to RT. Both thermal processings were perfomed also in a tubular oven.

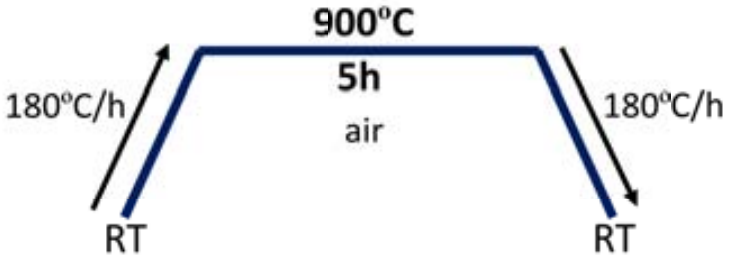


**Figure 3.10.:** Temperature heating profile used for LSMO patterns and devices.

### 3.4.4. $Ce_{0.9}Zr_{0.1}O_{2-x}$ thermal processing

Fig. 3.11 represents schematically the thermal profile used for CZO growth. From RT to 900°C, temperature was increased with a ramp of 10°C/min, then maintained at this temperature for 1h and then cooled to RT at also 10°C/min.

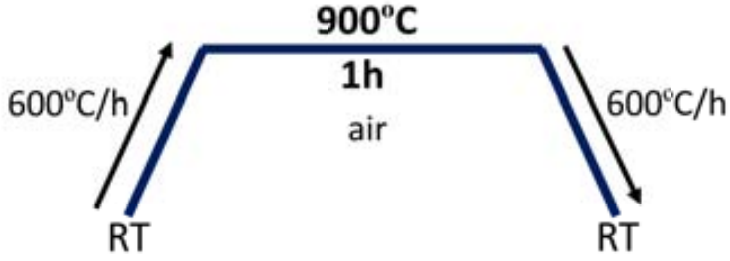


**Figure 3.11.:** Schematic representation of the CZO growth process.

# 3.5. Film characterization techniques

In this section we briefly describe the main characteristics of the techniques that have been routinely employed to characterize the $YBa_2Cu_3O_{7-x}$ (YBCO), $La_{0.7}Sr_{0.3}MnO_3$ (LSMO) and $Ce_{0.9}Zr_{0.1}O_{2-x}$ (CZO) systems object of this work. These include: morphological analysis by means of optical microscopy (OM) and Scanning Electron Microscopy (SEM), structural study using X-ray Driffraction (XRD), surface topography characterization by means of Atomic Force Microscopy (AFM) as well as magnetic and superconducting characterization by Vibrating Sample Magnetometer (VSM) and Superconducting Quantum Interference Device (SQUID) magnetometers and transport measurements by a PPMS (Physical Properties Measurement System). Each of these techniques comprise scientific, technical principles as well as operating methodologies that could lead to extended descriptions. So, the aim of this section is to provide the reader with a general overview of the working principles of these techniques, with the specific measurements developed with them and the instruments used for that.

## 3.5.1. Morphology, microstructure and texture

The morphology, (micro)structure and texture of layers and patterns have been investigated throughout this work by means of microscopic and X-ray Diffraction techniques.

### 3.5.1.1. Optical microscopy (OM)

The surface homogeneity of the as-pyrolized coatings was routinely investigated with an optical microscope. High resolution photographs were recorded through an Olympus BX51 microscope (5x and 10x objective) coupled to an Olympus DP20 camera.

### 3.5.1.2. Scanning Electron Microscopy (SEM)

Conventional SEM provides elemental, morphological and topographical information at magnifications of 10x up to 100000x. This kind of microscopy allows to obtain information about surface morphology, porosity, precipitates, grain size and particle distribution, for instance. Besides material evaluations, it is also used for quality control screening. Since the sample is investigated with electrons, it must conduct electricity. In the case of some bad conducting films, it would be necessary to coat them with a thin conductor layer such as gold.

The operation principle of a SEM is briefly outlined below. A beam of high-energy electrons (primary electrons) is focused on a sample placed in a vacuum chamber. To obtain the SEM image, the electron beam sweeps back and forth across the surface of the sample. Two types of electrons are produced as a result of the interaction between the sample and the primary beam: backscattered electrons (BSE) and secondary electrons (SE). Those removed electrons are collected by a positively charged detector and translated into signal. On one hand, BSE electrons with energies of the same order as the primary beam ($\sim$50KeV), provide information of the chemical composition of the sample

because its energy depends on the atomic number of the specimen. On the other hand, SE, with lower energies ( 20KeV), give information about the surface topography (2D). The beam can be focused to a final probe diameter around $10nm$. Despite the considerable depth of penetration of the incident primary electron beam, the re-emitted electrons (as secondary and backscattered) come from mean depths of $50nm$-$0.5\mu m$ depending on the density of the material. Asides from BSE and SE, characteristic X-rays are also emitted by the specimen which enable compositional information through analysis with a spectrometer. Peaks at energies characteristic of the elements within that area can be identified and the concentrations of the elements may be calculated.

SEM images were made using a FEI QUANTA 200 FEG located at ICMAB. SEM analysis has been applied routinely to characterize the film's surfaces of YBCO and LSMO coatings and patterns fabricated in this thesis. We have worked with an acceleration voltage around $\sim 10 - 15KV$ and the images were taken at the following magnifications: from 500x to 30000x.

#### 3.5.1.3. X-Ray Diffraction techniques (XRD)

X-rays are electromagnetic waves with wavelength $\lambda$ in the 0.1-100Å range. X-ray diffraction is based on the scattering of incident X-ray waves by the electronic density surrounding each atom in a crystal. Diffraction phenomena occur when the spacing between the crystal is in the order of the wavelength of the incident radiation, consequently, X-ray diffraction is a powerful tool to explore and characterize crystals. The scattered X-rays will destroy themselves except for the case in which the difference between the incident and the scattered wave vectors is a vector belonging to the reciprocal lattice, or, in other words, in accordance with Bragg's law, if the scattered rays are in-phase so that their difference in path is equal to an integer number $n$ of wavelengths [see Fig. 3.12(a)]:

$$n\lambda = 2d_{hkl}sin\theta$$

where $\lambda$ is the wavelength of the incident X-ray, $n$ is the reflection order, $\theta$ is the angle between the incident X-ray beam and the sample plane, and $d_{hkl}$ is the interplanar spacing between the $(hkl)$ family of planes. When Bragg's law is fulfilled, we have a constructive interference, i.e. the so-called diffraction peak or the Bragg reflection. Modifying the incidence angle $\theta$, one obtains a diffraction pattern where the intensity and spatial distributions of such Bragg peaks conform the fingerprint of the sample. XRD is thus routinely used for determining crystal structures, phase identification, crystalline quality, cell parameters, or the study of crystal structure and orientation of epitaxial layers and patterns.

The rotation of the sample with respect to the incident angle and to the detector enables to explore different XRD configurations from where different information can be obtained. In a $\theta/2\theta$ *diffraction pattern* [*Bragg-Brentano geometry*, Fig. 3.12(b)], the sample moves the angle $\theta$ and the detector simultaneously moves by the angle $2\theta$ while the X-ray tube remains stationary. Therefore, only the atomic planes parallel to the surface

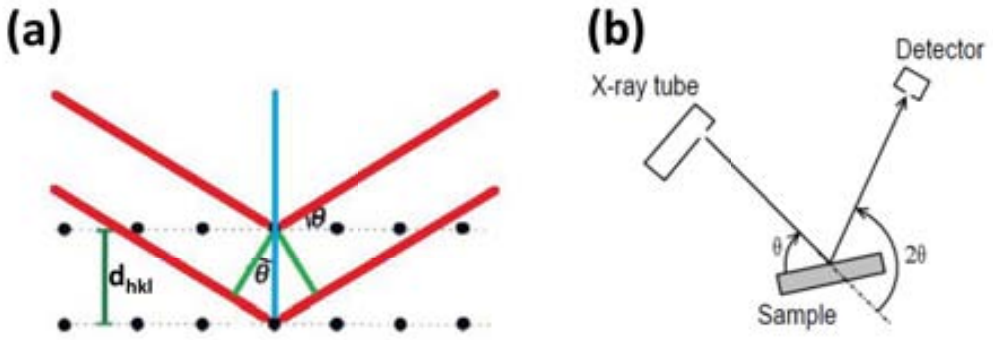


**Figure 3.12.:** (a) Sketch of the constructive interference (Bragg's law) between two incident X-rays on a crystal surface. (b) Geometry of the $\theta - 2\theta$ configuration.

plane will diffract in this configuration, i.e. we obtain information of the out-of-plane orientation of the crystal. The number, disposition and intensity of Bragg peaks in the diffraction pattern depend primarily on the symmetry and size of the unit cell, the arrangement of atoms within it and on the nature and wavelength of the radiation used. Moreover, the intensities are affected by the orientation distribution of the diffracting domains within the sample. Polycrystalline samples consist of randomly oriented crystallites in all possible orientations, so for every crystal plane that fulfills the Bragg condition at a certain value, there will be a diffraction peak. Conversely, in single crystals, the family of planes parallel to the sample surface is the only one giving a reflection peak. In the present work, $2\theta$-scans were performed to obtain information about the preferential crystallographic orientation and possible existence of secondary phases in oxide coatings.

Information about the out-of-plane texture of crystallites can be obtained by $\omega-scans$, also known as *rocking curves*. A $\omega$-scan is a scan at a fixed $2\theta$ angle and provides information about the orientation spread of the specific reflection being analyzed: the width of the peak obtained is proportional to the misorientation of the domain being measured. Rocking curves measurements performed throughout this thesis are the (005) for YBCO films and the (200) reflection for the CZO films, for instance.

The $\theta - 2\theta$ and $\omega$-scans performed through this research were done using either a Siemens D5000 or a Rigaku Rotaflex RU-200BV diffractometer located at ICMAB, using a Cu $K_\alpha$radiation $\lambda(K_{\alpha 1}^{Cu} = 1.5406\text{Å})$ and $\lambda(K_{\alpha 2}^{Cu} = 1.5444\text{Å})$. Data acquisition was typically performed with a $0.02^\circ$ step size.

The other XRD measurement performed in the characterization of the YBCO and LSMO coatings were *pole figure* measurements (also called *phi-scans*). In a pole figure measurement, a particular *hkl* reflection is selected and put it in Bragg condition. In order to do so, if the *hkl* planes are not parallel to the substrate, the sample has to be tilted an angle $\chi$ and rotated and angle $\phi$. The rotation angles are displayed in Fig. 3.13. It provides information about the in-plane texture of the film. The relation between the peaks appearing from the substrate and the film shows the in-plane epitaxy of the film. Pole figures can reveal oriented crystalline polulations not seen in $\theta - 2\theta$ scans as well as the fraction of randomly arranged crystallites.

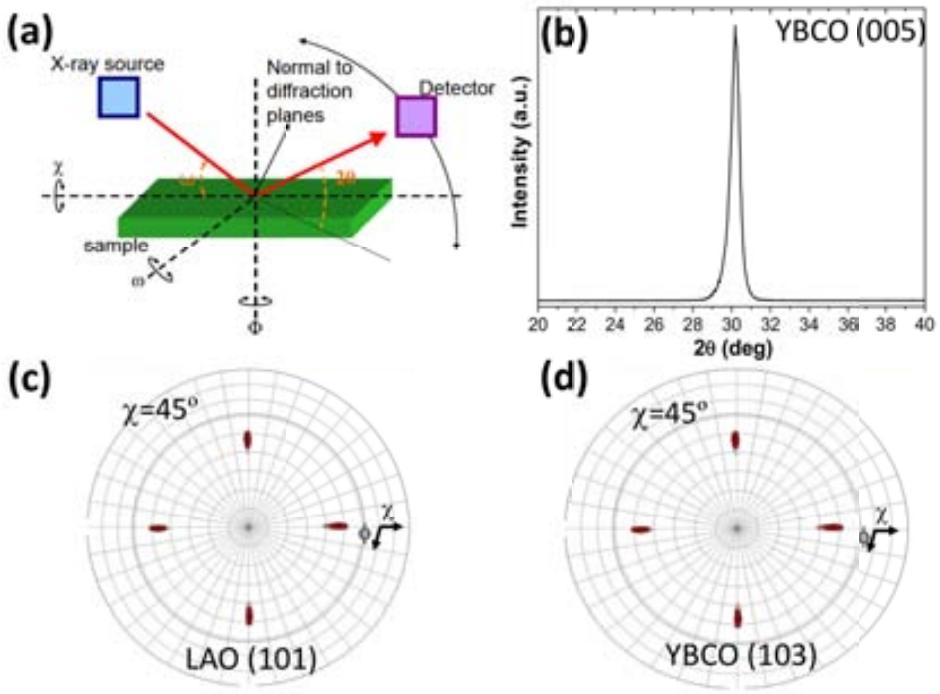


**Figure 3.13.:** (a) Schematic view of the nomenclature of angles that can be adjusted in XRD measurements. (b) $\omega$-scan of the (005) YBCO reflection at $2\theta$=38.5°. (c) and (d) Pole figure measurement of a YBCO film on LAO showing the YBCO(00l)||LAO(h00) and YBCO[00l]||LAO[00l] epitaxial orientation.

#### 3.5.1.4. Two-dimensional X-ray Diffraction (XRD$^2$)

As mentioned, conventional X-ray measurements are confined within a plane. Therefore, various additional sample rotations are required to gain knowledge about diffraction patterns out of this plane. This is a typical example of the problems avoided using a two-dimensional X-ray detector (XRD$^2$). These detectors enable to capture diffraction patterns in 2D directions, i.e. diffractions measurements are not longer confined within the diffraction plane [213], which permits simultaneously measuring large $2\theta$ and $\chi$ values ($2\theta$∼30° and $\chi$∼70°). Since different $\chi$ values are at the same time detected in a single frame, XRD$^2$ was very suitable to simultaneously analyze the polycrystalline and epitaxial part in a layer for texture evaluation and for phase identification. Consequently, in a single fast measurement we obtain not only the information relative to the $2\theta$ and $\chi$ values in which we center the sample, but also detect reflections at different $2\theta$ and $\chi$ values that give information on the out of plane texture of the sample ($\chi \neq 0$). The XRD$^2$-based studies presented in this work were done using the GADDS D8 Advance system from Bruker at ICMAB, where GADDS stands for General Area Detector System.

There exists a large variety of XRD$^2$ configurations to carry out a wide range of applicattions. The sketched diagram of the GADDS components is shown in Fig. 3.14a. It consists at least of a 2D- detector, X-ray source, sample alignment, sample positioning stage, monitoring device and the corresponding electronic and computer systems to visualize, store and treat the diffraction data.

For a bidimensional flat detector, the detector surface can be considered as a plane

which intersects the diffracted rays. For a single crystal, the diffracted beam points to discrete directions, which are imaged as points in the ideal case. For a polycrystalline sample, the diffraction pattern is formed by diffraction cones (see Fig. 3.14b).

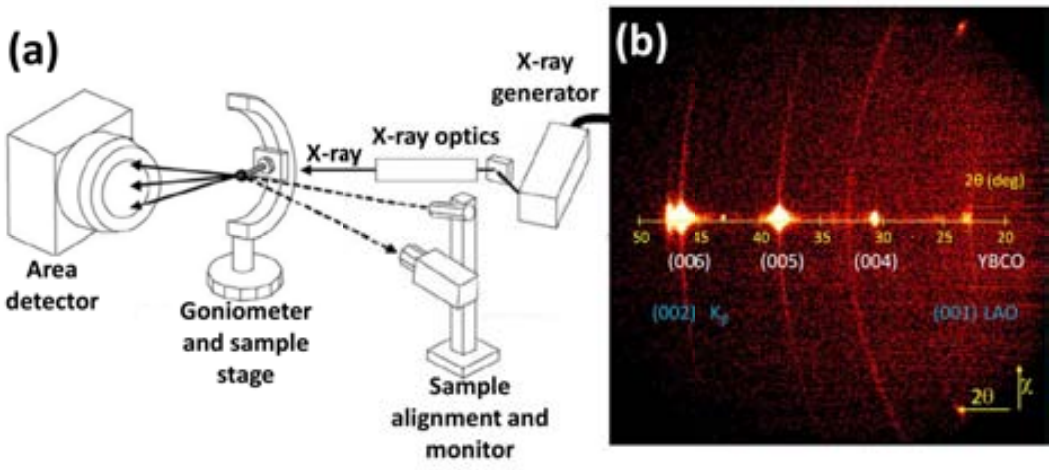


**Figure 3.14.:** (a) Main components of a XRD$^2$ GADDS system. Reproduced from [213]. (b) $2\theta - \chi$ frame obtained from a GADDS measurement on a YBCO film (thickness$\sim$700$nm$) on a (001)-LAO substrate. The spots indicate the epitaxial growth of the film, whereas the diffraction rings point out that there is also part of the volume randomly oriented.

Considering the bidimensionality of the detector, $2\theta$ scans are not needed in GADDS because the $2\theta$ range is already defined in the area detector. Thus the frames were acquired at a fixed $2\theta$ position. In the case of a powder sample any value of $\omega$ would satisfy the Bragg condition for the randomly oriented crystallites. However, in order to bring the different crystallographic planes of an epitaxial film to Bragg condition and thus visualize the diffracted spots in the 2D image is required to scan in $\omega$. An example of a 2D XRD diffraction pattern obtained with the GADDS is displayed in Fig. 3.14b. The sample was a YBCO film (thickness$\sim$700$nm$) grown on a (001)-LAO substrate. The horizontal direction covers the $2\theta$ values and the vertical direction represents $\chi$ values. The $2\theta - \chi$ frame shown in Fig. 3.14b was measured by a continuous $\omega-$scan, starting from $\omega_0$ =11 $^\circ$ till $\omega_f$=22$^\circ$ during 1800s. Data acquisition was performed at a fixed $2\theta = 39^\circ$, i.e. the detector is centered at the given $2\theta$ value which will be the center of the frame.

Diffraction profiles equivalent to those acquired from XRD punctual detector can also be obtained from 2D diffraction patterns integrating in $\chi$ over a selected $2\theta$ range. However, data integrated from XRD$^2$ patterns exhibits better intensity and statistics to carry out phase identification and quantitative analysis in textured samples. To have the complete phi-scan, we must rotate the sample about its normal axis and collect each of the frames. Integration in $\chi$ for the whole set of frames then produces a pole figure such the ones in Fig. 3.13c and d. At the selected $2\theta - \chi$ regions, $\phi$ scans were performed at every 1°. Each $\phi$ position was held for 20 seconds. As a result, we obtained 360° frames which can be viewed and evaluated using specific software.

#### 3.5.1.5. Atomic Force Microscopy (AFM)

AFM performance is based on the detection of forces acting at nanometric scale between the atoms of a sharp mechanical tip (the probe) and the sample surface. There is a variety of forces, from attractive to repulsive, whose relevance mainly depends on the tip-surface distance.

The tip is mounted on a soft spring (called cantilever); and the surface-tip interactions are indirectly measured through deflection of the cantilever. A scanner with piezoelectric components is used to move the tip and the sample relative to each other in all (x,y,z) directions. There exist different strategies to mesure deflections, however, beam deflected technique is among most commonly used methods. A four quadrant photodiode detects a laser beam which is reflected on the back side of the cantilever. When the cantilever is not deflected, the reflected beam strikes the centre of the photodiode system. Any movement of the cantilever results into a displacement of the reflected beam from the central position and, consequently, one of the photodiodes receives more light than the others. The four quadrant photodiode allows to quantify bending and torsion of the cantilever; so, it allows to measure both normal and friction forces between the tip and the sample surface. Changes of the control parameter are directly related to height variations at a given point of the surface. Scanning the whole x-y surface with the tip, topographic maps (3D) are obtained from the tip-surface interactions detected at each x-y point.

The AFM can operate in a varierty of modes depending on the purposes of the measurement and the environmental conditions. A common classification of imaging modes is based on static (contact) mode and a number of dynamic (non-contact) modes. The former measures the cantilever deflection, whereas the latter measures dynamic properties of the cantilever like resonance (frequency), amplitude or phase.

In the *contact mode*, the tip is brought close to the surface, typically at 5Å. During the initial contact, the last atoms of the tip feel a weak repulsive force due to the overlap of the electron orbitals with atoms of the surface of the sample, which causes the deflection of the cantilever. When this deflection of the cantilever is detected, the equipment changes the vertical position of the tip to keep the deflection at a reference value. Therefore, in this case, the scan is performed at constant force. This mode can also operate at constant height.

In the *non-contact mode*, the tip oscillates close or at its frequency of resonance. The tip is hung 50-150Å above the surface of the sample, thus it mainly sense attractive Van der Waals forces. The cantilever is constantly oscillating close to the surface without touching it, and forces are detected measuring changes in amplitude, phase or frequency. At the working region distance, attractive forces are considerably weaker than those detected in contact mode, so the resolution is lower.

There is another mode, the *intermittent contact mode*, also known as *tapping mode*, used along this work to evaluate the surface morphology and topography of the inkjetted CZO buffer layers. This mode arises as a good strategy to obtain high resolution images of sensible surfaces. The cantilever oscillates at a constant frequency close to its resonance, and the tip is intermittently touching the surface of the sample. As a result, lateral forces as well as problems related to friction, adhesion, electrostatic forces or other difficulties

are drastically reduced. So, if oscillating amplitude is sufficiently high, the tip does not attach to the layer because the cantilever has enough restoring force to overcome it.

AFM is especially used to obtain topographic images of surfaces in order to determine the homogeneity of the surface, the morphology of them and also to evaluate the *rms* roughness of those samples. The images presented in this work were done with an Agilent 5100 AFM system from Agilent Technologies installed at ICMAB. Images were taken in tapping mode and using silicon tips. Surface was typically scanned by the tip at $1 lines/s$. Fig. 3.15 shows a topographic image of a $Ce_{0.9}Zr_{0.1}O_{2-x}$ buffer layer on a commercial metallic tape with a *rms* roughness of $1.3nm$. Typical scans of $20x20\mu m^2$, $5x5\mu m^2$ and $1x1\mu m^2$ were performed at distinct zones of the sample. AFM images were processed with Mountains Map software from Digital Surf.

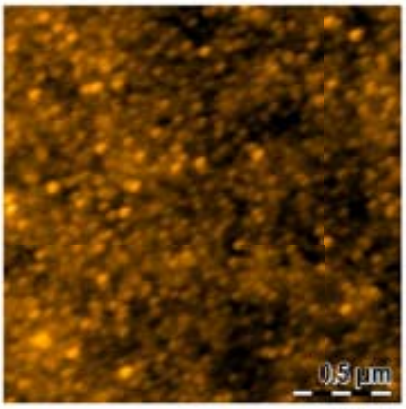


**Figure 3.15.:** Topographic AFM image of the central region of a CZO film over a commercial metallic tape. The scale in z is $\sim 10nm$. The measured *rms* roughness was $\sim 1.3nm$.

## 3.5.2. Thickness measurements

### 3.5.2.1. Atomic force profilometry

The layer thickness (substrate-film step) was also measured with a profilometer P16 from KLA Tencor, located at ICMAB. Profilometry is based on scanning force microscopy, i.e. detection of forces acting at nanometric scale between the atoms of a sharp mechanical tip and the surface of the sample. In the case of YBCO coatings, the substrate-film step was made by chemical etching using orthophosphoric acid diluted 1:10 in deionized water. A standard photoresist was previously deposited onto the film to protect the defined YBCO area and then obtain a step after its removal with acetone. The measurement of the step height was carried out in contact mode. Thickness of YBCO films after pyrolysis and growth was measured using this procedure. The dimensions and topography of YBCO and LSMO patterns (i.e. width and height) were also determined by means of profilometric analysis. Common errors in film thickness was in the range of $\sim 50nm$.

## 3.5.3. Magnetic and superconducting characterization

The magnetic and superconducting properties of YBCO and LSMO films and patterns were performed at ICMAB by expert members.

### 3.5.3.1. Inductive measurements: Superconducting Quantum Interference Device (SQUID) magnetometer

SQUID magnetometers are instruments with high sensitivity to measure in a non-destructive way the magnetic moment of a sample, from which the magnetization and magnetic susceptibility can be obtained. In the present work, DC-magnetometry was used to investigate the electromagnetic response of superconducting YBCO coatings to provide us an idea about the quality of the samples.

A dc-SQUID device consists of a superconducting loop with one or two non superconducting links inserted. These devices give rise to an output voltage signal, which is a periodic function of the flux passing through the superconducting loop. The magnetometer used consists of a SQUID detection system, and a precision temperature control unit. The detection system is composed by a set of pick-up coils, where the sample is located inside, which in turn are placed inside the superconducting coil which provides a uniform dc-magnetic field at the sample location. The magnetized sample, typically mounted in a c-axis configuration parallel to the applied magnetic field, is displaced inside the set of pick-up coils inducing an electrical current proportional to the magnetic flux variation. The signal is detected and amplified by means of the SQUID sensor detection coil in form of output voltage. The magnetic moment of the sample is thus proportional to the voltage variations detected by the SQUID sensor, with a resolution in the order of $10^{-9} A \cdot m^2$ ($10^{-6}$ emu). The whole system is located inside a helium cryostat which refrigerates the superconducting coil and allows a precise temperature control. To ensure good homogeneity of the magnetic field and temperature during measurements, displacements of the sample within the coils were not longer than $3cm$.

Field and temperature dependent magnetization curves of YBCO and LSMO coatings were measured at ICMAB using a commercial SQUID dc-magnetometer (Quantum Design) equipped with a 7T superconducting and a helium cryostat allowing temperature control between $5K$ to $400K$.

Fig. 3.16a and Fig. 3.16b display the critical current temperature and field dependence determined from magnetic measurements using the Bean critical state model [214] for a standard $300nm$ YBCO film deposited by inkjet printing. For the application of the Bean model, and therefore, to obtain accurate $J_c$ values, it is essential to know the thickness of the sample. In this sense, layer thickness were systematically measured by profilometry. The high value of $J_c$, and the ratio between $J_c(5K)/J_c(77K) = 6.9$ indicate the high quality of the as-grown YBCO film. From one side, to perform the $m(T)$ measurement, the sample is saturated at $5K$ and then the applied magnetic field is removed to measure the remanent magnetic moment by sweeping the T from $5K$ to $95K$ (Fig. 3.16a). From the other side, in the $J_c$ vs $\mu_0 H$ measurement, the sample is cooled down to $5K$. After saturating the sample at 5T, the magnetic moment is registered as the field is decreased down to $0T$(Fig. 3.16b).

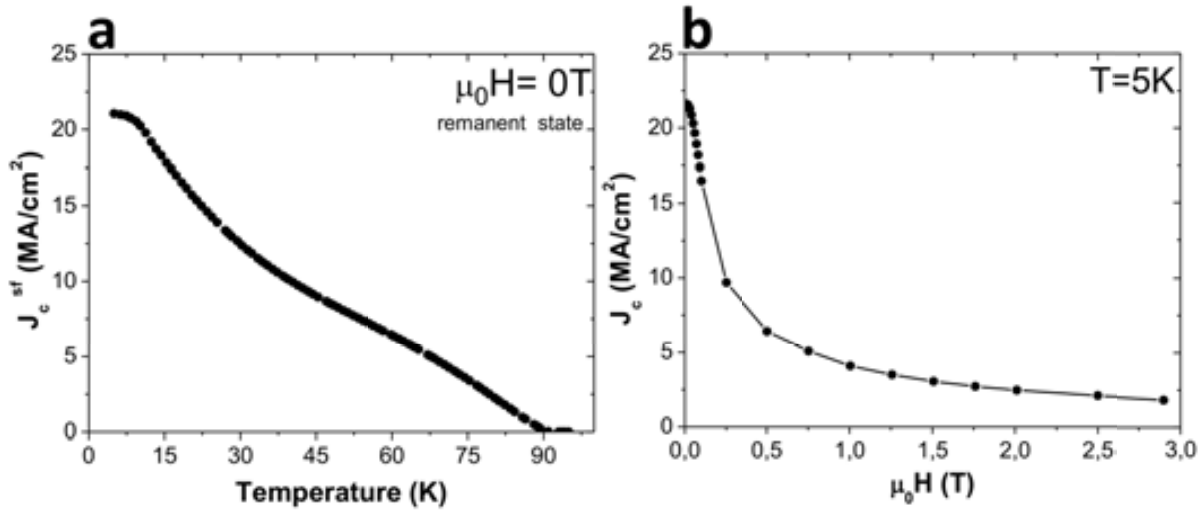


**Figure 3.16.:** (a) Critical current density as a function of the temperature and (b) Critical current density as a function of the applied magnetic field at $5K$, for an standard $300nm$ YBCO deposited by inkjet printing. Both measurements were performed with $H \parallel c$.

### 3.5.3.2. Transport measurements

Critical current densities can also be determined from electrical transport measurements from $I-V$ curves or, more generally, from $J-E$ curves since the critical current $I_c$ is defined as the maximum current that can flow in a superconductor without dissipation. When the applied current exceeds $I_c$, the resistance become non-zero and a drop in voltage is measured (see Fig. 3.17).

The electric transport measurements in the YBCO tracks on LAO were performed by an expert member of our research group using a Physical Properties Measurement System (PPMS) from Quantum Design, in fields between 0 and $9T$ and from 5 to $400K$. The system has also a nanovoltimeter and a dc/ac current source which can provide currents from $1\mu A$ to $2A$ with a resolution of $0.1\mu A$. During the transport measurements, the magnetic field was applied out of plane of the film. Silver metal contacts were evaporated on the films and post-annealed, ensuring resistance values below $10m\Omega$. The resistivity of the YBCO tracks was measured in a four-point configuration. In this four point configuration, a dc-current was introduced until a desired value $I$ between two contacts and the voltage is read between the two other pads. Those I-V curves may be obtained for different magnetic fields and temperatures. In the present research, the current required to develop an electric field of $3\mu V/cm$ inside the superconductor was the criterion used to determine $I_c$ and then $J_c$. Figure displays a typical $I-V$ curve at $77K$ and self-field of a set of YBCO tracks.

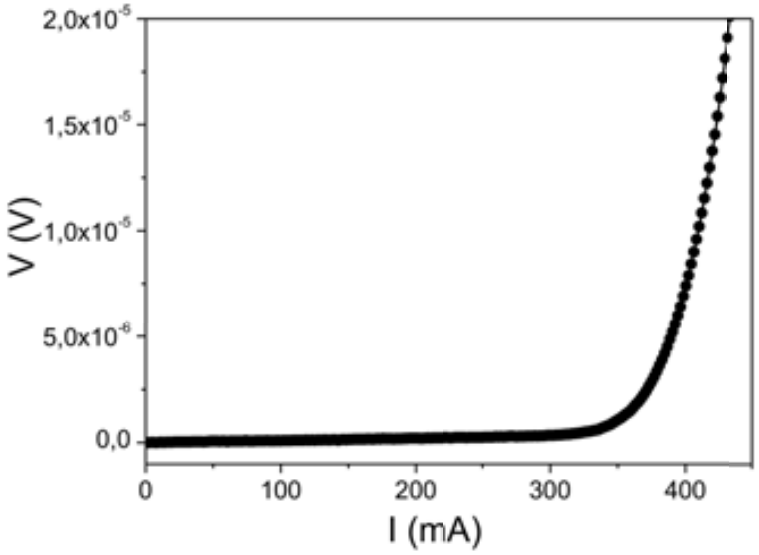


**Figure 3.17.:** Typical intensity-voltage curve of a set of inkjet printed YBCO tracks at $77K$ and self-field showing a $J_c$ of $1.1MA/cm^2$.

# 4. Drop formation

The surface flow, resulting in drop formation, is the second goal of the inkjet printing technology. For an optimum jetting, only a single stable drop must be generated. After providing a general description of the main stages of drop formation process, two differentiated sections will be recognized in the present chapter. The first sections discuss the influence of the ink rheological parameters and the driving actuation parameters on drop dynamics. Basically, the focus of this part is on investigating the ink viscosity and the operational driving parameters, first, qualitatively and then by means of quantitative characteristics. In this way, the evolution in time of the liquid thread, the length of the fluid filament prior to rupture, the pinch-off time and the drop ejection velocity are some of the analyzed features of the underlying fluid dynamics. Once a single droplet is formed, its final characteristics like drop velocity and drop volume should be known and adjusted. The second part of the present chapter correlates the rheological properties and driving parameters of the actuation waveform with the final drop characteristics (i.e. drop velocity and drop volume). Finally, an important application is shown, the drop size modulation.

Next Fig. 4.1 is a schematic roadmap of the primary inputs and outputs that take part on the present subject: the drop formation process.

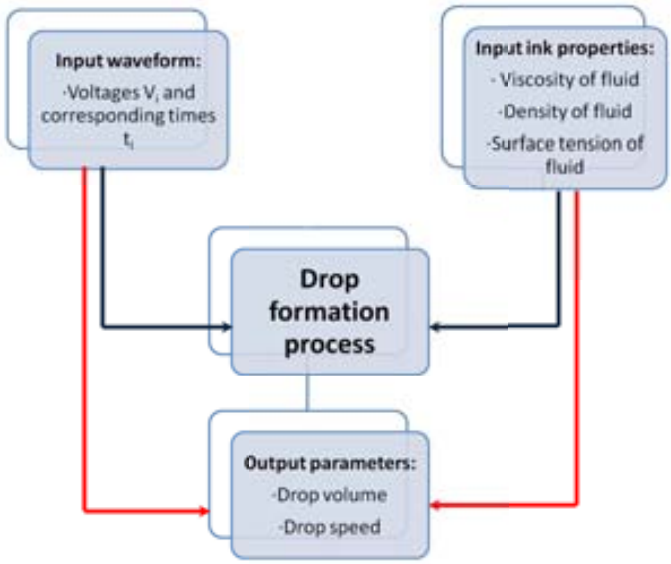


**Figure 4.1.:** Important input and output parameters which determine the drop formation process.

The second part of this chapter correlates the rheological properties and driving parameters of the actuation waveform with the final drop characteristics (i.e. drop velocity and drop volume).

## 4.1. Practical relevance

The efforts directed to understand the drop formation process become more than important to provide physicochemical comprehension in many inkjet printing aspects: from improving the control over drop position, through avoiding satellites and even to provide successful research in new application environments.

## 4.2. Historical overview

The study of drop formation has remained an active research area for over a century [126, 144]. Theoreticians, computational scientists and experimentalists have been attracted to the study of drop breakup [215].

By going beyond previous studies in this area, modern research on drop formation date from the contribution of Savart in 1883 [124]. From a theoretical point of view, what was missing in Savart's work is the realization that surface tension is the driving force that conducts jet breakup. The fundamentals of this work was established by Young [216] and Laplace [217], but it was not until 1849 when Plateau [218] recognized the crucial role of surface tension in drop dynamics. Following Plateau's insight, Rayleigh [126] added the flow dynamics to the description of the breakup process. He certainly failed to describe significant details of the jet breakup mechanism such as the satellite formation, but his work was useful to determine important parameters like the continuous length of the jet.

The second half of the 19th century was an era that saw a great resurgence of the interest of surface tension-driven phenomena, both from theoretical and experimental points of view. Some examples are the contributions of Eötvös [219], Quincke [220], Bohr [221] and Lenard [222]. Of special relevance is the contribution of Lenard who showed for the first time the origin of satellite drops. Bogy and Talke [11] also investigated the behaviour of droplet formation by applying a simple analysis of the acoustic wave propagation. After Bogy's work, the next contribution that could report significant progress in non-linear aspects of drop breakup was published in 1990. Peregrine and co-workers [223] exhibited photographic sequences of the events which occur during the breakup of the liquid thread. In 1993, Eggers [224] considered the viscous motion of an axisymmetric column of fluid with a free surface. In that paper, he put much effort to figure out the last stages of drop formation when the neck behind the drop becomes small.

In addition to the experimental studies mentioned in the previous paragraphs, numerical computational simulations of DoD drop dynamics have been conducted in the last times to provide more insights about the drop shape evolution and drop volume and speed characteristics. It is noteworthy to remark that a complete description of the fluid flow dynamics requires the use of algorithms which have to be able to solve the Navier-Stokes equations. Initial numerical simulations in the DoD inkjet printing field were carried out by Fromm [17], who used the marker-and-cell (MAC) method to obtain an approximate solution to those equations. Later, more complex algorithms have been used to solve approximations to the Navier-Stokes equations [225–233].

## 4.3. Tested inks and waveform design

In chapter 2 we showed that the relevant physicochemical parameters of the printing fluids may be classified in a serie of dimensionless groups (sec. 2.4.5). Tab. 4.1 displays the physicochemical properties (viscosity $\eta$, surface tension $\gamma$ and density $\rho$) of the inks studied in this first study. The values of surface tension and viscosity were selected to fall into the normal ranges to be compatible and fully jettable with our standard piezoelectric printhead.

For the experiments presented in this chapter, a commercial single nozzle piezoelectric actuated dispenser with a $60\mu m$ of nozzle diameter was used as a printhead. In the following experiments, the driving signal used to activate the piezoelement is a standard bipolar pulse schematically represented in Fig. 2.5, unless otherwise specified. The specific actuation conditions will be given in each particular case.

Next Tab. 4.2 displays the above mentioned group numbers for the fluids presented in the previous Tab. 4.1:

| **Solution** | **Viscosity** $\eta$ $(mPa{\cdot}s)$ | **Surface tension** $\gamma$ $(mN/m)$ | **Density** $\rho$ $(g/cm^3)$ |
|---|---|---|---|
| 1.5M ethanol based YBCO precursor solution | 7 | 22 | 1.1 |
| 0.5M ethanol based YBCO precursor solution | 1.5 | 21.5 | 0.883 |
| 100% ethanol | 1.1 | 22.2 | 0.788 |

**Table 4.1.:** Significant physicochemical properties of fluids in experiments on drop formation**.** All the measurements were performed at room temperature. Viscosity values were measured at low shear rates $(100s^{-1})$.

As might be observed, experiments were conducted over a set of fluids with similar surface tension and density, which can be considered constant for all the experimental working range. The slight variations in these properties make the difference in the acoustic

| **Solution** | **Re number** | **We number** | **Oh number** | **Z number** |
|---|---|---|---|---|
| 1.5M ethanol based YBCO precursor solution | 9.4 | 3 | 0.18 | 5.5 |
| 0.5M ethanol based YBCO precursor solution | 35.3 | 2.5 | 0.04 | 22.5 |
| 100% ethanol | 43 | 2.1 | 0.03 | 30.3 |

**Table 4.2.:** Dimensionless groupings for the three liquids under study.

velocities very small. In this sense, since only the viscosity is the ink property which varies in a more extent, we consider appropriate to present the different dynamics of drop formation according to the $Z$ dimensionless number presented in sec. 2.4.5.

Differences in $Oh$ (or $Z$) and $Re$ numbers are basically due to differences in the ink viscosity. Therefore, in this particular case, drop formation is mainly governed by the $Re$ and $Oh$ numbers [234].

Next section describes the main stages behind the single droplet formation process.

## 4.4. General description of drop formation

The droplet ejection phenomenon during the inkjet printing process is complex. A representative experimental sequence of images during the DoD drop formation is shown in Fig. 4.2, revealing the main features of drop formation dynamics [14, 203, 235–237]. We have selected to describe the key stages of fluid dynamics, an experimental sequence of a 1.5M ethanol based YBCO precursor solution with $Z$ number ∼5.5, at a drive voltage pair of $V_1$ =+38$V$/$V_2$= -38$V$ and corresponding times $t_{rise} \sim 2\mu s$; $t_{dwell} \sim 6\mu s$; $t_{fall} \sim 3\mu s$; $t_{echo} \sim 6\mu s$; $t_{final\,rise} \sim 2\mu s$ (Fig. 4.2).

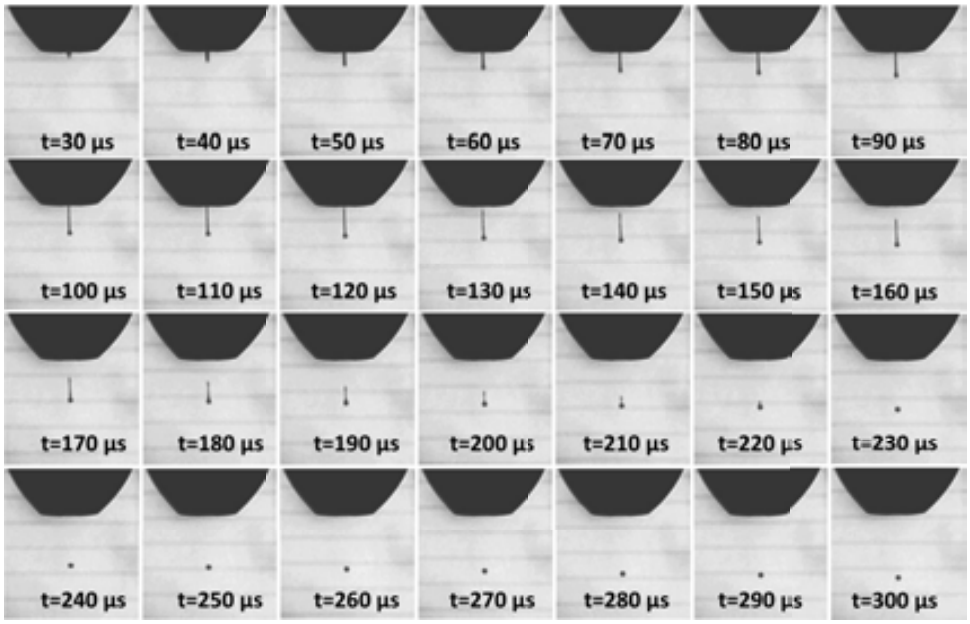


**Figure 4.2.:** Representative experimental time sequence of drop formation for a 1.5M ethanol based YBCO precursor solution ($Z \sim 5.5$) using a bipolar waveform with voltage amplitude $V_1 = +38V$; $V_2 = -38V$; corresponding times $t_{rise} \sim 2\mu s$; $t_{dwell} \sim 6\mu s$; $t_{fall} \sim 3\mu s$; $t_{echo} \sim 6\mu s$; $t_{final\,rise} \sim 2\mu s$ and frequency $f = 200Hz$. The number at the bottom of each frame indicates the elapsed time (time has passed from drop ejection). Interframe time was set at $10\mu s$.

### 4.4.1. Ejection, elongation and stretching of liquid thread

The competing effects of inertial, viscous and surface tension forces determine whether breakup will occur or not. Such as, $We$ number, and hence inertia, needs to be set large enough to ensure that drop breakup occurs and a drop is formed. On the contrary, when $We$ number is too low, drop ejection does not take place and the droplet is subjected to time periodic oscillations [231]. Similarly, $Re$ number also plays a crucial role in drop ejection. When it is too small, viscous dissipation impedes the formation of a drop, however, when is set too large, the possibility for satellites formation becomes higher. Sufficient large $We$ and $Re$ numbers enable overcome viscous dissipation and the energy associated when a new surface is generated during drop ejection. In the present case, the liquid ejection appears from the nozzle at an elapsed time of around $t \sim 30\mu s$. As time advances, the volume of liquid thread becomes sufficiently large that the increasing gravitational force over surface tension ($Bo \sim 1.8 \cdot 10^{-3}$) causes the liquid thread to rapidly elongate. During this elongation period, the filament length, that connects the bottom part of the falling droplet to the liquid pendant from the tube, increases. Moreover, the small negative pressure applied to the nozzle to prevent the drop dripping acts as a back-drawing force which may contribute to this fast liquid extension. The continued downward movement of the fluid causes a significant difference in axial velocity between the leading edge of the drop and the mass of the fluid attached to the nozzle, promoting the stretching of the liquid column at the same time that gradually changes its shape to a bulbous profile at $t \sim 60\mu s$. As stretching progresses, the liquid column necks generating a long liquid filament until breakup from the nozzle still occurs.

### 4.4.2. Necking and pinch-off of the liquid from the nozzle

As mentioned above, the axial motion of the liquid away from the nozzle together with the speed distribution along the thread produce the stretching of the liquid cylinder. This may lead to a subsequent second necking point close to the top of the leading drop, which divide the liquid thread in two differentiated regions: below the long tail, it takes a spherical shape, while above that approximates more like a liquid cone [223] (see Fig. 4.3). The thinning of the liquid column near the nozzle region produces the reduction of its diameter and, at last, the pinch off from the nozzle exit at an elapsed time of about $130\mu s$, creating a free liquid thread with a head that exhibits a nearly parabolic profile. The concept of pinch-off time is important in inkjet printing applications because determines the maximum rate of drop formation in the DoD printer. The tail properties and pinch-off in the jetting regime are mainly determined by the ink properties, such as the surface tension, density and viscosity, and the driving waveform parameters. Pinch-off will occur at the point with the largest variation of curvature because at this position the change of the capillary pressure and therefore the overall pressure gradient is the largest.

### 4.4.3. Recoil of free liquid column

When the liquid thread snaps off from the nozzle becomes an independent free-flying thread that rapidly recoils under the action of the surface tension. The shape of the

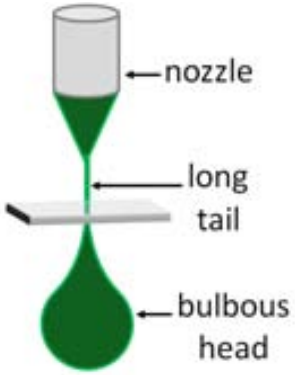


**Figure 4.3.:** Schematic representation of the morphology of the liquid thread during the evolution of the ejected liquid: the fluid filament necks leaving at its bottom part a bulbous drop profile, meanwhile above the head, close to the nozzle region, it may be considered as a liquid cone. The plane of symmetry wants to facilitate the observation of the different geometry of the liquid thread during elongation and stretching processes.

thread, however, depends on the competition of inertia and surface tension. An important observation might be extracted from the sequence displayed in Fig. 4.2 at time about $260\mu s$ after drop ejection. The contraction of the drop towards the spherical shape causes the drop to flatten and oscillate due to the excess of surface energy. These oscillations continue, albeit with decreasing amplitude due to viscous dissipation, until an equilibrium state is achieved at $t \sim 280\mu s$. The driving force for the whole recoiling process is the reduction of surface area towards a minimum value, corresponding to the spherical shape as mentioned before.

Until this point, it has been described an optimum jetting process, which means that, at the end, only a single droplet is generated. However, in some occasions, depending on the the ink physicochemical properties (see Fig. 4.4) and the activation conditions (see Fig. 4.5), the travelling liquid thread breaks up into a primary drop and multiple liquid threads which do not recombine and generate permanent satellites. These satellites are undesirable because they are detrimental to drop deposition precision. So, from the inkjet point of view, efforts must be done to tune ink characteristics and PZT actuation parameters in order to avoid their presence.

## 4.5. Influence of rheological and driving waveform on drop formation: qualitative analysis

### 4.5.1. Breakup of free liquid thread and formation of satellites

In next figures and by direct comparison with Fig. 4.2, it may be appreciated that drop dynamics response is affected under different circumstances.

From one side, Fig. 4.4 demonstrates that by applying the same piezoactuation parameters and only varying the rheology of the solution, drop formation is altered. For another side, Fig. 4.5 and Fig. 4.6 prove that by depositing the same ink and only modifying the drive voltage of the excitation signal, the fluid dynamics is deteriorated.

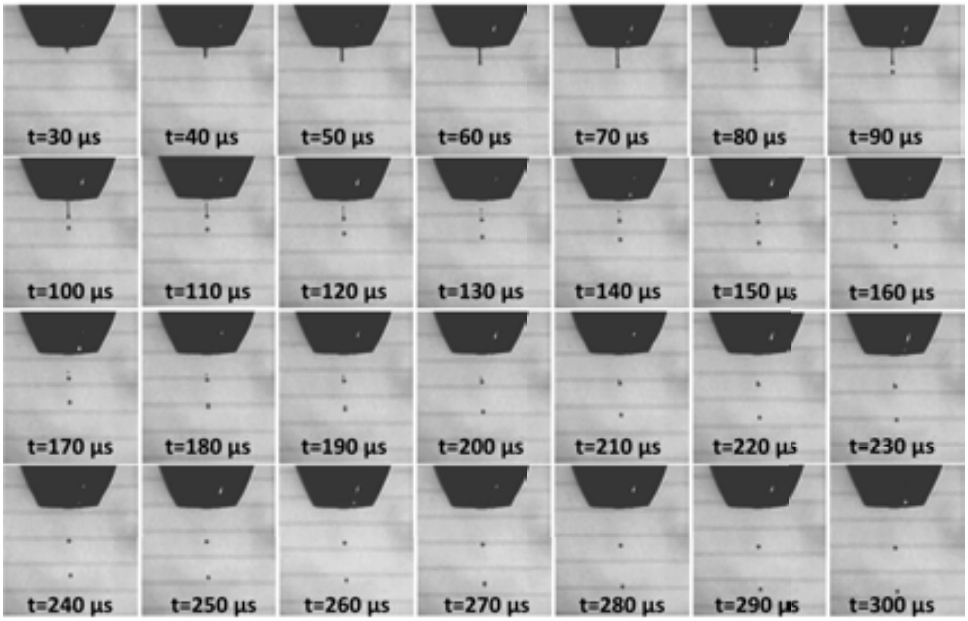


**Figure 4.4.:** Representative experimental time sequence of drop formation for a 0.5M ethanol based YBCO precursor solution $Z \sim 22.5$ using a bipolar waveform with voltage amplitude $V_1 = +38V$; $V_2 = -38V$; corresponding times $t_{rise} \sim 2\mu s$; $t_{dwell} \sim 6\mu s$; $t_{fall} \sim 3\mu s$; $t_{echo} \sim 6\mu s$; $t_{final\,rise} \sim 2\mu s$ and frequency $f = 200Hz$. The number at the bottom of each frame indicates the elapsed time (time has passed from drop ejection). Interframe time was set at $10\mu s$.

Next Fig. 4.4 shows the experimental drop formation sequence for a 0.5M ethanol based YBCO precursor solution (Z$\sim$ 22.5) with the same driving parameters used in the sequence displayed in Fig. 4.2. In Fig. 4.4, at $t \sim 70\mu s$, the liquid thread breaks up into two parts: a primary drop and a free liquid strand that contracts into a permanent satellite [236, 238], unable to merge with the primary droplet even after $t \sim 300\mu s$.

Alternatively, by using the same ink (1.5M ethanol based YBCO precursor solution, $Z \sim 5.5$) but changing the drive voltage of the piezoelement from $V_1 = +38V$; $V_2 = -38V$ to $V_1 = +43V$; $V_2 = -38V$ and maintaining the corresponding times at $t_{rise} \sim 2\mu s$; $t_{dwell} \sim 6\mu s$; $t_{fall} \sim 3\mu s$; $t_{echo} \sim 6\mu s$; $t_{final\,rise} \sim 2\mu s$, also satellites are formed (Fig. 4.5). As mentioned in chapter 2, sec. 2.5, the excitation of the piezoactuator is performed by the design of the corresponding waveform with defined amplitude and pulse width. Within the first part of this chapter, when we refer that actuation parameters are modified, it is limited only to the working voltages as the variety of drop singularities observed when the excitation voltage is modified is larger than when pulse width is changed.

Even more chaotic drop formation behaviour might be registered if the actuation parameters are far from being properly optimized. Next Fig. 4.6 shows the experimental sequence of drop ejection of the 1.5M ethanol based YBCO precursor solution, $Z \sim 5.5$, under the excitation voltages $V_1 = +70V$; $V_2 = -38V$ and pulse times $t_{rise} \sim 2\mu s$; $t_{dwell} \sim 6\mu s$; $t_{fall} \sim 3\mu s$; $t_{echo} \sim 6\mu s$; $t_{final\,rise} \sim 2\mu s$. A long liquid thread after $140\mu s$ is formed which breaks up into multiple permanent satellites.

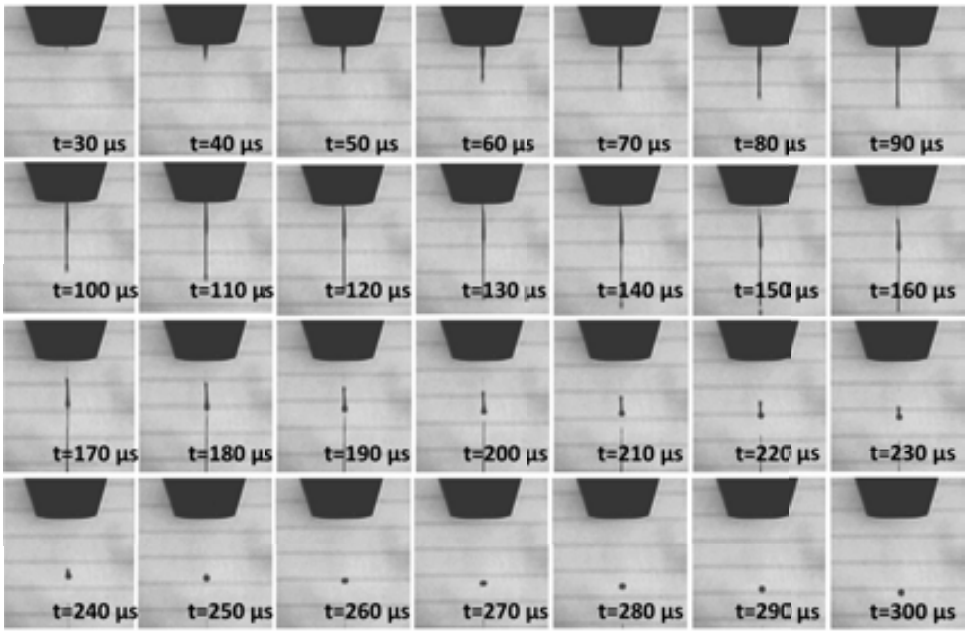


**Figure 4.6.:** Representative experimental time sequence of drop formation for a 1.5M ethanol based YBCO precursor solution ($Z \sim 5.5$) using a bipolar waveform with voltage amplitude $V_1 = +70V$; $V_2 = -38V$; corresponding times$t_{rise} \sim 2\mu s$; $t_{dwell} \sim 6\mu s$; $t_{fall} \sim 3\mu s$; $t_{echo} \sim 6\mu s$; $t_{final\,rise} \sim 2\mu s$ and frequency $f = 200Hz$. The number at the bottom of each frame indicates the elapsed time (time has passed from drop ejection). Interframe time was set at $10\mu s$.

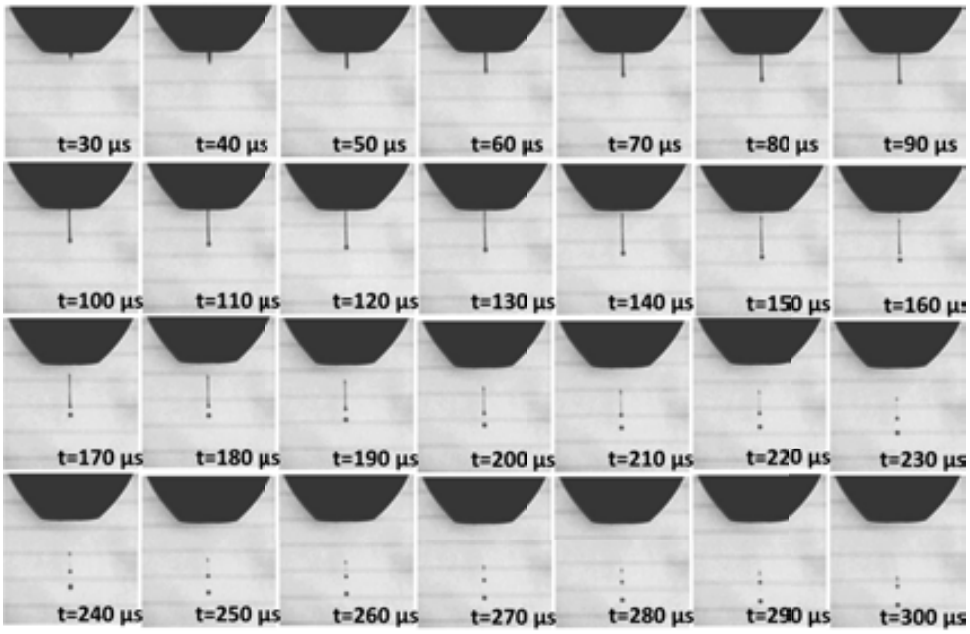


**Figure 4.5.:** Representative experimental time sequence of drop formation for a 1.5M ethanol based YBCO precursor solution ($Z \sim 5.5$) using a bipolar waveform with voltage amplitude $V_1 = +43V$; $V_2 = -38V$; corresponding times $t_{rise} \sim 2\mu s$; $t_{dwell} \sim 6\mu s$; $t_{fall} \sim 3\mu s$; $t_{echo} \sim 6\mu s$; $t_{final\,rise} \sim 2\mu s$; and frequency $f = 200Hz$. The number at the bottom of each frame indicates the elapsed time (time has passed from drop ejection). Interframe time was set at $10\mu s$.

Up to now, it has been demonstrated that for an adequate drop jetting process, it is mandatory to control both physicochemical properties of the ink and the driving parameters of the piezoelement.

To summarize, when a liquid thread is ejected from the nozzle, different situations might be considered (Fig. 4.7):

1. The liquid filament ejected from the nozzle breaks as a whole and contracts into a single droplet (Fig. 4.7a and represented in Fig. 4.2). This is the optimal situation required for inkjet applicability, cause it becomes to a unique single droplet.

2. The liquid thread ejected from the nozzle breaks into several parts generating multiple satellites (Fig. 4.7b and displayed in Fig. 4.4 to Fig. 4.6).

3. Sometimes, the liquid thread emerging from the nozzle breaks into different parts that, depending on the axial velocity of those, may recombine with the primary drop. This circumstance is reflected in Fig. 4.7c. It is a valid option for printing only if the recombination is produced before impacting on the substrate. If the recombination process takes place, the final droplet has a kinetic energy lower than the primary drop due to viscous dissipation during the merging process.

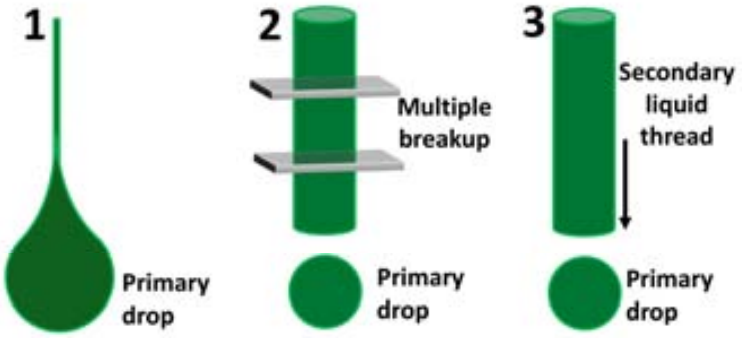


**Figure 4.7.:** Schematic representation of the multiple situations that may occur when liquid emerges from the nozzle.

Hence, Fig. 4.8 outlines the essential stages involved in fluid dynamics depending on $Z$ number and the driving parameters of the piezoactuator.

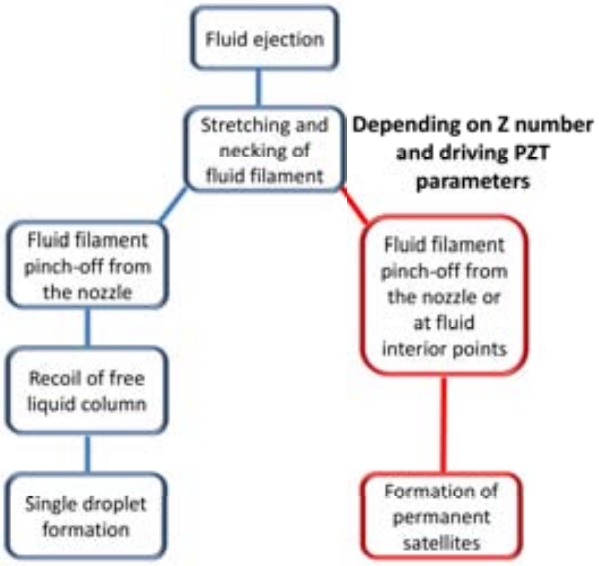


**Figure 4.8.:** Main common stages involved in drop formation depending on the ink properties and the PZT excitation parameters used.

## 4.6. Influence of rheological parameters on drop formation: quantitative analysis

In order to examine and discuss quantitatively the drop formation process, the positions of several representative points of the ejected liquid are plotted versus the time, to obtain the corresponding drop formation curves. The primary attention in this section is focused in determining how affects the viscosity of the ink to variables of great importance such as breakup length and breakup time and others like velocity of fluid as well as liquid shape evolution when the viscosity of the ink changes [18].

#### 4.6.0.1. Drop formation curves

From the sequential images obtained successively by changing the amount of delay time, the distance of the liquid head and tail from the nozzle are temporally monitored for the tested inks and presented in what we call drop formation or evolution curves [14, 236, 239, 240]. Fig. 4.9a depicts the shape of the liquid thread after rupture from the nozzle for the 1.5M ethanol based YBCO precursor solution at an actuation voltage of 38V/-38V (Fig. 4.2). In Fig. 4.9b, we present the trajectory of the ejected droplet as a function of the elapsed time for this fluid. The black coloured curve represents the round head trajectory which becomes the tip of the primary droplet and the red plot symbolizes the later tail trajectory of the liquid strand. The first red dot indicates the point at which the filament tail ruptures from the nozzle and the last one corresponds to the recoiling of the liquid thread and formation of a single drop. The slope of both curves draws the travel speed of the different parts of the liquid column.

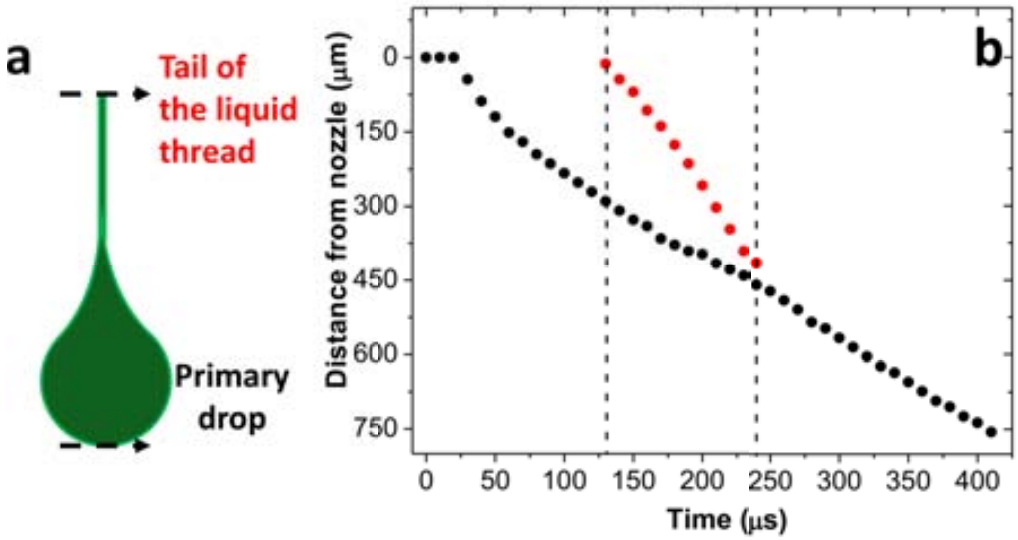


**Figure 4.9.:** Curve of drop formation corresponding to the sequential images displayed in Fig. 4.2. (a) Several representative points during the evolution of the ejected liquid after pinch-off from the nozzle. (b) Time dependent distance between the lead and tail ends relative to the nozzle.

It should be emphasized that those previous curves form a closed loop due to the recombination of the satellite and the primary drop at $\sim 250\mu s$ after drop triggering as observed in the experimental sequence. The liquid thread breaks up from the nozzle (onset of red curve) at approximately $t \sim 130\mu s$. The moment at which the head and the tail trajectories merged corresponds to the formation of the single droplet at $t \sim 250\mu s$. This graphical description divides the ejection in three differentiated stages separated as dashed lines: filament elongation until $t \sim 130\mu s$, filament recoiling till $t \sim 240\mu s$ and, finally, single droplet formation at $t \sim 250\mu s$. In the black curve is also worthly to be noted that at $t \sim 60 - 70\mu s$ and $t \sim 190 - 200\mu s$, two slopes changes are observed according to the momentum conservation rules. At $t \sim 60 - 70\mu s$, we observe a decrease of the drop speed due to the surface tension developed by the incipient liquid thread, which is starting to move. This force decreases at the same time that the thread enlarges until its rupture. Then, the liquid thread increases in diameter and shortens, increasing the surface forces and decreasing drop speed ($t \sim 190 - 200\mu s$) until the recoiling is produced at $t \sim 250\mu s$.

By analizing the drop evolution curve corresponding to the fluid dynamics of the 0.5M ethanol based YBCO precursor solution at a driving voltage of $38V$/-$38V$ (Fig. 4.4) and pulse width $19\mu s$, various conclusions could be drawn. In black colour (see Fig. 4.10b), it is represented the trajectory of the primary drop, which detach from the liquid filament at $t \sim 70\mu s$. The blue curve corresponds to the leading point of the secondary fluid filament generated after the first liquid breakup. Finally, the red plot correlates with the slower tail of this secondary liquid thread that separates from the nozzle at $t \sim 100\mu s$. The convergence of both blue and red curves points out the recombination of the upper and lower end of the second liquid thread to create a single droplet after an elapsed time of $\sim 240\mu s$. Contrarily, the black plot does not intersect to any curve revealing that the primary drop remains as a permanent satellite during all the ejection process.

This fact may be observed from the drop formation curve. The relative distance between the primary drop and the liquid thread increases with time, revealing that the primary drop remains as a permanent satellite and never merge with the tail before impacting into the substrate. In this case, the dashed lines divide the ejection mechanism in four differentiated stages: first, the elongation, stretching and filament rupture at $t \sim 70\mu s$, second, the liquid thread breaks off from the nozzle at t$\sim$ $100\mu s$, third the recoiling of this second thread and the last is the single droplet formation at $t \sim 240\mu s$.

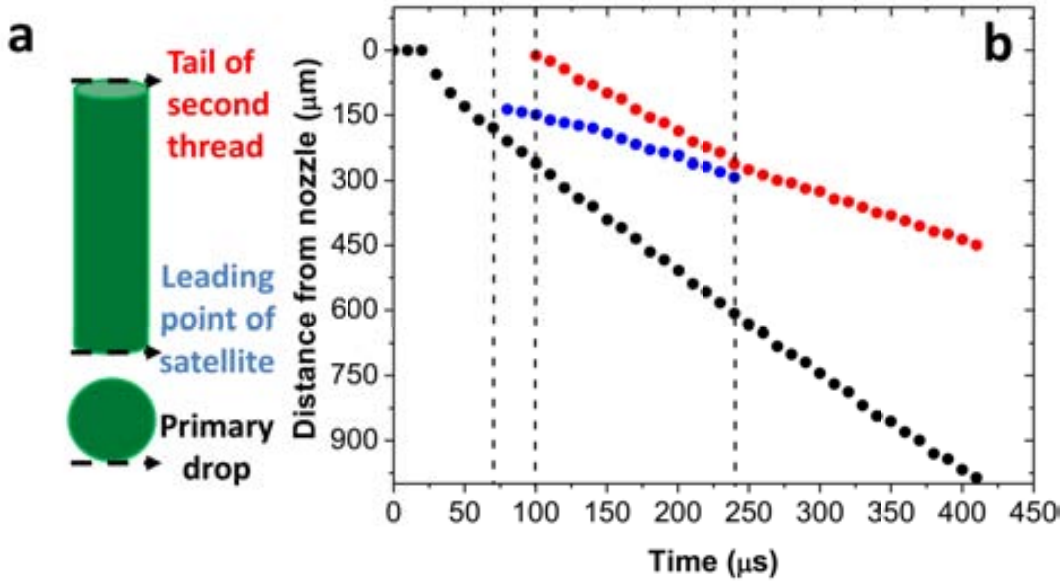


**Figure 4.10.:** Curve of drop formation corresponding to the sequential images displayed in Fig. 4.4. (a) Several representative points during the evolution of the ejected liquid after rupture from the nozzle and within the liquid thread. (b) Time dependent distance between the lead and tail ends and the primary drop relative to the nozzle.

Finally, Fig. 4.11 and Fig. 4.12 want to provide an idea about how complex might become drop behaviour when inadequate driving conditions are employed. This graph corresponds to the drop formation curve for the 100% ethanol ($Z \sim 30$) at an excitation voltages of $V_1 = +38V$; $V_2 = -38V$; and corresponding times: $t_{rise} \sim 2\mu s$; $t_{dwell} \sim 6\mu s$; $t_{fall} \sim 3\mu s$; $t_{echo} \sim 6\mu s$; $t_{final\,rise} \sim 2\mu s$, the same actuation conditions used for the previous inks. Coloured in black it is found the trajectory of the upper end of the primary liquid thread, which elongates until $t \sim 70\mu s$. At this point, breakup occurs and this primary liquid thread is divided into a second thread and a permanent satellite that will continue separately its flight. The evolution of the lower end of this second liquid thread is depicted in orange in Fig. 4.12, while the upper edge is shown in colour red. The anterior liquid thread detaches from the nozzle at approximately $t \sim 120\mu s$ and rapidly breaks into a permanent satellite, which its lower end is depicted in light blue in the graphical representation. The new free end of the second liquid thread is modelled by the light green curve. As time progresses, this second liquid thread is doubly ruptured from both ends at approximately $t \sim 160\mu s$ generating two more liquid threads. The evolution of the fresh edge generated from the rupture of the upper part of this second liquid thread is shown in magenta. Otherwise, the upper and lower bounds of the remaining second

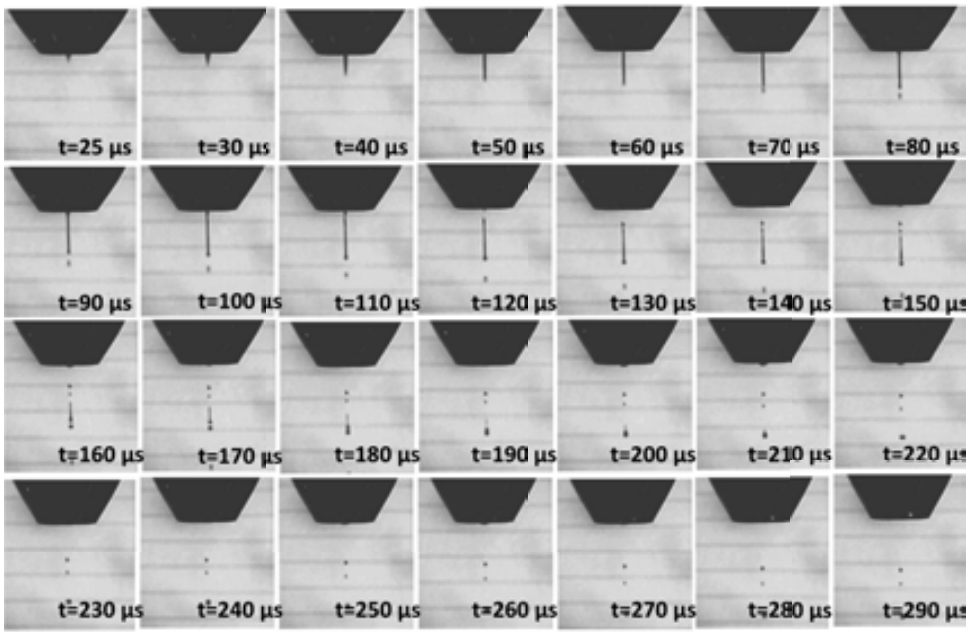


**Figure 4.11.:** Representative experimental time sequence of drop formation for 100% ethanol ($Z \sim 30$) using a bipolar waveform with voltage amplitude $V_1 = +38V$; $V_2 = -38V$; corresponding times $t_{rise} \sim 2\mu s$; $t_{dwell} \sim 6\mu s$; $t_{fall} \sim 3\mu s$; $t_{echo} \sim 6\mu s$; $t_{final\,rise} \sim 2\mu s$ and frequency $f = 200Hz$. The number at the bottom of each frame indicates the elapsed time (time has passed from drop ejection). Interframe time was set at $10\mu s$.

liquid thread are presented by the brown and navy blue trajectories, respectively. The premature second liquid thread merges with the fifth liquid thread (second faster satellite) at roughly $t \sim 230\mu s$ as can be seen by the convergence of the orange and brown curves of the drop evolution curve. To summarize, at the end of the ejection process, four permanent satellites are present, the same four curves that do not join with any others. The first rupture of the liquid thread and the final recombination of various parts of fluid are extreme positions of four sequential intermediate ruptures marked in the plot as vertical dashed lines.

Going deeply into the drop formation curves allow us to extract powerful information about other quantitative parameters of the overall fluid dynamics. Apart from the temporal history of the filament length, relevant parameters such as breakup length and breakup time, as well as ejection velocity can be determined [18]. Fig. 4.13 shows the variation of the filament length as a function of the delay time for the studied fluids. This plot indicates that the rupture time of fluids with lower $Z$ value is delayed. Fluids with higher $Oh$ number or lower $Z$ value have longer extended filaments and their rupture time is delayed. Also, it is worth to remark that the ligament length grows linearly with time before the liquid breaks up, while, when the recoiling process starts, filament length decreases as may be observed in the negative slope of those plots.

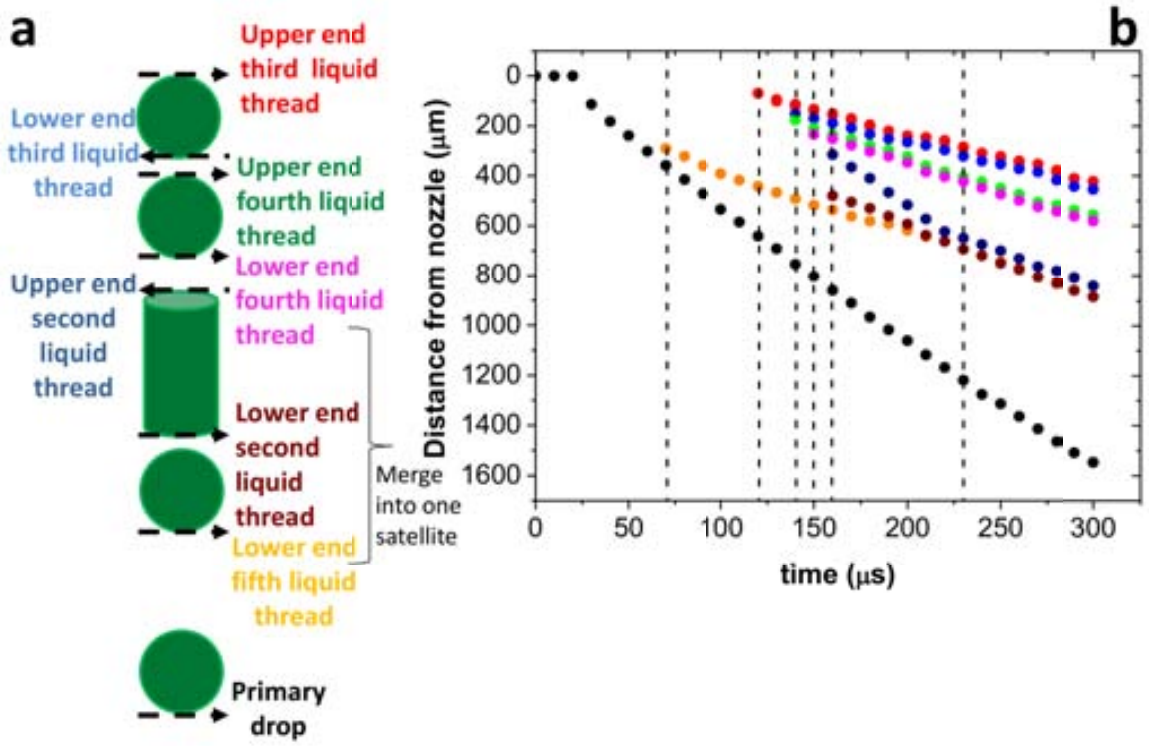


**Figure 4.12.:** Curve of drop formation corresponding to the sequential images displayed in Fig. 4.11. (a) Various representative points during the evolution of the ejected liquid after rupture within the liquid thread and from the nozzle. (b) Time dependent distance between the multiple liquid threads and the primary drop relative to the nozzle.

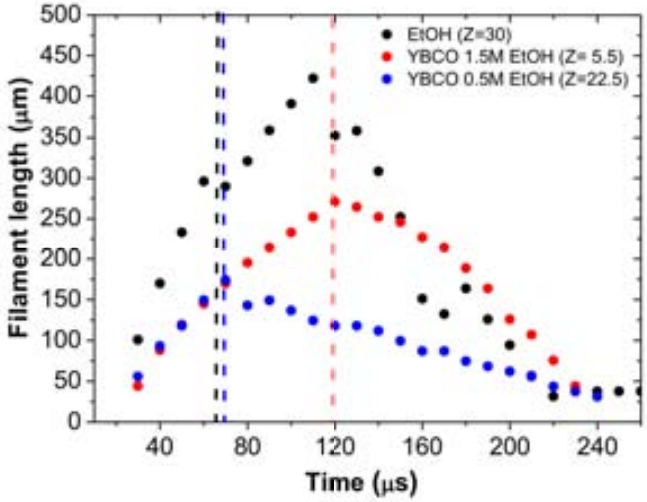


**Figure 4.13.:** Filament length variation as a function of the elapsed time for the three fluids with different Z values. Dashed lines indicate the time of liquid separation from nozzle for the liquid with $Z \sim 5.5$ and within somewhere in the middle of the liquid strand for the inks with $Z \sim 17$ and $Z \sim 30$.

The travel velocity of the ejected liquid thread before rupture and the relative velocity between the head and the tail at the moment of the breakup determines the jetting

dynamics of the fluid. In this way, the average velocity of the primary drop has been obtained by simple linear regressions of the previous plots. Those values obtained are the following: $1.8m/s$ for the $Z \sim 5.5$ fluid, $2.4m/s$ for the $Z \sim 22.5$ fluid and $5.4m/s$ when $Z \sim 30$. As may be noted, the travel velocity of the first ejected liquid thread, which becomes the tip of the primary drop, increases with increasing $Z$ for a given PZT actuation due to the non-damped oscillations inside the nozzle.

## 4.7. Influence of driving waveform on drop formation: quantitative analysis

The last presented section quantifies the impact of modifying the ink viscosity on the fundamental mechanism of DoD drop formation. In this section, the effects on changing the pulse amplitude of the PZT waveform on the ligament length, the elongation rate of the filament prior to rupture, the average velocity of the primary droplet as well as the time and length at pinch-off have been analyzed by processing the experimental flashed images [203, 236].

In Fig. 4.14, the variation of the distance from the nozzle to the leading edge of the primary drop at different voltage amplitudes and constant pulse width as a function of the elapsed time is displayed. The tested solution was the 1.5M ethanol based YBCO precursor solution. Pinch-off from the nozzle occurs at the last point represented in each of these plots. The ejected liquid snaps off from the nozzle in approximately $130\mu s$ for the lowest working voltage pair, at $t \sim 140\mu s$ for the intermediate amplitude voltage and at $\sim 170\mu s$ for the highest voltage.

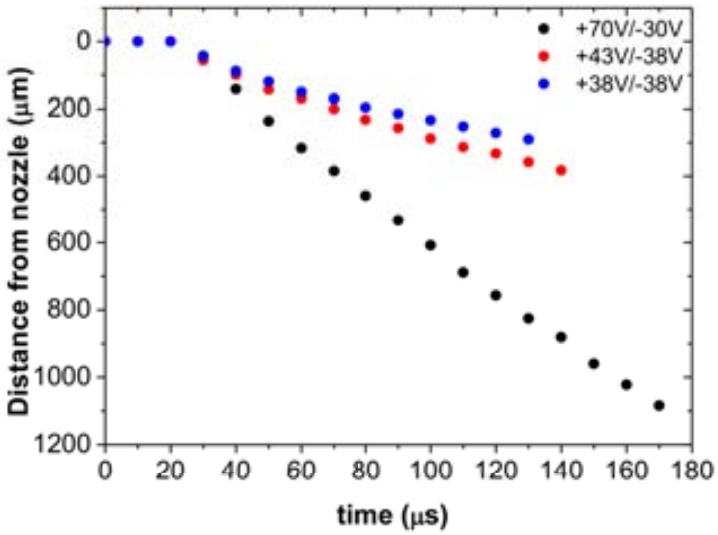


**Figure 4.14.:** Evolution of the distance from nozzle with time at different pulse amplitudes of driving signal. The model ink used in this study was the 1.5M EtOH based YBCO precursor solution printed at a constant pulse width of $19\mu s$. These drop formation curves correspond to the experimental images Fig. 4.2, Fig. 4.5 and Fig. 4.6. The highest time shown for each plot corresponds to the time of pinch-off from the nozzle.

Carrying out linear fittings to the pre-breakup data points, it is possible to obtain the average velocity of the leading droplet. Next Tab. 4.3 displays relevant parameters for the inkjet printing applicability point of view, such as time and length at pinch-off and the average velocity of the leading droplet prior to rupture.

| **Solution** | **Driving voltages** $(V)$ $(+V_1/-V_2)$ | **Pinch-o time** $(\mu s)$ | **Length of liquid thread at pinch-o** $(\mu m)$ | **Velocity of the leading edge** $(m/s)$ |
|---|---|---|---|---|
| 1.5M ethanol based YBCO precursor solution | +38/-38 | 130 | 290 | 2.5 |
| | +43/-38 | 140 | 380 | 3.1 |
| | +70/-38 | 170 | 950 | 7.3 |

**Table 4.3.:** Time and length at pinch-off and droplet speed of the leading edge for a 1.5M ethanol based YBCO precursor solution as a function of driving voltages.

The following observations might be extracted from the previous table. Firstly, the breakup time of the liquid thread for higher amplitudes is longer than that for lower voltages. Second, the limiting length or the filament length at rupture time increases with piezoactuator signal voltage. And third, the ink is ejected at high velocities for higher voltages amplitudes [18]. When the voltage pulse applied to the piezoelectric actuator increases, higher velocities of the leading drop are observed, thus generating longer threads that rupture after longer time.

## 4.8. Summary and conclusions

This first study has experimentally examined the dynamics of droplet formation by varying the rheological fluid properties and the pulse voltage of the PZT bipolar actuation WV using a single nozzle piezoelectric printhead. Concluding remarks of this part are written as follows:

Drop formation process is largely influenced by the PZT driving parameters and the rheological properties of the ink. A quantitative analysis to understand how these parameters affect drop formation fluid dynamics is of special importance.

As discussed in the previous experimental results, the time and length at rupture instant and the velocity of the leading drop are found to be crucially dependent on both the voltage amplitude and the ink viscosity. The length of the liquid thread and its surviving time increases considerably when the driving voltage increases. As the energy transduced to the fluid increases, longer threads become more unstable leading to multiple satellites. Moreover, the ejection speed of the leading end also increases as the drive voltage grows up due to the higher impulse imparted by the piezo. Alternatively, when $Z$ number decreases and, therefore, viscosity increases, the fluid filament stretches longer and becomes thinner, which in turn, makes higher the resistance of the liquid thread to flow axially. In this situation, drop velocity of the leading drop decreases as $Z$ decreases due to the enhanced

viscous dissipation. Special attention should be taken into account when long filaments are formed cause it has a direct effect to the possibility to generate single droplets at high frequencies, which is essential for high throughput deposition processes.

These observations clearly demonstrate the need to select appropriate ink physicochemical properties and adequate operational actuation conditions to obtain single drops with no satellites. If the single droplet comes from the recombination of a primary drop and a satellite, the distance required for such recombination is crucial to determine the minimum gap between the nozzle and the substrate.

Once single drop formation process is analyzed and the main parameters that significantly affect the process have been detected, a good printing quality demands precise performance criteria to be accomplished. The resulting drops are required to have a certain velocity to reduce the time of flight and therefore to reduce dot positioning errors. Besides, drop velocity plays an important role in splashing and re-bouncing processes [21]. Also, depending on the application under consideration, the performance requirement concerning drop volume varies. This is a remarkable feature of inkjet printing known as drop size modulation, which is a good way to find a trade-off between print quality and productivity. In addition, to avoid irregularities in the final coating or pattern, such drop characteristics must be reproducible.

The second part of this chapter deals with the understanding of how by tuning the driving waveform of the piezoactuator, drop velocity and drop size are tuned. In this sense, the amplitude and the pulse width of the actuation signal were systematically varied to investigate their influence on drop size and drop velocity [15, 241, 242].

## 4.9. Influence of driving waveform on drop size and drop velocity

The materials used in this second part of the chapter were the same inks presented in Tab. 4.1, with the addition of the ethyleneglycol, which has a viscosity of about $12mPa \cdot s$ at a shear rate of $100s^{-1}$, a surface tension $\gamma$ of $47.5mN/m$ and a density value of $1.113g/cm^3$, giving a Z value of $\sim 4.7$. Each experiment presented in this section was performed under certain PZT driving conditions shown in the corresponding part.

### 4.9.1. Minimum working voltage

For a given pulse, the voltage amplitude determines the magnitude of the volume change induced by the piezoelectric actuator. Increasing the voltage amplitude results in larger volume changes in the same amount of time. Consequently, there is a minimum voltage required to eject a drop.

Fig. 4.15 displays the minimum voltage required to form a drop for the different model fluids:

As will be presented in further sections, above this critical value, both volume and velocity of ejected droplets increase with voltage if all other waveform parameters are kept

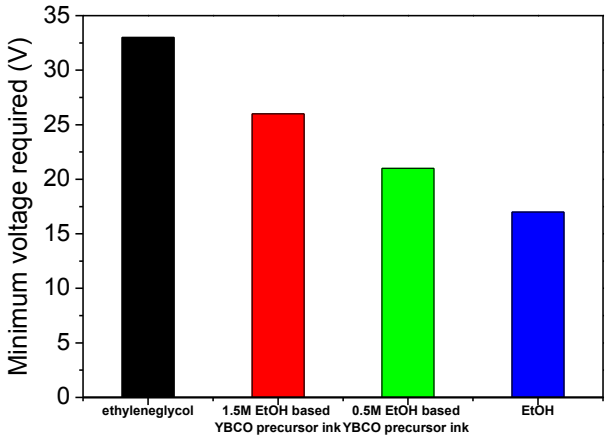


**Figure 4.15.:** Minimum voltage required to eject a drop for the different tested inks. Below this voltages, droplets could not be generated. The total pulse width in this experiment was constant for all the solutions and kept at $30\mu s$. Drop frequency was set at $f = 200Hz$.

constant. Below these pulse amplitudes, droplets could not be ejected. Therefore, each specific fluid has its optimum driving parameters. As may be noted in Fig. 4.15, when ink viscosity increases, larger voltage amplitudes are required to generate a drop due to the higher energy dissipation [176].

## 4.9.2. Drop velocity measurements

In our experiments, drop velocity is determined by optical methods. The drop under investigation is moved by adjusting the delay time between the pulse applied to the PZT and the strobe trigger, so that it coincides with one of the edge of a reference. The elapsed time is then increased until the drop reaches the next reference point. From this delay time increase ($\Delta t$) and the known distance between the two reference points ($\Delta x$), the drop velocity $v$ is calculated by using the expression $v = \frac{x}{t}$. Typical errors in drop velocity measurements are $\sim$5%.

### 4.9.2.1. Drop velocity as a function of pulse amplitude

Fig. 4.16a-b show some examples of the voltage amplitude dependence with drop velocity for different fluids. Fig. 4.16a corresponds to the drop velocity-voltage dependence for a 1.5M ethanol based YBCO precursor solution, while Fig. 4.16b displays the same dependence for 100% ethanol. Those figures reveals that the amplitude of the driving pulse clearly has a linear influence on the velocity of launched drops. As seen in Fig. 4.16, this trend is found to be independent of the fluid physicochemical properties.

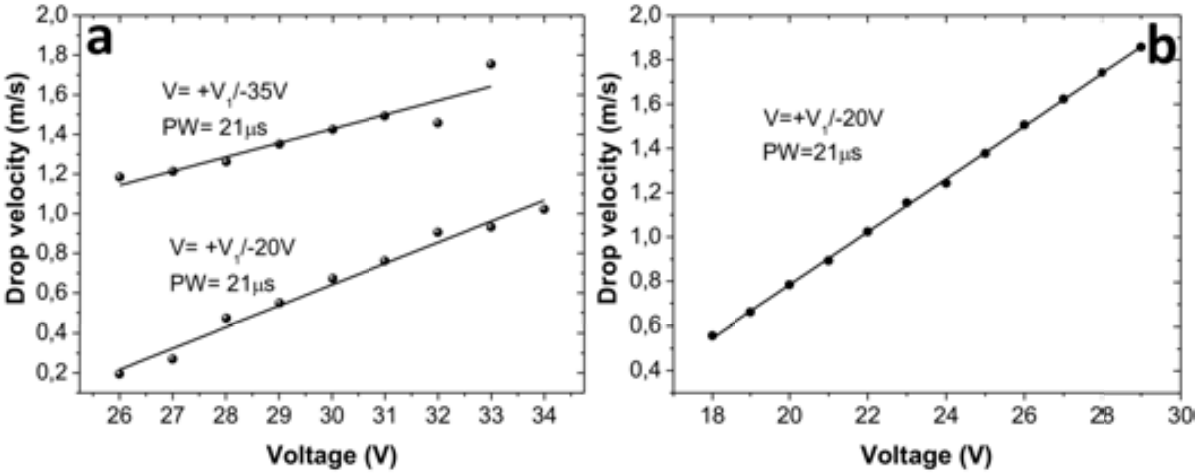


**Figure 4.16.:** Influence of the amplitude of the driving signal on the ejected drop velocity. (a) Drop velocity-voltage dependence corresponding to a 1.5M ethanol based YBCO precursor solution. (b) Drop velocity-voltage dependence for 100% ethanol. Pulse widths (PW) and voltages (V) are indicated in the corresponding plots at a frequency of $500Hz$. In this experiment, the driving voltage has been varied at a fixed pulse width for a bipolar waveform.

This behaviour might be explained taking into account that, for a constant pulse width, when the pulse amplitude increases, larger impulse is imparted by the PZT, therefore, droplets gain more kinetic energy exhibiting higher velocities.

#### 4.9.2.2. Drop velocity as a function of pulse width

Fig. 4.17a shows the drop velocity-pulse width dependence for a 0.5M ethanol based YBCO precursor solution. As may be appreciated, drop speed exhibits a maximum as a function of the driving pulse width [14, 15, 236]. The period at which this maximum peak occurs, marked in red in the plot, corresponds to the optimum pulse width, which is related with the inverse of the frequency of the fundamental oscillation mode of the liquid. By analyzing this plot, the maximum peak is located at $44\mu s$, which corresponds to a fundamental frequency of about $23KHz$, just in the range of the value reported by the manufacturer [243]. This fundamental mode can be slightly changed by the characteristics of the ink, essentially the density. In order to avoid the presence of harmonics in the actuation wave, we have used a sinusoidal excitation with a well defined period. Furthermore, when the dependence of drop velocity versus pulse width is plotted for the same fluid at different activation conditions (100% EtOH, Fig. 4.17b), this peak remains unchanged.

### 4.9.3. Drop volume measurements

Drop volume was directly determined by measuring the consumed ink volume of the reservoir by firing around $5 \cdot 10^6$ drops under a given excitation conditions. The number of fired drops is usually high to improve statistical quality of the results. Common errors in this kind of measurements are less than 5%.

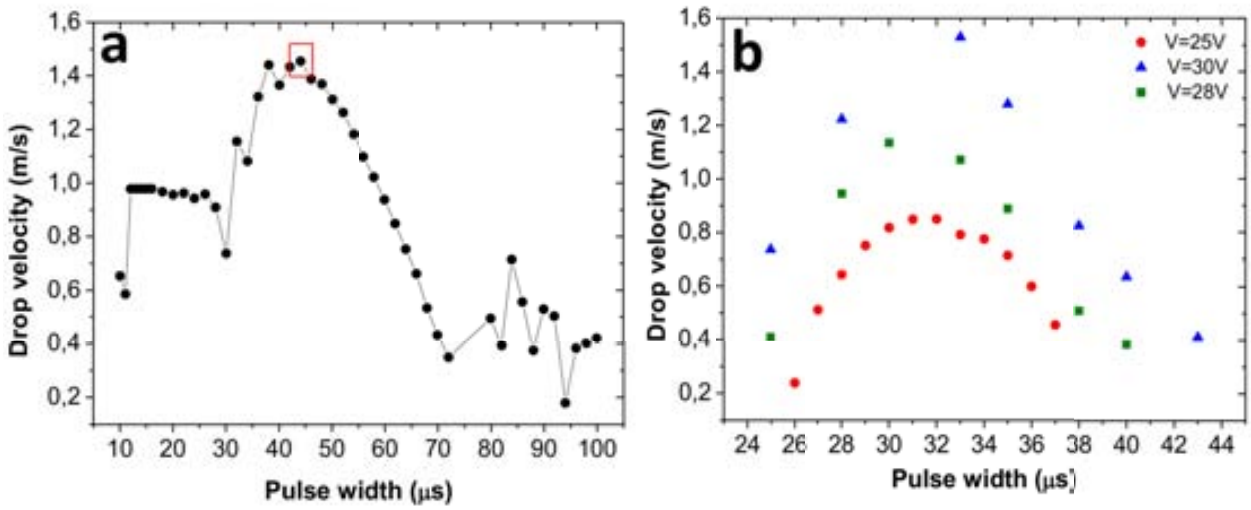


**Figure 4.17.:** Influence of the pulse width of the driving signal on the ejected drop velocity. (a) Drop velocity-pulse width dependence for a 0.5M ethanol based YBCO precursor solution. The red square marked in this plot matches with the fundamental oscillation mode of the liquid (see text). (b) Drop velocity-pulse width dependence for 100% ethanol at different excitation voltages.

#### 4.9.3.1. Drop volume as a function of pulse amplitude

The overall trend in Fig. 4.18 is that as the driving voltage increases, drop volume becomes larger due to the increased pressure wave inside the nozzle, which agrees well with the behaviour demonstrated in previous research [18, 242].

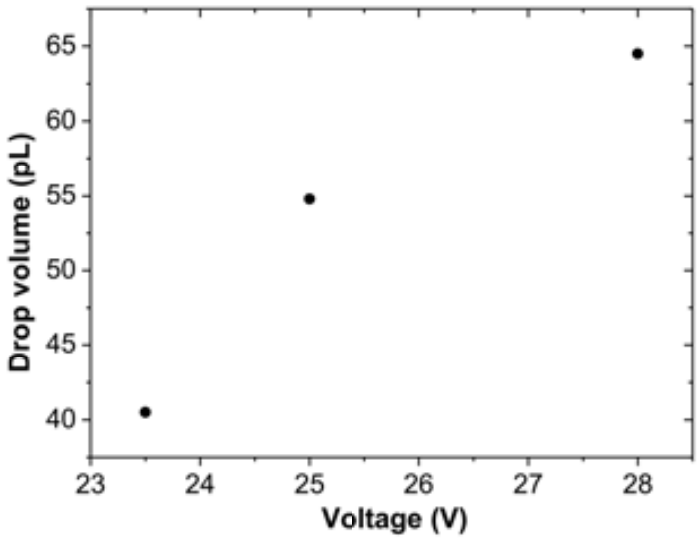


**Figure 4.18.:** Influence of the pulse amplitude of the driving signal on the ejected drop volume.

#### 4.9.3.2. Drop volume as a function of pulse width: drop size modulation

**State of the art**

In the framework of this section, literature about drop volume control was examined and one may realize that it can be found a huge variety of works on DoD drop formation where the diameter of drops are roughly the same as the diameter of the nozzle [40, 244–247]. In the bibliography is also possible to find lots of documents about numerous techniques for making drops much larger than nozzle radius [111, 248].

Nowadays, the demand for different methods for creating small microdrops and modulate the drop size has increased in order to improve the image quality and the pattern resolution. At least, two procedures may be performed to decrease drop size. An straightforward methodology is to reduce the orifice diameter [248]. However, by scaling down the orifice size, the problem of plugging and clogging becomes more serious [249]. Alternatively, various works in the long-existing problem of reducing the drop volume without decreasing the nozzle diameter have been published in the last few years. DoD inkjet printing has been demonstrated as a potential tool to reduce the drop size significantlly below the nozzle diameter by tuning the PZT excitation signals [111, 240, 246, 250–253]. For instance, Chen and Basaran [251] proposed a new waveform to generate drops of water-glycerin smaller than nozzle diameter (Fig. 4.19).

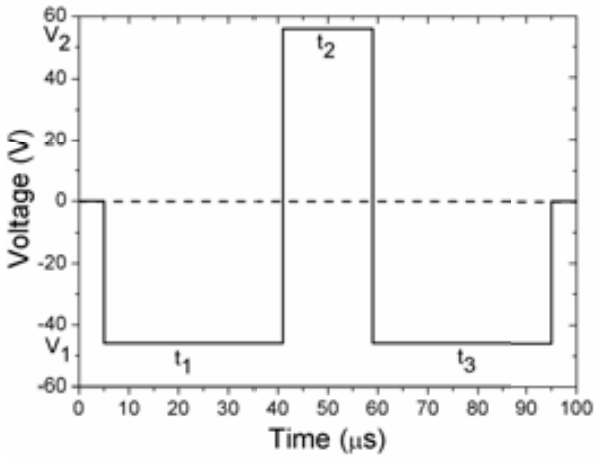


**Figure 4.19.:** Waveform voltage signal used in the experimental work of Chen and Basaran [251]. In this case: $V_1 = -46\,V$, $V_2 = +56\,V, t_1 = 37\,\mu s, t_2 = 18\,\mu s$, $t_3 = 36\,\mu s$.

This waveform consists of a succession of three square pulses. By applying the first negative voltage $V_1$, the fluid is propelled towards the orifice forcing the meniscus to bulge (Fig. 4.20a). In the second step (positive voltage, dwell time $t_2$; Fig. 4.20b) the fluid is withdrawn and strongly accelerated inside the nozzle. In the third step (negative voltage $V_1$, dwell time $t_3$) the main objective is to propel a "tongue" that protrudes from the tip of the primary mass of fluid (Fig. 4.20c). The presence of the "tongue" is caused by a small volume of liquid moving at very high speed relative to the nearby liquid and its length and speed depend on the voltage difference $V_1 - V_2$ (Fig. 4.20d). So, the key point is to avoid the recoiling of this "tongue" with the primary drop (Fig. 4.20e). Then, the

ejection only of the center of the core fluid after the large mass of liquid attached to the nozzle collapses back generates the small drop (Fig. 4.20f).

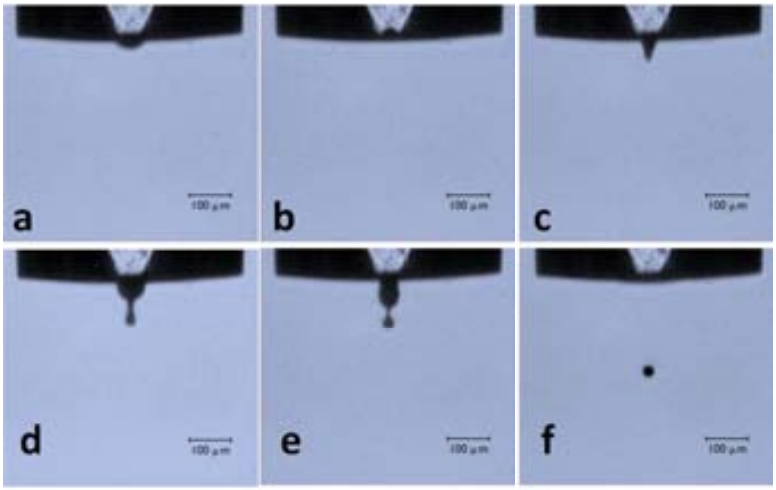


**Figure 4.20.:** Images of the drop ejection process according to the waveform displayed in Fig. 4.19. It is possible to follow the sequence tongue formation. Reproduced from [251].

Also, scientists from Purdue University proposed other waveforms based on complex meniscus movement [254, 255].

### Single nozzle piezoelectric printhead: experimental drop size modulation

In next lines, we exhibit our capability in drop size modulation. Particularly, in our study, we demonstrate that, in a bipolar waveform, by decreasing $t_{echo}$ from $25\mu s$ to $5\mu s$ (see Fig. 4.21) and keeping constant the other parameters, drop volume may be tuned from $50pL$ to $11pL$ by using the $60\mu m$ single nozzle diameter piezohead. This volume variation corresponds to a reduction of a 78%. The actuation parameters that provide the smallest

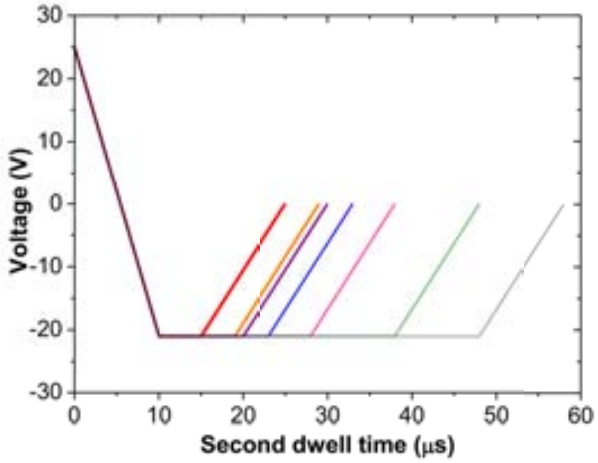


**Figure 4.21.:** Variation of second dwell time in a bipolar waveform according to sec. 2.5.

drop volume of $11pL$ are the following: $V_1 = +25V$; $V_2 = -21V$; and corresponding times $t_{rise} \sim 2\mu s$; $t_{dwell} \sim 5\mu s$; $t_{fall} \sim 3\mu s$; $t_{echo} \sim 5\mu s$; $t_{final\,rise} \sim 2\mu s$. Such $11pL$ drops are obtained by activating the *second oscillation mode of the liquid column* with a frequency nearly doubling that reported by the printhead manufacturer as fundamental ($\sim 20KHz$) [243]. However, it is thought that the larger ones are achieved by activating combinations of different harmonics. It will be concluded that by modifying the total pulse width by increasing the second dwell time, is possible to modulate drop size in a real time.

Next Fig. 4.22 displays the drop size modulation for a 0.5M ethanol based YBCO precursor solution at an excitation voltages of $+25V/-21V$.

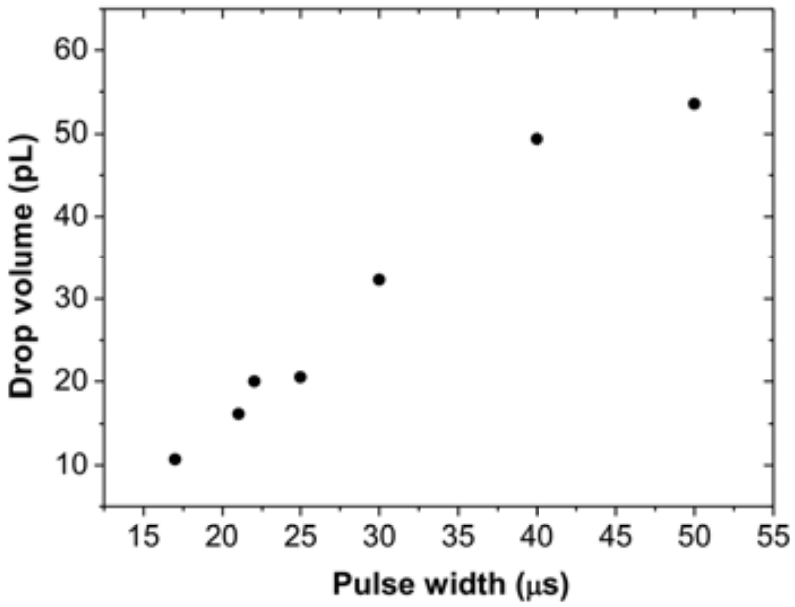


**Figure 4.22.:** Drop size modulation for a 0.5M EtOH based YBCO precursor solution. Mention that in this case the pulse width of the waveform was modified by selecting different echo times (from 3 $\mu s$ to 25 $\mu s$). For all the experiments, $V_1$ and $V_2$ were set at $+25V/-21V$ and the drop frequency was fixed at $800Hz$.

This fact is really interesting because it opens the possibility to produce drops of a given size in real time. However, the reduction of drop volume by tuning the total pulse width is accompanied by a corresponding change in drop velocity of $\sim$20%.

Until this point, the influence of varying the pulse amplitude and the pulse width on the final drop characteristics have been shown by using the single nozzle piezoelectric printhead.

### Single nozzle electromagnetic printhead: experimental drop size modulation

Next section is devoted to display the effects of the main parameters which control drop volume in the single nozzle electromagnetic printhead. Fig. 4.23 exhibits the drop volume dependence with the ink pressure, the valve opening valve time $\tau$ and the voltage applied to the coil for a 0.0125M propionic acid:isopropanol (1:1 in volume) CZO precursor ink ($\rho \sim 0.89 g/cm^3$).

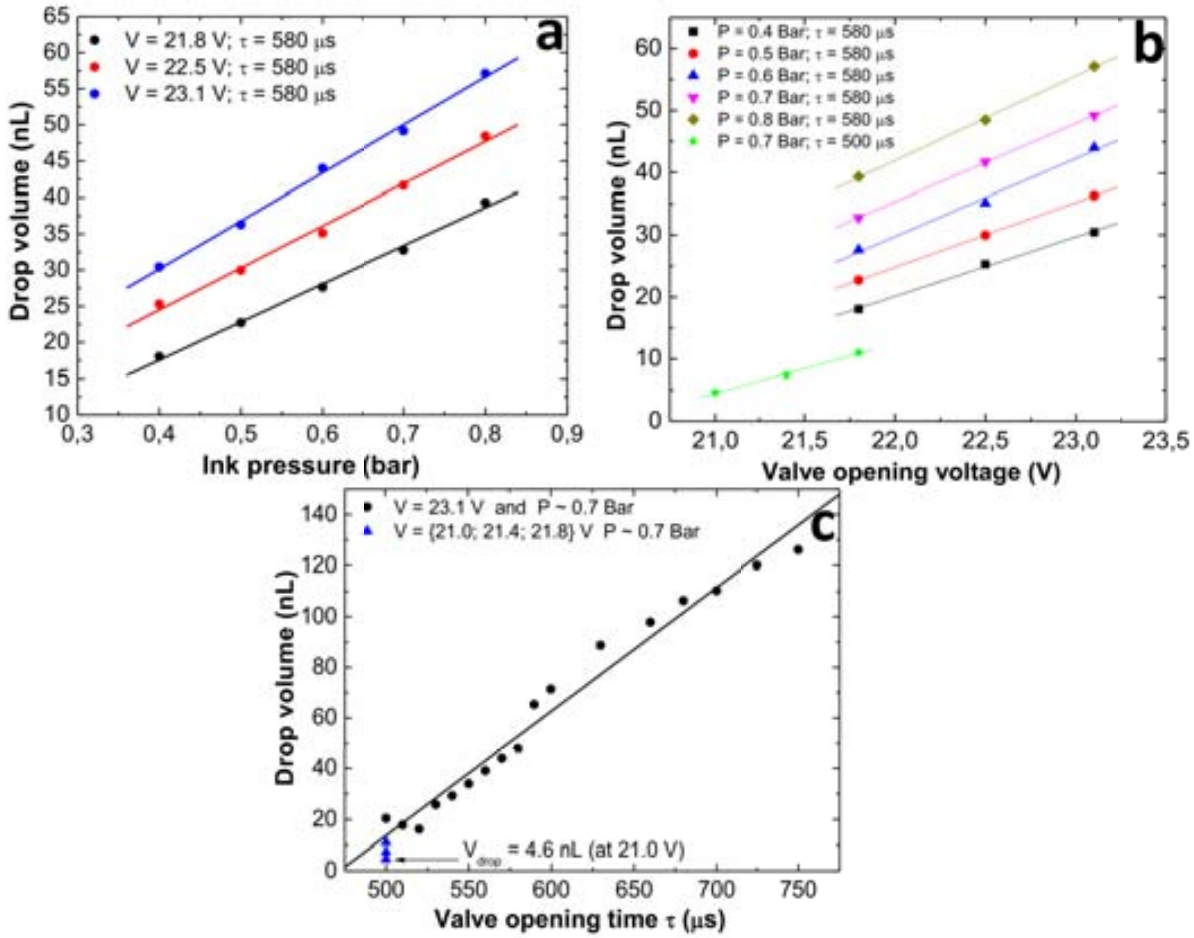


**Figure 4.23.:** Drop volume dependence on (a) ink pressure (b) valve opening voltage $V$ and (c) valve opening time $\tau$ using the electromagnetic single-nozzle printhead for a 0.0125M propionic acid:isopropanol (1:1 in volume) CZO precursor ink ($\rho \sim 0.89 g/cm^3$).

As may be appreaciated in the previous Fig. 4.23, the drop volume grows as increases the three complementary parameters: the valve opening voltage and time and the ink pressure. When more ink pressure is applied and the aperture of the valve and the time for which is kept opened are larger, drop volume also increases. In contrast to the piezoelectric systems, the electromagnetic valves can not match the small drop volumes of the piezo heads. In the case of the piezoelectric systems, the drop volume is in the $pL$ range, while in the electromagnetic solenoid valves, it is usually in the $nL$ or $\mu L$ range.

## 4.10. Summary and conclusions

In this section it has adressed how the driving conditions of the PZT actuator affect the drop ejection characteristics. In particular, the correlation between the driving parameters on the drop velocity and the drop volume has been investigated. Moreover, it is described a technique in which the volume of the ejected drop is significantly tuned by activating the second oscillation mode of the liquid column or other combinations of harmonics.

General conclusions of the second part of this chapter are outlined below:

The lowest driving voltage to form a drop is found to be deeply dependent on the fluid physichochemical properties. By comparing inks with similar density and surface tension, the minimum voltage to eject a drop increases with ink viscosity due to the higher viscous dissipation.

Drop velocity is found to show a linear relation with the driving voltage, because the impulse by the PZT is manifested by the drop velocity. Drop volume exhibits also a linear dependence with voltage amplitude. As voltage increases, larger pressure wave amplitudes are developed producing larger movements of fluid and consequently, bigger drops are formed.

For another side, when the pulse width is modified, both drop velocity and drop volume vary as well. Drop velocity as a function of pulse width shows a complex and periodic behaviour with a maximum peak that corresponds to the optimum pulse width. This optimum pulse width is defined as the pulse width for which a maximum drop velocity and drop size is achieved under certain driving conditions. In our particular case, due to the similar density and acoustic properties of the model fluids, this peak remains unchanged in position for the different tested fluids. In the same way, the optimum pulse width does not change when the voltage amplitude of the waveform is varied for the same ink.

The control of the input parameters of the waveform is essential to gain knowledge in the empirical search for creating small drops. As illustrated, the control of the bipolar actuating waveform design is an effective methodology to modulate drop volume by varying the total pulse width. It results as an efficient procedure to tune drop size in real time, however, it is accompanied by a reduction of drop velocity.

For a good drop speed and drop volume reproducibility, not only the operational driving PZT parameters are important. The slight negative pressure applied to stabilize the meniscus is also an indispensable parameter to adjust.

On the other hand, we have demonstrated that it is possible to produce single stable drops in regions where $Z$, the inverse of the Oh number, is significantly larger than 14 by tuning the excitation on harmonics of the liquid fundamental mode.

# 5. Drop-substrate interaction: the $YBa_2Cu_3O_{7-x}$ case

The main goal of this research, as mentioned before, is the manufacturing of functional ceramic oxides. Once the ink physicochemical properties have been characterized (chapter 3), together with their influence and the effects of the piezoelectric driving parameters on the single drop formation process (chapter 4), the next and last step is to understand the behaviour of merging drops and spreading onto the substrate to obtain controlled-shaped coatings and patterns. In the following chapters, it will be reviewed the process by which consecutive drops of the different studied ceramic systems interact between them and with the substrate to form the final deposit. In general therms, when a drop is ejected from the printhead, first it hits the substrate, then spreads on it and finally it comes to rest when the equilibrium state is reached.

## 5.1. Drop impact and spreading

The behaviour of a drop impacting on a substrate is controlled by several physical processes and can be driven by inertial forces, capillary forces and gravitational forces. As with in drop generation, the important dimensionless groupings in drop impact are the $Re$, $We$ and $Oh$ numbers. Typical fluids used along this research have density values close to $1 g/cm^3$, surface tensions much below $100 mN/m$ and drop diameters about $100 \mu m$. Under those length scales, $Bo << 1$, hence, gravitational forces can be neglected during impact and spreading. Thus, the dominant forces during these processes will be inertial and capillary. Schiaffino and Sonin [149,256], considered the impact of relatively low $We$ number drops on a solid surface. Although their analysis was for solidifying drops, the initial stages after drop impact can be divided into two regimes: impact driven and capillarity driven, where the transition occurs at a critical value of $We$ number. Moreover, these authors characterized the resistance to spreading in terms of the $Oh$ number, separating regimes of highly viscous and almost inviscous fluids. Fig. 5.1 shows the representation of the regimes of initial impacting drop behaviour. Besides, those authors [149,256] proposed a region, which falls into the region I of the graphical representation, where is suggested that stable drop formation takes place.

Other authors also reported that during drop impact and depending on the $We$ number, particular phenomena may be observed [113,156,159,257,258]. Van Dam and Le Clerc [113] demonstrated that drops deform and flatten when $We < 1.1$. Stow et al. [259] and Yarin [21] proposed that in droplets with $We$ numbers from 100 to 1000, splashing phenomenon occurs. If we have a look to the $We$ and $Oh$ numbers for the inks reported in this work (e.g. Tab. 4.2), it might be appreciated that they fall inside the conditions

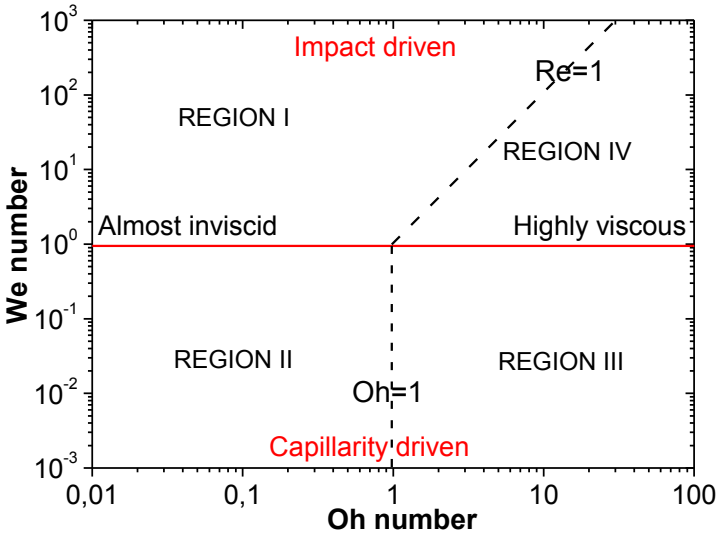


**Figure 5.1.:** Parameter space defined by axes of Oh and We numbers showing the driving force for the initial drop spreading after impact. The conditions for DoD inkjet printing fall in region I, indicating that initial drop behaviour is described by inertial or impact forces. Drawn following reference [10].

stablished by Schiaffino and Sonin [149, 256] for DoD inkjet printing (region I, Fig. 5.1). As our experimental $We$ numbers are below 100, in our printing experiments we do not expect neither splashing nor drop flattening.

## 5.2. Drop fusion and printed bead stability

Printing functional coatings or drawings require a severe trimming of the amount of ink deposited per unit area over the substrate [260]. It is critical, then, to evaluate the interactions between drops and with the substrate to create stable patterns, continuous coatings and more complex designs. The dynamics of the ink, the final characteristics of the drop (i.e. drop volume and drop speed), the ink evaporation rate and other parameters such as platform speed, are relevant aspects which affect drop fusion and spreading processes. Next Fig. 5.2 shows a schematic illustration of the fusion of drops to form a bead with a circular section. After the fusion of two drops with a diameter on the flight $2a$ and printed at a drop pitch $\triangle x$, a bead with a width $b$ that makes a contact angle $\theta$ is formed.

In next lines, we show the evolution of the morphology of inkjet-printed tracks by varying drop pitch. Also, it is developed a simple analytic framework to understand our results and establish limitations on inkjet-printed arrays.

In our case, drop pitch is the last parameter to adjust once ink properties and wettability were determined. It should be set assuring the adequate overlap and connectivity of drops to perform continuous features. When printing tracks, drop pitch can be deduced

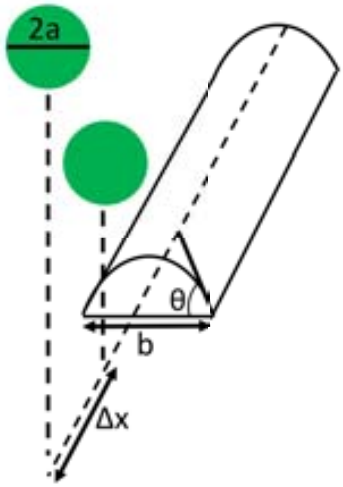


**Figure 5.2.:** Schematic image of the fusion of individual drops to form a continuous track. Based on an illustration originally published in [261].

from the different behaviours emerging when printed patterns across a range of drop pitch were examined.

Fig. 5.3 shows an optical microscopy sequence of different basic morphological arrays varying the drop pitch after a drying process at room temperature. In our case, the evaporation rate is low enough in order to maintain the ink physicochemical properties during drop fusion, keeping so the liquid evenly distributed across the track length. According to the quality of the mechanical system, the drop speed and other external conditions, an uncertainty in positioning and diameter of the printed drop appears. This value corresponds to a deviation $\delta$ between the actual drop boundary position and the expected one. Although this value is very low, it becomes relevant in the behaviour of deposited droplets in limiting cases leading to some irregularities or premature fusions in 1D (tracks) and 2D coatings. As observed in Fig. 5.3, at drop pitch $\Delta x$, clearly larger than diameter of the drop after impingement on the substrate, $b$, plus $\delta$ ($\triangle x \gg b + \delta$), no droplet overlap occurs and an array of separated drops was observed (Fig. 5.3a). From this figure, it is possible to deduce the average drop diameter after impingement onto the substrate ($b \sim 100\mu m$). At drop pitch in the range of $b$ plus $\delta$ ($\Delta x \sim b + \delta$), fluctuations $\delta$ can lead to disordered drop fusions when a newly arriving drop touches the previous one on the surface, still remaining in liquid form. Irregular bridging between drops may be observed (Fig. 5.3b). Bridge formation is generated because at an adequate drop spacing, the contact line expands until the point that touches the printed bead and expands into it. At drop pitch slightly smaller than drop diameter $b$ plus $\delta$ value ($\Delta x < b + \delta$), uniform drop fusion exists but the final liquid bead does show wavy sides (Fig. 5.3c-e). This twisted effect becomes less pronounced as the drop pitch is decreased (Fig. 5.3f,g). Continuous lines with constant base width and completely parallel sides (Fig. 5.3h) were formed by further lowering drop pitch, being the threshold to obtain parallel edges close to $70\mu m$.

Still further decreasing drop pitch, an important amount of ink needs to be handled and local broadenings were again recovered. In Fig. 5.3i, the waving structure was rescued

by ejecting five drops at each position, while maintaining drop pitch at $50\mu m$. In this case, in contrast with the previous ones where the interaction with the substrate defines the liquid behaviour, it is the liquid surface tension, rheology, and evaporation rate which rule the fluid arrangement.

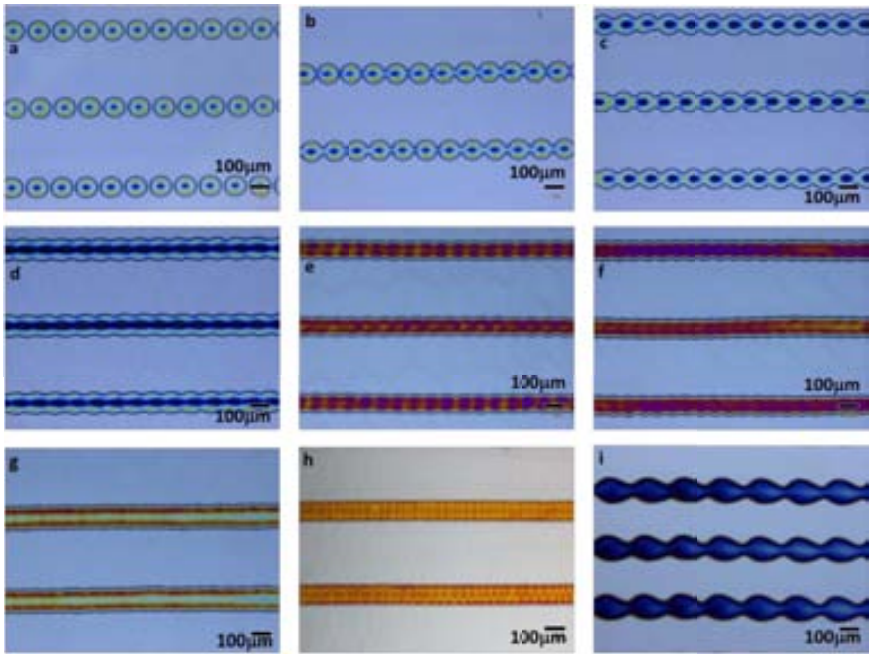


**Figure 5.3.:** Optical images of the printed arrays on LAO substrate after a drying process at RT varying the distance between adjacent drops: (a) $125\mu m$ (b) $117\mu m$ (c) $111\mu m$ (d) $100\mu m$ (e) $83\mu m$ (f) $74\mu m$ (g) $69\mu m$ (h) $50\mu m$ (i) $50\mu m$ (see text). In the case of picture (i), droplet volume is five times higher than in the previous images. Drop pitch decreases from left to right and from top to bottom. Each line is formed by one printed dots.

### 5.2.1. Model for drop shape and criteria for printed bead stability

As we will now discuss, the previous experimental sequence shows that the behaviour of the overlapping drops is in good agreement with theoretical models and previous experimental works [149, 256, 262, 263]. Considering the interaction of the ink with the substrate, the rheological and wetting properties of the ink and the dynamics of drop solidification, Davis [262] examined the stability of a bead on a flat surface subject to the following limitations: (a) beads whose contact angle at the line is fixed, and the contact line is free to move, (b) beads whose contact angle is a function of the moving contact line speed with a limiting value at zero line speed, and (c) beads whose contact angle is free to change during bead formation, but the contact line is pinned. For a better clarity of the different situations, an image reflecting the different mechanisms is displayed below (Fig. 5.4).

According to the experimental results displayed in Fig. 5.3, we have experimental evidences that the contact line is pinned ($\theta_{rec} \neq \theta_{adv}$; see appendix) and the contact angle is found between the advancing and the receding values. In the micrograph sequence, it may be clearly appreciated that the width of the bead does not increase even though the

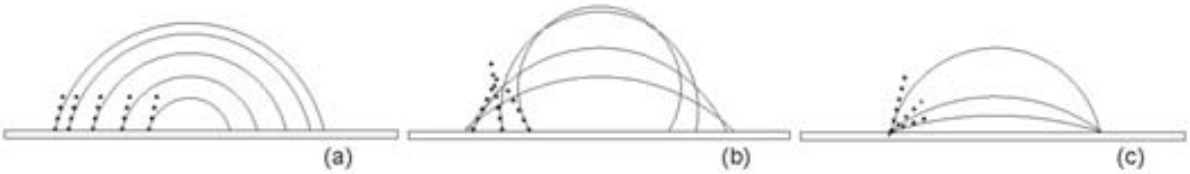


**Figure 5.4.:** The stability of a bead under different situations, according to Davis [262]. (a) the contact angle at the line is fixed and the contact line is free to move. (b) the contact line is free to move but the contact angle value depends on the contact line speed with a limiting value at zero line speed. (c) the contact line speed is pinned and the contact angle changes during bead formation.

number of drops per unit area increases, which is a direct sign of contact line pinning. However, we do not have any evidence by means of which mechanism contact line is arrested. Literature [264–266] reported that some inhomogeneities present on the surface or the intrinsic roughness of the substrate may induce contact line pinning, but the huge number of possible pinning sources and their possible combinations make that subject really complex (see appendix). Up today it is not absolutely clear that roughness and dirt are the only causes for the pinning of drop boundaries. Nevertheless, this discussion overhelms the scope of this work.

In the present study, it is pointed out that the width of the bead, $b$, is similar to the base diameter of separately deposited droplets as drop pitch $\Delta x$ is decreased. This suggests that the bead's contact line has been arrested and the bead has grown in the axial direction towards the neighbour drops, instead of spreading outwardly. This fact agrees with Davis' proposal, also experimentally confirmed by Schiaffino and Sonin's work [256], which predicted the experimental conditions that liquid beads are stable. Although these previous analyses were performed for solidifying drops, similar model assumptions can be applied to our experimental data due to the strong pinning of the contact line observed in the liquid beads of Fig. 5.3. In agreement with Derby's observations [10], the dynamics of drop deposition by itself define an intermediate state between the equilibrium advancing and receding states due to the hysteresis of the wetting process, where the wetting line is pinned. According to it, when the amount of liquid pushes the contact angle to cross the advancing contact angle threshold, the wetting line moves away.

The different beads shown in Fig. 5.3 were obtained by dispensing droplets of a 0.5M YBCO-TFA precursor solution with a diameter $2a = 41\mu m$, where $a$ is the drop radius in flight. They were ejected at drop pitch ranging between $50\mu m$ and $125\mu m$ using the driving piezoactuator parameters presented in Tab. 5.1.

The drops arrived on the target with a speed of about $1m/s$. The corresponding dimensionless physical parameters $We$, $Re$, $Z$ and $Bo$ numbers were established for our patterning ink at: $We$∼2.4, $Re$∼ 26.5, $Z$∼17 and $Bo$∼$1.4 \cdot 10^{-3}$. Reis and Derby [15] proposed that stable drop generation occurs between $1<Z<10$, being the upper limit defined by satellite formation, while the lower boundary is limited by the great relevance that viscous forces reach at high $Z$ numbers. Zhang [236] redefined the range for stable drop formation at $Z < 14$. The reported data give values slightly larger, $Z$ ∼22. This $Z$ number corresponds to a satellite formation regime [10]. Also, $We$ number is lower than that required for drop formation [10]. However, both criteria depend on the drop activation mechanism. As mention in sec. 4.9.3.2, some authors [251] showed that it is

possible to generate drops with a diameter smaller than nozzle orifice by using a double excitation approach to the piezoactuator. As described, this double excitation consists of a first activation corresponding to the fundamental drop, with lower energy than required for ejection, and a following one corresponding to the second oscillation mode of the meniscus. This harmonic has energy enough to develop and eject the small drop. In this study, in order to avoid a double excitation, we directly stimulate drop formation by using only the second oscillation mode of the liquid column in the dispenser. The pulse period was set nearly at half of the fundamental oscillation mode of the liquid column in the nozzle [243].

In agreement with the low value of $Bo$ number and for drop sizes typical of inkjet printing, gravitational effects are negligible compared to the surface energy involved during the impact and spreading processes. This low value enables to assume the deposited drop as a spherical-cap shaped once static equilibrium is reached. When drop is isolated, its volume $(4/3)\pi a^3$ is deposited in a spherical-cap limited by the contact circle of diameter $b$ and contact angle $\theta$ with the substrate [256, 263]. Furthermore, the drop after impingement on the substrate has the full volume of the drop on flight (i.e. it is assumed volume conservation between the drop and the spherical cap). With these assumptions, Gao and Sonin [263] put forward a simple geometric model which relates the diameter of the droplet on the flight $2a$, with the base diameter of the resulting isolated drop, $b$, and the contact angle, $\theta_{sph}$ (5.1):

$$\frac{b}{2a} = \left( \frac{4\, sin^3\theta_{sph}}{(1 - cos\, \theta_{sph})^2(2 + cos\, \theta_{sph})} \right)^{\frac{1}{3}} \text{ assuming } \theta_{sph} < 90^{\circ} \tag{5.1}$$

In the set of pictures displayed in Fig. 5.3, only Fig. 5.3a corresponds to purely isolated drops. However, picture Fig. 5.3b gets the same maximum width than Fig. 5.3a, although the amount of liquid is larger due to drop fusion. This means that the pinning of the contact line is strong enough to get a stable position. In the beads with connected drops (Fig. 5.3c-e), the contact angle $\theta$ is larger in the fusion traits, approaching the advancing value, while $\theta$ decreases tending to the receding contact angle in the regions of maximum width. Reduction of drop pitch leads to an increase of the amount of liquid per unit area, and a consequent increase of the contact angle that achieves the advancing value in the

| **Jetting parameters** | **Value** |
|---|---|
| Rise time ($\mu s$) | 2 |
| Dwell time ($\mu s$) | 7 |
| Fall time ($\mu s$) | 3 |
| Echo time ($\mu s$) | 7 |
| Final rise time ($\mu s$) | 2 |
| Voltage up ($V$) | +25 |
| Voltage down ($V$) | -21 |

**Table 5.1.:** Driving parameters used to activate our piezoelectric demand mode inkjet device in the study of basic morphological arrays varying the drop pitch.

fusion traits before the regions of maximum width. It leads to a local growth of the bead width in the fusion traits. As we decrease drop pitch, the deposited beads tend to show parallel boundaries. In this case, the volume of fired drops does not fit the spherical-cap tending to be cylindrical, when stable beads are obtained.

Fig. 5.5 drafts in simple terms the basic parameters that take part in the spherical and cylindrical assumptions to predict the bead width, $b$:

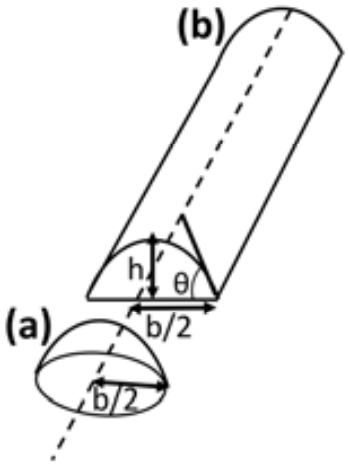


**Figure 5.5.:** Assumptions of the drop shape for the 1D analytical model. (a) spherical cap shape model. (b) cylindrical cap shape model.

For the cylindrical limit, the ratio $b/2a$ can be related with the contact angle $\theta_{cyl}$ by the equation 5.2 [263]:

$$\frac{b}{2a} = \left( \frac{2\pi \, sin^2\theta_{cyl}}{3(\theta_{cyl} - sin\,\theta_{cyl}\, cos\,\theta_{cyl})} \frac{2a}{\Delta x} \right)^{\frac{1}{2}} assuming\, \theta_{cyl} < 90^{o} \tag{5.2}$$

The contact angle in the spherical and cylindrical limits should be maintained in the range between the advancing and receding values where the pinning of the wetting line is effective. Fig. 5.6 shows the computed contact angle, $\theta_{cyl}$, as a function of drop pitch by using the cylindrical assumption for continuous beads, equation 5.2, and the spherical approach, equation 5.1, for isolated drops. In this last approach, we only took the first three cases. Using the angle computed for isolated drops, $\theta_{sph}$, as a limit of the contact angle $\theta$, we can observe that continuous beads tend to achieve the same angle as the amount of liquid accumulated between the pinned lines tends to increase approaching the advancing contact angle value, similar to $\theta_{sph}$.

This increase is mainly due to the fact that the cylindrical approach assumes the whole volume to be fit in a cylinder cap of width $b$. This approach underestimates the angle when the bead is not stabilised, but marks the limit for the minimum drop pitch before the bead boundaries move out increasing its width. Then, a decrease of drop pitch enhances track width. The optimal pitch corresponds to the volume per unit length of

a cylindrical cap of contact angle $\theta_{cyl}$ $\theta_{sph} \sim \theta_{adv}$. In our case, with equation 5.2, we obtain $\theta_{cyl} \sim 22°$considering the pinned width $b \sim 100\mu m$, and drop radius $a \sim 20\mu m$, the minimum drop pitch that could be achieved is $\Delta x \sim 51\mu m$. Shorter drop pitch leads to wider tracks. Although this model was proposed for drops pinned by solidification, wetting hysteresis is also in the origin of track formation. It is worth to remark that $\theta$ values obtained using both approaches are larger than those measured by DSA standard measurements (<10°). This difference could be understood by comparing the $Bo$ number in both cases. For DSA experiments, $Bo > 1$; $10^4$ times larger than the case of drops dispensed by the printhead. An extensive discussion about this point could be found in reference [267].

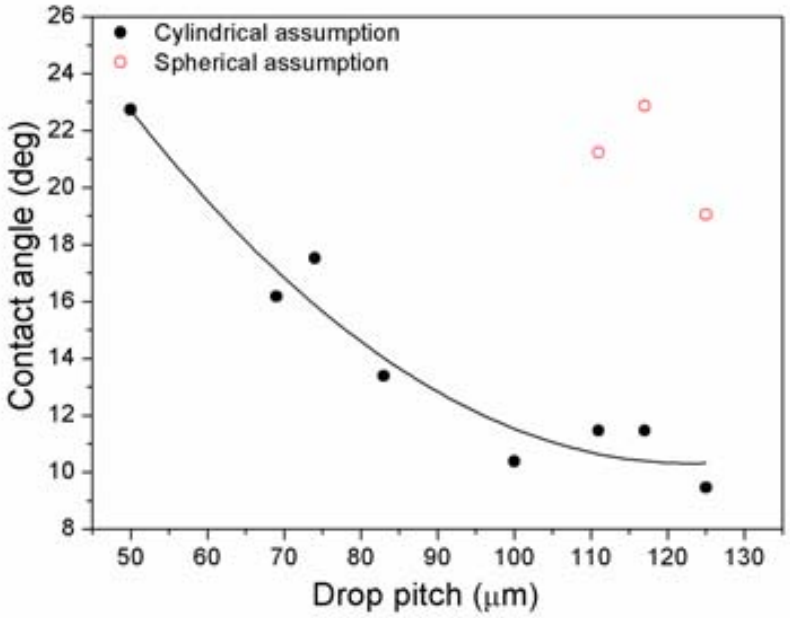


**Figure 5.6.:** Contact angle $\theta$ as a function of drop pitch computed for spherical (empty red dots) and cylindrical (solid black dots) assumptions. Isolated printed drops approach the maximum contact angle $\theta$. Cylindrical approach tends to the maximum $\theta$ as the amount of liquid per unit area increases.

A particular phenomenon called *bulging effect* is shown in Fig. 5.3i. The stability of the line is removed due to the presence of a serie of regular bulges connected by ridges. This bulge instability was first investigated by Duineveld [268], who modelled its behaviour as a result of a dynamic instability (see next sec. 5.3.1).

## 5.3. Particular bead morphologies

### 5.3.1. Bulging effect

Duineveld [268] explained this instability in terms of two competing flows within the bead: a flow down the bead and an axial spreading along it due to capillarity. He

proposed that this instability is dynamic dependent and occurs because the contact angle of the deposited drop exceeds the advancing contact angle of the line removing one of the constraints of bead stability proposed by Davis [262]. When the amount of ink per unit area and/or the rate of drop deposition is too large, the capillary spreading can not reduce the drop curvature and the liquid flows down the bead forming a bulge. Stringer [260] stablished a criterion for the onset of the bulging instability, in terms of a dimensionless velocity $U_T^*$ (i.e. the velocity at which the substrate moves divided by the drop pitch), and a function $g$ of the advancing contact angle $\theta_{adv}$ and a dimensionless drop spacing $p^*$; $g\ (p^*,\ \theta_{adv})$. Thus, the condition they obtained for printed line stability was:

$$U_T^* > g(p^*, \theta_{adv})\ with\ U_T^* = \frac{U_T \eta}{\gamma}$$

where $U_T$ is the platform velocity, $\eta$ the ink viscosity and $\gamma$ is the surface tension of the ink.

The function is detailed and described in [260]. By plotting both variables, $U_T^*$ and $g\ (p^*,\ \theta_{adv})$, it is possible to define a parameter space which delimites the threshold for bulging instability.

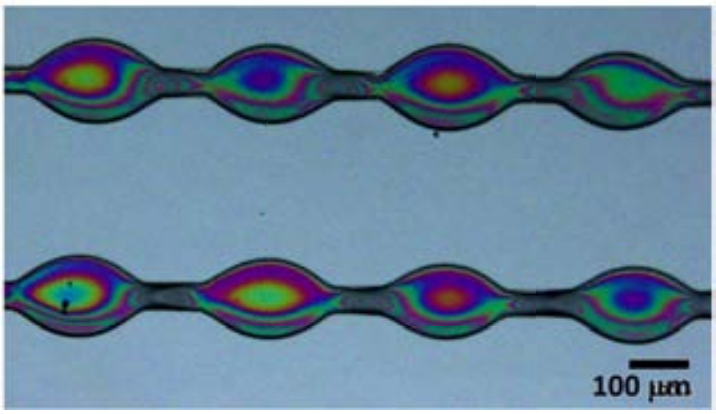


**Figure 5.7.:** Printed track bulging instability after drying at RT of a 0.3M $BaTiO_3$ propionic based ink on LAO substrate with a drop spacing of $26\mu m$. The substrate moved at $10mm/s$.

## 5.3.2. Drop drying and coffee stain effect

The final process to attain the desired deposit is the solvent evaporation. This drying process is absolutely crucial in determining the quality of the final pattern or deposit. A phenomenon which may be observed when drop evaporation occurs is the so-called *coffee stain effect* [16, 171, 269–271], characterized by leading a ring-shaped deposit. Deegan [269] first proposed that if the contact line is pinned when evaporation occurs, combined with an enhanced evaporation rate close to the contact line, it leads to the coffee ring effect. Since these are generic conditions, coffee-staining may occurs whenever solutions or suspensions are handled. A well-known example of this effect is the brown ring left when a drop of coffee dries on a solid surface (see Fig. 5.9a).

In a well-spread drop, the surface area is larger at the edges (see circled region in Fig. 5.8), close to the contact line, which enhances the diffusion of solvent from the drop surface promoting faster evaporation. Thus, the difference in evaporation rate between the bulk and the regions near to the contact line produces a fluid flow towards the edge of the drop, where the solute may be accumulated forming a ring of particles of dried solid. This ring-like deposit remains there pinning the contact line which results in a decrease of the receding contact angle as liquid evaporates.

**Figure 5.8.:** Photograph of a well-spread drop. The circled region evaporates faster than the bulk region due to the larger surface area.

Fig. 5.9b sketches the factors that take part during evaporation of a drop of radius $r$ on a solid surface. The evaporative flux $J(r)$ reduces the height of the drop at every point $r$. Without flow from the bulk of the drop to the edges, the evaporation process reduces the height of the drop progressively and the whole drop shrinks as drawn in Fig. 5.9b1. However, if the contact line is pinned, the diameter of the drop remains constant (i.e. the drop-substrate area is unaltered). As the droplet loses mass through evaporation, the contact angle and the drop height decrease until the receding angle is reached. Therefore, to prevent that shrinkage, the liquid must flow outwardly as indicated by the black arrows

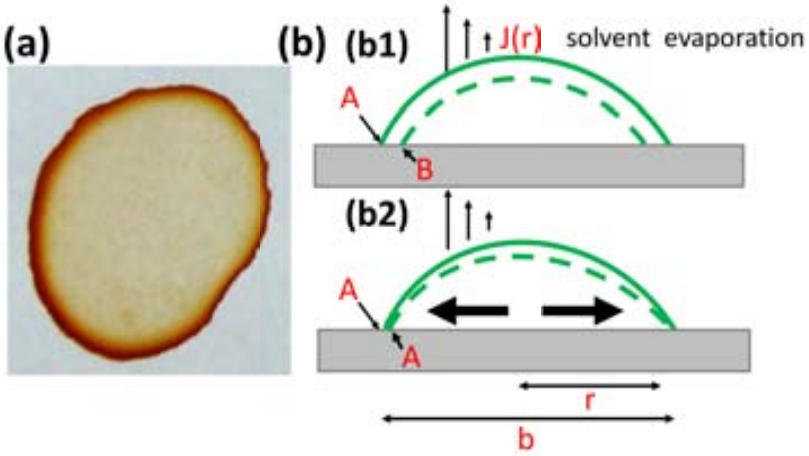


**Figure 5.9.:** (a) A photograph of a dried coffee drop showing the coffee stain effect. The brown perimeter is produced by a dense accumulation of coffee particles. (b) Schematic illustration of the evaporation induced flow. (b1) If the contact line is not pinned, the evaporation reduces the drop volume corresponding to the region between the solid and the dashed green lines and, thus, the whole drop shrinks. Under these conditions, the contact line moves from position A to B. (b2) However, in the opposite side, if the contact line is arrested, the retreat from A to B is not possible and there must be a flow that replenishes the lost volume of fluid. The black arrows show the direction of the compensating flow and the position of the contact line A.

in Fig. 5.9b2. This flow must stay constant with time until evaporation has finished. Other variables apart from vapour pressure of the solvent, such as drop pitch and drop impact speed are relevant parameters which have an important role in the coffee ring effect [36].

The following Fig. 5.10 shows the profile of a YBCO track where is possible to observe the previous described coffee ring effect. In this example, the YBCO track was built by 10 times depositing a 0.5M ethanol based YBCO precursor solution which contained a 3% by weight of $PEG_{8000}$ (MW=8000g/mol). The profile provides two sharp ridges at the edges of the pattern due to the evaporation induced flow which cause a denser accumulation of solute in those regions.

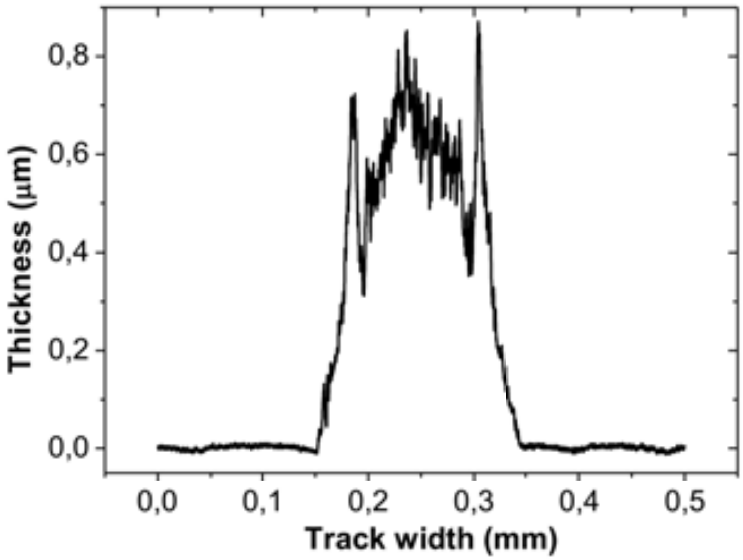


**Figure 5.10.:** Profilometric analysis of a YBCO track showing the coffee stain effect. In this case, it was used a 0.5M ethanol based YBCO precursor solution with a 3% by weight of $PEG_{8000}$. To built the track, 10 depositions were performed on top of each other. The ridges at the edges of the profile indicate a higher density of solute in those regions due to the evaporation flow towards the edges of the structure. The drop pitch was set at $16\mu m$ and the substrate platform moved at $10mm/s$.

## 5.4. $YBa_2Cu_3O_{7-x}$ patterns: printing multifilamentary structures

For flexible electronics and, particularly, for integrated circuit fabrication, the patterning of samples to be used as conductors, dielectrics and thus transistors imply the printing of tracks. Ideal lines for processable electronics would be smooth, narrow and straight, which require a precise control of the behaviour of inkjet-printed structures.

Specially, patterning of straight lines has a specific application in the development of HTS tapes with low AC losses. Single superconducting coatings on wide metallic tapes proved to have very high AC losses in self and external fields [272]. It has been demonstrated that dividing the full coating into multifilamentary stripes as thin as possible, substantially reduce AC losses, as the creation of large area current loops is impeded by the inter-track separation [273]. The current studied inkjet printing technology enables

to directly print YBCO tracks without the need to use masks or without pre-patterning the substrate to create specific regions where the material remains, for instance, in the case of lithographic techniques [274].

In this way and in order to advance in the field of AC losses reduction, this section seeks to advance in the formation and control of uniform and continuous YBCO tracks. In the next sections, the experimental sequence followed to obtain those YBCO tracks is detailed.

In the introductory chapters, it has been mentioned the importance of having a firm grasp of the ink physicochemical properties and the contact angle which makes the ink with the substrate to control the morphology of the final deposit. Besides, to obtain tracks it is necessary to find an ink with wetting hysteresis ($\theta_{adv} \neq \theta_{rec}$), which means a strong pinning of the contact line.

The starting solution tested for YBCO patterning was the selected ink employed for obtaining continuous YBCO layers: the 0.5M EtOH based YBCO precursor solution with the physicochemical properties described in the next Tab. 5.2. As we are interested on making fine patterns, we looked for jetting parameters which give drop volumes as small as possible by setting the total pulse width nearly half of the pulse width corresponding to the fundamental frequency of the device (sec. 4.9.3.2). The initial jetting parameters applied are presented in Tab. 5.3. In the beginning tests, only one deposition (i.e. number of depositions covering the same route) was performed. Through all this section of making multifilamentary YBCO structures, the piezoelectric dispenser with a nozzle diameter of $60\mu m$ was used.

| | **0.5M ethanol based YBCO precursor solution** |
|---|---|
| Density $\rho$ $(g/cm^3)$ | 0.883 |
| Surface tension $\gamma$ $(mN/m)$ | 21.5 |
| Viscosity $\eta$ $(mPa \cdot \mathrm{s})$ | 1.5 |

**Table 5.2.:** Relevant physicochemical properties of the 0.5M EtOH based YBCO precursor solution. Viscosity measurement was carried out at a shear rate of $100s^{-1}$. All the measurements were performed at room temperature.

| Jetting parameters | Value |
|---|---|
| Rise time ($\mu s$) | 2 |
| Dwell time ($\mu s$) | 7 |
| Fall time ($\mu s$) | 3 |
| Echo time ($\mu s$) | 7 |
| Final rise time ($\mu s$) | 2 |
| Voltage up ($V$) | +25 |
| Voltage down ($V$) | -21 |

**Table 5.3.:** Jetting parameters used to print the YBCO tracks shown in Fig. 5.11. Drop volume under these conditions was $\sim 15pL$.

Next Fig. 5.11a shows the general view of the YBCO array onto $LaAlO_3$ (LAO) single-crystal after YBCO growth process and their optical characterization after pyrolysis process (Fig. 5.11b). The printing parameters employed in this test are displayed below:

| Solution | 0.5M ethanol based YBCO precursor solution |
|---|---|
| Drop pitch ($\mu m$) | 25 |
| Line pitch ($\mu m$) | 500 |
| Number of depositions | 1 |

**Table 5.4.:** Printing parameters employed to obtain the YBCO tracks displayed in Fig. 5.11.

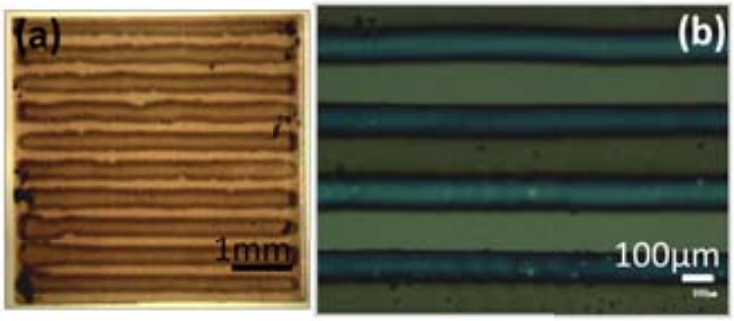


**Figure 5.11.:** YBCO tracks characterization by optical microscopy printed using a 0.5M ethanol based YBCO precursor solution onto a (5x5)$mm$ LAO single crystal. The contact angle ink-substrate is $<10^o$. (a) General look of the whole patterned sample after YBCO growth (sec. 1.2). (b) Optical microscopy of the previous tracks at 5X after pyrolysis process (see sec. 1.2). As might be appreciated, irregular tracks have been obtained.

As can be seen in Fig. 5.11, after growth process, irregular YBCO tracks, with non-parallel contact lines and with two ridges at the edges of the track were achieved. The contact angle which made this solution with the LAO single crystal substrate was under

the measurable value with reasonable precision (<10°). The non-homogeneous distribution in thickness obtained along the transversal direction was confirmed, first, by optical microscopy and, then, by profilometric measurements. The results obtained by profilometry (not shown herein) reveal that the average width of the tracks is around 325-350$\mu m$ with an average thickness of 60$\mu m$. The low thickness reached can be enhanced, for instance, by means of multideposition processes.

In order to increase the homogeneity along the track lenght, we tried to reduce the ink spreading by tailoring the physicochemical properties of the solution. Besides, by controlling the interaction between the ink and the substrate, thinner tracks may be obtained which is also desirable for AC applications. Particularly, next attempt was to modify the ink formulation by introducing an additive to increase the viscosity of the solution. The motivation to increase the ink viscosity lies in the possibility to slow the solution movement before the contact line is frozen and the width of the track is fixed. The metal concentration was maintained at 0.5M, but $PEG_{8000}$ (Sigma Aldrich, MW=8000$g/mol$) was added into the solution. At that time, we decided to use $PEG_{8000}$ as an additive to increase the viscosity of the solution due to the long trajectory of our research group working on this polymer. It has been demonstrated that by adding up to 30% by weight of $PEG_{8000}$ into the precursor solution, homogeneous YBCO films might be obtained with no degradation of the superconducting performances and without changing significantly the pyrolysis processing conditions.

The ink physicochemical properties of the 0.5M ethanol based solution with a 3% w/w of $PEG_{8000}$ are detailed in the consecutive table:

| | **0.5M ethanol based YBCO precursor solution + 3% w/w $PEG_{8000}$** |
|---|---|
| Density $\rho$ $(g/cm^3)$ | 0.91 |
| Surface tension $\gamma$ $(mN/m)$ | 21.3 |
| Viscosity $\eta$ $(mPa \cdot s)$ | 3 |

**Table 5.5.:** Relevant physicochemical properties of the 0.5M ethanol based YBCO precursor solution with a 3% w/w $PEG_{8000}$. Viscosity measurement was carried out at a shear rate of $100s^{-1}$. All the measurements were performed at room temperature.

In the following tables, we present the jetting variables used to form tracks with the previous solution and the printing configuration employed in such case:

| **Jetting parameters** | **Value** |
|---|---|
| Rise time ($\mu s$) | 2 |
| Dwell time ($\mu s$) | 7 |
| Fall time ($\mu s$) | 3 |
| Echo time ($\mu s$) | 7 |
| Final rise time ($\mu s$) | 2 |
| Voltage up ($V$) | +28 |
| Voltage down ($V$) | -28 |

**Table 5.6.:** Jetting parameters used to print the YBCO tracks shown in Fig. 5.12.

| **Solution** | **0.5M ethanol based YBCO precursor solution + 3% w/w $PEG_{8000}$** |
|---|---|
| Drop pitch ($\mu m$) | 25 |
| Line pitch ($\mu m$) | 600 |
| Number of depositions | 1 |

**Table 5.7.:** Printing parameters employed to obtain the YBCO tracks displayed in Fig. 5.12.

Fig. 5.12a exposes the aspect of a set of inkjet printed tracks using the 0.5M ethanol based YBCO precursor solution with a 3% by weight of $PEG_{8000}$ onto LAO single crystal. The measured contact angle for this solution onto the substrate was <10°. Fig. 5.12b shows a magnified image of those previous tracks after pyrolysis process.

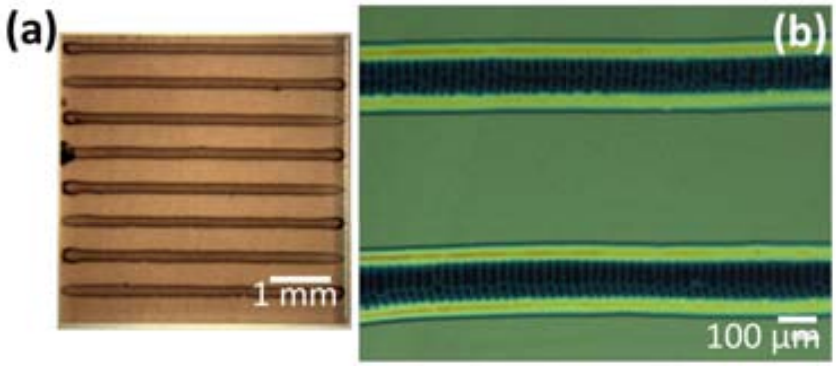


**Figure 5.12.:** YBCO tracks onto LAO single crystal substrate characterization by optical microscopy. In this case, the solution used for printing was a 0.5M ethanol based YBCO precursor solution with a 3 % $PEG_{8000}$ by weight and the contact angle ink-substrate was <10º. (a) General look of the whole patterned sample after YBCO growth. (b) Optical microscopy at 5X magnification of the previous tracks after pyrolysis process. From the general view, it can be observed that YBCO tracks with parallel contact lines have been achieved. By evaluating a zoomed image of the central region of two of those tracks it may be observed a particular cross-linked morphology that joins both edges of the track.

From Fig. 5.12a it may be observed that by increasing the viscosity from $2mPa \cdot s$ to $3mPa \cdot s$, tracks with parallel contact lines were reached. By comparing the width of the tracks by using the previous mentioned solutions, a clear difference might be appreciated. Maintaining the solution concentration but introducing PEG into the solution, it was feasible to decrease the track width from 325-350$\mu m$ to 200-225$\mu m$, which suggests that the width of those tracks may be regulated by controlling the viscosity, minimizing the spreading of the ink, when the same solvent vapour pressure is used.

However, having a look to Fig. 5.12b, it is observed that during drying and pyrolysis processes, the strong pinning of the contact line induces a longitudinal stress, which we infer on the basis of the formation of a thin net of wire-like polymeric residue. We attribute this particular morphology to alterations in the plastic flow of the film during the decomposition of the organic matter at ∼300°C due to the presence of the additive. To evaluate if there is an experimental procedure to vanish this particular wire-like structure or to planarize this particular morphology, we decided to increase the number of depositions using the previous YBCO precursor solution with the PEG additive. At the same time, it allows us to enhance the track thickness, which is also important for YBCO CC's applications.

In the following Fig. 5.13 it is presented the SEM images of the inkjet printed tracks onto LAO substrate after the complete YBCO growth process after a total of 10 depositions. By analyzing the structure of the as-grown YBCO tracks, it seems that the wire-like transversal structure observed before tend to vanish, achieving good homogeneity at all length scales. Width lines around 200$\mu m$ and an average thickness at the center of the track around 630$nm$ were thereby obtained. 2D-XRD diffraction pattern for the as-obtained tracks (not shown herein) shows a very intense diffraction cone at $2\theta$ ∼38.2 °corresponding to the (103) YBCO polycrystalline fraction, which means that YBCO phase is not c-axis oriented (i.e. YBCO has not grown following an epitaxial relationship).

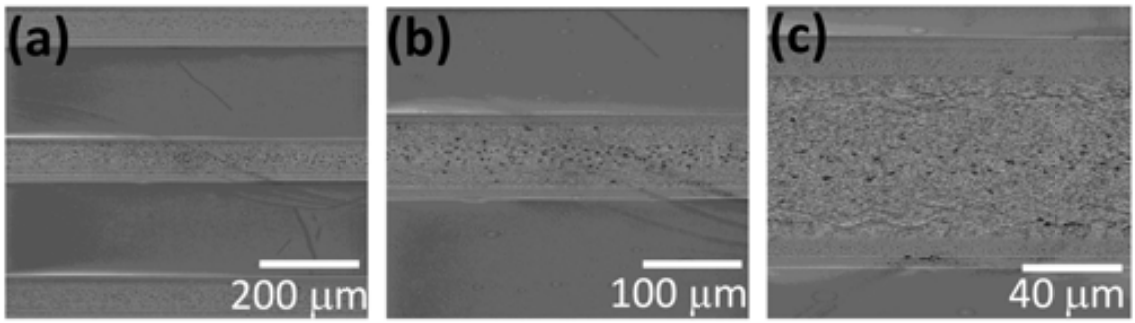


**Figure 5.13.:** SEM images of the as-grown YBCO tracks on LAO after growth process at different magnifications. The magnification from left to right is: (a) 400X, (b) 800X, and (c) 2000X. The ink used to print those tracks was a 0.5M ethanol based YBCO precursor solution with a 3% w/w of $PEG_{8000}$. The total number of depositions printed on top of each other was 10.

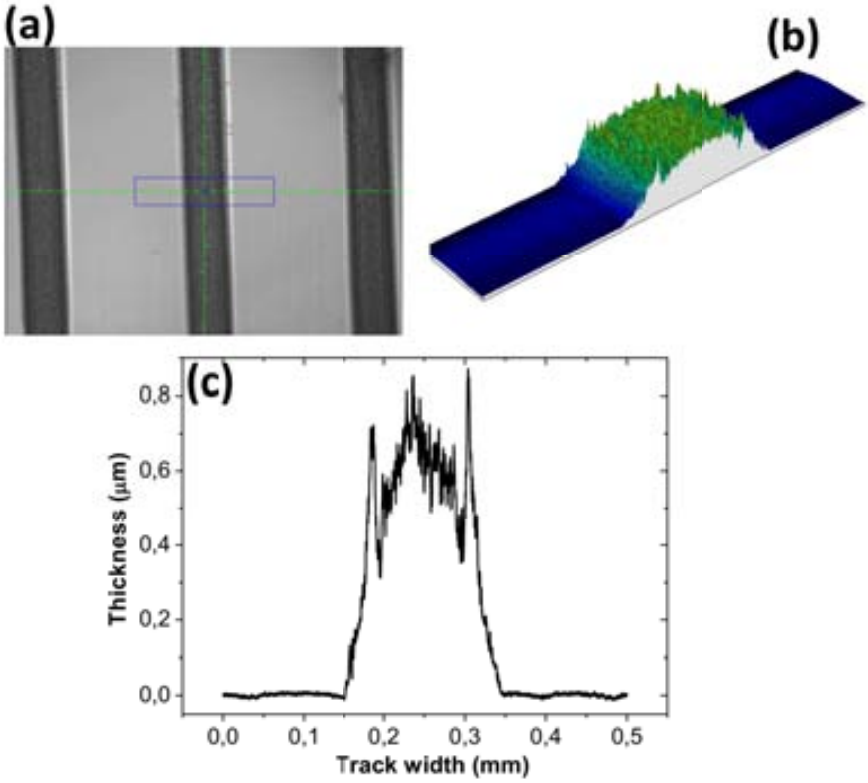


**Figure 5.14.:** Profilometric characterization of the YBCO tracks after 10 depositions by using a 0.5M ethanol based ink with a 3% w/w of $PEG_{8000}$. (a) YBCO track region of (500 x 90)$\mu m$ longitudinal and vertical directions analysed by profilometry. (b) 3D image and (c) Cross-sectional profile of the region framed in blue in (a) showing the above-described coffee stain effect.

These results mean that further optimization of the deposition and growth processes should be performed in order to avoid the polycrystalline YBCO phase. Furthermore, Fig. 5.14 also shows the cross sectional profile of one YBCO track where it may be appreciated the above mentioned coffee stain effect (see sec. 5.3.2). The jetting and printing parametres used to obtain this array of tracks are the same detailed in Tab. 5.6 and Tab. 5.7 but in the latter case the number of depositions was increased up to 10.

### 5.4.1. Inter-track optimization distance

Inter-track distance has to be set large enough in order to avoid coupling of tracks but, at the same time, close enough to have the maximum number of tracks per sample. To perform that, we started playing with the solution detailed previously which contains PEG. Since the width of a printed track consisting in one deposition and using the ethanol with a 3% w/w of PEG solution is about 200$\mu m$, we screened inter-track distances from 300$\mu m$ to 600$\mu m$ in the space of 100$\mu m$. In parallel tests, we systematically changed drop pitch between 10$\mu m$ and 25$\mu m$ and number of depositions to see if tracks printed at a fixed inter-track distance finally merge or not. For instance, tracks consisting on 8 depositions and printed using a drop pitch of 25$\mu m$ at an inter-track distance of 300$\mu m$ finally they joined when the previous solution ethanol/PEG was employed. So, for next

experiments, we set the inter-track distance at $400\mu m$ to assure that tracks are completely decoupled independently of the number of depositions performed.

In that point, and following some information found in the literature regarding coffee stain effect, the next assay was to combine in the ink formulation two solvents: one of low boiling point and, therefore, high vapour pressure and another of higher boiling point and hence lower vapour pressure. We chose the combination of ethanol and 1,3-propanediol (Sigma Aldrich) due to the high difference in evaporation rate of both solvents ($T_{bp}$(EtOH)$\sim$78°C) and ($T_{bp}$(1,3-propanediol)$\sim$215°C) and because they do not form an azeotropic mixture. YBCO precursor solutions prepared with a % by weight of 1,3-propanediol up to 12.5% w/w were stable until, at least, six months.

So the next tested solution was a 0.5M ethanol based YBCO precursor solution with a 5% by weight of 1,3-propanediol. The ink physicochemical properties of this solution are displayed in the successive Tab. 5.8:

| | **0.5M ethanol based YBCO precursor solution + 5% w/w 1,3-propanediol** |
|---|---|
| Density $\rho$ $(g/cm^3)$ | 0.90 |
| Surface tension $\gamma$ $(mN/m)$ | 22.5 |
| Viscosity $\eta$ $(mPa \cdot s)$ | 2.5 |

**Table 5.8.:** Relevant physicochemical properties of the 0.5M ethanol based YBCO precursor solution + 5% w/w 1,3-propanediol. Viscosity measurement was carried out at a shear rate of 100 $s^{-1}$. All the measurements were performed at room temperature.

The activation variables applied to the PZT for an stable ejection of the above-described solution and the printing configuration used are specified in next Tab. 5.9 and Tab. 5.10, respectively:

| **Jetting parameters** | **Value** |
|---|---|
| Rise time $(\mu s)$ | 2 |
| Dwell time $(\mu s)$ | 7.3 |
| Fall time $(\mu s)$ | 3 |
| Echo time $(\mu s)$ | 7.3 |
| Final rise time $(\mu s)$ | 2 |
| Voltage up $(V)$ | +25 |
| Voltage down $(V)$ | -21 |

**Table 5.9.:** Jetting parameters used to print the YBCO tracks shown in Fig. 5.15.

| **Solution** | **0.5M ethanol based YBCO precursor solution + 5% w/w 1,3-propanediol** |
|---|---|
| Drop pitch ($\mu m$) | 20 |
| Line pitch ($\mu m$) | 400 |
| Number of depositions | 4 |

**Table 5.10.:** Printing parameters employed to obtain the YBCO tracks displayed in Fig. 5.15.

Therefore, by using a distance between droplets of $20\mu m$ and a distance between lines of $400\mu m$, it was found to be possible to obtain independent, continuous, straight, and uniform YBCO tracks. In Fig. 5.15(a,b), we show optical micrographs of those tracks after pyrolysis process at 310°C for 30min. In order to increase the thickness of YBCO tracks, four over-printings with an intermediate drying step at room temperature between depositions were performed (Fig. 5.15).

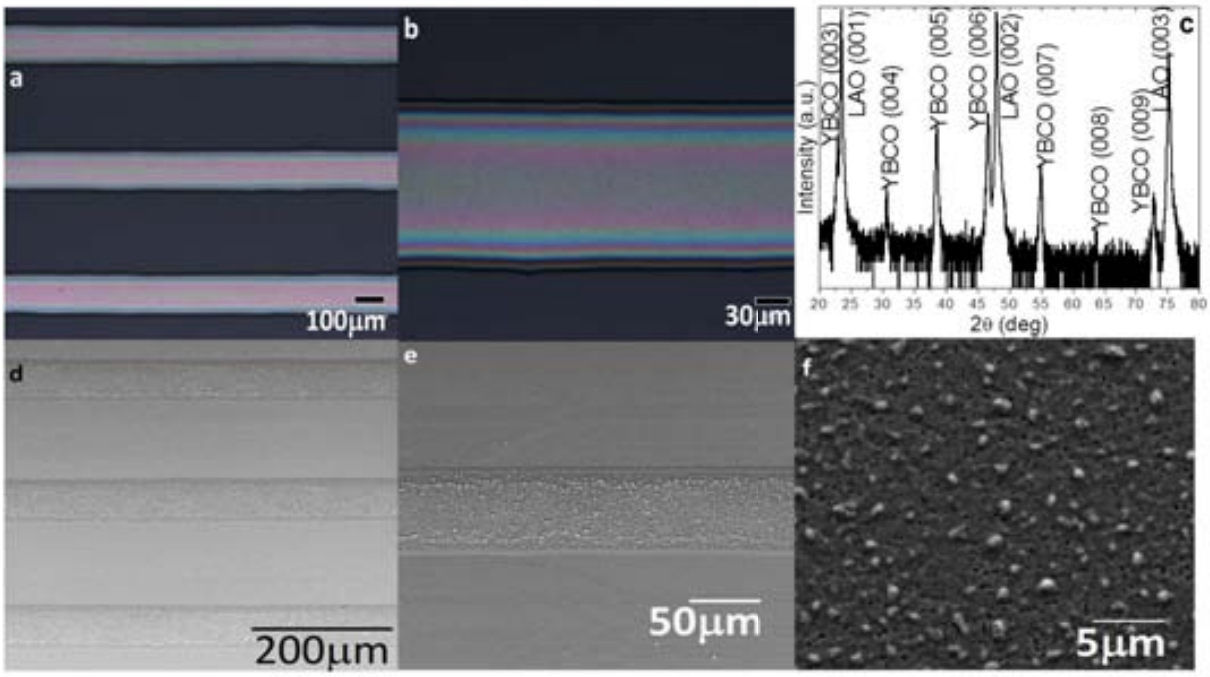


**Figure 5.15.:** (a) and (b) Optical microscopy images of printed lines on LAO after pyrolysis with dot pitch of $20\mu m$ and line pitch of $400\mu m$ after four over-printings subsequently printed on top of each other (a) 5X objective (b) 10X objective. (c) $\theta$–$2\theta$ XRD pattern of as-grown YBCO tracks. (d), (e) and (f) SEM micrographs of the previous inkjet printed YBCO tracks on LAO after growth process. The magnification from left to right is: 500X, 1000X, 10000X.

Printing over previously dried paths enables pinning the boundaries of the previous bead due to the smaller surface energy between the ink solvent and the soluble dried bead. The track thickness can then be increased but enhancement of the width is avoided. As

can be observed in Fig. 5.15, YBCO lines after pyrolysis were continuous, uniform, with a constant base width of nearly $150\mu m$ and with completely parallel sides. It is also remarkable that the so called coffee ring effect is not observed [269, 271]. After YBCO growth, XRD experiments were performed to identify the composition and structure of these as-grown tracks. XRD pattern (Fig. 5.15c) exhibits only the presence of (00l) reflections, which means that YBCO has epitaxially grown onto the single-crystal LAO substrate, as expected from the low film-substrate mismatch. YBCO tracks were also morphologically characterized by SEM (Fig. 5.15d-f) displaying high homogeneity and uniformity along all the track length.

In order to determine the critical current density ($J_c$) of the sample, profilometric measurements were performed to determine the cross section profile. As observed in Fig. 5.16, lines shaped like segments of a cylinder sector, with a base width of $150\mu m$ and a thickness value on the centre of the track around $300nm$ were thereby obtained. The convex profile found for the tracks shows a distribution of the ink coherent with its surface tension and capillary forces. The computed cross-sectional area results to be $\sim 45\mu m^2$.

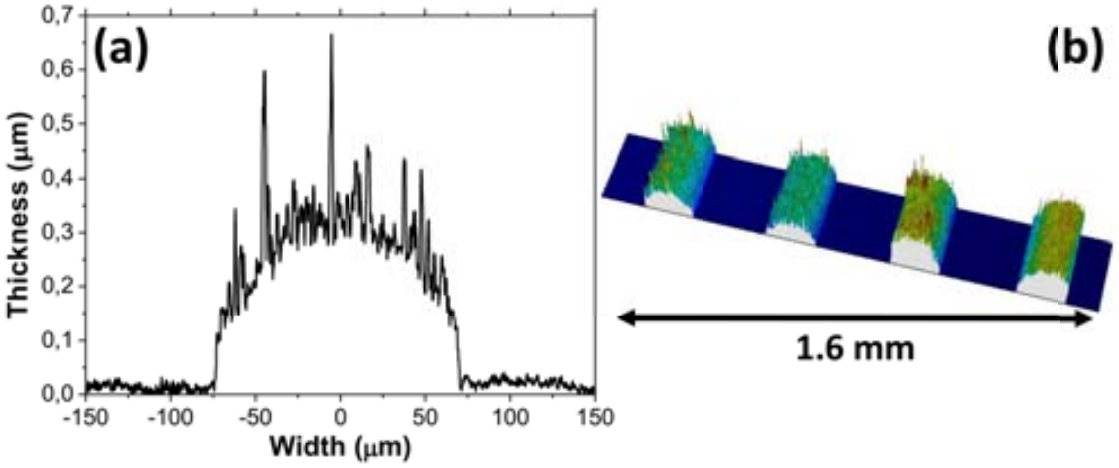


**Figure 5.16.:** Typical dimensions of YBCO tracks onto LAO substrate by using the 0.5M ethanol based YBCO precursor solution with a 5% by weight of 1,3-propanediol. (a) Cross-sectional profile and (b) 3D image of these inkjet printed YBCO tracks. The drop pitch and the distance between line centres were set at $20\mu m$ and $400\mu m$, respectively.

By using the so obtained cross section value, $J_c$ measurements were performed by the four probe standard transport method employing a $3\mu V/cm$ electrical field criterion obtaining a maximum $J_c$ at self field and $77K$ of $1.1MA/cm^2$.

In Fig. 5.17 we present the dependence of $J_c$ with the magnetic field parallel to (00l) axis measured by injecting current along four tracks at the same time (Fig. 5.17 red opened dot line) and only two tracks at the same time (Fig. 5.17 blue closed dot line). From Fig. 5.17, it is clear that we have obtained two identical results measuring two sets of tracks demonstrating the high homogeneity achieved in the deposited tracks.

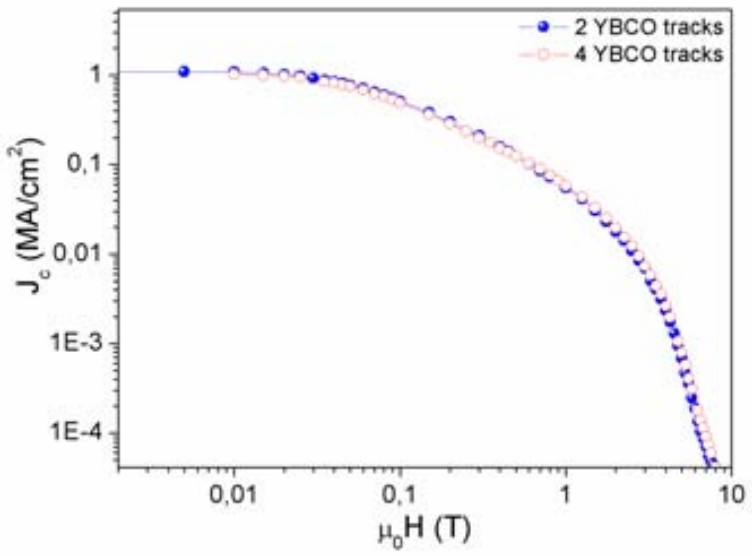


**Figure 5.17.:** Magnetic field dependence of the critical current density ($J_c$) measured for two tracks (closed symbol) and four tracks (opened symbol).

By comparing the rheological and wetting properties of the solution which allow us to obtain homogeneous, uniform and continuous coatings (Tab. 5.8) with the ones presented in Tab. 5.2, only slight differences in $\rho$,$\gamma$ and $\eta$ are detected, therefore, only those ink physicochemical characteristics may not explain the observed behaviour. An important parameter that might help us to explain the formation of such homogeneous and uniform tracks when the second solvent is added is the contact angle that makes the ink with the substrate, which includes the interaction energy with the single crystal solid substrate.

When we monitor the evolution of a $2\mu L$ sessile drop of a 0.5M ethanol based YBCO precursor solution and a $2\mu L$ of another sessile drop of the same solution containing 5% by weight of 1,3-propanediol onto a LAO single crystal substrate, some differences may be noticed: from one side, in the case of the 0.5M ethanol based YBCO precursor solution, immediately after drop deposition, the ink makes a contact angle with the substrate of less than 10°. This contact angle decreases until evaporation finishes. From the other side, when a $2\mu L$ drop of the 0.5M ethanol based YBCO precursor ink with 5% w/w of 1,3-propanediol is deposited, it spreads until achieves the advancing contact angle of about 10°. After few seconds, the drop contracts achieving the receding contact angle of about 25°. We think that the increase of the fluid contact angle, corresponding to a larger ratio of 1,3-propanediol in the mixture, is the main reason why the spreading is limited when 1,3-propanediol is added into the ink.

## 5.5. Going to narrower YBCO tracks

As previously mentioned, AC losses strongly depends on the track width. In this regarding, we are interested on decreasing the line width. In order to advance in this

field, different experimental measures were considered. First, the solution composition was modified by incrementing the 1,3-propanediol content from a 5% to a 12.5% by weight. Then, drop volume was decreased until a nominal value of $10pL$ by using the Dimatix multinozzle printer DMP2800.

Tab. 5.11 shows the ink rheological and wetting properties of the 0.5M ethanol based YBCO precursor solution with a 12.5% w/w of 1,3-propanediol, which will be the ink used until the end of this YBCO patterning section:

| | **0.5M ethanol based YBCO precursor solution + 12.5% w/w 1,3-propanediol** |
|---|---|
| Density $\rho$ $(g/cm^3)$ | 0.88 |
| Surface tension $\gamma$ $(mN/m)$ | 24.6 |
| Viscosity $\eta$ $(mPa \cdot s)$ | 2 |
| Contact angle on LAO (°) | 17 |

**Table 5.11.:** Relevant physicochemical properties of the 0.5M ethanol based YBCO precursor solution with a 12.5% w/w 1,3-propanediol. Viscosity measurement was carried out at a shear rate of $100s^{-1}$. All the measurements were performed at room temperature.

Therefore, the increase in surface tension and contact angle of the previous solution in contrast to the solution presented in Tab. 5.8, together with the decrease of drop volume will enable to obtain narrower structures.

Next Fig. 5.18 displays an example of two tracks printed using the solution with the physicochemical properties displayed in Tab. 5.11. As can be observed, using two nozzles simultaneously and with only one-layer width, features as thin as $40\mu m$ may be achieved, which means a reduction in contrast to the $60\mu m$ PZT dispenser of about 65 %. The photo of the as-deposited precursor YBCO tracks was taken by the fiducial camera of the Dimatix printer.


**Figure 5.18.:** Optical image of two precursor YBCO tracks printed using the Dimatix DMP2800 printer and the solution with the physicochemical properties displayed in Tab. 5.11. Tracks after deposition around $40\mu m$ were achieved by using two nozzles simultaneously.

# 5.6. Track width modulation

## 5.6.1. Effect of 1,3-propanediol content

In the case of the single nozzle piezoelectric printhead with $60\mu m$ of nozzle diameter, finer resolution from $150\mu m$ to $110\mu m$ features may be achieved through further optimization of solution composition by incrementing the 1,3-propanediol content from 5% to 12.5% by weight.

## 5.6.2. Effect of drop pitch

A decrease in line width is observed when the drop pitch is increased. With increased drop pitch less material is deposited per unit length, resulting in thinner structures. Fig. 5.19 presents YBCO precursor tracks after inkjet printing deposition by using two nozzles of the DMP system, a drop pitch of $5\mu m$ and with a two layer multideposition process, which enable to reach a final track width about $150\mu m$. In contrast, by using the same printing conditions and only modifying the drop pitch from $5\mu m$ to $20\mu m$, Fig. 5.21b, the width of the track decreases from $\sim 150\mu m$ to $\sim 75\mu m$.

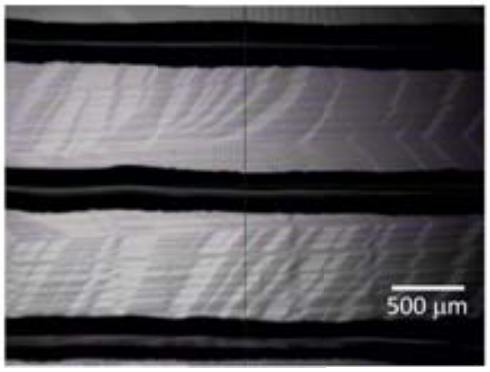


**Figure 5.19.:** YBCO precursor tracks after 2 depositions using 2 nozzles. Drop pitch, substrate temperature and cartridge temperature were set at $5\mu m$, 30ºC and RT, respectively.

## 5.6.3. Effect of number of nozzles and number of consecutive depositions

Playing with the number of nozzles printing at the same time, it is also possible to tune track width. To exemplify this fact, two track sequences are presented below. In both studies, the PZT driving waveform was exactly the same, drop pitch was maintained at $20\mu m$, substrate temperature at 30°C, cartridge temperature at RT and the number of layers on top of each other was increased gradually. In the first study, all the 16 nozzles ejected concurrently (Fig. 5.20), meanwhile, in the second example (see Fig. 5.21), the number of working nozzles was set at 2.

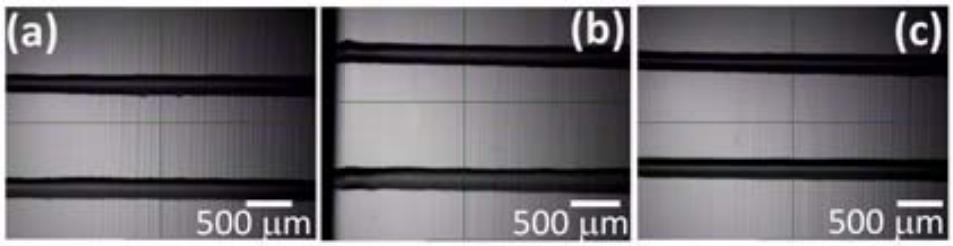


**Figure 5.20.:** YBCO precursor tracks after printing deposition. Drop pitch, substrate temperature, cartridge temperature were set at $20\mu m$, 30ºC and RT respectively. In this case, all 16 nozzles were working simultaneously. The number of layers deposited on top of each other increases gradually from left to right. (a) 1 deposition (b) 2 depositions (1 on top of the first one) (c) 3 total depositions.

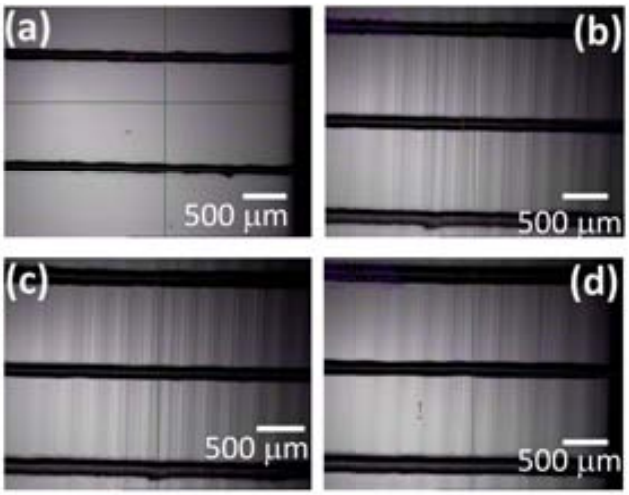


**Figure 5.21.:** YBCO precursor tracks after printing deposition. Drop pitch, substrate temperature, cartridge temperature were set at $20\mu m$, 30ºC and RT respectively. In the experiment, only 2 nozzles were printing at the same time. The number of layers deposited on top of each other increases gradually from left to right and from top to the bottom. (a) 1 deposition (b) 2 depositions (1 on top of the first one) (c) 3 depositions (d) 4 total depositions.

As increases the number of nozzles printing at the same time, the volume ejected therefore increases thus growing the final track width. Next table show the track width data as the number of layers on top increases for the example in which only 2 nozzles were printing at the same time (Tab. 5.12).

| **YBCO 0.5M ethanol based + 12.5% w/w 1,3-propanediol** | **Track width after inkjet deposition** ($\mu m$) |
|---|---|
| 1 deposition | 40 |
| 2 depositions | 75 |
| 3 depositions | 70 |
| 4 depositions | 75 |

**Table 5.12.:** Track width evolution when 2 nozzles print simultaneously and the number of depositions increases gradually. The substrate used was a (5x5)$mm$ LAO single crystal.

As may be discerned from the previous table, the track width is kept constant as the number of layers on top scales. We can ascribe this fact, again, to the pinning of the contact line after the first deposition (see sec. 5.2) enhanced by the heating of the substrate up to 30°C which promotes faster solvent evaporation.

### 5.6.4. Effect of substrate temperature

Heating up the substrate during the printing process was tested to check if the ink-jetting quality of YBCO precursor lines improved.

Fig. 5.22 shows the inkjetted YBCO precursor tracks under the same experimental conditions employed in Fig. 5.21b but heating the substrate until 45°C. At this temperature, there is no balance between the evaporation of the solvent and ink spreading, and the average line width increases significantly from $75\mu m$ to $120\mu m$. Raising the temperature of the substrate increases the bleeding of the ink since the ink viscosity decreases significantly when temperature increases.

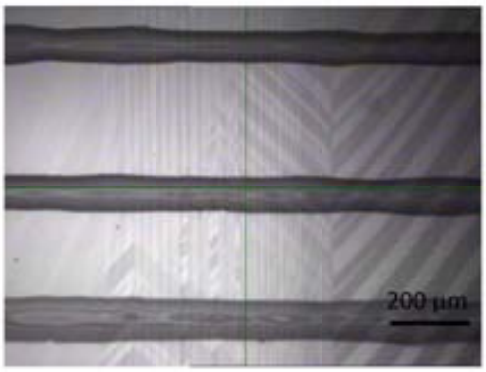


**Figure 5.22.:** Effect of ink-jetted tracks quality on substrate temperature. YBCO precursor tracks after 2 depositions using 2 nozzles of the printer set-up. Drop pitch, substrate temperature and cartridge temperature were fixed at 20 $\mu m$, 45ºC and RT respectively. In this case, track width increases from $75\mu m$ to $120\mu m$.

## 5.7. Track thickness modulation

### 5.7.1. Effect of number of consecutive depositions

Different tests were conducted varying the number of depositions and maintaining constant the rest of parameters (i.e. the ink, drop and line pitch and the drop volume). The solution used to study the dependence of number of depositions on the track thickness was the mentioned 0.5M ethanol based YBCO precursor solution with a 3% by weight of $PEG_{8000}$. Tab. 5.13 reflects the average thickness of the YBCO tracks as a function of the number of depositions:

| **Number of depositions** | **Average track thickness** $(nm)$ |
|---|---|
| 1 | 120 |
| 5 | 300 |
| 10 | 630 |

**Table 5.13.:** Track width evolution with the number of depositions. The number of depositions means the number of layers printed on top of each other. In between depositions, an intermediate drying process at RT during $3min$ was performed.

As it is expected, the average track thickness increases as the number of layers printed on top increases. Mention that a drying process of few minutes at RT was performed between depositions.

## 5.8. Printing arbitrary YBCO patterns

In next section, we will demonstrate that by using inkjet printing technique, it is also possible to print arbitrary shaped patterns [179] reflecting the feasibility of this technique to draw patterns whose array design is not aligned with the printing direction, combining both small surfaces and straight lines.

Next Fig. 5.23 shows an example of an arbitrary YBCO pattern. The printout of the logo of our research institute (Fig. 5.23a) has been performed over different kind of substrates. Fig. 5.23b displays the appearance of the pattern after printing deposition over paper (Fig. 5.23b) and onto a (10x10) LAO single crystal after YBCO growth (Fig. 5.23c). In Fig. 5.23d a zoomed view, taken with SEM of the as-printed pattern after YBCO growth is shown.

As exhibited in Fig. 5.23, a high resolution pattern is achieved as a result of the high repeatability in drop placement and drop volume and the high resolution of the positioning system.

Fig. 5.24a confirms a c-axis oriented YBCO growth for the inkjet printed logo. The sample has been tested for homogeneity by Hall mapping the remanent field after magnetizing the sample up to full penetration [275]. This is a powerful tool to understand the current distribution generated in the magnetization process of a sample. The local value of the normal field is measured point by point during the application of an external magnetic field and plotted in the magnetic field map shown in Fig. 5.24b. As can be seen, the distribution of trapped magnetic field once the superconducting state is achieved in a field cooling process to 77K is in good agreement with that expected from the Bean approach [214, 276]. The currents are ordered in loops and the presence of unconnected loops is obviously related to the different superconducting islands. Each of them give a peak in the magnetic profile. As a general conclusion, the distribution of the magnetic flux is in good agreement with that expected for an homogeneous deposition (Fig. 5.24).

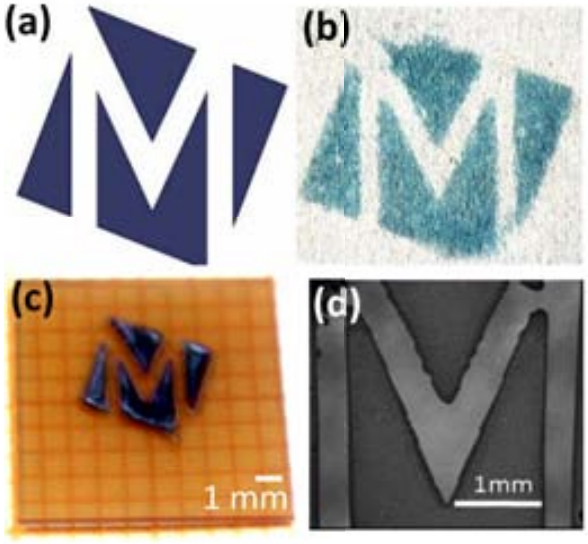


**Figure 5.23.:** (a) Logo of our ICMAB research institute. (b) Inkjet printed logo after deposition and drying onto conventional paper. (c) Inkjetted logo after YBCO growth process on LAO single crystal. (d) Zoomed image taken by SEM of the ICMAB logo after YBCO growth process.

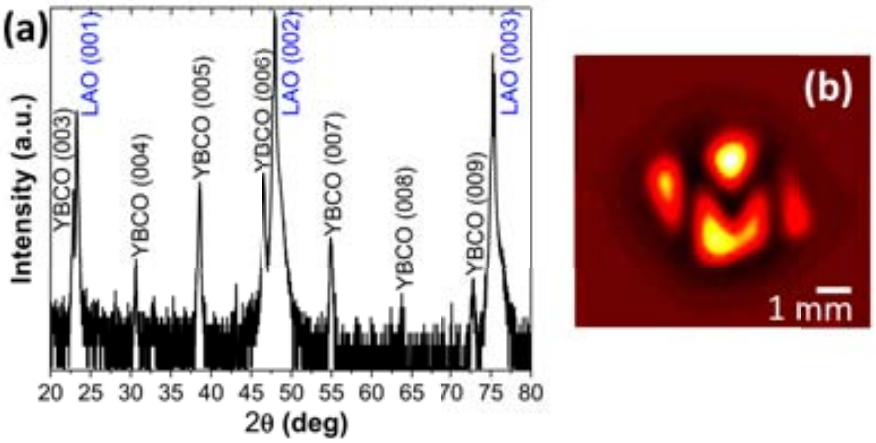


**Figure 5.24.:** (a)$\theta - 2\theta$ XRD pattern of the ink jetted ICMAB logo after YBCO growth. YBCO has grown maintaining the same texture than the substrate. (b) Hall mapping of the remanent magnetic field trapped by the YBCO coating where it can be observed the good homogeneity of the deposition.

## 5.9. Summary and conclusions

In the present work, we have demonstrated the feasibility of growing epitaxial multi-filamentary structures and extended patterns on LAO single crystal using different piezo-electric DoD inkjet printers by proper adjustements of rheological and wetting parameters of the TFA-YBCO precursor solutions. The control of the physicochemical ink properties has been shown to be a crucial point to tune the dynamical properties of the ink when impinging onto the susbtrate to consequently guide the final morphology of the deposit.

First, we have presented a sequence of different basic morphological arrays varying

the drop pitch which fits well with the theoretical mechanisms proposed for continuous track formation.

The analyses of the presented results for YBCO tracks on LAO single crystals allow us to prepare a general layout of the requirements that we have observed that must be fulfilled for the formation of those mutifilamentary structures. They can be summarized in the following points:

- Contact line pinning cannot be a handicap for track formation. It is crucial to choose systems that are fully pinned, that is, they have a strong hysteresis (i.e. $\theta_{adv}$ and $\theta_{rec}$ are different). At least, two possibilities of contact line pinning should be contemplated: from one hand, $\theta_{adv}$ and $\theta_{rec}$ might be essentially distant and different from 0 or from the other side, $\theta_{adv}$ should be large enough than 0 and $\theta_{rec}$ 0.

- Elimination of the coffee stain effect also enhances the quality of tracks. Control of solvent evaporation rate to minimize flow induced by evaporation might also help to obtain homogeneous and continuous coatings, and therefore, avoid coffee staining.

- Elimination of bulging effect also helps to achieve straight tracks. This can be conciliate by adjusting the drop pitch and the velocity of the platform selecting an ink with a controlled $\theta_{adv}$ after each printed line.

These conditions can be satisfied by choosing the appropriate inks $(\rho, \eta, \gamma)$ and substrates $(\theta)$. After optimizing the ink properties and the drop deposition protocol, we have shown that highly homogeneous tracks with average thickness of $\sim 300nm$ and $\sim 150\mu m$ wide were obtained showing a maximum $J_c$ at self field and 77K of $1.1MA/cm^2$. In our case, the tuning of the contact angle ink-substrate is performed by adding a second solvent of higher boiling point. We propose that the key issue which allow us to explain the morphological differences in the YBCO tracks printed using the ink which combines ethanol plus 1,3-propanediol in contrast to those deposited using the ink with ethanol as unique solvent lies in the increase of the contact angle in the first case together with a strong pinning of the contact line. Nevertheless, the singular morphology observed after pyrolysis process when an ethanol based YBCO precursor solution contains PEG is used may be attributed to the contraction that is produced during the thermal processing, which leads to stresses that generate a thin net of wire-like polymeric structure.

It has been also shown the feasibility of using CSD precursors in combination with inkjet printing technology to obtain both tracks and extended patterns by adapting the ink rheology, selecting the appropriate solvent and by properly tuning the drive conditions. Besides, it has been demonstrated several ways for track width and thickness modulation. For track width modulation, by decreasing the drop volume, thinner features may be achieved. This was performed by tuning the volume ejected, drop pitch and number of successive depositions by means of a multinozzle printer with nozzles that eject a nominal drop volume of $10pL$. Also, the tune of the ink formulation by increasing the content of 1,3-propanediol is another approach for track width modulation. Alternatively, by sistematically increasing the number of depositions, the thickness of tracks may be adjusted. Therefore, an understanding of the formation of tracks or beads is a good starting point to optimize the obtention of well-defined, uniform and continuous layers.

## 5.10. $YBa_2Cu_3O_{7-x}$ coatings: printing of single layers

Within the framework of the present study, we focus on the obtention of YBCO continuous coatings by using the CSD-TFA-inkjet printing route (see sec. 3.1.1.1). In the second part of this chapter, we present an overview of the experimental sequence followed to obtain YBCO layers with good superconducting performance. It requires a tight control of the solution formulation, drop volume and drop pitch in order to achieve homogeneous films with controlled thickness [277]. As substrates, $LaAlO_3$ (LAO) perovskite single crystals as ideal substrates are used as a proof of concept to later transfer the results onto Ni-5% W metallic tapes. A study of film thickness adjustment which allows to make a rough estimation about film porosity will be briefly presented. Preliminar results of YBCO coatings on Ni-5% W tapes are also shown.

# Towards long-length coated conductors

## 5.11. Printing of single YBCO layers on LAO single crystal: assessing the optimum printhead and precursor solution

Through this section, we present the experimental progression to obtain continuous and homogeneous YBCO coatings onto (5x5)$mm$ LAO single crystal substrates. As mentioned in chapter 3, three types of printheads were tested along this research: a single nozzle electromagnetic printhead with a 90$\mu m$ nozzle diameter, a commercial single nozzle piezoelectric actuated dispenser with a 60$\mu m$ nozzle diameter and a multinozzle piezoelectric printer with 16 nozzles and a nominal drop size of 10$pL$.

It could be adequate to think that as the main goal of this part is the manufacturing of single YBCO layers, larger drop volumes would be desired to cover large areas. Going in this way, that was the reason why the experimental sequence to obtain YBCO layers started with the inkjet printing by using the single nozzle electromagnetic printhead.

By using the electromagnetic printhead, square matrices with the same drop spacing in both directions (i.e. in the slow-print (left to right) and fast print (top-to-bottom) directions) were built up in a raster-scan method sec. 2.5.2, then in next experiments only one drop pitch will be provided. For each test, the valve opening time was set at the minimum position (i.e. 550$\mu s$), and then we screened the valve opening voltage and ink pressure to the minimum values to eject the smallest amount of liquid. This procedure was followed to assure a good ink distribution onto the substrate. Those minimum parameters were found after an optimization process, that is the reason why in next tables are called optimum printing parameters. In this first section of the chapter, (10x10)$mm$ LAO substrates were used as substrates.

### 5.11.1. Single nozzle electromagnetic printhead

After an initial test with methanol anhydrous (Sigma Aldrich, 99.8%) and for a first screening of the different printing variables (i.e. valve opening time, valve opening voltage and ink pressure), the printing procedure continued with a 1.5M methanol based YBCO precursor solution prepared from separated salts (sec. 3.1.1.2). It was decided to start from a 1.5M total metal concentration methanol based YBCO precursor solution (see Tab. 5.14), without any formulation correction for analogy to the standard YBCO precursor solution used in our research group to grow high-quality YBCO films by spin coating.

Thus, in this case, the optimum parameters to obtain a continuous coating are displayed in next Tab. 5.14:

| **Solution** | **1.5M methanol based YBCO precursor solution** |
|---|---|
| Valve opening time ($\mu s$) | 550 |
| Valve opening voltage ($V$) | 26.7 |
| Ink pressure ($bar$) | 0.8 |
| Drop pitch ($mm$) | 0.8 |

**Table 5.14.:** Optimum parameters for the 1.5M methanol based YBCO precursor solution to obtain a continuous coating by using the electromagnetic printhead. Only one drop pitch is presented because the printing matrix used was a square.

The drop pitch value shown in the following tables corresponds to the minimum distance which enables to obtain a continuous coating. Smaller drop pitches produce thicker coatings. Then, the minimum thickness in a given ink-substrate combination is determined by the spacing required for drop overlap.

| | **1.5M methanol based YBCO precursor solution** |
|---|---|
| Density $\rho$ ($g/cm^3$) | 1.174 |
| Surface tension $\gamma$ ($mN/m$) | 22.5 |
| Viscosity $\eta$ ($mPa \cdot$ s) | 4.5 |

**Table 5.15.:** Relevant physicochemical ink properties for the 1.5M methanol based YBCO precursor solution. Viscosity measurement was carried out at a shear rate of $100 s^{-1}$. All the measurements were performed at room temperature.

Fig. 5.25 shows the drop pitch optimization to obtain a continuous YBCO coating using the 1.5M methanol based YBCO precursor solution. In Fig. 5.25, drop pitch in

the longitudinal direction (x direction) was decreased from left to right, from 0.65$mm$ to 0.6$mm$, and from top right to bottom left from 0.6$mm$ to 0.5$mm$, meanwhile in the vertical direction, drop pitch was fixed at 0.65$mm$ in both upper figures and decreases from top to the bottom left from 0.65$mm$ to 0.6$mm$ and in the lower row from left to right from 0.6$mm$ to 0.5$mm$.

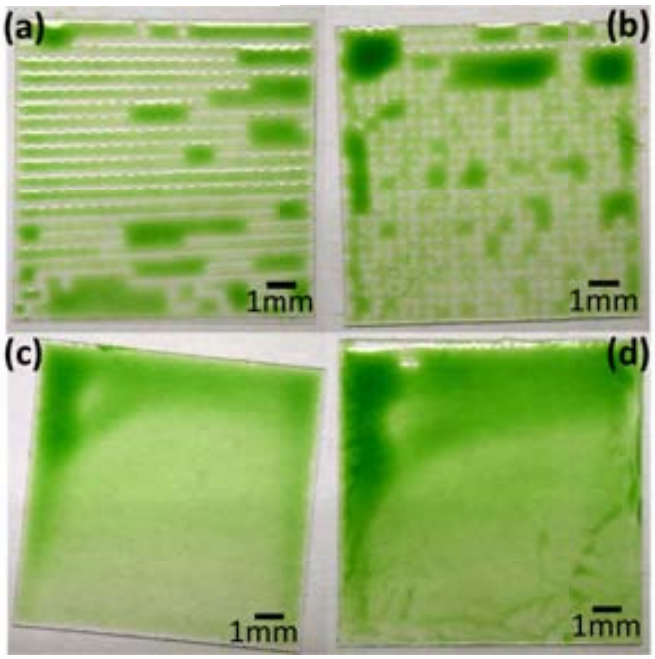


**Figure 5.25.:** Experimental sequence obtained by depositing a 1.5M methanol based YBCO precursor solution. Longitudinal and vertical drop pitches were modified within this succession. Longitudinal and vertical drop pitches in the different pictures are, respectively: (a) (0.65$mm$ x 0.65$mm$), (b) (0.6$mm$ x 0.65$mm$), (c) (0.6$mm$ x 0.6$mm$) and (d) (0.5$mm$ x 0.5$mm$).

An understanding of the rheological and wetting effects during the printing of films is necessary for improving the homogeneity of films to realize well-controlled shapes. A very interesting phenomena may be observed in Fig. 5.26. If the amount of liquid on the substrate is too large or, otherwise, if the vapour pressure of the ink is too low, when the printing process advances, the excess of liquid is progressively dragged to the previous printed lines in order to minimize the surface area. At the edges of the substrate also might be appreciated the accumulation of fluid due to the extra curvature of the substrate boundaries. These 2D liquid displacements eventually lead to a fluid accumulation in the region where the printing has started forming non-homogeneous coatings [268]. This liquid flow might be explained as a joint of different factors: the large ejected volume from the EM printhead (in which $V_{drop}$∼tens of nL), together with the low viscosity of the solution which do not limit the spreading of the ink. Probably, the use of parallel printing, instead of a single nozzle printhead, would avoid this effect.

For improved clarity, Fig. 5.26 shows the above-mentioned process of progressive fluid accumulation. Due to surface tension, thicker regions are obtained in the first printed area, that after the thermal processing at low temperatures (310°C) leads to cracks and other kind of inhomogeneities.

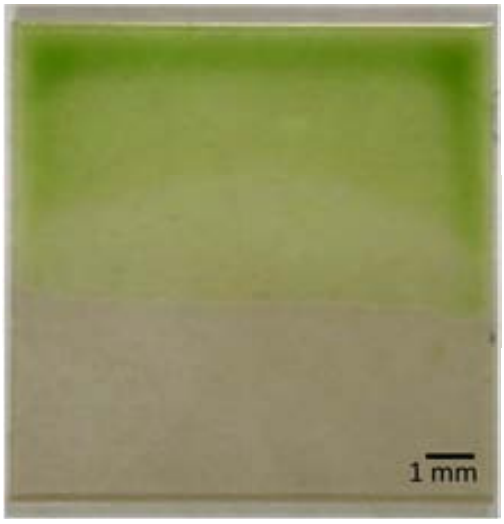


**Figure 5.26.:** General appearance of the coating after deposition. The ink used in this case was a 1.5M methanol based YBCO pecursor solution. The parameters used during the printing process are detailed in Tab. 5.14. In this experiment, the substrate used was a (10x10)$mm$ LAO single crystal. Longitudinal and lateral distance between drops were set at 0.8$mm$. The image was taken with Optical Microscopy.

Several strategies were devised to cope with this inconvenience:

1. To print a pattern larger than the substrate dimensions: it would avoid possible edge effects. This first proposal directly yielded similar results that the ones exhibited in Fig. 5.26. Mention that from this point and to avoid possible edge effects, all the patterns to be printed with the electromagnetic device were designed 2$mm$ larger than the substrate dimensions.
2. Increase the viscosity of the YBCO precursor solution. This rheological modification would alter the dynamics of the ink, slowing down the spreading process and allowing to keep away the movement of the contact line. This approach would be a feasible solution to fix the width of the bead when the printing process is going on.

After concluding that covering printing distances larger than substrate dimensions, non-homogeneous coatings were obtained by using the electromagnetic printhead, the second approximation was attempted. The main goal at this time was to obtain a YBCO precursor solution with higher viscosity and surface tension values to reduce its mobility onto the substrate and fix the solution through evaporation until the equilibrium state is achieved.

The initial strategy followed was to maintain the same solvent (methanol) and introduce a suitable organic additive to increase the viscosity of the ink.

In the search for appropriate organic additives to tune film features, three factors need to be considered:

- The chemical stability of the additive with the TFA precursors salts has to be taken into account because their interactions with the solute can enhance or, otherwise, decrease the stability of the resulting solution producing its complete destabilization and precipitation.

- The rheological properties of the solution need to be set within an adequate range from the deposition methodology point of view. Besides, the final film homogeneity and thickness are modified by them.

- Finally, the thermal stability of the modified solutions should be considered because it influences both the decomposition time and temperature, as well as the plastic flow of the film during the pyrolysis process.

Since many years ago, our group started an investigation screening to determine the suitability of different organic additives for YBCO-TFA solutions. Relevant results in spin coating showed that the introduction of additives such as triethanolamine (TEA) and polyethyleneglycol (PEG) allows to obtain homogeneous YBCO coatings with high $J_c$ without changing the processing conditions of the pyrolysis process [278]. From one hand, it was demonstrated that the introduction of a 62% by weight of TEA in the 1.5M solution allows us to achieve YBCO layers of about $600nm$ with $J_c$ at self field and $77K$ around $3MA/cm^2$. From another hand, the addition of a 30% by weight of PEG gives YBCO films of about $400nm$ with $J_c{\sim}2MA/cm^2$ [278].

We started considering the TEA additive (Sigma Aldrich). Therefore, various solutions with different content of TEA were prepared in order to evaluate how viscosity and surface tension change when the TEA content increases (see next Fig. 5.27).

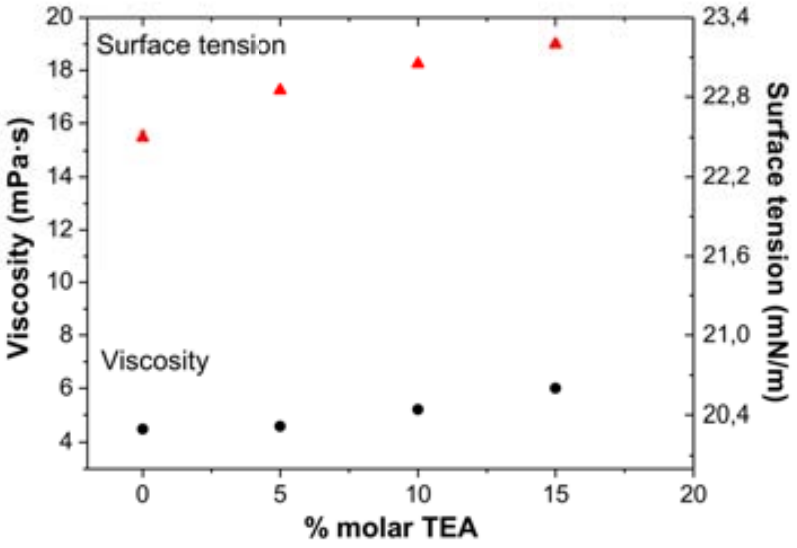


**Figure 5.27.:** Surface tension (red triangles) and viscosity (solid black dots) values of several YBCO/TEA precursors solutions as a function of TEA content. As can be observed, when TEA content increases, both surface tension and viscosity are enhanced. Values of viscosity are measured under a shear rate of 100 $s^{-1}$. Viscosity and surface tension measurements were performed at RT.

The previous solutions were stable during at least six months. Because our present goal is to increase the solution viscosity to avoid ink flowing, we decided to test the solution that contains a 15% molar of TEA which has the following physicochemical properties:

| **Solution** | **1.5M methanol based YBCO precursor solution +15% molar TEA** |
|---|---|
| Density $\rho$ $(g/cm^3)$ | 1.184 |
| Surface tension $\gamma(mN/m)$ | 23.2 |
| Viscosity $\eta$ $(mPa \cdot \mathrm{s})$ | 6 |

**Table 5.16.:** Relevant physicochemical ink properties for the 1.5M methanol based YBCO precursor solution with a a 15% molar of TEA. Viscosity measurement was carried out at a shear rate of $100s^{-1}$. All the measurements were performed at room temperature.

The optimum printing parameters were set for this solution at:

| **Solution** | **1.5M methanol based YBCO precursor solution +15% molar TEA** |
|---|---|
| Valve opening time $(\mu s)$ | 550 |
| Valve opening voltage $(V)$ | 27 |
| Ink pressure $(bar)$ | 1 |
| Drop pitch $(mm)$ | 0.5 |

**Table 5.17.:** Optimum printing parameters to get a continuous coating onto a LAO substrate for the 1.5M methanol based YBCO precursor solution that contains a 15% molar of TEA. The density, surface tension and viscosity of the ink are 1.184 $\mathrm{g \cdot cm^{-3}}$, 6 $\mathrm{mPa \cdot s}$ and 23.2 $\mathrm{mN \cdot m^{-1}}$, respectively.

Next figure shows the whole appearance of the coating obtained using the previous solution (Tab. 5.17).

Once again, due to the large liquid volumes employed, the high mobility and the low pinning of the ink onto the substrate, during the printing process, the fluid moves along the substrate leading to a non-homogeneous coating with a strong accumulation of the liquid in the upper part (Fig. 5.28a), which eventually leads to cracks and other heterogeneities after pyrolysis process (see Fig. 5.28b).

During all the preceding experiments, the solvent used for the different solutions was methanol. It is worthly to remark that in the previous printing screening, the clogging of the nozzle became a severe problem due to the skin generated at the orifice while evaporation occurs. It may be attributed to the low boiling point of methanol ($T_{bp} \sim 65$ °C). The fast evaporation rate of this solvent may produce the progressive formation of a residual solid at the orifice which finally clogs the nozzle and impede the ink ejection.

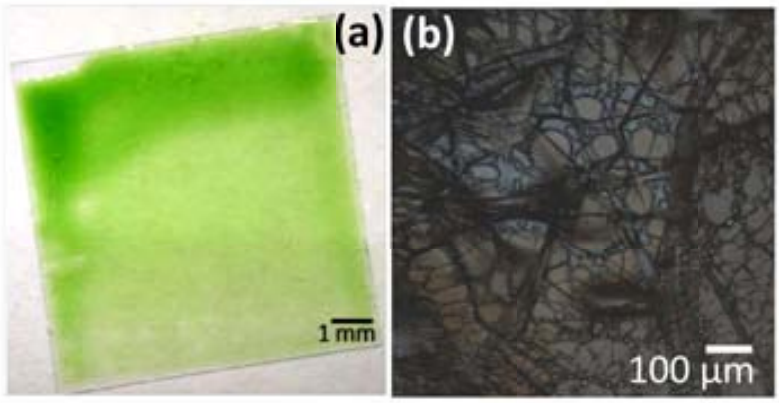


**Figure 5.28.:** YBCO coating using a 1.5M methanol based YBCO precursor solution with a 15% molar of TEA over LAO single crystal. (a) Global aspect of the coating after inkjet deposition. An agglomeration of liquid appears at the upper part and edges of the substrate. (b) Central part of the sample: due to liquid accumulations, non-homogeneous regions in thickness lead to cracks and film inhomogeneities after pyrolysis process at low T.

To surmount this problem and with the aim to slightly increase the ink evaporation rate, the solvent of the precursor ink was changed from methanol to ethanol ($T_{bp} \sim 78$ °C). In this sense, a $1.5M$ ethanol based YBCO precursor solution was prepared. The solvent modification results in the following rheological parameters changes (Tab. 5.18):

| | **1.5M methanol based YBCO precursor solution** | **1.5M ethanol based YBCO precursor solution** |
|---|---|---|
| Density $\rho$ $(g/cm^3)$ | 1.174 | 1.075 |
| Surface tension $\gamma$ $(mN/m)$ | 22.5 | 21.8 |
| Viscosity $\eta$ $(mPa \cdot \mathrm{s})$ | 4.5 | 6.4 |

**Table 5.18.:** Relevant physicochemical ink properties for the 1.5M methanol and ethanol based YBCO precursor solutions. All the measurements were performed at room temperature. Viscosity measurements were carried out at a shear rate of $100s^{-1}$.

Using the EM printhead, the experimental results obtained with this ethanol based YBCO precursor solution were comparable with the ones achieved for the previous shown methanol based solution and, consequently, we will obviate their presentation herein.

At that time, we considered that an interesting possibility could be try to manipulate lower amounts of liquid by pointing out to thinner coatings. For this purpose, the dilution of the original 1.5M ethanol based YBCO precursor solution from 1.5M to 0.5M was the next step. In order to compensate the loss of viscosity due to the decrease of solution concentration, it was added a 6% w/w of $PEG_{8000}$ (MW=8000$g/mol$, Sigma Aldrich).

Next Tab. 5.19 details the optimum printing variables to for a full covering using a 0.5M ethanol based YBCO precursor solution which contains a 6% by weight of $PEG_{8000}$

(see Tab. 5.20). The relevant printing parameters used in this case are listed in the consecutive table.

| **Solution** | **0.5M ethanol based YBCO precursor solution + 6% w/w PEG** |
|---|---|
| Valve opening time ($\mu s$) | 550 |
| Valve opening voltage ($V$) | 23.2 |
| Ink pressure ($bar$) | 0.65 |
| Drop pitch ($mm$) | 0.48 |

**Table 5.19.:** Optimum printing parameters to obtain a continuous coating for the 0.5M ethanol based YBCO precursor solution with a 6% by weight of PEG by using the electromagnetic printhead onto a (10x10) $mm$ LAO substrate. Only one drop pitch is presented because a squared printing matrix was used.

| | **0.5M ethanol based YBCO precursor solution + 6% w/w PEG** |
|---|---|
| Density $\rho$ ($g/cm^3$) | 0.868 |
| Surface tension $\gamma$ ($mN/m$) | 21.3 |
| Viscosity $\eta$ ($mPa \cdot$ s) | 3.1 |

**Table 5.20.:** Relevant physicochemical ink properties for the 0.5M ethanol YBCO precursor solution with a 6% w/w of $PEG_{8000}$. All the measurements were performed at room temperature. Viscosity measurement was carried out at a shear rate of $100s^{-1}$.

Fig. 5.29a exhibits the general aspect of an inkjet printed coating by using the previous solution. It may be noticed in this figure that, although a small accumulation of liquid is observed in the upper part of the sample, the surface of the sample is more homogeneous than the previous ones presented until this point due to the lower volume to manage. For this reason, we decided to pyrolyse the sample to see the fluid behaviour at low temperatures. The resultant surface of the film is displayed in Fig. 5.29b. As only slight colour differences may be appreaciated in the optical micrograph of Fig. 5.29b, it is possible to conclude that an acceptable thickness homogeneity is achieved by using this ink. Moreover, in the 2D-XRD pattern shown in Fig. 5.29c, only (00l) YBCO reflections are observed coherently with a c-axis oriented YBCO growth, although the presence of the small diffraction cones in the XRD pattern indicates a slight misorientation between grains ($\sim 8°$). Probably, further adjustements of the printing deposition and ink distribution would give flatter surfaces. Remarkable features of Fig. 5.29d are the low degree of porosity and the absence of $ab$ planes. In this case, the thickness of the film was around $100nm$ giving a $J_c$ of $1.1MA/cm^2$ at $77K$ and self field.

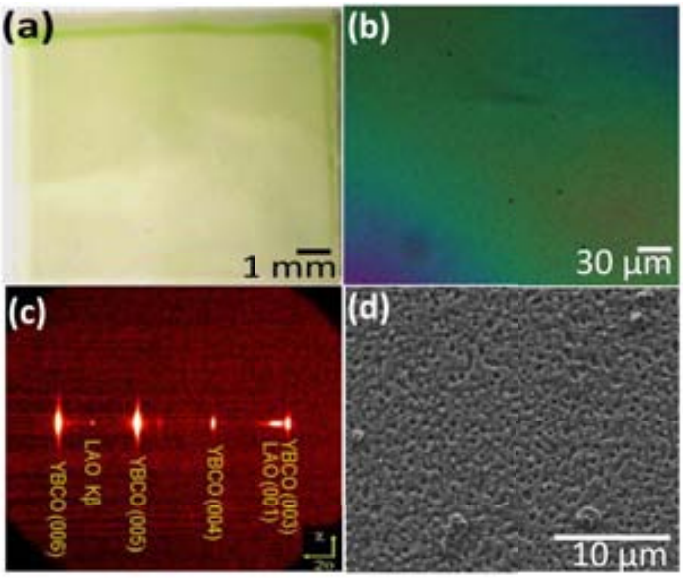


**Figure 5.29.:** Morphological and structural characterization of an inkjet YBCO coating using the EM head and a 0.5M ethanol based YBCO precursor solution with a 6% by weight of $PEG_{8000}$. (a) General overview of the sample. (b) Optical micrograph of the sample after pyrolysis process. (c) Two-dimensional XRD pattern of the as-grown YBCO film. (d) SEM micrograph of the pyrolised sample shown in (a).

Due to the complexity to correctly distribute the liquid onto the substrate by using the electromagnetic printhead, we decided to substitute the single nozzle electromagnetic dispenser for a single nozzle piezoelectric device of $60\mu m$ of nozzle diameter. As previously demonstrated in chapter 4, the possibility to tune drop volume according to the actuation parameters of the printhead and the physicochemical properties of the ink made that at that point, the main objective was to create smaller drops by means of the piezo printhead to control in a more accurate way the ink arrangement. Roughly speaking, the change from the electromagnetic device to the piezoelectric one could expect a decrease in drop radius of about 73% (the assumed average drop diameter on the flight is about $150\mu m$ for the electromagnetic printhead and around $40\mu m$ for the piezoelectric device). Thus, the volume relationship ($V_{rel}$), given by the expression $V_{rel}=\left(\frac{V_{drop\ EM}}{V_{drop\ PZE}}\right)^3 = \left(\frac{150\mu m}{40\mu m}\right)^3$, is ∼53. The drop volumes considered in this relation are average values since, as seen in chapter 4, they strongly depend on the ink rheological properties, among other factors.

## 5.11.2. Single nozzle piezoelectric printhead

The experiments presented above outline the relevance of adjusting the drop volume and the physicochemical properties of the ink to obtain continuous and uniform coatings. Next sections shows the printing optimization followed to obtain continuous and homogeneous coatings by using the single piezoelectric printhead with a $60\mu m$ nozzle diameter.

Until this point, the experiments performed with inks that contain PEG as additive provided non-homogeneous coatings. We attributed this fact to the particular fluid dynamics of such type of inks. Hence, the experimental sequence using the piezoelectric

printhead started maintaining the solution concentration at 0.5M without the introduction of any additive. The important physicochemical properties of this ink are presented in the following table:

| | **0.5M ethanol based YBCO precursor solution** |
|---|---|
| Density $\rho$ $(g/cm^3)$ | 0.883 |
| Surface tension $\gamma$ $(mN/m)$ | 21.5 |
| Viscosity $\eta$ $(mPa \cdot s)$ | 1.5 |

**Table 5.21.:** Relevant physicochemical ink properties for the 0.5M ethanol based YBCO precursor solution. Viscosity measurement was carried out at a shear rate of $100s^{-1}$. All the measurements were performed at room temperature.

Mention that from now on all the printing experiments presented were perfomed on ($5mm$ x $5mm$) LAO single crystals. The contact angle it makes with the LAO substrate is below 10°.

Chapter 4 (sec. 4.9.2.2 and sec. 4.9.3.2) details the dependence on drop size and drop volume of the actuation parameters of the piezoelement by using a 0.5M ethanol based YBCO precursor solution. These previous tests showed that with the operational parameters displayed in next table, a drop volume of about $30pL$ and drop speed ∼1 m/s, could be adequate for drop pitch settings:

| **0.5M ethanol based YBCO precursor solution** | **Value** |
|---|---|
| Rise time $(\mu s)$ | 2 |
| Dwell time $(\mu s)$ | 11 |
| Fall time $(\mu s)$ | 3 |
| Echo time $(\mu s)$ | 11 |
| Final rise time $(\mu s)$ | 2 |
| Voltage up $(V)$ | +25 |
| Voltage down $(V)$ | -21 |

**Table 5.22.:** Operational driving parameters of our 0.5M ethanol based YBCO precursor solution.

Since the formation of films consist of the merging of $n^{th}$ lines, the next step was print two rows of drops by scanning a range of drop pitch until drop overlap occurs. After the first line is printed from left to right with a constant drop spacing $\triangle x$, the second line is printed from right to left with the same dot spacing $\triangle x$ as shown in Fig. 2.7. The first

drop pitch tested was $200\mu m$ in both directions and the resulting drop pattern is shown in Fig. 5.30.

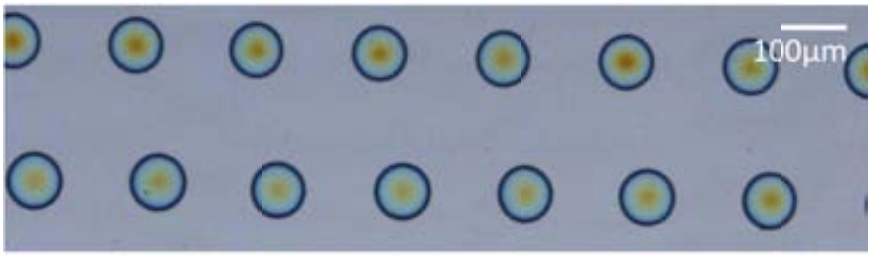


**Figure 5.30.:** Drop pattern after deposition with the PZT single nozzle printhead and drying at room temperature. Drop pitch was set in this experiment at $200\mu m$ in both directions. The solution and substrate used in this deposition was, respectively, a 0.5M ethanol based YBCO precursor solution and a (5x5)$mm$ LAO single crystal. The printing parameters are shown in Tab. 5.22.

From this Fig. 5.30, drop diameter may be easily deduced ($\sim 90\mu m$). As shown in Fig. 5.30, setting drop pitch at $200\mu m$, drops do not merge anymore. The sequence of two consecutive lines printed at a constant drop spacing in both directions was performed as well at drop pitches of $100\mu m$, $70\mu m$, $60\mu m$, $50\mu m$, $40\mu m$, $30\mu m$ and finally $15\mu m$ (Fig. 5.31).

The colour distribution observed in the optical micrographs could give us an idea of the thickness oscillation present in the films. As might be appreciated in the previous Fig. 5.31, the more homogeneous coating was obtained at drop pitch between $15\mu m$ and $30\mu m$. After this drop pitch screening, the coming step was to print a complete coating by designing a $7mm$ x $7mm$ squared matrix. Continuous layers with an acceptable

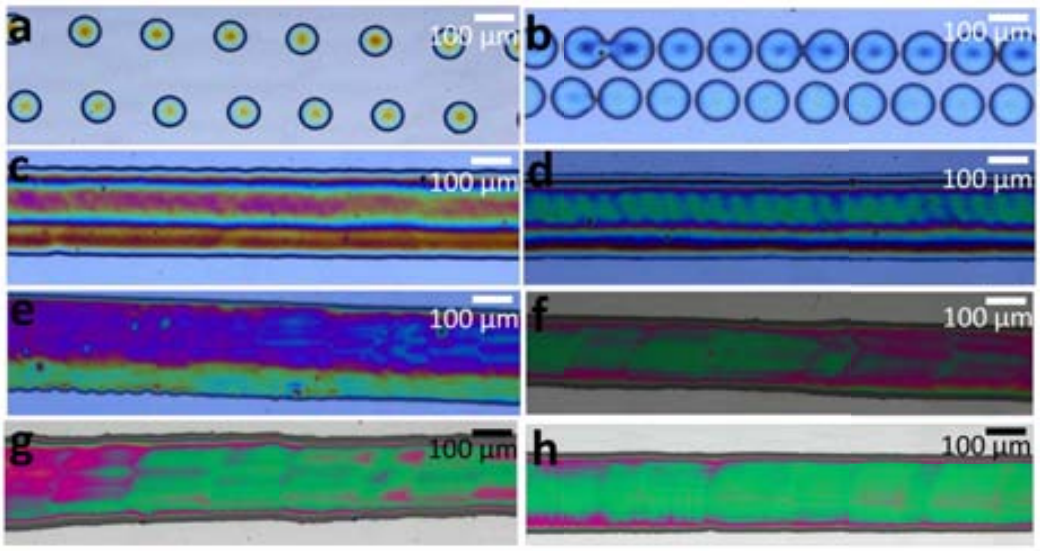


**Figure 5.31.:** Optical images of the two printed arrays varying the distance between drops using a 0.5M ethanol based YBCO precursor solution onto a (5x5)$mm$ LAO substrate after a drying process at RT. For the different experiments, the drop pitch was set at: (a) $200\mu m$ (b) $100\mu m$ (c) $70\mu m$ (d) $60\mu m$ (e) $50\mu m$ (f) $40\mu m$ (g) $30\mu m$(h) $15\mu m$. Drop pitch decreases from left to right and from top to the bottom.

homogeneity were achieved by adjusting both line and drop pitch between $19\mu m$ and $30\mu m$. Taking into account that drop volume under the experimental working conditions shown in Tab. 5.22 is around $30pL$, and the scanned drop pitch interval goes from $19\mu m$ to $30\mu m$, it would give YBCO coatings from $250nm$ to $650nm$, providing an adequate range of film thickness to evaluate and compare their morphological, structural and superconducting properties with the standard spin-coated YBCO films prepared in our group. TFA-YBCO films were inkjet-printed onto $5mm$ x $5mm$ LAO single crystals using a 0.5M ethanol based YBCO precursor solution and the optimized printing parameters yet detailed in Tab. 5.22.

Fig. 5.32 exhibits the aspect of the central part of several inkjet printed samples after pyrolysis process. The thermal processing followed is presented in sec. 3.4.2. Any drop pitch within the range from $19\mu m$ to $30\mu m$ is smaller than drop diameter and, therefore, assures drop overlap. In these experiments, the unique difference we would expect between those samples is their final thickness as only the density of drops is changed. Later in sec. 5.11.3 will be demonstrated that film thickness may be easily controlled by modifying drop density in terms of drop pitch. As drop pitch increases, thicker films are obtained [183].

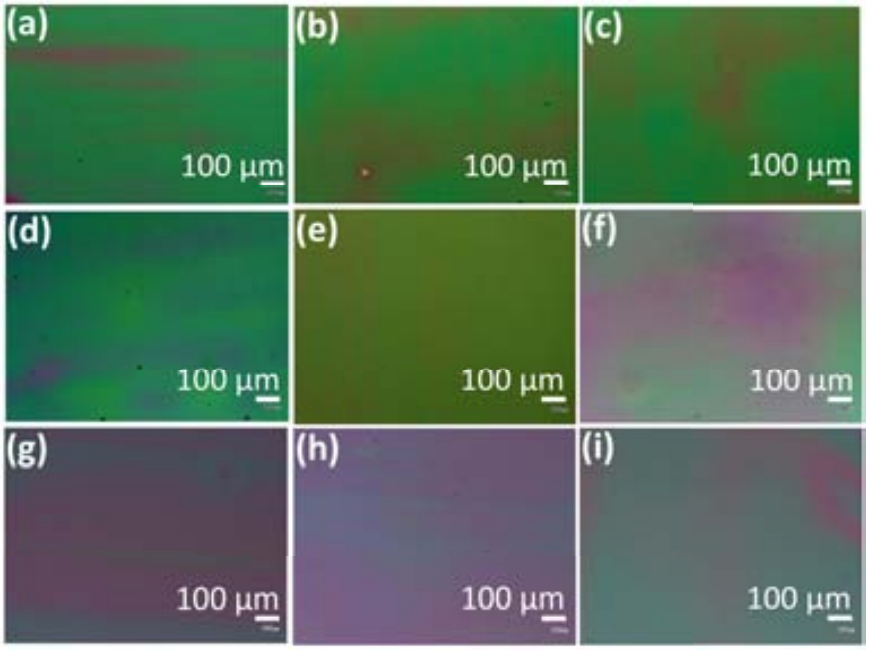


**Figure 5.32.:** Typical optical microscopy images of inkjetted YBCO precursor films after pyrolysis process taken in the central part of the sample using the single nozzle piezoelectric printhead. The drop pitch working range was set between $19\mu m$ and $27\mu m$. In particular, in the different printing experiments, drop pitch was set at (a) $27\mu m$, (b) $26\mu m$, (c) $25\mu m$, (d) $24\mu m$, (e) $23\mu m$, (f) $22\mu m$, (g) $21\mu m$, (h) $20\mu m$, (i) $19\mu m$ in both directions. Note that continuous, crack-free layers with an acceptable homogeneity have been achieved. Sometimes, different defects caused by dust are also observed on the surface of the sample. As substrate, LAO (5x5)$mm$ was used. The driving parameters employed are presented in Tab. 5.22.

The following Fig. 5.33 presents the optical images of the boundaries of some examples of inkjet printed samples. Crack-free boundaries with the typical edge effects were obtained by varying drop pitch within $19\mu m$ and $27\mu m$.

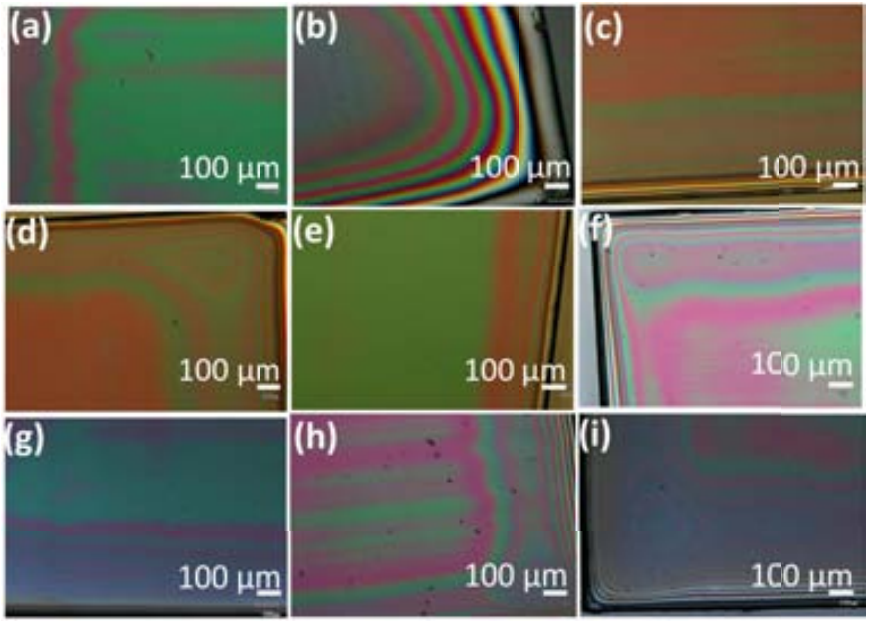


**Figure 5.33.:** Typical optical microscope images of the edges of inkjetted YBCO precursor films after pyrolysis process onto (5x5)$mm$ LAO substrate using the single nozzle PZT printhead. In this study, drop pitch was varied between 19$\mu m$ and 27$\mu m$. In these tests, drop pitch was fixed at (a) 27$\mu m$, (b) 26$\mu m$, (c) 25$\mu m$, (d) 24$\mu m$, (e) 23$\mu m$, (f) 22$\mu m$, (g) 21$\mu m$, (h) 20$\mu m$, (i) 19$\mu m$. As can be perceived, the edges of the films either do not have cracks after the low-temperature pyrolysis process. The driving parameters of the piezoactuator are displayed in Tab. 5.22.

By further lowering drop pitch beyond 18$\mu m$, the as-deposited samples develop macrocracks (see Fig. 5.34) due to relaxation of tensile stresses during the thermal treatment presented in Fig. 3.7. There are different reasons that can cause shrinkage and tensile stresses in the film during the pyrolysis step: one is the evaporation of the solvents, another is the decomposition of the metallorganic precursors and, finally, the crystallization of new phases. Therefore, a suitable control of the stress relaxation is needed to avoid crack formation. Some additional optimization of the deposition and/or pyrolysis conditions for drop pitch below 18$\mu m$ is still required to optimize the properties of these thicker films.

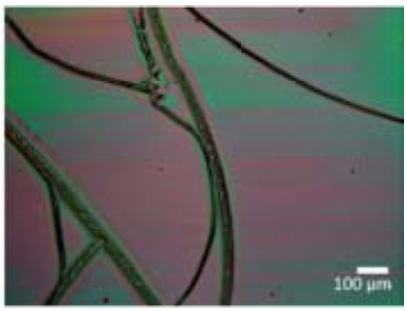


**Figure 5.34.:** Optical microscope image of a macrocrack-developed YBCO precursor film onto LAO single crystal. Drop pitch in this trial was set at 18$\mu m$. The pyrolysis conditions used in this case are the ones specified in sec. 3.4.2.

#### 5.11.2.1. YBCO coatings characterization

In next sections, the morphological, structural and superconducting characterization of several TFA-YBCO inkjet printed films onto LAO single crystal will be presented. The YBCO coatings displayed in the following blocks were obtained by ejecting a 0.5M YBCO precursor solution (Tab. 5.21) by applying the actuating parameters shown in Tab. 5.22.

We firstly report the fully characterization of a $\sim 300nm$ TFA-YBCO coating ($V_{drop} \sim 30pL$; density of drops$\sim 1.6 \cdot 10^{-3}$drop$/\mu m^2$) for comparison with the spin-coated YBCO layers prepared in our research group at ICMAB.

#### 5.11.2.2. Morphological characterization of a $\sim$300$nm$ YBCO coating

To analyse the surface quality of the layers after pyrolysis and to study the microstructure of the as-grown YBCO films, optical microscopy and scanning electron microscopy (SEM) have been employed. As may be appreciated in Fig. 5.35a, optical microscopy images after the pyrolysis process at 310°C reveal a continuous, flat, homogeneous and crack-free layer (Fig. 5.35a). Moreover, we have investigated the surface morphology of these YBCO coatings by SEM. Fig. 5.35b displays a typical SEM image of an homogeneous YBCO film after growth. It shows some degree of porosity, a full absence of *ab* planes and a high homogeneity as expected in a properly controlled epitaxial YBCO growth [73].

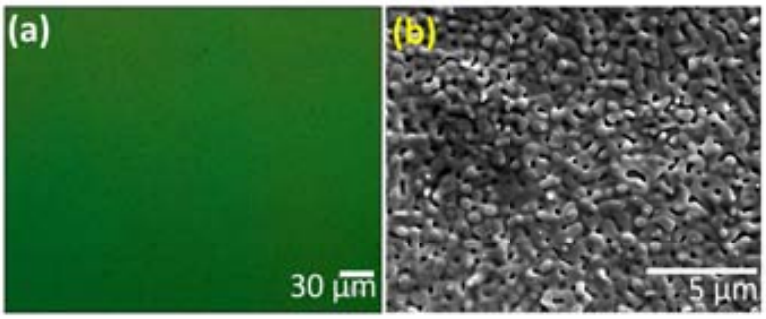


**Figure 5.35.:** Full YBCO coating inkjetted from TFA-based precursors on LAO single crystal susbstrate. (a) Optical image of the pyrolyzed film (b) SEM micrograph after the complete thermal processing. The YBCO film thickness after processing is $300nm$ giving a $J_c \sim 1.2MA/cm^2$.

#### 5.11.2.3. Structural characterization of a $\sim$300$nm$ YBCO coating

The crystalline structure of the films was analysed by X-ray diffraction techniques: GADDS [213], $\theta - 2\theta$ scan, $\omega$-scan and $\varphi$-scan. The achievement of an epitaxial growth is evidenced by the absence of polycrystalline rings in the 2D-XRD pattern obtained by GADDS (Fig. 5.36a). In Fig. 5.36b, YBCO is nearly phase pure and only (00l) reflections are observed coherently with a c-axis aligned YBCO. Fig. 5.36c and d show in detail the X-ray texture results obtained from YBCO $\omega$- and $\varphi$—scans for the analysed film. The high crystalline perfection of the YBCO is demonstrated by the rocking curve value, $\Delta\omega$=0.6°, measured on the (005) YBCO reflection. Moreover, this film also shows a good in-plane texture confirmed by the $\varphi$-scan of (103) YBCO peak= 1.5°, Fig. 5.36d. They revealed a

very good epitaxial texturing. The orientation relations are YBCO(00l)||LAO(h00) and YBCO[00l]||LAO[00l].

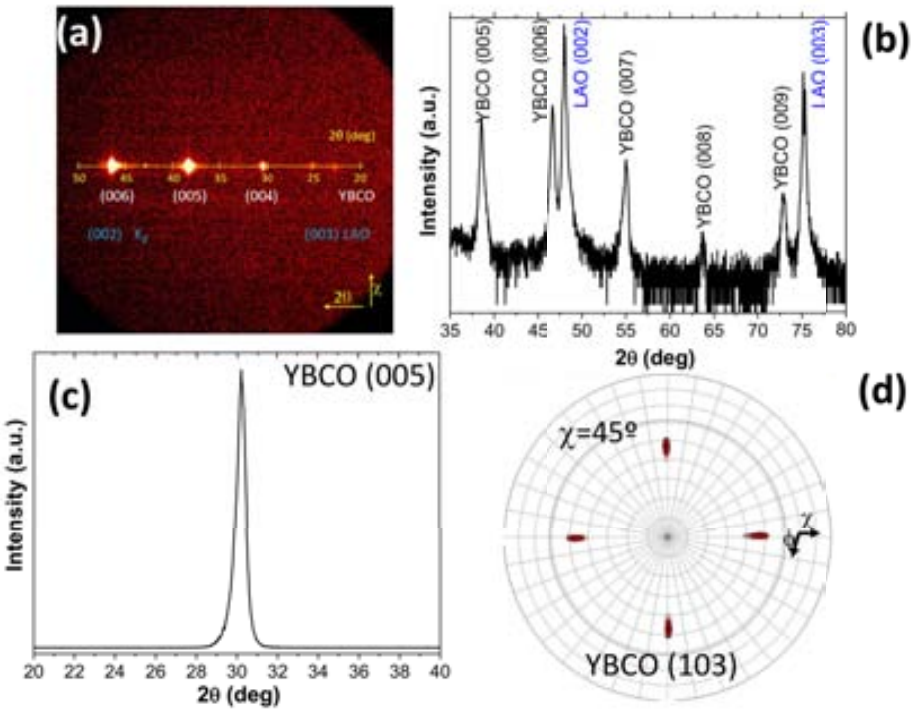


**Figure 5.36.:** Structural XRD characterization of a $300nm$ YBCO coating. (a) XRD pattern (2D detector). (b) $\theta - 2\theta$ XRD diffraction pattern both showing a c-axis oriented YBCO growth where only the (00l) reflections are present. (c) $\omega$-scan of the (005) YBCO reflection with FWHM$\sim$0.6º and (d) Pole figure of the $(103)_{YBCO}$ reflection confirming the cube-on-cube epitaxial relationship. The $\varphi$-scan of the (103) YBCO reflection provides a FWHM$\sim$1.5º.

#### 5.11.2.4. Superconducting properties of a $\sim$300$nm$ YBCO coating

Now we will turn our interest to the superconducting properties of the YBCO film analysed with a SQUID magnetometer. In Fig. 5.37a we present a typical measurement of the critical current density $J_c$ as a function of temperature at zero applied magnetic field for the $300nm$ superconducting coating. The magnetic moment has been measured in the remanent state of the superconducting layer and $J_c$ values have been obtained from the magnetic moment applying the Bean Critical State model [214].Fig. 5.37b represents a typical measurement of the magnetic moment as a function of the applied magnetic field along the c-axis at 5K for the previous superconducting film. From the results of these figures, several comments are in order. First, the high critical current densities ($J_c$(sf, 5 K)$\sim$21 MA/cm$^2$ and $J_c$(sf, 77 K)$\sim$3 MA/cm$^2$) indicate that the YBCO layer is of good quality, evidencing the compatibility of the TFA route with the inkjet printing methodology. Moreover, the critical temperature ($T_c$; the T where the magnetization starts to drop off) was determined by inductive measurements. $\Delta T_c$ was determined using the criterion: $\Delta T_c = T(0.9M_{max} - 0.1M_{max})$ where $|M_{max}|$ is the maximum magnetization. As it is observed in Fig. 5.37c, the film shows a sharp transition and a good $T_c$ value of (90.3 $\pm$ 4.8) K.

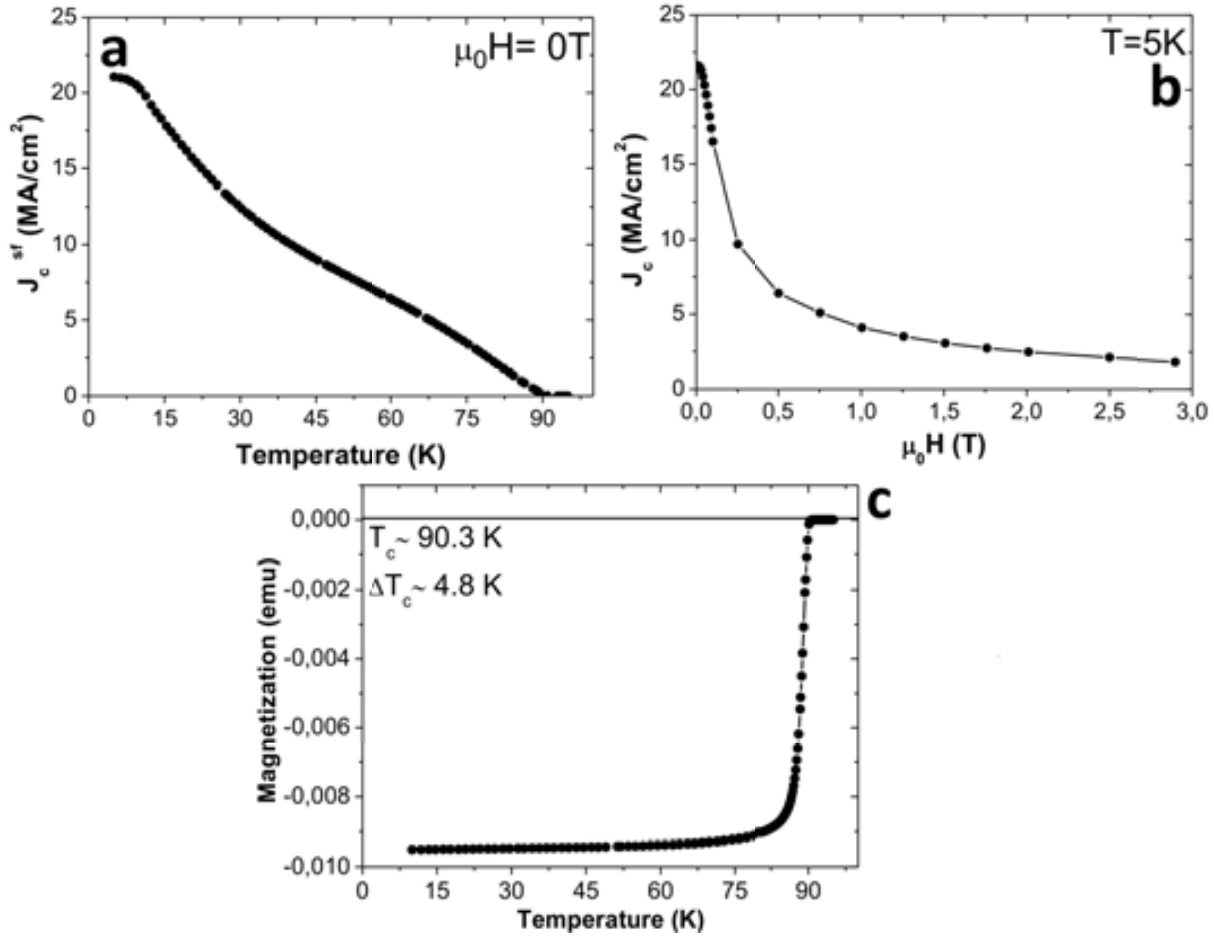


**Figure 5.37.:** Superconducting measurements performed on the 300 nm YBCO/LAO sample. (a) Temperature dependence of the critical current density (b) Magnetic field dependence of the critical current density and (c) ZFC for the 300 nm YBCO coating studied.

### 5.11.3. Film thickness tuning by inkjet printing

For any application of YBCO coatings on coated conductors, it is essential to select deposition techniques which allow an accurate control of the film thickness. In the spin coating and dip coating processes, film thickness is regulated through solution concentration as well as, introducing suitable additives in the precursor solution to adjust ink viscosity or performing multideposition processes with separate intermediate pyrolysis steps in between.

In this sense, one of the advantages to exploit of the inkjet printing technology is that an easy control of the film thickness may be achieved by adjusting the number of drops per unit area [109].

In this study, YBCO films were inkjet printed as a function of the dot pitch to build up different film thickness. The printed solution was a 0.5M EtOH based YBCO precursor solution. The plot of measured thickness versus number of drops per unit area is shown in Fig. 5.38. The line with empty dots corresponds to the film thickness after pyrolysis process and the one with solid dots after the YBCO film growth. Referring to Fig. 5.38, it

is clear that film thickness can be easily controlled by modifying the number of drops per unit area in terms of drop pitch. Assuming constant drop pitch in both print directions, the number of jetted drops per unit area in printed films is inversely proportional to this constant drop spacing value squared. Therefore, the measured thickness increases monotonically as drop spacing decreases and droplet density increases.

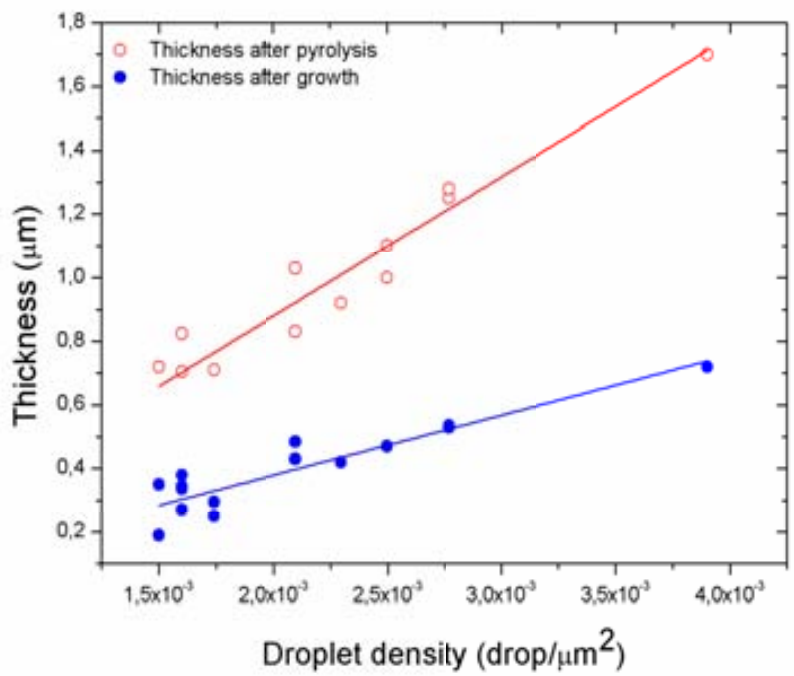


**Figure 5.38.:** Film thickness as a function of droplet density by using a 0.5M ethanol based YBCO precursor solution. The empty red dots correspond to the film thickness after pyrolysis process, the solid blue marks correspond to the film thickness after the YBCO film growth process assuming a drop volume $V_{drop}$~30 pL.

Due to the fact that the whole volume of solution dispensed during the printing process is used to cover the sample, it is easy to predict the thickness of the deposited layers. Considering $V_d$ the drop volume ($\mu m^3$), $\nu$ the number of drops per unit area (drop/$\mu m^2$), $c$ the total metals concentration (M) in the starting precursor solution, $c_b$ the concentration of metals (M) in the ceramic bulk (single crystal), $c_p$ the concentration of metals (M) in the resulting film after pyrolysis, $c_g$ the concentration of metals (M) in the as-grown ceramic film, $\tau_b$ the hypothetic thickness of the coating layer assumed as non porous bulk ($\mu m$), $\tau_p$ the thickness of the film after pyrolysis process ($\mu m$) and $\tau_g$ the thickness of the film after growth process ($\mu m$), it is possible to deduce the thickness of the coating layers in any case considering the droplet volume $V_d$ and the number of drops per unit area $\nu$:

$$\tau_i = \frac{V_d\, c\, \nu}{c_i} \qquad i \,\epsilon\, \{b, p, g\} \tag{5.3}$$

According to 5.3, the thickness of the layer $\tau_i$ depends linearly on the number of drops

per unit area $\nu$, as shown in Fig. 5.38. The slope $s_i$ of each straight line allows computing the compacting degree, $c/c_i$, of the corresponding layer from the volume of the drop $V_d$:

$$\frac{c}{c_i} = \frac{s_i}{V_d} \quad i \epsilon \{b, p, g\} \tag{5.4}$$

Therefore, combining equation 5.3 and equation 5.4, the thickness $\tau_i$ of each layer could be obtained by the expression:

$$\tau_i = s_i \nu \quad i \epsilon \{b, p, g\} \tag{5.5}$$

The slopes of the plots shown in Fig. 5.38 were obtained by linear fitting of the experimental data points. The obtained values were: $s_p$=439.1$\mu m^3$/drop, $s_g$= 189.3$\mu m^3$/drop giving compacting rates of about 2.3 from pyrolysis to growth.

With the previous operational printing parameters and the standard YBCO growth described in chapter 3, up to 600$nm$ thick homogeneous and c-axis oriented YBCO coatings have been obtained by inkjet printing on LAO single crystal. In what follows, a fully characterization of a 600$nm$ YBCO coating on LAO substrate is displayed. The YBCO precursor solution used in the test was the mentioned 0.5M EtOH based YBCO precursor solution. To activate the piezoelement, the driving parameters employed are the ones detailed in Tab. 5.22. The number of drops per unit area in that test was $2.8 \cdot 10^{-3}$ drops/$\mu m^2$.

#### 5.11.3.1. Morphological characterization of a ∼600$nm$ YBCO coating

Optical microscopy images after pyrolysis process exhibit a homogeneous and crack-free surface. An example of those images is shown in Fig. 5.39a. Moreover, it is worth mentioning that the YBCO film is predominantly c-axis grain oriented indicated by the flat surface with the typical hills and holes shown in the SEM micrograph as expected in a c-axis oriented YBCO.

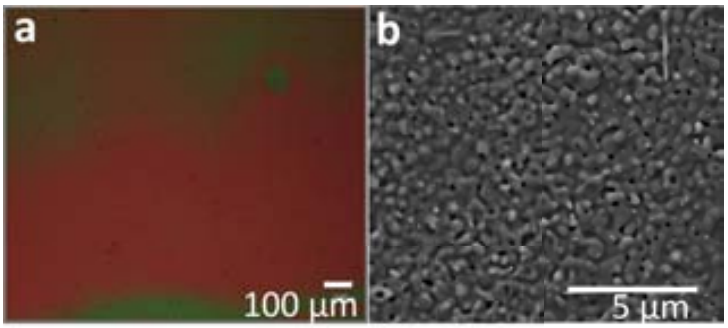


**Figure 5.39.:** General overview of the resulting surface of the sample after pyrolysis process. (a) Optical image of the resulting surface after pyrolysis process at 310ºC. A crack-free layer is obtained after the low decomposition process. (b) SEM micrograph of the ∼600 nm YBCO film. The surface morphology is relatively smooth, but pores, precipitates and few *ab* grains are visible.

### 5.11.3.2. Structural characterization of a ∼600$nm$ YBCO coating

The absence of polycrystalline rings in the GADDS pattern confirms an epitaxial YBCO growth (Fig. 5.40a). In Fig. 5.40b, (00l) reflections are observed coherently with a c-axis oriented YBCO together with small amounts of OF as shoulder from the (001) LAO peak and a weak peak of BYF at 41.1°. It indicates an incomplete precursor conversion [5, 279]. It is important to remark that the growth conditions have to be optimizied for these thicker coatings to avoid these precursors phases and obtain a fully YBCO conversion. Whereas the coexistance of both (00l) YBCO reflections with some small quantitites of precursor phases, the epitaxial quality of the YBCO film is also corroborated by the rocking curve value, ($\triangle\omega \sim 0.7°$), measured on the (005) YBCO reflection and the $\varphi$-scan of the (103) YBCO reflection ∼1.6°, Fig. 5.40d. We can observe from these results that the final in-plane YBCO texture maintains that of the underlying substrate.

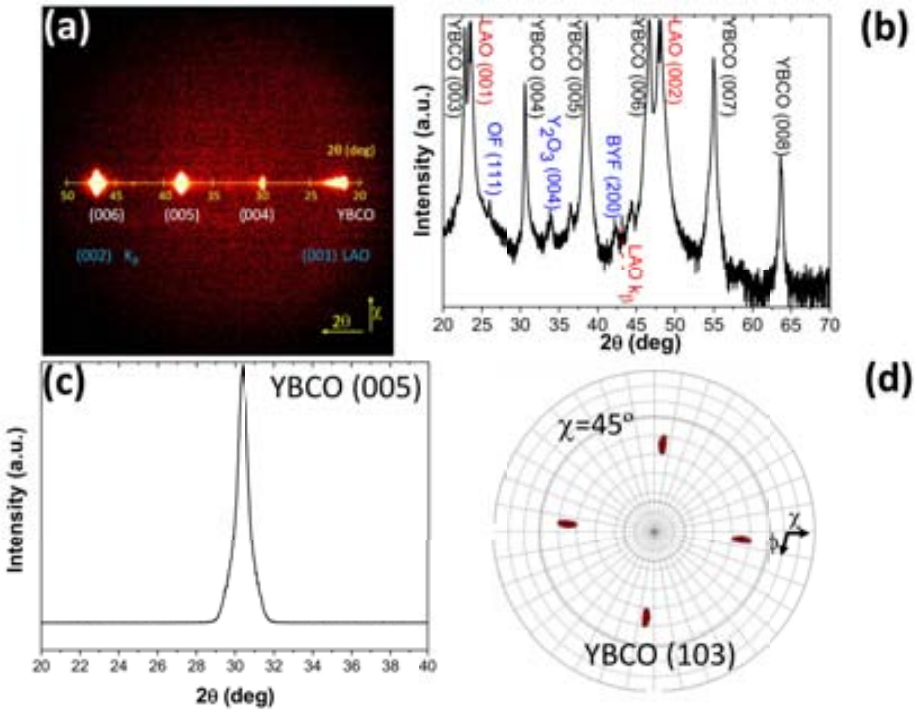


**Figure 5.40.:** Structural XRD characterization of a 600$nm$ YBCO coating. (a) XRD pattern (2D detector). (b) $\theta - 2\theta$ XRD diffraction pattern both showing a c-axis oriented YBCO growth where only the (00l) reflections are present. (c) $\omega$-scan of the (005) YBCO reflection with FWHM∼0.7º and (d) Pole figure of the $(103)_{YBCO}$ reflection confirming the cube-on-cube epitaxial relationship. The $\varphi$-scan of the (103) YBCO reflection provides a FWHM∼1.6º.

### 5.11.3.3. Superconducting properties of a∼600$nm$ YBCO coating

The superconducting properties of the YBCO layer are displayed in next Fig. 5.41. Fig. 5.41a shows the temperature dependence of the critical current density for the previous YBCO film. The magnetic field dependence of the critical current density for this sample is shown inFig. 5.41b. The $J_c$(sf, 5 K)∼10 MA/cm$^2$ and $J_c$(sf, 77 K)∼1.2 MA/cm$^2$ indicates that CSD can lead to epitaxial thick films with relative high critical current densities. The YBCO coating shows a good $T_c$ (∼ 90.8 K) and a transition $\triangle T_c \sim 5K$.

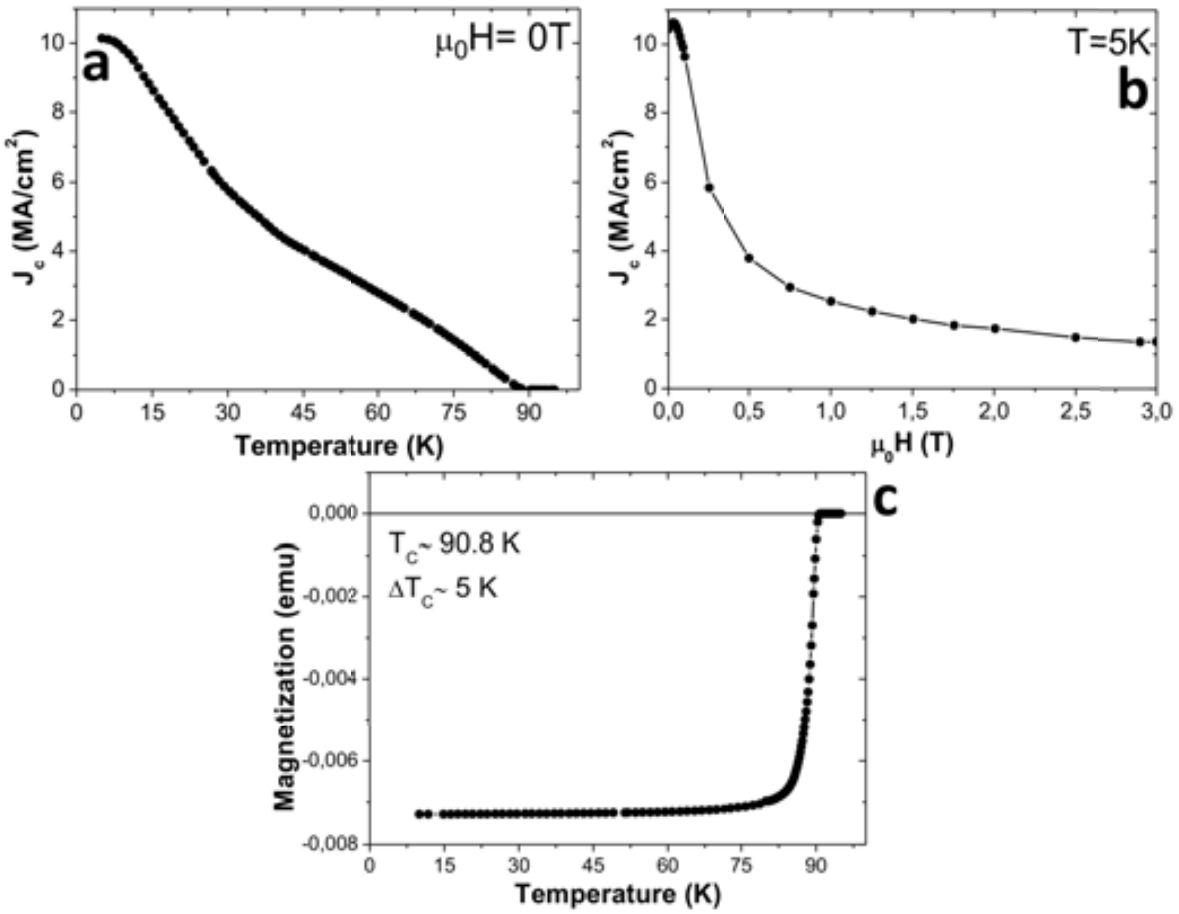


**Figure 5.41.:** Superconducting measurements performed on the 600 nm YBCO/LAO sample. (a) $J_c$ as a function of temperature (b) $J_c$ as a function of the magnetic field. (c) Temperature dependence on the magnetization (ZFC).

Both XRD characterization and $J_c$ dependence upon temperature and magnetic field are very sensible magnitudes that reflect the film microstructure. The presence of small precursors phases together with the larger misorientation in and out of plane obtained for the thicker sample agrees well with the smaller computed $J_c$ at 77K and self field. Moreover, if the thicker samples are more porous than the thinner ones, it also can be a limiting factor from the point of view of the flowing current. All these joint of factors, together with some additional optimization of the deposition and/or growth processes are still required to improve the superconducting properties of those thicker films.

To summarize, the inkjet printing of continuous layers on LAO single crystal substrates has been demonstrated by the overlapping of tracks which results in continuous layers once drop pitch is adjusted from $19\mu m$ to $27\mu m$.

### 5.11.4. Multinozzle Dimatix printer

Several tests were also performed with the Dimatix multinozzle printer DMP-2800. By playing with the number of active nozzles and drop spacing, continuous and homogeneous YBCO coatings from $150nm$ to $250nm$ were achieved. The electrical signal that triggered the drop ejection in the following tests is presented in the image below (Fig. 5.42):

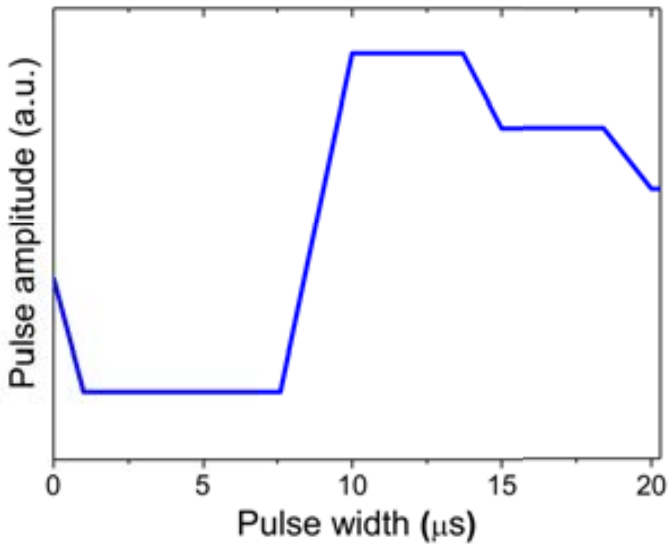


**Figure 5.42.:** Typical signal single pulse waveform used for the 0.5M ethanol based solution using the Dimatix printer.

Next Tab. 5.23 shows the data of the variables that were adjusted to obtain the YBCO coatings by means of the Dimatix printer. In this section we only present the example of three coatings varying the number of active nozzles during the printing and the drop pitch. The other variables were fixed at the optimum value considered during their screening. The substrate temperature was increased a little bit to favour evaporation solvent but not too much to avoid sudden evaporation and volcano formation.

| Sample | A | B | C |
|---|---|---|---|
| Number of active nozzles | 2 | 3 | 6 |
| Drop spacing ($\mu m$) | 15 | 13 | 13 |
| Substrate temperature (° C) | 35 | 35 | 35 |
| Cartridge temperature (° C) | RT | RT | RT |
| Firing frequency ($KHz$) | 5 | 5 | 5 |
| Number of depositions | 1 | 1 | 1 |

**Table 5.23.:** Experimental printing conditions used to achieve continuous coatings by using the Dimatix printer DMP2800. The YBCO precursor ink was a 0.5M ethanol based YBCO precursor solution.

Fig. 5.43 depicts the morphological characterization of the previous inkjetted samples after deposition (row a1-c1), after pyrolysis process (row a2-c2) and after YBCO growth

process (from a3 to c3) on LAO single crystal by using a 0.5M ethanol based YBCO precursor solution.

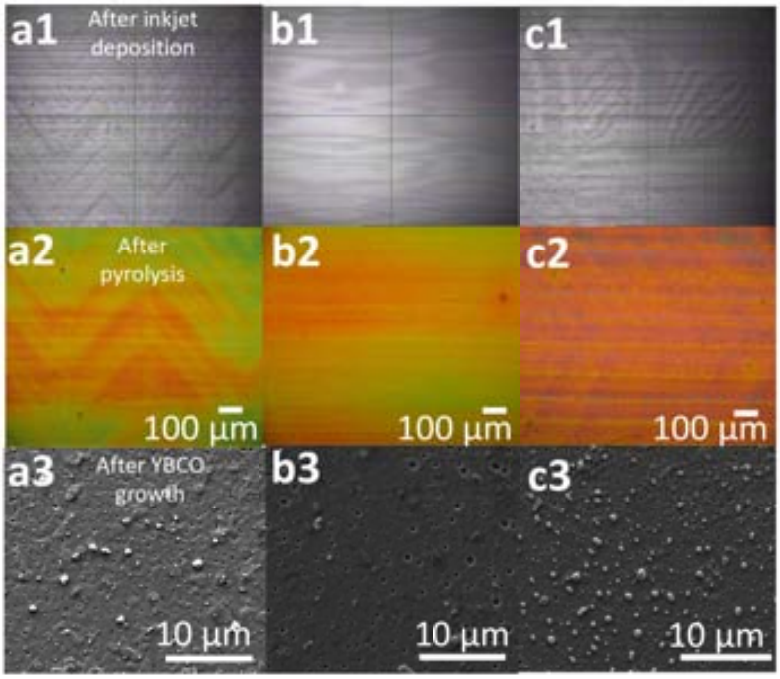


**Figure 5.43.:** Morphological characterization by OM and SEM of the coatings obtained by using the Dimatix multinozzle printer. The ink used was a 0.5M ethanol based YBCO precursor solution and LAO (5x5) mm single crystals were used as substrates. Simultaneously, different nozzles were used in each case: (a) 2 nozzles. (b) 3 nozzles and (c) 6 nozzles. The first row corresponds to the optical images after inkjet deposition, the second serie after pyrolysis process and the third one after complete YBCO growth.

The first row of Fig. 5.43 provides inspection of the printed pattern immediately after ink deposition. These images were taken by the fiducial camera that disposes the printer. The second line corresponds to the central region of the coatings after pyrolysis process at 310°C. Those images were taken by optical microscopy. Finally, the third line displays the morphology obtained by SEM where the typical terraced surface with some precipitates confirms an epitaxial YBCO growth. It may be appreciatted that no *ab* grains and a remarkably low degree of porosity are observed in the samples of Fig. 5.43.

To obtain the critical current density of the samples ($J_c$), profilometric measurements were performed in order to determine their thickness. The computed thickness for the anterior samples and the corresponding $J_c$ values achieved by inductive measurements are shown in Tab. 5.24:

| **Sample** | **A** | **B** | **C** |
|---|---|---|---|
| Thickness after YBCO growth ($nm$) | ∼150 | ∼180 | ∼250 |
| $J_c$ (at self field and 77K) ($MA/cm^2$) | 4.8 | 2.8 | 3 |

**Table 5.24.:** Profilometric and inductive $J_c$ measurements for the coatings obtained by using the Dimatix printer.

As an example, only the structural and superconducting characterization for sample A is detailed in the following lines.

Structural characterization based on XRD[2](Fig. 5.44a) have pointed out that YBCO film has grown according to the epitaxial relation (001)YBCO[110]||(001)LAO[100]. The XRD $\theta$-$2\theta$ scan yields to stronger (00l) peaks indicating the high quality of the film. The structural characterization was further studied by out-of-plane $\omega$-scan and in-plane $\varphi$-scan measurements (Fig. 5.44c and d) revealing the excellent texture of the ceramic film obtained.

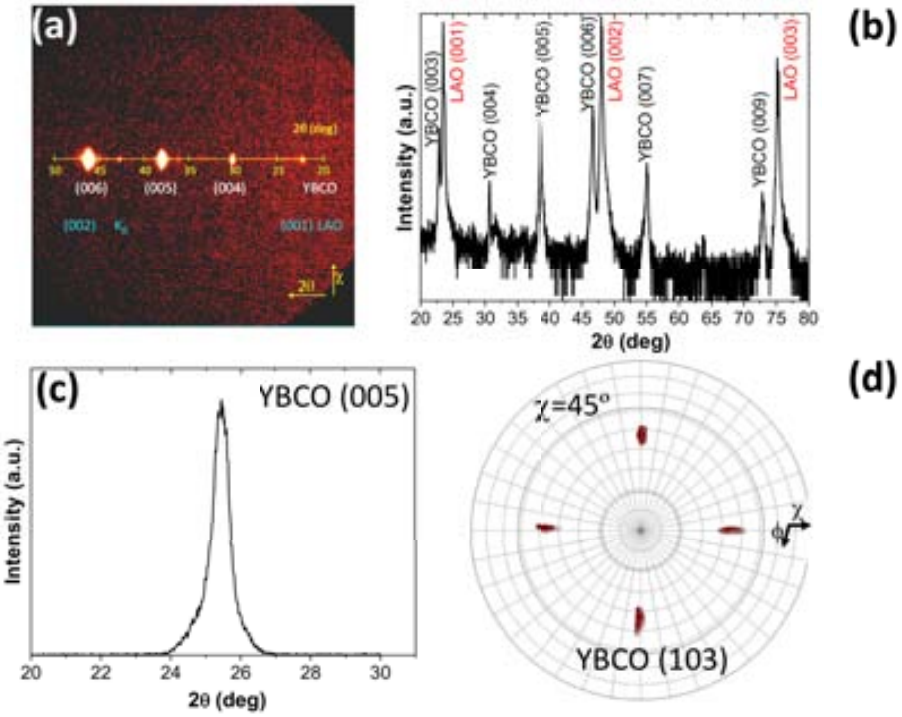


**Figure 5.44.:** Structural XRD characterization of a 150$nm$ YBCO coating printed used the Dimatix printer. (a) XRD pattern (2D detector). (b) $\theta - 2\theta$ XRD diffraction pattern both showing a c-axis oriented YBCO growth where only the (00l) reflections are present. (c) $\omega$-scan of the (005) YBCO reflection with FWHM$\sim$0.6º and (d) Pole figure of the $(103)_{YBCO}$ reflection confirming the cube-on-cube epitaxial relationship. The $\varphi$-scan of the (103) YBCO reflection provides a FWHM$\sim$1.5º.

In Fig. 5.45a we present the typical $J_c$ dependence with the temperature at zero applied magnetic field. Fig. 5.45b displays the $J_c$ dependence upon the magnetic field applied parallel to (00l) YBCO axis at 5K. In Fig. 5.45c we present the typical measurement of the magnetic moment as a function of temperature at zero applied magnetic field for sample A. From the ZFC (Fig. 5.45c) we observed that this film presents a $T_c$ of 89.6 K being well consistent with the high $J_c$ disclosed in Fig. 5.45a ($J_c$(sf, 77 K)$\sim$4.8 MA/cm$^2$; $J_c$(sf, 5 K)$\sim$ 41 MA/cm$^2$ ).

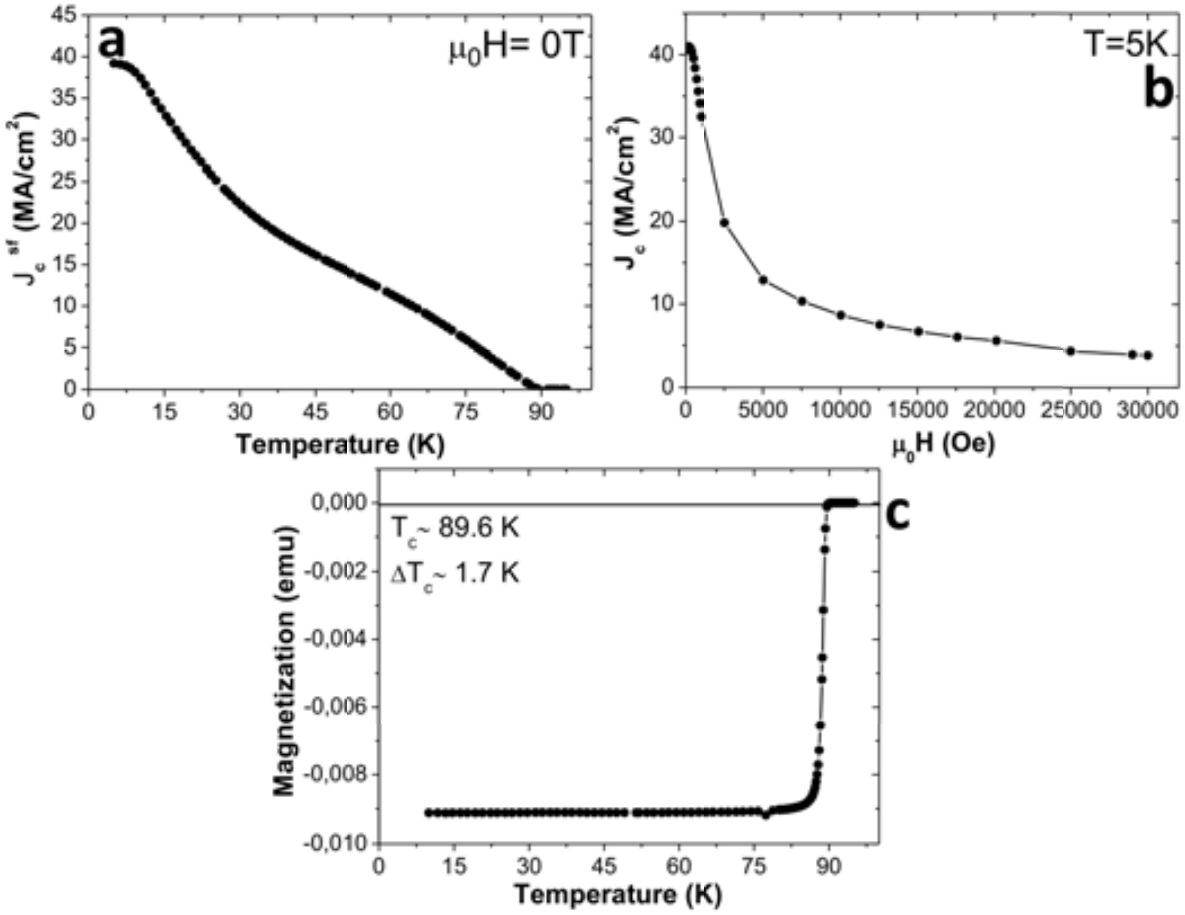


**Figure 5.45.:** Superconducting characterization of sample A. (a) $J_c$ dependence versus temperature at zero applied magnetic field. (b) $J_c$ as function of the magnetic field applied along c-axis. (c) Standard measurement of magnetization cooling the sample at zero field (ZFC).

## 5.12. Printing of single YBCO layers on metallic substrates: preliminary results

As mentioned in the introductory chapter, high quality long length coated conductors require of a flexible textured tape-shaped template on which is deposited the epitaxial superconducting film. The fundamental concept of using a textured template with an epitaxial HTS gave birth to the 2G HTS wire technology (see sec. 1.4.2). Also, the quality of the surface of these metallic substrates, such as cleanliness, planarity [106], roughness and bending plays a significant role for the buffer and YBCO growth. For that reason, the first step to be performed when printing onto metallic tapes is the fully characterization of these as-received tapes, which covers from a morphological analysis (presence of voids, cracks, etc. on their surface) to a structural characterization. A very important parameter, the surface planarity, quantifies the % of flat terraces existing on the surface and determines the success in obtaining a c-axis oriented YBCO growth. It has been set that this planarity must be at least larger than 70% for obtaining well-textured YBCO

coatings [106].

Preliminary studies of YBCO inkjet printing over metallic tapes started similarly that the ones on LAO single crystal, by adjusting drop pitch to assure drop overlap (see Fig. 5.46).

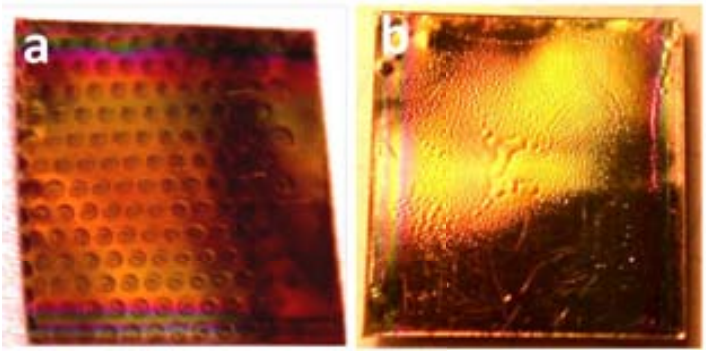


**Figure 5.46.:** Drop pitch adjustment over an all solution coated conductor: $^{MOD}CeO_2/^{MOD}LZO/^{RABIT}$Ni-W coated conductor from Zenergy Power GmbH, now Deutsche Nanoschicht GmbH. Drop pitch was decreased from 140$\mu m$ in (a) to 20$\mu m$ in (b).

The YBCO precursor ink was deposited onto an all-solution coated conductor with the following buffered architecture: $^{MOD}CeO_2/^{MOD}LZO/^{RABIT}$Ni-W from Zenergy Power GmbH (Rheinbach, Germany). Since the goal of this study was to obtain continuous and homogeneous coatings on metallic buffered substrates, the starting YBCO precursor solution we employed was the last ink ejected for YBCO growth on single crystals: the 0.5M ethanol based YBCO precursor solution and the actuating parameters used to drive the piezoelement are the ones displayed in Tab. 5.22.

In next lines, it is presented the morphological, structural and superconducting characterization of an YBCO coating over a metallic tape.

#### 5.12.0.1. Morphological characterization

The morphology of the YBCO coating deposited on $^{MOD}CeO_2/^{MOD}LZO/^{RABIT}$ Ni-W buffer architecture after pyrolysis and growth processes is displayed in Fig. 5.47. Fig. 5.47a corresponds to the whole surface view after pyrolysis process. Fig. 5.47b is an optical microscopy zoomed image of the central region of the sample after pyrolysis. Some scratches coming from the blank tape, apart from some pores and dust, may be appreciated. SEM micrographs (Fig. 5.47c) indicate that no *ab* grains are formed on the surface of the substrate, although some precipitates may be noticed.

#### 5.12.0.2. Structural characterization

Fig. 5.48 shows the structural characterization by means of XRD of the previous YBCO film studied.

As can be observed in figure Fig. 5.48a, at $2\theta \sim 19.3^{\circ}$ and $2\theta \sim 37.2^{\circ}$ it is detected the $NiWO_4$ phase. Although this CC architecture contains a double LZO and a thinner

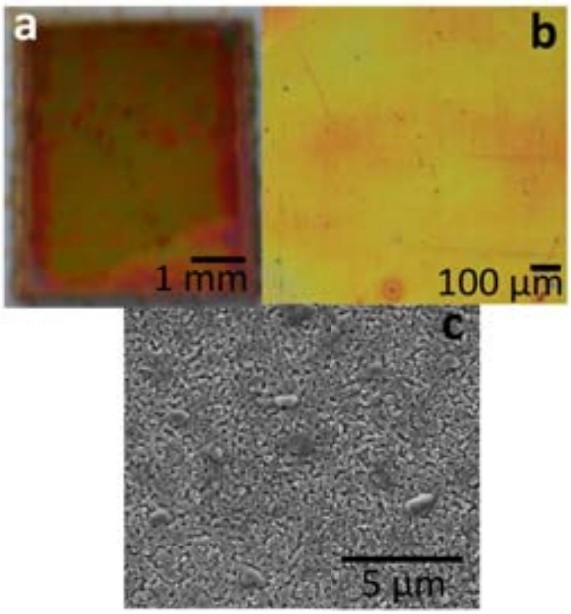


**Figure 5.47.:** Morphological characterization of a $^{MOD}$YBCO/$^{MOD}$$CeO_2$/$^{MOD}$LZO/$^{RABIT}$Ni-W coated conductor (a) General view of a (6x4)$mm$ precursor YBCO coating after pyrolysis process. (b) Zoomed optical image of the central part of the sample presented in (a). (c) SEM planar morphology of the previous sample. A compact YBCO surface with a very low degree of porosity is shown in this SEM micrograph. No *ab* grains are observed on the surface of the YBCO coating.

$CeO_2$ buffer layers which act as chemical barriers and prevent oxygen diffusion down to the substrate, Ni substrate is oxidized, thus, further optimization of the YBCO growth process is necessary in order to avoid the metal oxidation. In fact, an intense research in our research group at ICMAB is continuing in this field. However, in spite of the chemical reactivity between Ni and oxygen coming from the growth atmosphere, an epitaxial YBCO growth has been obtained as may be observed in both Fig. 5.48a and Fig. 5.48b. From the XRD pattern, $BaCeO_3$ is detected with two different orientations (100) and (110). This confirms chemical reactivity in the interface between YBCO and CZO [280]. Special precaution must take into account in order to avoid the oxidation of the bare metal substrate and the reactivity between YBCO and $CeO_2$ to form $BaCeO_3$ because is a critical parameter to $J_c$ properties [281]. Indeed, the presence of large amounts of $BaCeO_3$ in YBCO/$CeO_2$ interface has also been reported by other authors [282].

#### 5.12.0.3. Superconducting characterization

With regard to the superconducting properties, we can note a decrease of the $J_c$ for the YBCO on $^{MOD}$$CeO_2$/$^{MOD}$LZO/$^{RABIT}$Ni-W compared with the YBCO on LAO single crystal of the same thickness ($3.2MA/cm^2$ vs $0.7MA/cm^2$ at $77K$ and self field). Here we suggest that the strong reduction of the total flat area of the $CeO_2$ cap layer in the coated conductor (ideally from ∼99.9%) of planarity of the single crystal to ∼31 % of planarity ($^{MOD}$$CeO_2$ of the CC) leads to a non-planar interface with the YBCO phase which enhances granularity of the YBCO layer of the CC providing misorientated grain boundaries). Further work is now underway in order to improve superconducting

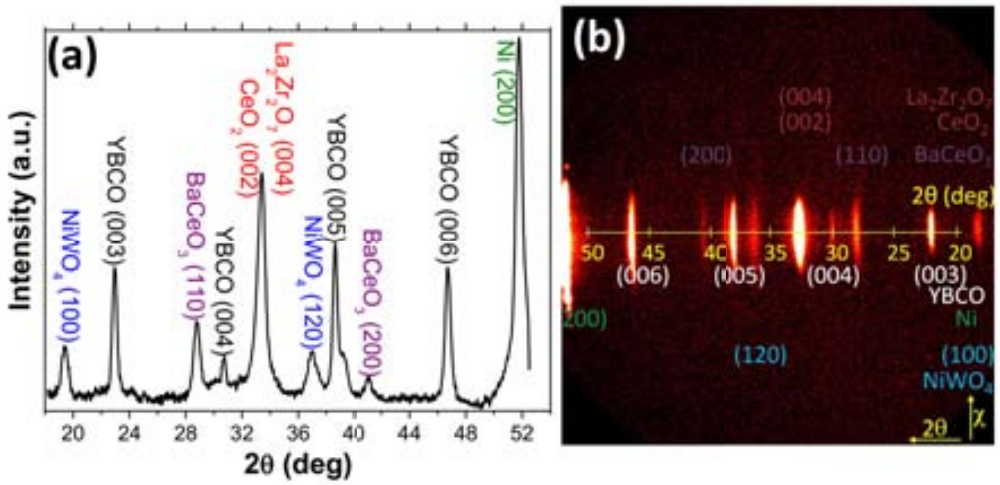


**Figure 5.48.:** Structural characterization of the $^{MOD}$YBCO/$^{MOD}$CeO$_2$/$^{MOD}$LZO/$^{RABIT}$Ni-W coated conductor. (a) XRD $\theta$-$2\theta$ scan and (b) 2D-XRD pattern of the previous $^{MOD}$YBCO/$^{MOD}$CeO$_2$/$^{MOD}$LZO/$^{RABIT}$Ni-W coated conductor.

performances of these CC. In the case of this CC, the $T_c$ onset was found to be $87K$. For the samples grown on metallic substrates we observe a broaden transition width when inductive measurements are performed. This broadening may be ascribed to the low current percolation in some regions of the sample due to the presence of grain boundaries.

However, recent results in our research group demonstrate the feasibility to obtain by inkjet printing $\sim 800nm$ YBCO coatings on commercial $^{PLD}$CeO$_2$/$^{ABAD}$YSZ/SS metallic tapes but optimization of the pyrolysis heating process is ongoing in order to improved the superconducting performances.

## 5.13. Summary and conclusions

In the second part of this chapter, we have demonstrated the feasibility of growing epitaxial YBCO ceramic coatings on LAO single crystal using different types of DoD dispensers by proper adjustements of rheological and wetting parameters of CSD-YBCO precursor solutions and also by controlling the amount of volume ejected. The control of the physicochemical ink properties has been shown to be a crucial point to overcome the ink dynamics when impinging onto the substrate, the ink-substrate interaction and consequently to guide the final film morphology. Among the solutions tested, the inks constituted of ethanol proved to be the most appropriate to obtain homogeneous coatings. Moreover, selecting a proper drop pitch which assures drop overlap before evaporation and solidification is another key factor to obtain continous YBCO films.

Critical currents as high as $3MA/cm^2$ at $77K$ and self field were reached in films deposited onto LAO substrates with $400nm$ thickness, while in films up to $600nm$, $J_c$ decreases to $1.2MA/cm^2$ at $77K$ and self field, thus showing that there exists some room for improvement of the deposition and/or growth of these films. It demostrates that performances of CSD-inkjet printed films are comparable to those obtained by the conventional

spin coating technique. We would like to remark that an all-sol gel coated conductor $^{MOD}$YBCO/$^{MOD}$$CeO_2$/$^{MOD}$LZO/ Ni has been grown by inkjet printing but significant degradation of $J_c$ ($J_c$(77K and self field) $0.7MA \cdot cm^{-2}$) is observed. This reduction can be directly related to the reduced total flat area. Further work in this field is ongoing in order to optimize both the inkjet deposition and YBCO growth processes.

Moreover, our work stresses that by adjusting the number of drops per unit area, film thickness can be varied in a controlled way, as the thickness depends linearly on the number of drops per unit area. Also, compacting rates along the steps of the heating treatments can be computed by determining the slopes of the corresponding linear dependences being the results repeatable for different tested batches and experiments. It is worth to stress that larger film thickness might also be achieved by enhancing the solution concentration or through multideposition process.

Different YBCO coatings were prepared by means of a multinozzle commercial printer by tailoring the number of active nozzles during the inkjet printing process and drop pitch. YBCO coatings from $150nm$ to $250nm$ were achieved with a $J_c$ as high as $4.8MA/cm^2$ at $77K$ and self field.

# 6. Drop-substrate interaction: the $La_{0.7}Sr_{0.3}MnO_3$ case

Taking into account that one of the goals of the thesis is to explore different flexible and cost-effective production systems based on inkjet printing, this chapter is focused on the obtention of ferromagnetic $La_{0.7}Sr_{0.3}MnO_3$ layers and patterns by inkjet using solvent and water based inks [283], taking special attention to the formulation of environmental friendly LSMO precursor solutions. In the following sections, the experimental sequence and strategies to obtain those coatings will be briefly described. The characterization of the LSMO films and patterns will then be deeply displayed. Moreover, different strategies for LSMO device manufacturing will be discussed and the corresponding pattern characterization shown. Finally, it will be shown the great potential of the available substrates for coated conductors technology for LSMO magnetoresistive device manufacturing.

## 6.1. $La_{0.7}Sr_{0.3}MnO_3$ coatings: printing of single layers

## 6.2. Printing of single LSMO layers on single crystal

LSMO full layers and patterned coatings were produced, all of them were shown to be electrically conductive with resistances in the range of 10–100 kΩ as expected for LSMO phase. According to the drop pitch, it is possible to obtain continuous layers with thickness that depend on the substrate, the concentration of the solution, and the number of drops per unit area. Adequate overlapping of drops should be obtained by adjusting drop volume, the ink used to print and the desired final thickness. For the growth of LSMO, we followed the steps detailed in sec. 3.4.3 of chapter 3. In brief, the LSMO precursor solution is inkjet printed over the substrate. Then, the subsequent annealing step was performed in a high temperature furnace in air, at 900°C and 5h. Identical processing conditions were applied independent of the LSMO precursor used. Before the LSMO growth, the susbtrates were heat-treated according to the standard procedure described in chapter 3.

## 6.3. LSMO ink development

As a first step and based on the previous experience existing in our research group at ICMAB for LSMO growth of films and nanoestructures [284], two approaches were initially chosen for growing LSMO epitaxial coatings on single crystal substrates:

- The first approach, named '*all-propionate route*', was described by Hasenkox et al [285]. Briefly, stoichiometric amounts of metal propionates were mixed and dissolved in a large excess of propionic acid under *RT* conditions.
- The second contemplated approach, called from now on, '*all-acetate route*', starts from the metal acetates in water [286, 287]. Stoichiometric amounts of metal acetates were mixed, and different stabilizers and modifiers introduced, in order to control the wetting, rheology and stability of the solution.

### 6.3.1. First approach: 'all-propionate route'

The first ink development approach for LSMO coatings was based on the work developed in the research group [284,288]. An initial 0.3M solution concentration, with respect to Mn, based on Mn, La and Sr propionates, was prepared and further diluted ten times down to 0.03M. The relevant ink physicochemical properties of this 0.03M propionate based LSMO precursor solution are given in next Tab. 6.1:

| | **0.03M propionate based LSMO precursor solution** |
|---|---|
| Density $\rho$ $(g/cm^3)$ | 0.990 |
| Surface tension $\gamma$ $(mN/m)$ | 22 |
| Viscosity $\eta$ $(mPa \cdot s)$ | 1 |

**Table 6.1.:** Relevant physicochemical properties of the 0.03M propionate based LSMO precursor solution. All the measurements were performed at room temperature. Viscosity measurement was carried out at $100s^{-1}$.

The solution remains stable and clear for almost one month storage. Having a look to those parameters, we would expect that the preceding rheological and wetting properties lead to homogeneous coatings since surface tension and viscosity are specially small, which should favour the full coverage of the surface.

#### 6.3.1.1. Single nozzle electromagnetic printhead

The previous solution was dispensed by means of the single electromagnetic dispenser. As in the YBCO case, drop size was adjusted in order to work with the minimum drop pitch which allow us a continuous ink distribution over the single crystal substrate. Optimum drop pitch was set at $0.15mm$ that with drops of about $300\mu m$ in diameter and taking into account that the contact angle of this ink with the substrate is $<10°$, it leads to a full coverage of the substrate. The best results were found for a voltage of $23.5V$ and an opening time of $550\mu s$ for which a drop volume of around $50nL$ was obtained. The printing conditions that allow full coverage of the surface of the substrate are exhibited in next Tab. 6.2:

| Solution | 0.03M propionates based LSMO precursor solution |
|---|---|
| Valve opening time ($\mu s$) | 550 |
| Valve opening voltage ($V$) | 23.5 |
| Valve opening pressure ($bar$) | 0.6 |
| Drop pitch ($mm$) | 0.15 |

**Table 6.2.:** Jetting parameters for the 0.03M propionate based LSMO precursor solution to obtain a continuous coating by using the electromagnetic printhead onto a (10x10) $mm$ LAO substrate. Only one drop pitch is presented because a squared printing matrix was used.

Fig. 6.1 shows the optical images of the so-obtained LSMO coating after thermal treatment. Fig. 6.1a corresponds to a one-layer LSMO coating, while Fig. 6.1b is a two-layer LSMO coating where the second deposition was performed on top of the first after being thermally treated at 900°C.

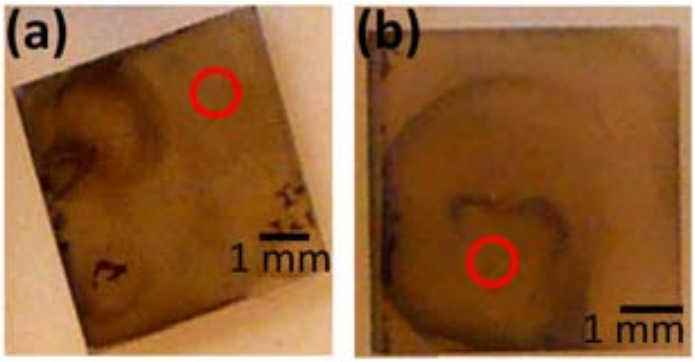


**Figure 6.1.:** Optical images of the LSMO coatings after the thermal treatment exposed in Fig. 3.9 and using a 0.03M propionate based LSMO precursor solution. (a) one-layer LSMO coating (b) two-layers LSMO coating. The second coating was deposited over the first one previously deposited and thermally treated.

After the thermal treatment, the LSMO coatings do not exhibit a homogeneous thickness as can be observed in Fig. 6.1, where dark (i.e. thicker) and colourless regions are both present in the samples. The so-obtained coatings show a typical drying pattern consisting in a series of rings that originate from the inhomogeneity in surface energy when drying [269].

To avoid this pattern, one possible solution may be the increase of ink viscosity to decrease the ink flowing.

SEM images of the red circled regions shown in figure Fig. 6.1 were performed and are displayed in Fig. 6.2:

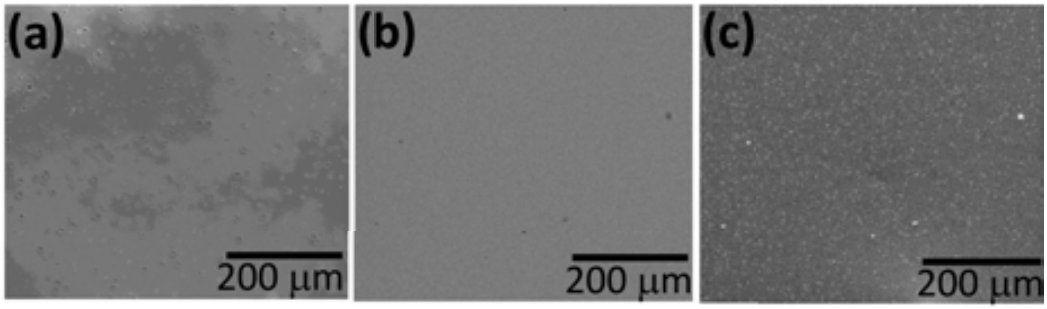


**Figure 6.2.:** SEM images of the LSMO coatings obtained by inkjet printing a propionate based LSMO precursor solution. (a) corresponds to the one-layer LSMO coating. (b) and (c) to the two-layers LSMO coating.

Fig. 6.2a corresponds to a SEM image of the red circled region of the one-layer LSMO coating. In the final microestructure, after LSMO formation, it can be appreciated the formation of some holes attributed to regions that suffer strong stresses during drying and thermal processing.

SEM micrographies corresponding to the framed region marked in the optical image of the two-layer LSMO coating are exemplified in Fig. 6.2b and Fig. 6.2c. Once more, the latter sample alternates flat regions which reveals the typical morphology for a granular manganite layer with other rougher regions and particular configurations that display small grains or even holes. We believe that the lack of film thickness homogeneity could be attributed to the mobility of the fluid before the propionic acid completely dries due to its relative high boiling point ($T_{bp} \sim 141°C$).

Further studies to improve the rheology of the 0.03M propionate based LSMO precursor solution were developed. A set of aliquots was taken in order to add systematically ethyleneglycol (EG) in proportions of 10%, 20% and 30% by volume (v/v). Then, each sample was heated until 40°C, 60°C and 100°C during $4h$ and then rheological tests were carried out. The criterion used to select EG to increase ink viscosity was its relatively high viscosity (16 $mPa \cdot s$ at RT), good miscibility with propionic acid in the studied proportions and the successful previous printing research undergone with the electromagnetic printhead with this additive.

No difference within the error range in the viscosity was detected between the samples with the same EG content, thus indicating that no polimerization process is expected, being indicative of the ink stability. Thus, the solution with a content in EG of 30% by volume was selected to continue with the ink optimization process. Next stage was to evaluate the surface tension. These values at ambient conditions were $\sim 33 mN/m$ for all the samples with a 30% of EG. Since the previous experience with YBCO unveils that it may difficult the obtention of an homogeneous coating, with such large value of surface tension, it was decided to introduce a tensioactive into the ink formulation. Different standard tensioactives were extensively studied. Finally the non-ionic surfactant Triton X-114 was the selected one due to the efficiency reported in the literature [289, 290].

Different tests varying the amount of surfactant Triton X-114 from 0.15% to 1.7% in volume were conducted to check how surface tension decreases as surfactant concentration increases. Surface tension values of the inks with the extreme quantities of surfactant

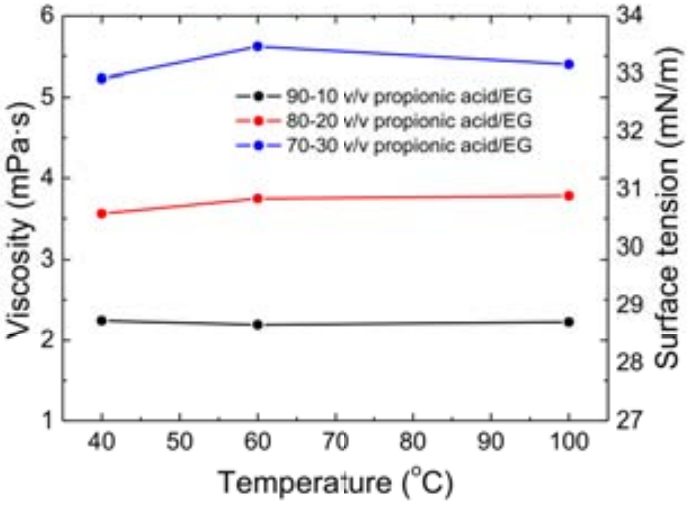


**Figure 6.3.:** Ink viscosity as function of temperature applied during 4h to the 0.03M propionate based LSMO precursor solution with different proportions of EG.

range from $22.3 mN/m$ to 29 $mN/m$. Contact angle measurements on LAO substrate after the standard thermal treatment of this 0.03M propionate based solution with the different doses of surfactant as received and after the standard treatment gave values below 10°, i.e. the solution perfectly wets the substrate.

Hence, the addition of the surfactant allows diminishing the surface tension, and therefore, the contact angle without altering the value of the viscosity. The lowest surface tension value achieved was for the solution with a 1.7% in volume of Triton X-114 which shows a surface tension of about 22.3 $mN/m$, together with the low fluency provided by the EG, seem adequate to obtain homogeneous and large surface coating.

The main characterization of the LSMO film grown from a 0.03M (in Mn) propionate based LSMO precursor ink rheologically corrected is examined in the following section.

#### 6.3.1.2. Epitaxial relationship, microstructure and electric transport properties

To be able to identify the LSMO structure, we conducted $\theta - 2\theta$, 2D-XRD experiments, and SEM analysis. Fig. 6.4a and Fig. 6.4b show, respectively, the XRD intensity profile obtained from the standard diffractometer and the 2D-GADDS pattern of the LSMO coating grown from a 0.03M ink in Mn.

Since $\theta - 2\theta$ scans of the film gives no peaks other than the (00l) LSMO, we can deduce that the LSMO grows epitaxially on LAO, i.e (001)LSMO[100]||(001)LAO[100], which we attribute this fact to the low mismatch between LAO and LSMO cell parameters. The results of the $\theta - 2\theta$ scan also indicate a fully relaxed film, where the LSMO has its bulk lattice value ($a_{LSMO}$~3.873Å) slightly shrinked in-plane in order to match the LAO lattice parameter ($a_{LAO}$~3.79Å). It is expected that such LSMO coating should be fully relaxed given their thickness ($\sim 300nm$). Furthermore, the addition of surfactant does not modifies the diffraction pattern which repeat the same peak distribution than without surfactant addition.

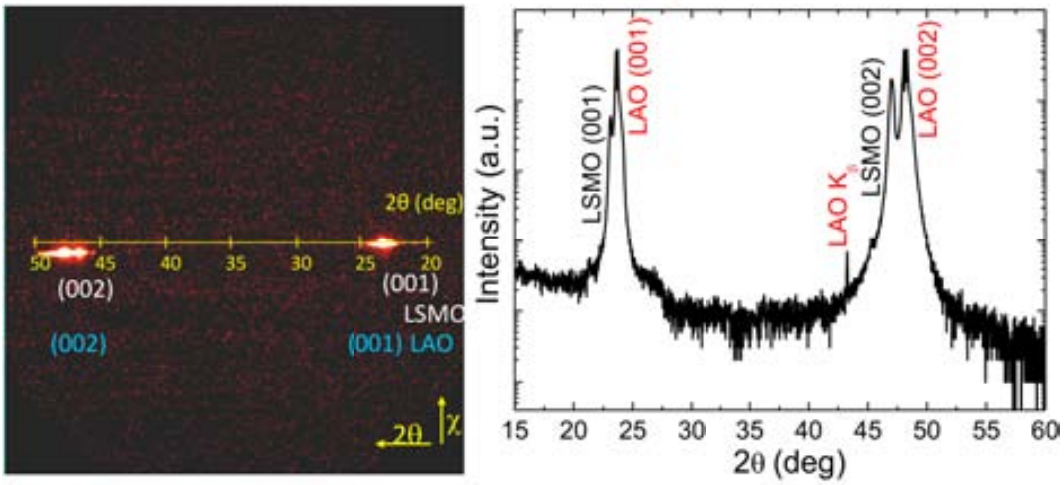


**Figure 6.4.:** (a) 2D-XRD pattern and (b) standard XRD pattern of the LSMO coating obtained from a 0.03M propionate based LSMO precursor solution with a 1.7% v/v of surfactant Triton X-114 and 30% in volume of EG.

Besides single deposition processes, multideposition processes have been also performed. A double coating was obtained by first jetting an initial layer and next, depositing an additional layer on top after a heating process at 900°C. The layer obtained is also epitaxial (not shown in the document) [179] and the increase in amplitude of the LSMO XRD peaks is in correspondence with the increasing thickness. The so-obtained epitaxial layers show ferromagnetic behavior corresponding to the LSMO ceramic crystals. Conductance tests were also carried out showing higher conductivity which agrees well with the higher thickness of the double LSMO coating. Isothermal magnetization analysis show that magnetic moment scales with the thickness of the sample.

Fig. 6.5a displays the microstructure of the LSMO continuous coating on LAO single crystal substrate obtained by jetting the propionate based ink for evaluation of coating characteristics, thickness and uniformity. The SEM image displayed in the previous Fig. 6.5a was taken by tilting the setup 60°, which gives a thickness of the layer in the range of about $300nm$. Moreover, it may also be appreciated the low porosity of the coating so-obtained.

In addition, electric transport measurements of the CSD-inkjet printed LSMO film were also investigated. The temperature dependence of resistivity, $\rho(T)$, in Fig. 6.5b, was measured in the standard four-probe geometry using a physical properties measurement system (PPMS, Quantum Design) showing the metal behaviour expected for the LSMO films.

The metal-insulator transition is not perceived since the analysis was stopped before achieving the Curie temperature ($T_c \sim 360K$). Thus, summarizing, the developed propionate based LSMO precursor solution with surfactant and rheologically controlled, allow us to grown single and double LSMO coatings with a cube on cube orientation. Besides the stability of the solution was tested for at least one month giving satisfactory results, opening the possibility to scale solution batches.

Although the use of a propionate based LSMO precursor ink was shown as a promising

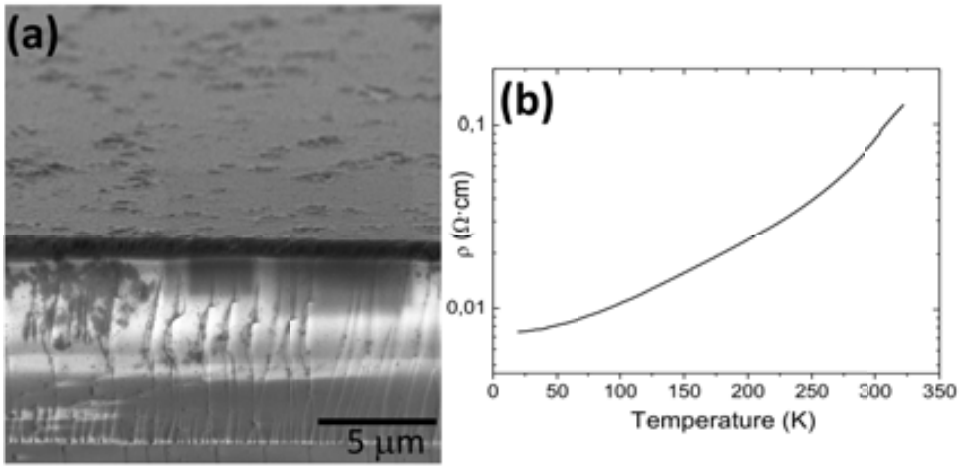


**Figure 6.5.:** (a) SEM micrography of a LSMO coating on LAO single crystal substrate using the EM printhead and a propionate based LSMO precursor ink with a 1.7% by volume of surfactant and 30% in volume of EG. The cross section image was obtained by tilting the setup 60°(b) Temperature dependence of the resistivity for the studied LSMO coating.

route regarding LSMO full coatings, an alternative and greener way which avoids the use of organic acids was considered.

## 6.3.2. Second approach:'all-acetate route'

### 6.3.2.1. Ink optimization

A more environmental friendly system based on the acetate salts was prepared by dissolving separately the corresponding Mn, La and Sr acetates in mili-Q water at ambient conditions. Since the resultant water based LSMO precursor ink has a very large surface tension ($\gamma$ $\sim$72$mN/m$) and, therefore contact angle ($\theta$ $\sim$90°), we would not expect a good coverage and spreading onto the substrate. In this understanding, as the aim of this section is to produce full and continuous LSMO coatings, intense efforts were put for wetting and rheological adjustements.

First attempt consisted of dissolving the metallic acetates in the minimum amount of mili-Q water and then control the rheological and wetting properties of the ink and adjusting the final concentration with a solution 90% ethanol 10% water in volume. It was possible to reduce surface tension and contact angle to proper values for wetting, but the solution was not stable for more than few hours, which make the inkjet printing deposition not possible. To solve this problem, it was considered the idea to introduce into the ink formulation with the rheological solution 90% ethanol 10% water (v/v), a chelating agent in order to stabilize the precursor metallic ions. The first tested chelating agent was the citric acid. If its addition (i.e. addition rate and stirring speed) were not properly controlled, the solution becomes unstable and the precipitation of the metallic citrates takes place. As this weak point affects tremendously the repetitivity and scalability of the ink, some attempts were performed in order to redissolve this gel. The introduction of acidificant agents was done. An excess of citric acid and controlled amounts of a HCl:$H_2O$

(1:1) solution (10% in volume) causes the immediate redissolution of the precipitate, obtaining a transparent and colourless solution.

Since the previous solution was stable only for a few days, the next proof to increase solution stability was change the chelating agents for the different metallic acetates. Tartaric acid was also tested giving successful results, however, the ink stability was greatly increased when Sr and La acetate salts were separately dissolved in water containing glycine and Mn acetate was dissolved also in water with ethylenediaminetetraacetic acid (EDTA) in substitution of the citric acid. After homogenization, the three metallic acetates were mixed and the rheological ethanol/water 90/10 v/v solution with an adequate amount of $PEG_{20000}$ were finally introduced for rheological adjustements. Other combinations of the rheological solution ethanol/$H_2O$/$PEG_{20000}$ such as ethanol/$H_2O$/polyvinilpyrrolidone (PVP)/dietilamine, polyethyleneimine (PEI), PVP with diethanolamine and PEI with diethylamine were also tested providing rheological and wetting parameters very similar without improving significantly the printing results.

Very long term stability improvements for the more environmental friendly acetates based LSMO precursor solutions was one issue specially considered. Basically, the main concern is the contact with air that oxidize the Mn metal. The previous as-prepared acetate based LSMO precursor solution hermetically sealed under Ar with their proper packing were stable for more than two months.

Two acetate based LSMO precursor solutions using glycine and EDTA as chelating agents with a 0.01M and 0.04M concentrations in Mn were prepared following the protocol described in sec. 3.1.2.2. For these 0.04M and 0.01M in Mn, the relevant rheological and wetting properties are summarized in Tab. 6.3:

| | **0.04M (in Mn) acetate based LSMO precursor solution** | **0.01M (in Mn) acetate based LSMO precursor solution** |
|---|---|---|
| Density $\rho$ $(g/cm^3)$ | 0.917 | 0.873 |
| Surface tension $\gamma$ $(mN/m)$ | 25.3 | 24 |
| Viscosity $\eta$ $(mPa \cdot s)$ | 3.2 | 1.6 |

**Table 6.3.:** Relevant physicochemical parameters for the 0.04M and 0.01M acetate based LSMO precursor solutions. In those cases, the chelating agents were glycine and EDTA and the concentration and rheology were adjusted using a solution based on EtOH/$H_2O$/$PEG_{20000}$. All the measurements were performed at room temperature. Viscosity measurement was carried out at a shear rate of 100 $s^{-1}$.

The contact angles $\theta$ of these inks onto LAO single crystal substrate were lower than 10°.

#### 6.3.2.2. Single nozzle electromagnetic printhead

LSMO coatings from those solutions were successfully obtained by means of the electromagnetic printhead. In next lines a fully characterization of one of these LSMO layers obtained from the 0.04M precursor solution (average thickness $\sim 30nm$) is extensively presented.

The printing parameters employed to obtain the LSMO film are depicted in the following Tab. 6.4:

| **Solution** | **0.04M (in Mn) acetate based LSMO precursor solution** |
|---|---|
| Valve opening time ($\mu s$) | 550 |
| Valve opening voltage ($V$) | 26 |
| Ink pressure ($bar$) | 0.6 |
| Drop pitch ($mm$) | 0.3 |

**Table 6.4.:** Printing parameters for the 0.04M acetate based LSMO precursor solution to obtain a continuous coating by using the electromagnetic printhead onto a (5x5) $mm$ LAO substrate. Only one drop pitch is presented because a squared printing matrix was used.

#### 6.3.2.3. Morphological characterization

The morphology of a LSMO film grown on LAO substrate from a 0.04M acetate based precursor solution is shown in Fig. 6.6:

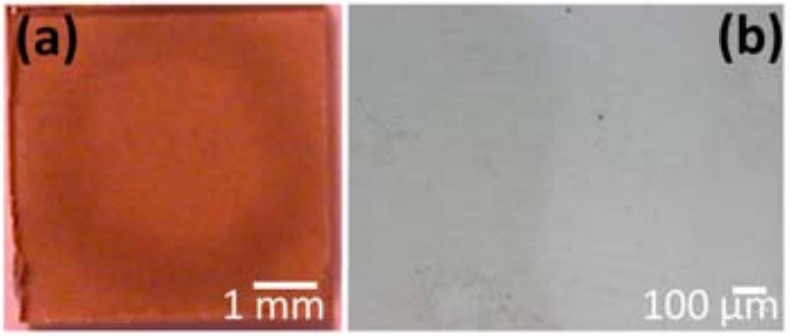


**Figure 6.6.:** (a) General view and (b) optical image of the central part of the LSMO coating obtained from the precursor solution with 0.04M in Mn on a (5x5)$mm$ LAO. A continuous and homogeneous film without discontinuities is obtained.

In Fig. 6.6 is manifested the quality of the inkjetted LSMO coating. Fig. 6.6a exhibits the general look of the full coating on LAO while Fig. 6.6b corresponds to a zoomed image of the central part of the coating presented in (a). In both figures, it may be appreciated that a continuous and homogeneous LSMO layer without defects is achieved. Similar results were obtained for the coating printed by using a 0.01M in Mn acetate LSMO percursor solution.

#### 6.3.2.4. Structural characterization

As in all the previous samples, $\theta - 2\theta$ XRD experiments were conducted to identify the LSMO structure. Fig. 6.7 shows the $\theta - 2\theta$ XRD profile for two different samples: two

LSMO layers obtained from 0.04M and 0.01M acetate LSMO precursor solutions. From Fig. 6.7, no peaks other than (00l) were present in the XRD pattern, demonstrating the films are single phase and in good epitaxy, i.e (001) LSMO‖(001) LAO. Moreover, it can be noticed that for the sample with 0.01M concentration (average thickness$\sim 12nm$), $\theta-2\theta$ XRD measurement was unable to resolve the LSMO peaks. The main difficulties stem from the small amount of material (which yields to low signals) and from the fact that the susbtrate peaks, very intense, fall next to the LSMO peaks. The structural comparison provides the same results than in the case of the LSMO coatings from propionate precursor solutions.

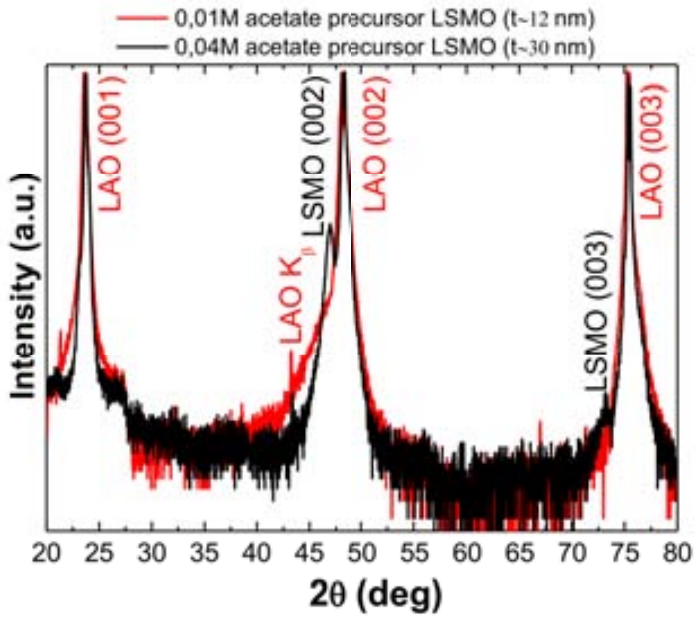


**Figure 6.7.:** Comparison of the $\theta - 2\theta$ XRD measurements done for two different samples: two LSMO films grown out of 0.01M and 0.04M acetate precursor solutions.

#### 6.3.2.5. Macroscopic magnetic and magnetotransport characterization

We now move to the study of the magnetic and transport properties of the 0.04M LSMO film decribed above. Magnetic measurements were done using a superconducting quantum device magnetometer (SQUID) at temperatures from 5 to 300K and varying magnetic fields from 0 to 7T. Fig. 6.8 shows the resulting isothermal magnetization loops (after substracting the magnetization of the bare substrate) at 10K and 300K for the 0.04M precursor solution coating. The LSMO coatings grown on LAO and annealed at 900°C during 5h showed ferromagnetic hysteresis up to room temperature (RT). Those results are in agreement with the expected ones for this ceramic as reported elsewhere [89]. At 10K and 300K, the saturation magnetic moments for the 0.04M LSMO film were $m_s \sim 2 \cdot 10^{-4} emu$ and $m_s \sim 1 \cdot 10^{-4} emu$, respectively.

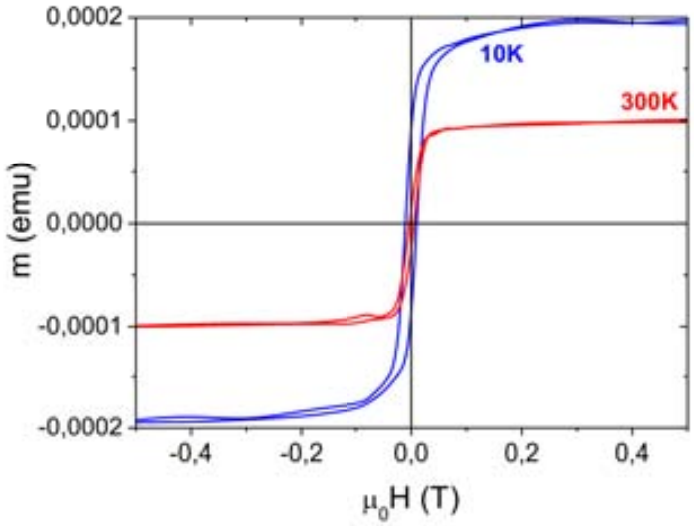


**Figure 6.8.:** Magnetization loops at 10K and 300K for the 0.04M (average thickness$\sim 30nm$) LSMO acetate based layers. The 0.04M LSMO film displays saturation magnetizations of about $m_s \sim 2 \cdot 10^{-4} emu$ at $10K$ and $m_s \sim 1 \cdot 10^{-4} emu$ at $300K$, which corresponds to volumetric magnetizations $M_S \sim 266.7 emu/cm^3$, $M_S \sim 133.3 emu/cm^3$ respectively as deduced from film thickness.

With this data it is possible to calculate the total volume of material from the thickness value assuming an homogeneous distribution throughout the whole (5x5)$mm$ substrate. Also, the remanence value is $m_r \sim 9 \cdot 10^{-5} emu$ and $2 \cdot 10^{-5} emu$, and the cohercitive field $\mu_0 H_c \sim 0.01$T and 0.004T at 10K and 300K, respectively. The magnetization loop of a 0.01M LSMO film on LAO measured under the same conditions than the previous presented, reveals lower saturation magnetization and higher cohercitive values, according to the lower precursor concentration.

After LSMO growth, conductance tests were performed to this sample at random points showing all of them conductivity. The conductivity value for the 0.04M LSMO ranges between $20K\Omega$ and $60K\Omega$.

The magnetoresistance MR, defined as $-MR = R(H = 0) - R(H)/R(H = 0)$ (in %), of the LSMO film (0.04M acetate precursor solution) grown on LAO is plotted in Fig. 6.9b. The left panel shows the temperature dependence of the resistance from where the MR curve is calculated (right panel). The temperature dependence of resistance of the LSMO film shows that is metallic from 370K to low temperatures, being the metal-insulator transition temperature ($T_p$) of this sample about 370K, comparable to that of LSMO bulk value and consistent with other reports [80, 91, 291].

For zero applied magnetic field, this LSMO film shows the maximum resistivity value of $\rho \sim 9.7 \cdot 10^{-3} \Omega \cdot cm$ (average thickness measured by profilometry $\sim$30 nm). This number is of the same order of magnitude than the maximum resistivity value $\rho \sim 1.4 \cdot 10^{-3} \Omega \cdot cm$ obtained for CSD-derived LSMO 0.3M films (thickness$\sim$25 nm) that exhibit magneto-transport properties comparable to LSMO bulk [90]. Regarding magnetoresistance values, 0.04M film shows a maximum MR of $\sim$30% on LAO, which is 2.7 times higher than the usual MR value registered for the aforementioned bulk-like LSMO thin films (MR$\sim$11%) [292]. The sharpest MR curve corresponds to a temperature very close to $T_c$

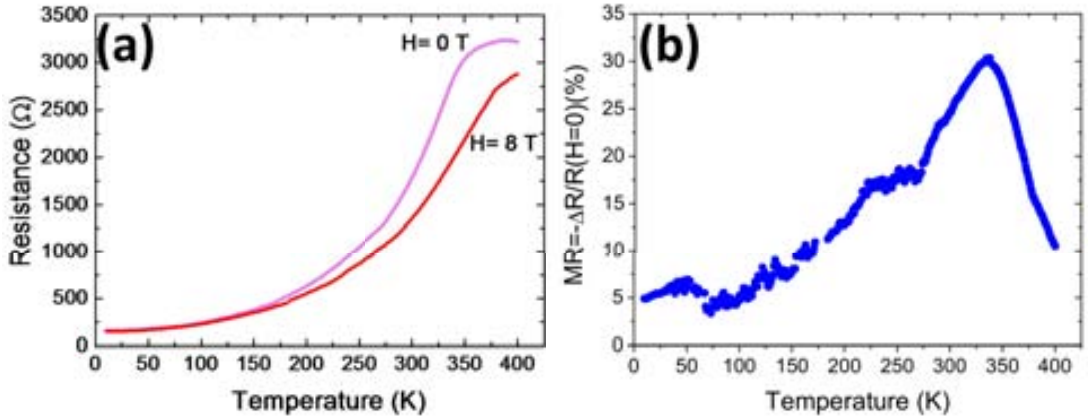


**Figure 6.9.:** Magnetoresistance of a 0.04M acetate based chemically grown LSMO layer. The left panel (a) shows the resistance dependence with temperature at zero applied magnetic field (upper magenta line) and at H=8T (lower red line), applied perpendicular to the film. The right panel (b) shows the magnetoresistance, MR, defned as $-MR = [R(H = 0) - R(H = 8T)]/R(H = 0)$ (in %).

and so the above studied LSMO/film display the most appealing performances for real applications.

Therefore, to summarize, an effort was made to develop this alternative LSMO precursors which are more environmental benign. This is certainly a remarkable aspect if we consider that the 'propionate route' uses propionic acid as solvent, which may cause the progressive corrosion of the printhead. LSMO precursor inks starting from acetates precursor salts were optimized to obtain, after a proper rheological control, epitaxial LSMO coatings with good morphological, structural and magnetic properties.

## 6.4. Summary and conclusions

Two systems based on propionate and acetate precursors were investigated and used as LSMO precursors from LSMO coating. Rheology of the solutions was studied in order to achieve a good stability, jettability and adequate interaction with the substrate by adding suitable surfactants and viscosity modifiers. Coatings were performed by means of the electromagnetic printhead from a 0.03M (in Mn) propionate based and 0.04M (in Mn) acetate based LSMO precursor inks. After the corresponding thermal treatment for LSMO growth, XRD patterns obtained are compatible with epitaxial growth. Furthermore, isothermal magnetization and magnetoresistive behaviour of the samples is coincident with that expected for the LSMO bulk system. Magnetoresistive coefficients of about 30% were obtained at T above room temperature. Although further ink adaptations to improve ink stability are required, concerning acetate based LSMO precursors inks, medium scale reproduction of 1L has been successful.

## 6.5. $La_{0.7}Sr_{0.3}MnO_3$ patterns

### State of the art

Within the last years, solution-processable electronics have centered great consideration and research. Inkjet printing of metal precursor inks has been accepted for the manufacturing of microelectronics applications, including conducting wiring for circuitry [293] and radio frequency identification (RFID) tags [294], organic thin-film transistors (TFT's or OFET's) [22, 295], organic light emitting diodes (OLEDs) [296], organic photovoltaics disposable displays and sensor arrays [297].

When simple additive processing is implemented in a continuous reel to reel system with novel low-cost materials, the potential to further decrease the production costs of integrated microelectronics, especially compared to those for the established silicon processing, is immense.

For instance, representative images of inkjet-printed features from state-of-the-art works in the literature [271] are included in Fig. 6.10.

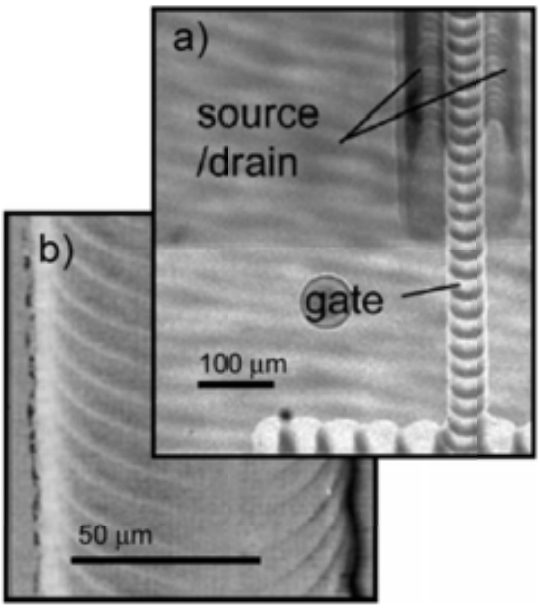


**Figure 6.10.:** (a) and (b) Micrographs of inkjet-printed TFT with pedot contacts [271].

In both (a) and (b) cases, we see that in order to create a straight line, smoothness was sacrificed. In printed integrated electronics, the various roles of the electrically active materials lead to different engineering constrictions. For instance, in a transistor, the gate line must be as narrow and smooth as possible, however, the source and drain need smooth edges with a controlled separation but their width is less significant. Otherwise, to mention another example, for organic LEDs, smoothness and film uniformity are crucial for achieving uniform emission.

## $La_{0.7}Sr_{0.3}MnO_3$ patterning on single crystal

In next sections, we will review the potential of inkjet printing to the deployment of functional devices and its contribution to the large scale manufacturing of those devices.

In our case, the starting point towards functional devices began by using the electromagnetic printhead and a 0.04M acetate based LSMO precursor solution by printing a patterned layer of independent drops on LAO single crystal (see Fig. 6.11). In this case, to draw that pattern, drop pitch was set at $650\mu m$.

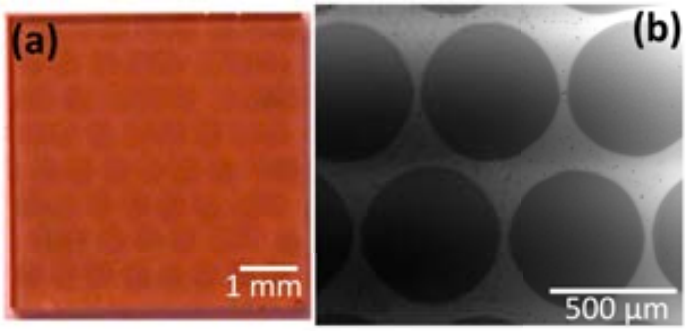


**Figure 6.11.:** (a) General top view of a patterned dotted LSMO sample by employing the EM printhead and a 0.04M acetate based LSMO precursor solution. Drop pitch was the same in the horizontal and vertical directions (∼650 $\mu m$). (b) SEM micrograph where drop size can be easily appreciated (drop diameter ∼550 $\mu m$).

In Fig. 6.11b, drop size is clearly visible (drop diameter was around∼$550\mu m$), reflecting the high wettability of the ink with the substrate. Dot thickness in this case was in the range of $50nm$, approximately six-fold thinner than the case depicted in Fig. 6.5 where drop overlapping increases the amount of material for coatings in a similar ratio. In order to obtain thicker drops than those shown in Fig. 6.11 it is necessary to increase the solution concentration or, otherwise, increase the ink surface tension to decrease the spreading of the individual drops.

In the same way, LSMO epitaxial lines have also been obtained with similar results (not shown herein). In both cases, drop and track structures are well observed. Different set of experiments were done in order to control the dimensions of both, drops and tracks, and go to narrower features. First observations pointed out to move to the piezoelectric printhead to obtain lower drop volumes and control, in such a way, drop spreading.

Summing up, in the precedings sections, it has been demonstrated that LSMO coatings might be obtained by means of the electromagnetic printhead. Since we are interested on finner features for magnetoresistive device manufacturing, we decide to replace from now on the EM dispenser for the piezoelectric one due to the possibility to obtain lower drop volumes and then for its better capacity to disperse the ink on the substrate and trim the thickness by controlling the drop pitch.

## 6.6. LSMO magnetoresistive devices

In the framework of EFECTS project [298], the main goal was to get profit about the properties of the functional electroceramics for industrial applications. In this scope, a fully inkjet-printed LSMO magnetoresistive device designed as a magnetically driven analogic position encoder has been developed as an example of functional device by using the low cost and flexible inkjet technology combined with the CSD methodology. The development of greener inks for LSMO films provide us a very crucial implement for the demonstration of a fully CAD/CAM LSMO magnetoresistive device. In that understanding, in next sections, it has been printed a circular Wheatstone bridge for position encoding with branch's resistances of about $10k\Omega$. Magnetoresistance variations nearly 0.6% and 0.4T at RT are achieved by covering the LSMO path with standard Fe-B ferromagnets. Moreover, to test the reliability of the system, it was made the reproduction of the device on LAO and STO single crystals and over other polycrystalline substrates such as alumina, quartz and metallic Ni-W tape. Due to the successful results obtained in the laboratory scale, the middle up scaling of the LSMO device was performed in collaboration with the spin-off OXOLUTIA S.L. by printing a serie of 20 LSMO devices using a 512 nozzle printhead on metallic tape with a resolution of (720x1440)$dpi$ and a drop volume of $14pL$.

Basic analog sensors typically consist of variable resistors with an sliding contact. This type of mechanical contact encoders has a short life, estimated in the best cases in some tens of thousands of operations, due to the constant rubbing of the sliding part in continuous movement systems.

Digital and analog encoders can also be drawn by physical techniques such as PLD, sputtering, etc. but these techniques are hampered by their complex process technology and the need of lithography for the patterning. Screen printing with powder pastes could be another choice for patterning but each kind of sensor would require a specific screen so customizing would not be immediate and could result expensive for short series of devices. Although digital encoders are already available in the market, contactless analog encoders obtained by inkjet printing allow us to exploit the new options that offers electroceramics in combination with CSD in the sense that this technology offers a huge versatility to switch the deposited material and pattern design on the flight without printing interruption allowing a more customized manufacturing process. This enables to incorporate in the same printout both encoder and circuitry, decreasing therefore, the cost by unit. In addition, the absence of any mechanical contact that may be damaged due to friction, increases the reliability and lifetime of the device nearly 1000 times compared to the conventional carbon paths.

Essentially, positional encoders are a fundamental part in, for instance, positioning feedback systems in servomechanisms, in back-view mirrors of transports, in seat position memories, in inkjet printing encoders and in valve servoactuators to mention but a few applications.

Moreover, the use of colossal magnetoresistive materials in substitution to the sliding contact carbon film encoders allows us substantial variations in the resistance when a magnetic field is applied. It could be used, for instance, in position sensing when the magnetoresistive path is proportionally covered by a magnet.

Taking into account the mentioned feasibility of inkjet printing to make patterns, it was decided to print a LSMO magnetoresistive device, as an example. In that understanding, the manufacturing of the whole LSMO magnetoresistive device would consist basically in two steps: the drawing of the device with a LSMO precursor ink by inkjet deposition and the corresponding thermal treatment to obtain the LSMO phase.

### 6.6.1. The contactless analog encoder: the concept

Essentially, a Wheatson bridge consists of four resistors or their equivalent in serie where the resistances can change from R to R+$\delta$R values. For each pair of resistors, marked in green and blue in Fig. 6.12a, the resistance changes from a maximum value ($\delta R_{max}$) to 0 and continues from 0 to $\delta R_{max}$ in the complementary pair of resistors (see Fig. 6.12b). This resistance change can be converted into a physical property like position and exploit the system as, for instance, a positioning analog encoder (i.e. a device that converts an electrical signal to position data).

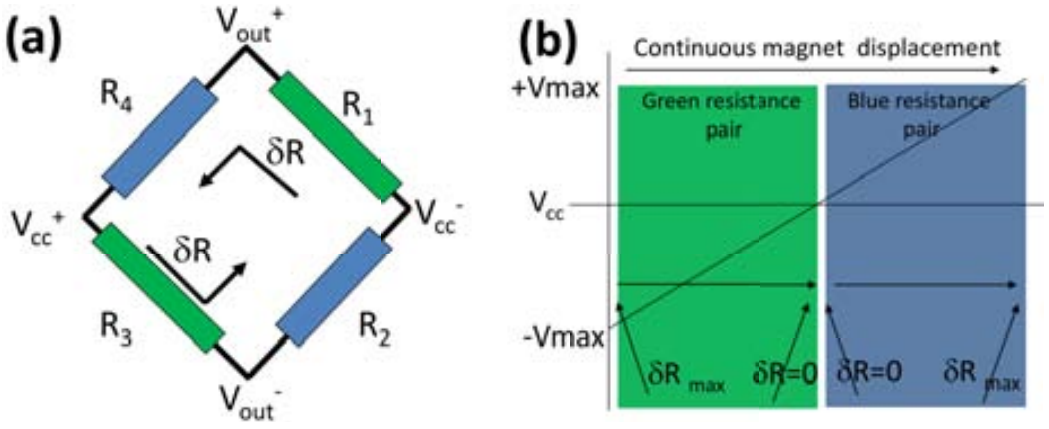


**Figure 6.12.:** (a) Schematic representation of a Wheatson bridge. (b) Sketch of the resistance evolution of the device. When a magnet rotates in a circular configuration over the path from the green pair to the blue one, the resistance, and then, the measured voltage value goes from a minimum ($V_{min}$) value in the green pair to a maximum value ($V_{max}$) in the blue one.

Before establishing and deciding the final pattern, different geometries for magnetoresistive detection have been considered (see Fig. 6.13). All designs include the contact pads for electrical connections.

In the first case (Fig. 6.13a), a resistor with two contact pads was studied. Secondly, it was considered a symmetric squared shaped closed full bridge with four equidistributed pads. Thirdly, a linear opened half bridge configuration was examined. Finally, in a fourth case, a rotational full bridge was contemplated with four contact pads equidistributed around a round path also of magnetoresistive material. For practical applications, the magnetic assembling, moves linearly in case of figure Fig. 6.13c or rotates (Fig. 6.13b and Fig. 6.13d) over the magnetoresistive path as displayed in figure Fig. 6.13 allowing resistance changes. The configurations from Fig. 6.13b to Fig. 6.13d constitute a Wheatston

bridge which is unbalanced according to the position of the magnets. The unbalanced voltage ($V_{out}$) is directly proportional to the angular position of the magnets. The simplest geometry (Fig. 6.13a) was printed to check solution behaviour and to study if the resistance of the branches is strongly influenced by the rastering direction.

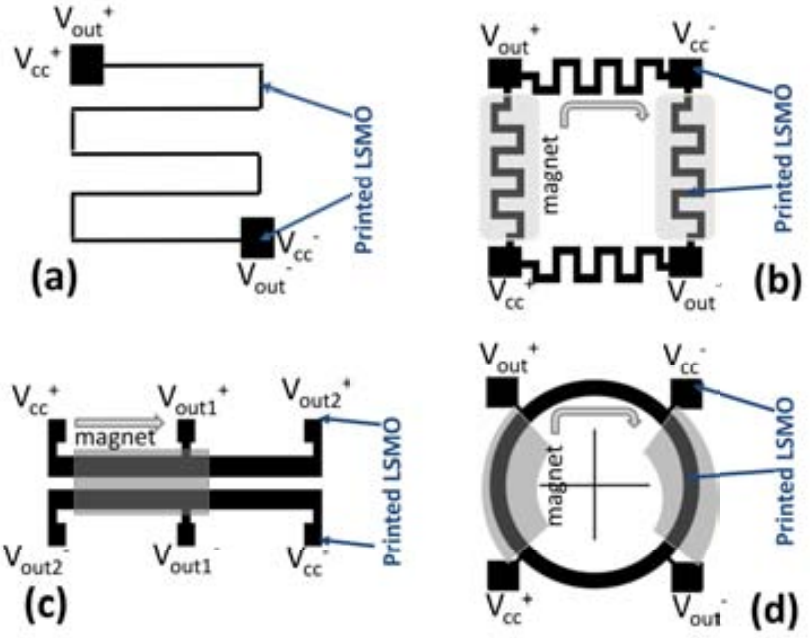


**Figure 6.13.:** Conceptual detail of the magnetoresistive contactless sensor. (a) resistor (b) full bridge (c) lineal analog encoder (d) circular analog encoder. All designs include the contact pads for electrical connections.

## 6.6.2. Printing the LSMO magnetoresistive path by means of the single nozzle piezoelectric printhead

### 6.6.2.1. Preliminary inkjet printing results

By combining the advantages offered by the two previous described solutions for LSMO films; the propionate and acetate based LSMO precursors solutions, another LSMO precursor ink was developed for LSMO patterning. It takes benefit about the stability of the propionate based LSMO precursor solutions with the greener and more environmental friendly solvents employed in the acetate based LSMO precursor solutions. Therefore, for LSMO patterning, the ink deposition was done from an as-prepared 0.05M (in Mn) LSMO precursor ink. The ink is based on $H_2O$/isopropanol/propionic acid in a ratio of 65/34/1 (% volume). The set of rheological and wetting parameters of this solution is depicted in Tab. 6.5:

| | **0.05M acetate LSMO precursor solution $H_2O$/isopropanol/propionic acid (65:34:1) in volume** |
|---|---|
| Density $\rho$ $(g/cm^3)$ | 1.020 |
| Surface tension $\gamma$ $(mN/m)$ | 36.5 |
| Viscosity $\eta$ $(mPa{\cdot}s)$ | 1.3 |

**Table 6.5.:** Relevant physicochemical parameters for the 0.05M water based LSMO precursor solution. All the measurements were performed at room temperature. Viscosity measurement was carried out at $100s^{-1}$.

The contact angle of the ink displayed in the previous Tab. 6.5 with heat-treated single crystals was <10°. This is the LSMO precursor ink developed for LSMO patterning.

Preliminary printing trials with the single nozzle piezo printhead started drawing some of the above presented devices on LAO and STO single crystals (see Fig. 6.14).

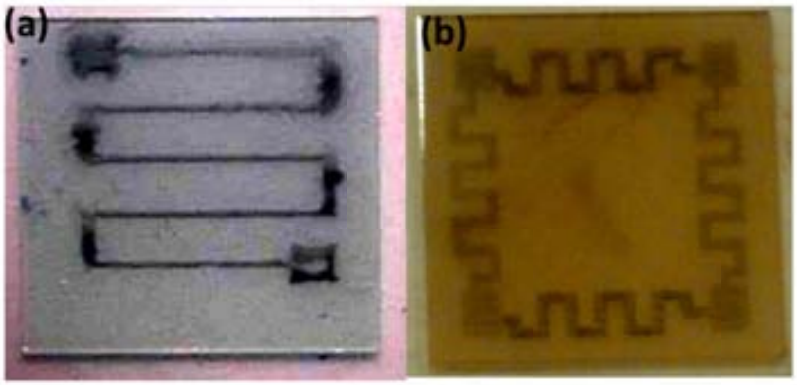


**Figure 6.14.:** Preliminary results of LSMO devices on single crystal. (a) Resistor with two contact pads on STO (b) Squared shaped full bridge on LAO single crystal. In both cases, after inkjet deposition, the sample was heat treated to obtain the desired LSMO phase.

After LSMO growth, conductive measurements were performed on the device leading to a specific resistance (i.e. the resistance between the squared contact pads divided by the total length of the device) around $8M\Omega/m$.

#### 6.6.2.2. Preliminary magnetotransport measurements

In order to establish the main parameters of the device, magnetoresistive behaviour was first determined in the squared shaped device presented in Fig. 6.14b. According to the results (see figure Fig. 6.15), the expected change of resistance (magnetoresistance coefficient, MR) of the LSMO path for a magnetic field of 0.4T, which is a typical values easily achievable for the conventional NdFeB magnets, was nearly 0.6% at room temperature.

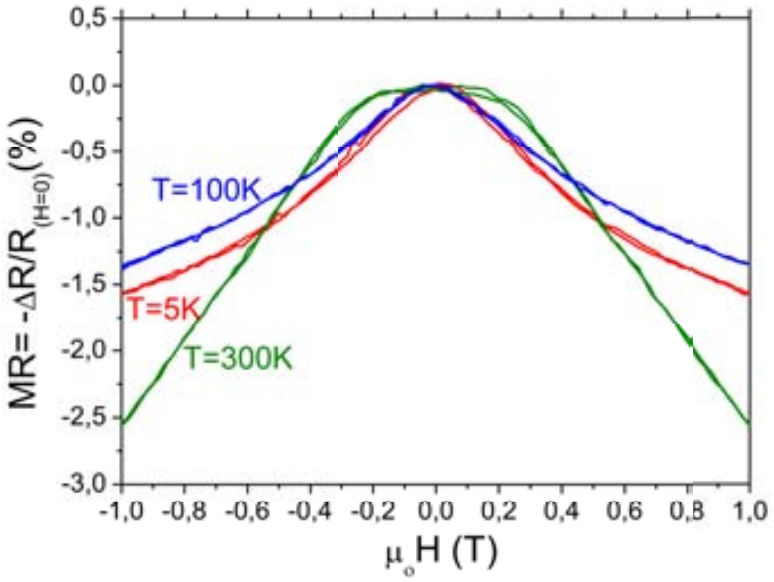


**Figure 6.15.:** Magnetoresistive characterization of the LSMO squared-shaped magnetoresistive device presented in Fig. 6.14b at 5K, 100K and 300K. As can be observed, the magnetoresistance MR in the range of 0.4T and RT (green curve) increases up to approximately 0.6%.

To evaluate if some device deviations may produce a significant performance decay which could make reconsider the viability of the manufacturing process, theoretical calculations were performed for a full bridge and half bridge Wheatston configuration showing a linear response between $V^{+}_{out}$ = 0.022V and $V^{-}_{out}$= -0.022V ($V_{cc}$= 9V), when the bridge in a half cycle of the detector in the rotational configuration was unbalanced 90°, or a half of the full displacement in the lineal shape. In Fig. 6.16, those results for the circular sensor are presented.

Amplification with a gain of 200 could produce a full loop of $9V$ corresponding to the supply voltage $V_{cc}$ demonstrating so the reliability of the system. The calculations assume that there is no mismatch in the resistance of each branch when it stays in zero position, i.e. the bridge is balanced. Otherwise, if exists a mismatch in the resistance of the different branches, it would introduce three effects: an offset in the unbalanced voltage, i.e. a phase displacement of 45°would not correspond to a balanced bridge ($V_{out} = 0$), also, it would produce a decreasing of the sensibility (the slope of the line represented in Fig. 6.16 would be smaller) and a loss of linearity would be observed. They show that a mismatch in the range of 30% would not mean an important decay of the system performance. Although the sensitivity is not strongly dependent on the unbalanced voltage, a good resistance balance is desirable, and therefore, the homogeneity of the paths during the manufacturing process should be ensured. In our case, the dispersion of the resistance value is about 10-20% including the contact pads, although further optimization to reduce this value for a real scale production is ongoing.

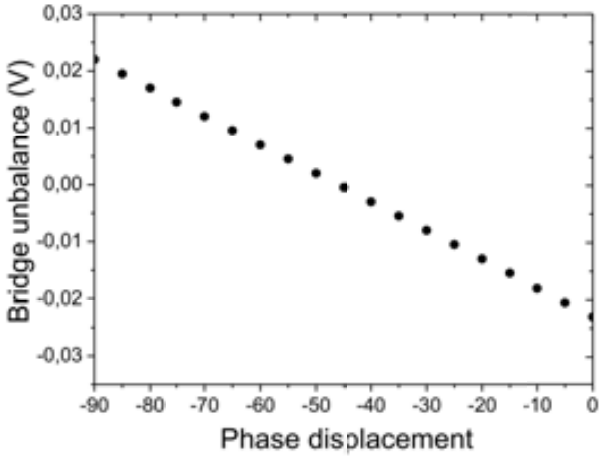


**Figure 6.16.:** Voltage loop in a half cycle of the magnetoresistive device presented in Fig. 6.13d supplied with a voltage $V_{cc}$ of $9V$.

Moreover, it is worth mentioning that in all the drawings, transverse lines to the device have been printed in a rastering mode. During printing, drops are ejected in both directions. No misalignment is observed indicating that high precision is achieved which is a fundamental requirement for the manufacturing of electronic devices based on functional ceramics.

Due to the circular configuration is the most extended device, effort was performed to print round connected devices. Mention that the viability tests and printing optimization were developed on (10x10)$mm$ LAO and STO single crystal substrates. In the following sections, it will be deeply described the experimental sequence to obtain connected LSMO round patterns whose external diameter and width of the circular path are $9.5mm$ and $0.75mm$, respectively, and the contact pad side is about $1.4mm$. Again, the thickness of the device can be regulated by adjusting drop volume, drop pitch and number of depositions. The reason of chosing these two single crystal substrates stemed from the different sign of lattice mismatch $\epsilon$ with the LSMO.

#### 6.6.2.3. Inket printing of the LSMO magnetoresistive paths

The best jetting parameters found for stable ejection of the LSMO 0.05M (in Mn) with water/isopropanol and propionic acid (Tab. 6.5) are summarized in Tab. 6.6:

| Jetting parameters | Value |
|---|---|
| Rise time ($\mu s$) | 2 |
| Dwell time ($\mu s$) | 5.5 |
| Fall time ($\mu s$) | 3 |
| Echo time ($\mu s$) | 5.5 |
| Final rise time ($\mu s$) | 2 |
| Voltage up ($V$) | +27 |
| Voltage down ($V$) | -22 |

**Table 6.6.:** Jetting parameters used to print the LSMO magnetoresistive device with a 0.05M (in Mn) $H_2O$/isopropanol/propionic acid (65/34/1 % in volume) LSMO precursor ink. Those parameters were selected as the optimum printing ones to print the magnetoresistive device.

After printing, the samples were sintered under air atmosphere as follows: until 900 °C with a ramp-up rate of 5°C/min, then 1h at 900°C and ramp-down rate of 5°C/min till RT.

By depositing the previous LSMO precursor solution with the parameters displayed in Tab. 6.6 and as it is shown in Fig. 6.17, a non-connected pattern was obtained. Probably, the low interaction of the feedstock water based ink with the STO susbtrate and the low filling factor used in this experiment (i.e. number of drops per unit area) make that after one layer deposition, drops do not merge due to its relatively high surface tension and, therefore, contact angle ink/substrate, as previously anticipated.

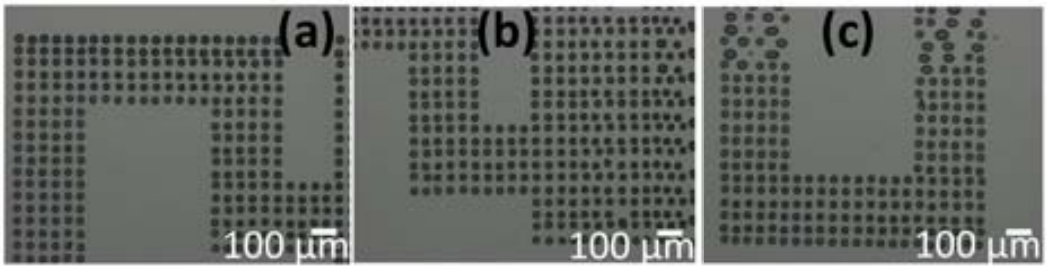


**Figure 6.17.:** Regular distribution of drops on STO single crystal. (a) to (c) correspond to optical micrographs of the LSMO pattern after inkjet deposition unveiling the low interaction ink-substrate. Drops do not merge in any direction. Occasional fusion of drops promotes distorted regions due to ink surface tension and/or small errors of drop positioning. Drop density in this trial was set at $4 \cdot 10^{-4}$ $drop/\mu m^2$ (which corresponds to a drop pitch of 50 $\mu m$ in both directions).

On the left most picture (Fig. 6.17a), although drops do not merge anymore, the regularity of the pattern is well observed and the design is correct in a global scale. As already commented, with the inkjet printing system implemented in our research laboratory, it is possible to obtain high precision in drop positioning, but local defects during the printing process (e.g. increase of drop size by occasional drop fusion) promotes distorted regions to several printing rows as shown in the most right pictures (Fig. 6.17b to Fig. 6.17c). This kind of defects could be attributed to the relatively high value of the

ink surface tension or small variations in the position of drops. From the pattern drawn, drop size is in the range of $40\mu m$.

Also, as it could be observed in Fig. 6.17a and b, very small deviations in the vertical direction are appreciated when it is crossed from one row to another. This small difference is explained as being due to the direction of printhead travel.

It is important to point out that high precision in the positioning of drops is necessary to avoid pattern irregularities and therefore large mismatches between the branches of the pattern. In this respect, homogeneous, connected and continuous patterns are desirable.

Given this fact, two strategies were attemped to improve the liquid management over the substrate and improve then the pattern resolution and accuracy:

1. Printing the LSMO device using the 2D interlacing technique: this approach increases density of drops and therefore, the filling factor (i.e. number of drops per unit area), and could be interesting to employe it in cases where the interaction ink-substrate is low. Basically, in this technique, the drops of the previous layer are dried and act as a pinning center for the successive depositions.

2. Substrate coating with a solution that contains 5% by weight of polyethyleneimine, PEI (Aldrich; 30% PEI water solution) in methanol anhydrous (Aldrich) to enhance the wettability of the ink on single crystal by enhancing the surface energy of the substrate.

#### 6.6.2.4. 2D interlacing technique

The interlaced methodology implies that the lines that make up the picture or design are drawn in an alternating fashion. The corresponding pattern is divided in complementary pixels for consecutive printing. In our case, the continuous array was separated in four different layers (see schematic illustration in Fig. 6.18a). To draw that pattern, first are ejected all the even numbered yellow drops from top to bottom and from left to right, then the printout is dried at RT, afterwards, we proceeded to fill all the red drops followed by the printing of the even blue drops and finally the green odd drops. Between layers, an intermediate drying process at RT was performed. Layers 1 and 3 were written from left to right and layers 2 and 4 from right to left. In figure Fig. 6.18, the black arrows indicate the direction of printing. As in this technique, alternate drops are dispersed within a line in the first pass of the printing and in the second pass, the printing begins with an offset filling the area between the printed drops; the key point comes in the amount of time allowed for the material to spread and dry before the next layer is printed. Therefore, it is really important to lay great stress on assuring that when the second layer has to be printed, the first one is completely dried because this first layer is designed to pin the successive drops in the free locations.

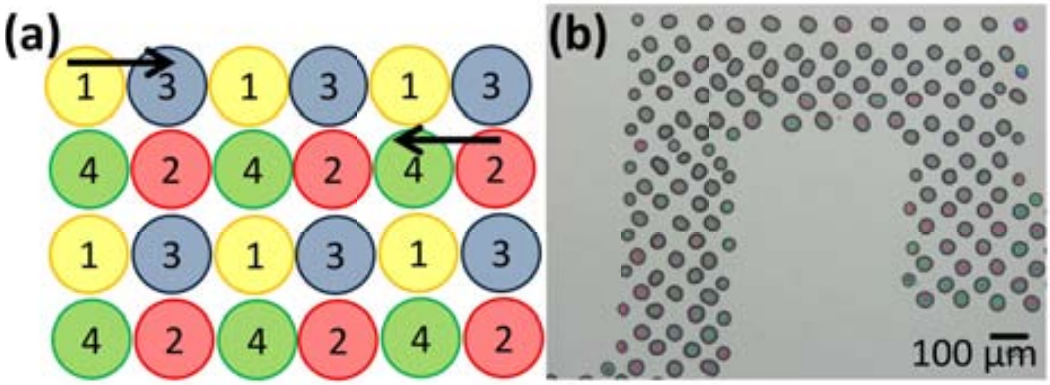


**Figure 6.18.:** (a) Schematic representation showing in what consists the interlaced technique. Black arrows indicate the sense of printing. (b) General view of the as-printed pattern after 4 deposited interlaced layers on STO substrate. Drop density in this example was set at $1.6 \cdot 10^{-3} drop/\mu m^2$. Random drop fusion takes place with no succesful results cause when the following layer is printed, the previous one remain in liquid form and there is no pinning which allows to set drop position in the correct place.

In principle, interlacing technique allows printing at larger distances that may contribute to better drop distributions which may avoid propagation of local distortions. Preliminar experiments were performed at a drop pitch a little bit larger than drop diameter. Four layers for each pattern were deposited. Drop density in that case was set at $1.6 \cdot 10^{-3}\ drop/\mu m^2$ considering the four depositions. By analyzing Fig. 6.18b, an array of independent drops was obtained. The big drops observed in the previous figure result from the fusion of at least two consecutive drops. Two possible reasons could explain this particular ink behaviour. One cause could be that when the second layer is printed, the first layer remains in liquid state, therefore, when drops coming from the new layer touches the previous deposited ones, liquid movements and displacements take place producing random drop fusions. Another reason may be the low filling factor used in the experiment (i.e. number of drops per unit area). To try to improve uniformity and resolution of inkjetted patterns, 2D interlacing trials were realized at a drop pitch significantly smaller than drop diameter. In the previous experiment presented in Fig. 6.18b, the number of drops per unit area was set at $1.6 \cdot 10^{-3} drop/\mu m^2$ in contrast to the $1.2 \cdot 10^{-2} drop/\mu m^2$ used in the next trial.

In this last case, although drop pitch is more than 2 times smaller than drop diameter, it would be expected that there is enough liquid to obtain a connected pattern. Again, what we believe that occurs in those experiments is that when next layer is printed, the previous one is not completely dried, therefore, it does not pin the successive drops and the flowing of the liquid generates those deformed and irregular patterns.

In order to get a better control of drop positioning and to ensure the continuity of the printed paths, the surface energy of the substrate has been promoted by pre-cleaning the surface of the substrate with a solution with a 5% by weight of PEI in methanol to enhance the wettability of the ink with the substrate (second strategy abovementioned).

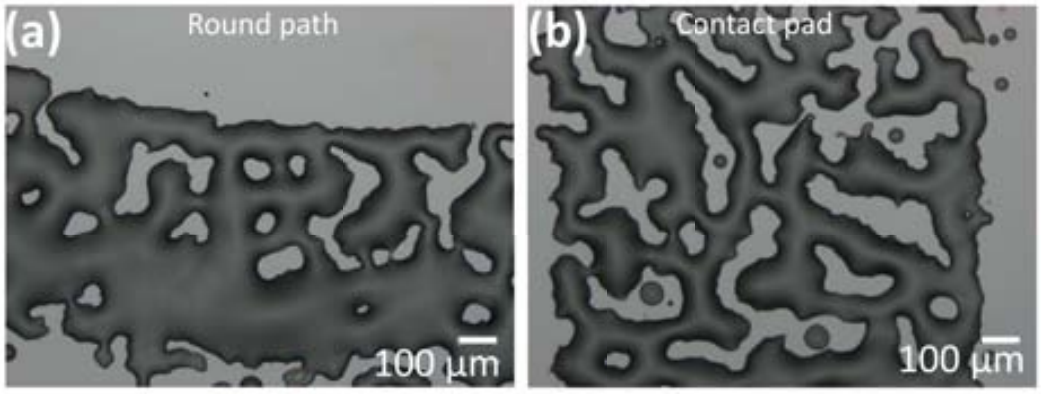


**Figure 6.19.:** (a) Round path and (b) contact pad of the rotational LSMO magnetoresistive device on STO single crystal. As may be appreciated, even increasing the number of drops per unit area, irregular features with large voids are obtained. Drop density is this example was set at $\sim 1.2 \cdot 10^{-2} drop/\mu m^2$.

#### 6.6.2.5. Substrate pre-treatment

The evolution with time of the LSMO precursor solution of Tab. 6.5 on STO and/or LAO single crystals was monitored by means of the sessile drop technique (see sec. 3.2.4.1). Interesting conclusions may be extracted from the analysis of next Fig. 6.20. That Fig. 6.20 displays 10 frames at different times after deposition of a $2\mu l$ drop of the LSMO ink used for device printing where a clear ink retraction as time advances is simply perceived [256]. From time $t = 0s$ to $t = 25s$ the ink progressively spreads until it achieves the advancing contact angle value ($\theta_{adv}$ $\sim$10°) from which then slowly retracts at the same time that evaporation is occuring until the bead's width is pinned, which belong to a possible situation postulated by Schiaffino and Sonin [149, 256] and detailed in Fig. 5.4.

Surface chemistry is of key importance in determining wetting behaviour. Much research has been devoted to modify the surface chemistry of various solids in order to obtain specific wetting properties. Standard chemical means to do this are, for instance, the plasma treatment [299] or the silanization [300]. By such treatments, one modifies the chemical properties of the surface of the material, and hence the surface energy of the substrate with liquids, vapours, or other solids. For surface wettability, in addition to surface chemistry, surface forces such as van der Waals or electrostatic forces (long-range intermolecular forces) or hydrogen bonds are important.

Essentially, the treatment of the surface's substrate we performed consisted of rubbing the surface of the substrate with a wipe previously impregnated with an alcoholic solution with a 5% PEI by weight, wait few seconds for drying and then, proceed with the printing on top.

Next Fig. 6.21 shows the effect of the pre-treatment of the surface of the substrate with the alcoholic solution with PEI.

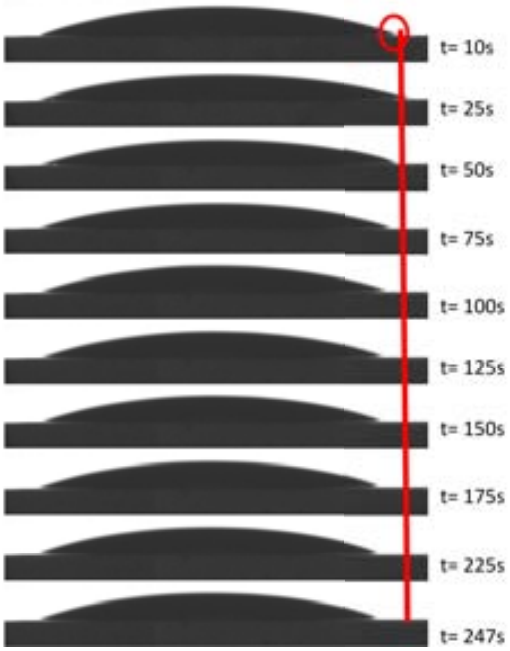


**Figure 6.20.:** Temporal evolution of the LSMO precursor ink used for device printing over STO single crystal without surface treatment (physicochemical characteristics displayed in Tab. 6.5). As may be observed, as time advances, the ink retracts at the same time that evaporation occurs until the width of the bead is pinned [149, 256].

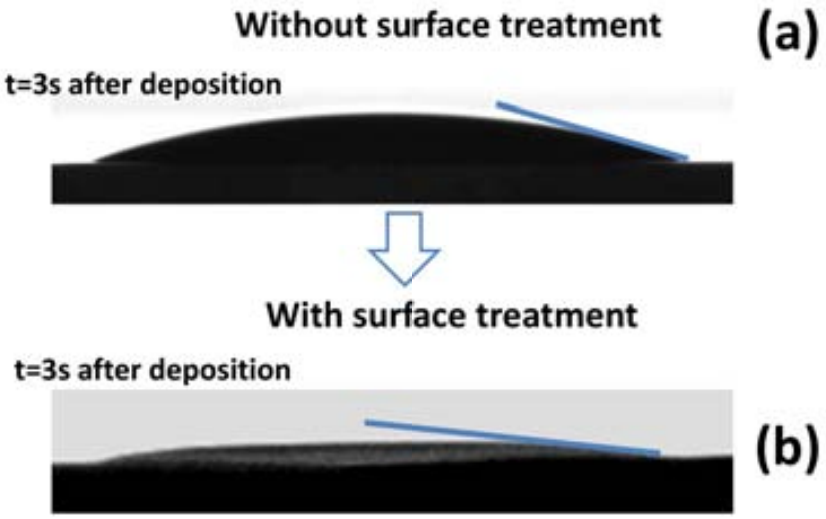


**Figure 6.21.:** Effect of surface substrate pre-treatment with a solution which contains a 5% by weight of PEI in methanol. (a) The LSMO precursor ink was deposited without treating the surface of the substrate. (b) The LSMO precursor ink was deposited after treating the surface of the substrate with the mentioned solution.

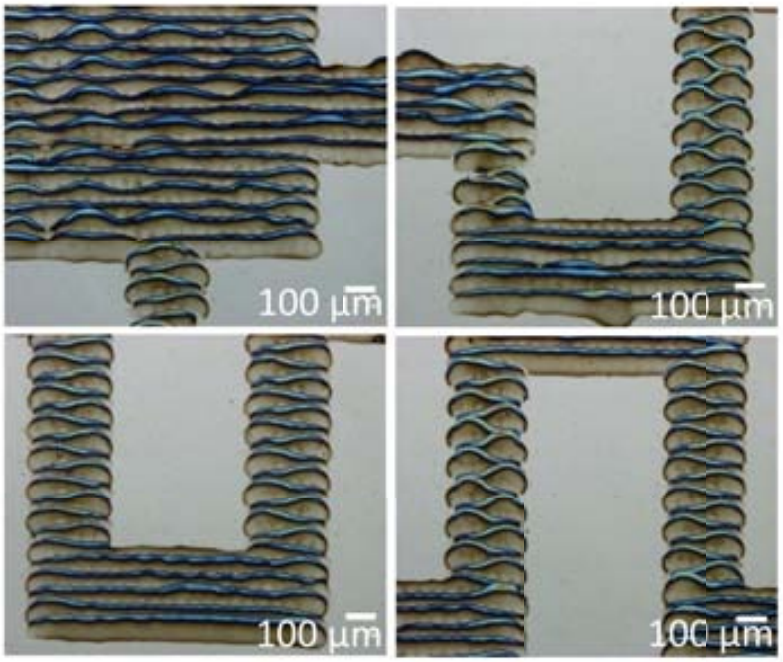


**Figure 6.22.:** Optical micrographs of different regions of a LSMO device after printing on STO. The substrate before printing has been coated with a methanolic solution that contains a 5% by weight of PEI. The number of drops per unit area in this case was set at $4 \cdot 10^{-4} drops/\mu m^2$ (drop pitch of 50 $\mu m$ in both directions). The printing parameters used for drop formation are detailed in Tab. 6.6.

As may be observed in the previous Fig. 6.22, by ejecting $4 \cdot 10^{-4} drop/\mu m^2$, the final pattern was only connected in one direction (x axis). After analyzing by optical microscopy the inkjet-printed device when the substrate is cleaned with the previous mentioned alcoholic/PEI solution (Fig. 6.22), important changes are noted when compared with non-treated substrates. By doubling the number of drops per unit area with a second layer deposition (not shown herein), a connected pattern in both directions was accomplished. It is interesting to point out that the saturation of the substrate's surface with this methanol/PEI solution enhances ink-substrate wettability in such a way that makes possible the obtention of fully connected patterns even using drop densities lower than the one used in the interlaced approach case of Fig. 6.18. By using $4 \cdot 10^{-4} drop/\mu m^2$ (in contrast to the $1.6 \cdot 10^{-3} drop/\mu m^2$ of Fig. 6.18), the work of adhesion is sufficiently increased to obtain fully connected patterns. To determine the role of this solution, different types of nitrogenated compounds were tested. Concentrated ammonia was also one of the chemicals which increases the interaction ink-substrate which suggests that could exist long range supramolecular interactions between the non-shared pair of the N atom and the corresponding metallic and oxygen atoms of the substrate terminations.

The enhancement of the ink wettability with the substrate entails a smaller contact angle hysteresis than when printing on a non-treated substrate, which prevents the retraction of the contact line towards the bead's center.

By raising the wettability of the ink with the substrate, we were able to further improve the quality of the footprint, although, it introduces an extra manufacturing cost comparable to the printing of an additional layer. As we will show later, the same effect

of increased wettability could be achieved by introducing the monomer PEI into the ink formulation instead of rubbing the surface of the substrate with a MeOH/PEI based solution.

## 6.6.3. Characterization of the LSMO magnetoresistive device on single crystal

In the following section, a complete characterization of a low offset magnetoresistive bridge for non-contact sensing on a (10x10)$mm$ STO single crystal substrate is displayed. For simplicity, we decided to display only the fully characterization for the LSMO device onto STO, but it might be absolutely extended also to LAO single crystals.

The LSMO precursor employed was the one presented in Tab. 6.5 whereas the set of driving parameters applied to eject the drop are the ones presented in Tab. 6.6. In the experiment, drop density was $4 \cdot 10^{-4} drop/\mu m^2$ dispensed in four different layers. Each layer was printed using a drop pitch of $50\mu m$ and in-between depositions, a drying process with dry nitrogen was carried out at RT. After the printing process, the sample was subjected to the corresponding LSMO growth process (Fig. 3.10).

### 6.6.3.1. Morphological characterization

Fig. 6.23 displays the appearance of different areas of the magnetoresistive device when printing on a chemically pre-treated STO substrate before inkjet deposition. It can be perceived that a continuous and connected coating was achieved. In these optical images, the printing direction can be deduced (black arrow in the optical micrographs) and, particularly, in Fig. 6.23b and Fig. 6.23d, the pixels of the image may also be appreciated.

Fig. 6.24a depicts the whole 10x10$mm$ sample on STO after LSMO growth, while in Fig. 6.24b, the corresponding SEM pictures show the typical morphology of the granular manganite layer. It is worth to remark that the final layer shows to be epitaxial although the granular aspect of the surface obtained by the sinterization of the grains grown around the different seed nuclei. This is due to the epitaxial growth from the textured surface of the substrate.

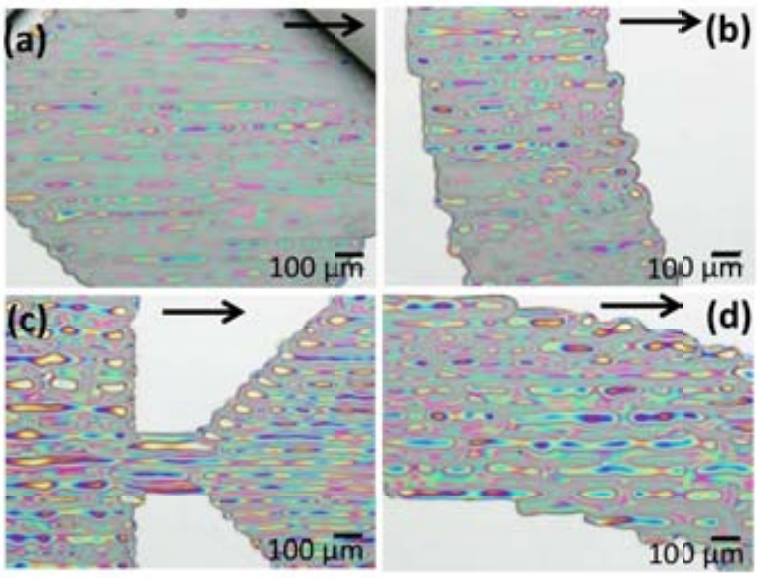


**Figure 6.23.:** Morphological characterization of the LSMO magnetoresistive device on STO single crystal. Optical micrographs of different regions of the precursor LSMO magnetoresistive device after inkjet printing deposition. Before inkjet printing, the STO substrate was chemically treated with a methanolic solution with a 5% by weight of PEI to enhance the wettability with the water based LSMO precursor ink. Optical micrographs reveal a fully connected pattern in both directions after the substrate surface pre-treatment. (a) Contact pad (b) Round path (c) Region of connection between the round and the contact pad (d) Round path. The inkjet deposition consisted of a multideposition of 4 layers with a drying process in between depositions at RT with dry $N_2$. The number of total drops per unit area was $1.6 \cdot 10^{-3} drop/\mu m^2$ considering the 4 depositions ($4 \cdot 10^{-4}$drop/$\mu m^2$per deposition) and a squared (50x50)$\mu m$ matrix was used.

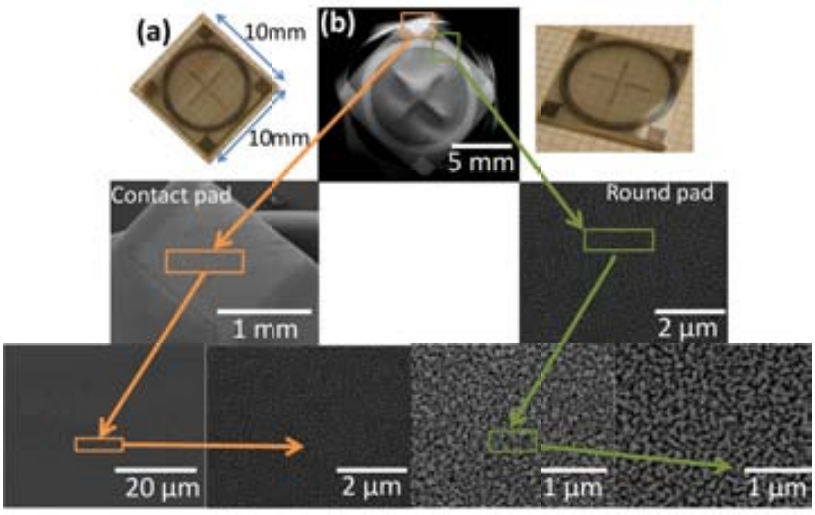


**Figure 6.24.:** Morphological characterization of the LSMO magnetoresistive device on STO single crystal. (a) Optical microscopy of the general view of the magnetoresistive bridge made by rastering on a (10x10) STO substrate. (b) SEM micrographs of the contact and the round pads of a LSMO device on STO after sintering at high temperatures displaying the typical morphology of a polycrystalline layer.

### 6.6.3.2. Structural characterization of LSMO patterns

A structural analysis points out that under the above-mentioned growth conditions, LSMO grows epitaxially on STO and LAO single crystals with the expected orientation (001)LSMO||(001)STO/LAO (Fig. 6.25). These results are shown in the (110)-LSMO pole figure displayed in Fig. 6.25b, where there appear four peaks at $\chi = 54°$corresponding to the angle between (110) and (100)-planes. LSMO-(110) peaks are localized at values separated 90°as corresponds to the cubic structure, indicative that LSMO grows cube on cube about [001]-STO axis (Fig. 6.25 b and c), i.e. LSMO[100]||STO[100].

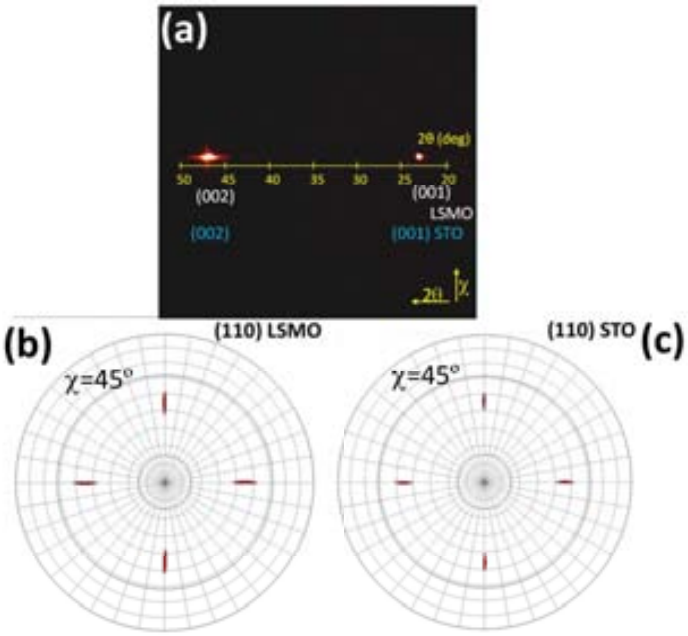


**Figure 6.25.:** XRD characterization of the LSMO magnetoresistive device on STO and LAO single crystals (a) GADDS on STO (b) pole figure of the (110)-LSMO peak (c) pole figure of the (110)-STO reflection.

### 6.6.3.3. Macroscopic magnetic and transport properties of LSMO patterns

We now move to the study of the magnetic and transport properties of the LSMO patterns using the VSM and the PPMS systems at temperatures between 5 and $300K$ and varying fields from 0 to 1T. LSMO devices grown on STO and LAO (average thickness $t \sim 80$ nm), and annealed at 900°C for 1h, showed ferromagnetic hysteresis up to $300K$. Fig. 6.26a and Fig. 6.26b shows the resulting magnetization loops at 300K. Fig. 6.26b displays a zoom-in from 0.15 to -0.15$T$ of the previous magnetization loop displayed in Fig. 6.26a. Magnetization loops in both LAO and STO single crystal substrates are similar with a saturation magnetic moment $m_s \sim 6.4 \cdot 10^{-4} emu$ for the LSMO/STO presented in figure Fig. 6.26, remanence values for the LSMO/STO device of $\sim 3.4 \cdot 10^{-4} emu$ and cohercitive fields $\mu_0 H_c \sim 3.7 \cdot 10^{-3} T$.

Conventional resistance measurements with a multimeter gave resistance values for each brange of the device in the range between 10 $k\Omega$ and 20 $k\Omega$ within a mismatch of

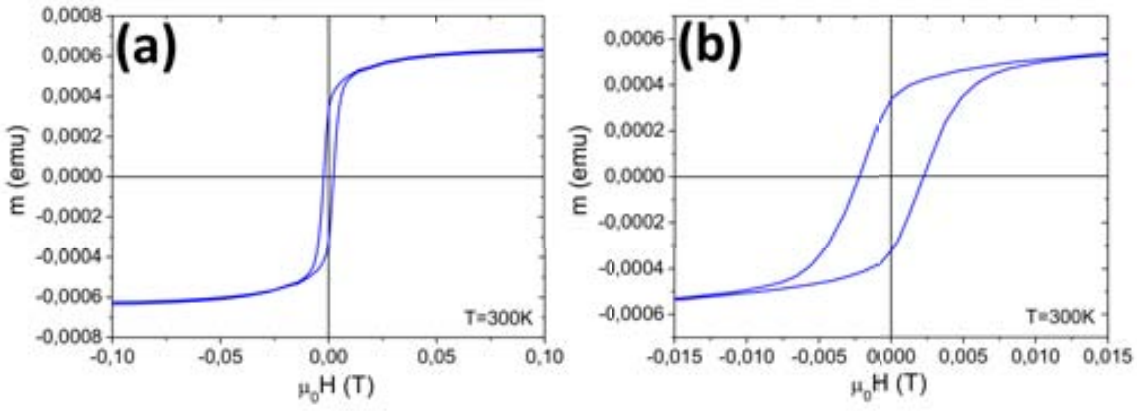


**Figure 6.26.:** Magnetic characterization of the LSMO device on STO single crystal. (a) Magnetization loops (T=300K) for LSMO/STO device. The device display a saturation magnetization $m_s \sim 6.4 \cdot 10^{-4} emu$, which corresponds to a volume magnetization $M_s = 333.3 emu/cm^3$, as deduced from the film thickness $t = 80nm$ value. (b) Zoom-in from -0.015 to 0.015T of the magnetization loop presented in figure (a).

about 20% including the contact pads. Wider round magnetoresistive paths (Fig. 6.23c) are being in development to further decrease the resistance value of the device.

In addition to macroscopic magnetic properties, transport properties of the CSD-derived LSMO devices were also investigated.

The temperature dependence of the magnetic moment is given in Fig. 6.27a. The temperature dependence of resistivity ($\rho(T)$) was measured in the standard four-probe

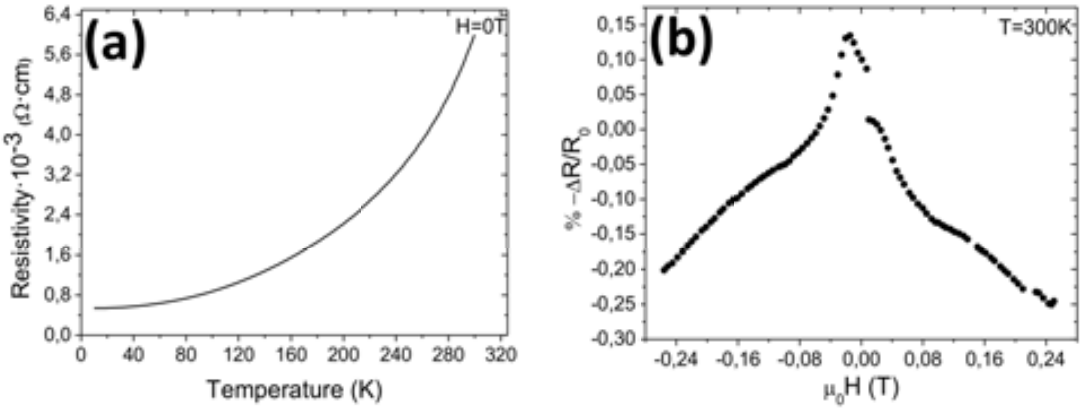


**Figure 6.27.:** Magnetotransport characterization of the LSMO device on STO single crystal. (a) Dependence on the temperature of the resistivity of a LSMO/STO device. In this experiment, no magnetic field was applied during the experiment. (b) Magnetoresitance curve at T=300K for the LSMO/STO device.

geometry, using a Physical Properties Measurement System (PPMS, Quantum Design). Fig. 6.27a shows the $\rho$ vs $T$ behaviour of the LSMO device on STO (average thickness ∼80 nm) displaying the typical metal behaviour at temperatures below $T_c$. The curve of that figure gives a Curie temperature $T_c$∼370K. For such $t$ value (t ∼80 nm), LSMO shows bulk-like properties, as expected in manganites. As can be observed, for zero applied magetic field, this LSMO/STO device exhibit a maximum resistivity value at 300K of $\rho \sim 1.3 \cdot 10^{-3}\Omega \cdot$ cm, comparable to the maximum resistivity value, $\rho \sim 1.4 \cdot 10^{-3}\Omega, \cdot$ cm obtained for the CSD-derived solution 0.3M LSMO films ($t \sim 25$ nm) which exhibit magnetotransport properties comparable to bulk LSMO [27,41,91,292].

The magnetoresistance MR, defined as $MR = [R(H) - R(H = 0)]/R(H = 0) \cdot 100$ of the LSMO/STO device presented along this section is plotted in Fig. 6.27b. That device shows a maximum MR of ∼ 0.35% both on LAO and STO at T=300K and H=0T.

Even though the different lattice mismatch between the LSMO/STO and LSMO/LAO no apreciable differences were observed in the morphological, structural, magnetic, and magnetotransport properties.

#### 6.6.3.4. Profilometric characterization

Next Fig. 6.28a displays a SEM micrograph of the LSMO device where the sample plane was tilted 60°downwards to obtain higher contrast and compute the thickness of the LSMO film. In that figure, the averaged thickness is around $80nm$ taking into account that appreciable thickness variations exists along the width of the LSMO path as displayed in the representative profile of Fig. 6.28b.

If we take a look on the 2D profile obtained (Fig. 6.28b), it could be appreciated a saw-tooth-like structure. Further optimization of the drop pitch in both directions is necessary to try to avoid this kind of effect.

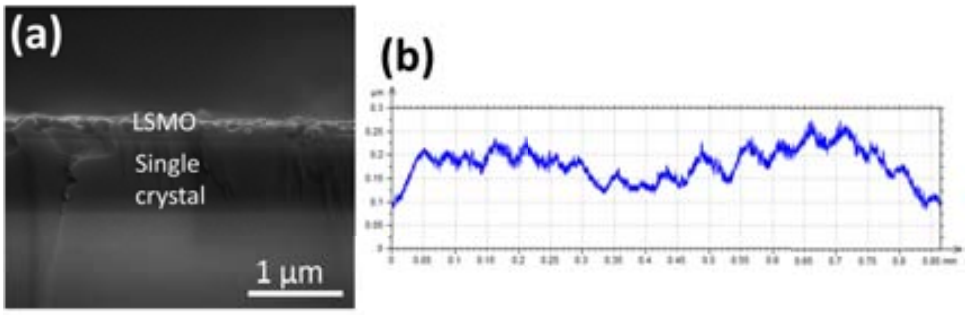


**Figure 6.28.:** Morphological and profilometric characterization of the LSMO magnetoresistive device on STO single crystal. (a) SEM micrograph of a cross section of the device which shows the LSMO layer. The sample plane was tilted 60º downwards in order to obtain higher contrast to calculate the LSMO film thickness. (b) Profilometric analysis of the LSMO device on STO. Even the final pattern presents a saw-tooth like structure, the so obtained average film thickness is ∼80 nm.

Again, such results have also been confirmed in LSMO devices printed on both STO and LAO single crystals.

Based on the very promising results in terms of final properties of LSMO patterning on single crystals and focused on further research, reproduction and upscaling on magnetoresistive device was carried out onto single crystal.

Furthermore, a full electronics testing system has been developed as seen in Fig. 6.29 in order to test the final performance of the inkjetted LSMO devices. The system includes a voltage reference, a differential amplifier and an offset corrector.

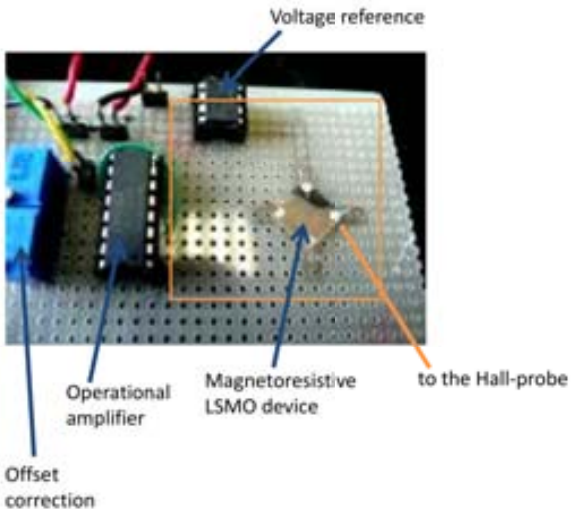


**Figure 6.29.:** Full electronics testing system of the inkjetted LSMO devices for quality testing.

## 6.6.4. Reproduction of the LSMO magnetoresistive device

In order to evaluate the reproducibility of the inkjet printing process and to assess the suitability of this equipment, 20 LSMO devices on (10x10)$mm$ LAO and STO substrates were printed using the single nozzle piezo head (see Fig. 6.30). Each one consisted of four depositions and were also printed using the LSMO precursor ink of Tab. 6.5 with the printing conditions displayed in Tab. 6.6.

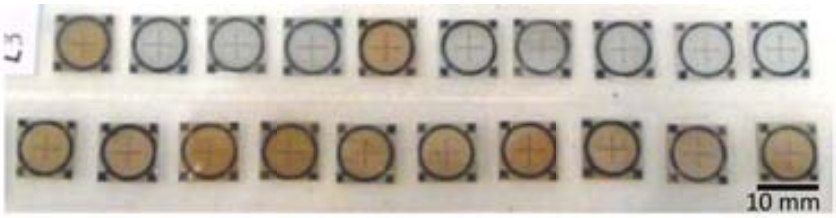


**Figure 6.30.:** Serie of 20 LSMO full bridges printed over LAO (brown substrates) and STO single crystals (white substrates) to show the feasibility of the inkjet printing technology.

### 6.6.5. Printing the LSMO magnetoresistive path by means of a multinozzle printer

Besides, experiments with a Dimatix multinozzle printer were performed. Taking advantage of the small drop volume dispensed for that printhead (nominal drop volume ∼10 pL) and, therefore, the possibility to obtain highly resolution patterns, inkjet printing of that rotational LSMO magnetoresistive device was taken into account. Various tests in order to obtain the best printed device in terms of homogeneity and continuity were performed through drop pitch tuning, substrate temperature modification, number of depositions and number of nozzles.

Fig. 6.31 shows the effect of varying drop pitch on the printing of the magnetoresistive device with the multinozzle printer. In the first row (Fig. 6.31 row (a)), only one nozzle was used in one layer deposition with a number of drops per unit area of $2.5 \cdot 10^{-3} drop/\mu m^2$. In the final pattern, lines were connected through a very thin sheet of liquid but a pronounced wavy structure was obtained as could be appreciated by naked eye. This featuring structure was softened by adding a second deposition on top with the same number of drops per unit area using also one nozzle (Fig. 6.31 row (b); drop density in this test was $5 \cdot 10^{-3} drop/\mu m^2$). Thicker devices were built by employing higher drop densities.

An example of a single layer deposited using a drop density of $4.4 \cdot 10^{-3} drop/\mu m^2$

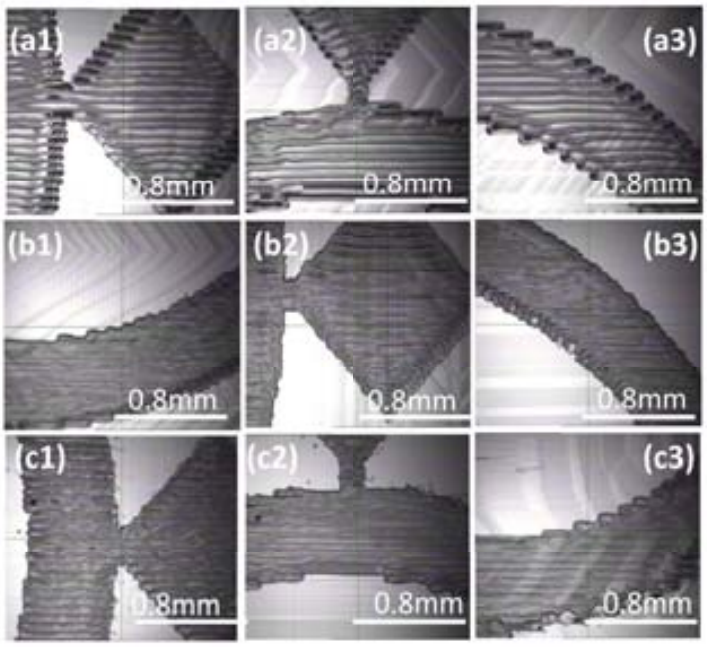


**Figure 6.31.:** Optical micrographs of LSMO magnetoresistive devices printed using a Dimatix multinozzle printer. In the three cases, during the inkjet deposition only one nozzle was used. Drop density was set at (a) $2.5 \cdot 10^{-3} drop/\mu m^2$ (corresponding to 1 deposition) (b) $5 \cdot 10^{-3} drop/\mu m^2$ (2 depositions) and (c) $4.4 \cdot 10^{-3} drop/\mu m^2$(1 deposition). Optical micrographs were taken using the drop watcher integrated in the same multinozzle system.

is shown in the third row of Fig. 6.31. The printing drop spacing in Fig. 6.31c has been increased so as to obtain more homogeneous profiles in a single layer deposition process and using only one nozzle in the printing process as well.

Furthermore, the influence of the substrate temperature was studied and no changes were observed in the ink distribution after deposition. After evaluating such effect, and for operational simplicity, in posterior tests, substrate temperature was maintained at RT. The fact that the three ink constituent solvents ($H_2O$, propionic acid and isopropanol) boil at higher temperature than the maximum adjustable temperature for the substrate holder could be the reason why there are no appreciable changes in the final pattern morphology if the temperature of the substrate is changed.

Next section shows the basic characterization of one example of LSMO device on LAO single crystal printed with the multinozzle Dimatix printer.

#### 6.6.5.1. Characterization of a LSMO printed device using the multinozzle printer

To evaluate the structural, morphological and electrical properties, a fully characterization of an inkjet-printed device using the multinozzle printer was performed.

Fig. 6.32 sums up the complete morphological and structural characterization of the LSMO printed device using the mentioned printer.

The morphological characterization by optical microscopy of the round path unveils areas with different brown tones Fig. 6.32a corresponding to regions with different thickness as confirmed in the profile of the magnetoresistive path in Fig. 6.32e. In order to examine the crystal structure of the LSMO system after the annealing at high temperatures to form the desired LSMO phase, XRD measurements were performed. Only (00l) reflections are present in the XRD pattern proving that LSMO grows cube on cube on top of LAO/STO, i.e.$(001)_{LSMO}[100]\|(001)_{LAO\ STO}[100]$. Figure Fig. 6.32b shows the zoomed-in $\theta - 2\theta$ scan from 46°to 49°to better appreciate the (002) LSMO peak of two different devices printed using various number of drops per unit area. Black and blue plots correspond to different LSMO devices with number of drops per unit area of $2.5 \cdot 10^{-3} drop/\mu m^2$ and $4.4 \cdot 10^{-3} drop/\mu m^2$, respectively. Both samples exhibit the (002) LSMO peak at $2\theta \sim 46.9°$, which the (001) LSMO peak (not shown in this XRD pattern) was no detectable in any case. The increase in the intensity of the (002) LSMO peak is in agreement with the larger film thickness (i.e. higher number of drops per unit area) of the LSMO device represented in blue line. The epitaxial relationship is also confirmed by the non-appearance of polycrystalline rings in the 2D-GADDS diffraction pattern.

Fig. 6.32d shows a SEM micrograph of the circular LSMO path. Note that the morphology is the typical corresponding to an epitaxial layer. Analazing the thickness profile obtained by scanning all the path width (Fig. 6.32e), it may be observed a noticeable saw tooth-shaped structure where averaged variations in the range of $20nm$ are easily appreciated. This may be attributed to an excessive drop overlap. In this way, the number of drops per unit area should be decreased to adjust drop overlap. Further work in that understanding is currently underway. In order to avoid this featured pattern, printing experiments with several nozzles at the same time would be desirable.

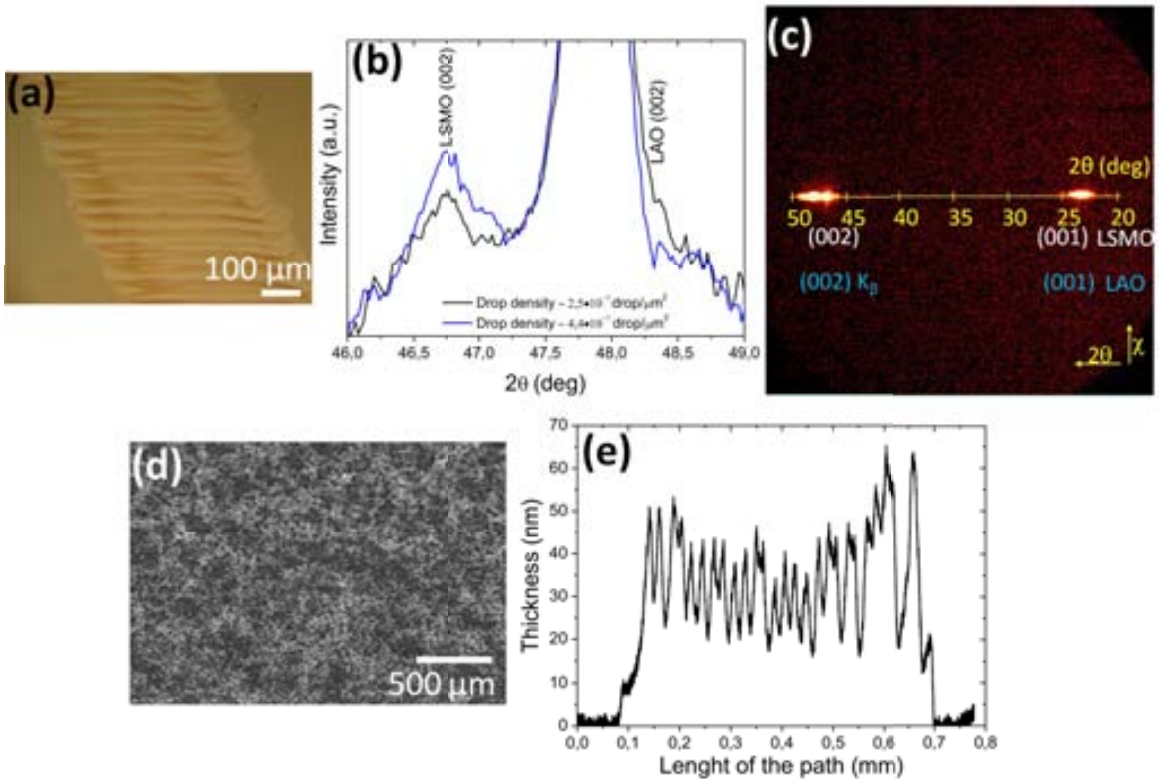


**Figure 6.32.:** Morphological and structural characterization of a LSMO device deposited by means of the Dimatix multinozzle printer.(a) Optical micrograph of a portion of the round LSMO precursor path. (b) Structural characterization by means of standard XRD of a section of the path shown in (a). A zoom-in of an extended $\theta - 2\theta$ pattern is displayed. Blue and black lines correspond to two different devices printed with different number of drops per unit area; $2.5 \cdot 10^{-3}$drop/$\mu m^2$ plotted in blue and $4.4 \cdot 10^{-3}$drop/$\mu m^2$, in black. The increase in intensity observed is in accordance with the expected larger thickness of the device printed using higher number of drops per unit area. (c) 2D-XRD pattern: no polycrystalline diffraction cones are present in the spectra revealing the highly epitaxial relationship of the so-obtained sample. (d) It shows the microestructure of the LSMO device noticing the typical grain structure of an epitaxial layer. (e) Profilometric analysis of the corresponding LSMO device where a saw teeth like structure is observed.

Also, conductive measurements for a set of 14 LSMO trials printed applying the same driving conditions using the same decribed ink and only varying drop spacing from $15\mu m$ to $25\mu m$ provided resistance values of around $10 - 20k\Omega$ with dispersions including the electrical contact pads in the range of 15%.

Different printing tests using more than one nozzle at the same time were carried out with no successful results. It was possible to print the pattern, but in all cases, it may be recognized a strong decrease of the print quality that may be ascribed basically to non-matched velocities (situation reflected in Fig. 6.33a) and misdirected nozzles (Fig. 6.33b) or combination of both printhead jetting issues. Thus, an obvious optimization of the jetting process when multiple nozzles are working at the same time is necessary by adjusting the driving waveform (i.e. the corresponding times and voltages for each individual nozzle) and selecting proper cleaning procedures to avoid poor jetting performance.

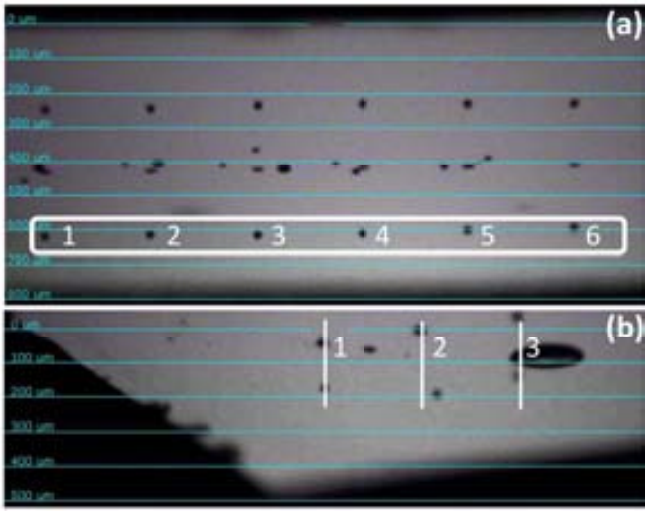


**Figure 6.33.:** Illustration of nozzles ejecting off axis as well as mismatched drop velocities that produce poor sustainability and jetting performance. In figure (a) there are multiple nozzles ejecting at different velocities. Only drops ejected from nozzles 2 and 3 run at the same velocity, while it could be noticed that nozzle number 1 is indeed running faster than nozzles 2 and 3. Otherwise, drops from nozzle number 6 are slower than drops from nozzle 2 and 3. Further waveform tuning should be performed to make the same all drop velocities. (b) It illustrates a jet ejection of nozzle 2 off axis from right to left. Special insistence on cleaning methodologies should be taken into account in order to avoid misdirected drops and poor print quality.

The promising results obtained for the LSMO device on single crystals encouraged us to devote effort towards decreasing the cost of the magnetoresistive devices. Due to electrical and magnetic properties of manganites are also observable in cheaper polly-crystalline substrates, tests over polycrystalline alumina and fused silica (quartz glass) were also performed in order to reduce the total cost of the manufacturing process. As starting point, we have used standard alumina substrates ($Al_2O_3$) of common application in electronics. Firstly, LSMO tracks have been printed over alumina using a 0.1 M LSMO precursor ink with rheological correction. The same printing conditions exposed in Tab. 6.6 were used in those polycrystalline substrates. Wettability of the ink with the alumina substrate was sufficient to obtain an homogeneous ink layer. After heat treatment at 900°C in air, the obtained resistance of the sample was in the range of kΩ. The structure of the LSMO was observed by SEM for tracks of about $250\mu m$ wide (Fig. 6.34).

The so-obtained layer shows problems of delamination in the parts where the thickness is higher, but the thinner regions of the track show good adherence. Fig. 6.34a (lower left corner) shows the LSMO tracks with the "peeling" effect. A more detailed insight can be observed in Fig. 6.34b, where good quality of the grains may be appreciated. The limit of the track can be seen over the grains of $Al_2O_3$, some of them being only half coated. Only over the pores, the coating is thick enough to connect the LSMO grains in a sponge-like structure. However, conductance tests show that tracks were fully connected.

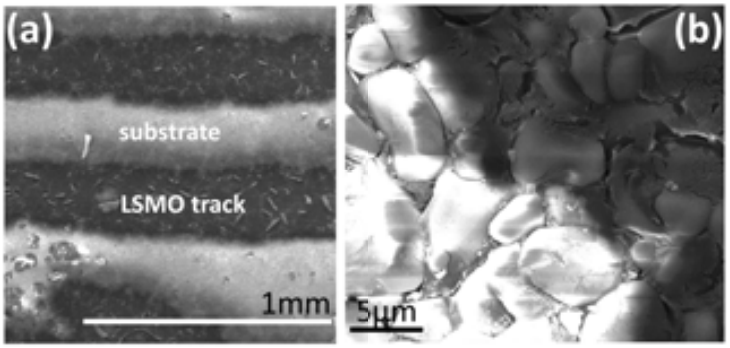


**Figure 6.34.:** Detail of LSMO printed tracks over commercial polycrystalline alumina ($Al_2O_3$). (a) Porosity of alumina causes stress in the thicker regions of the coating producing a "peeling" effect (lower left side). On the right figure (b) it can be distinguished the behavior of the thinner wetted parts, clearly opposite to the thicker ones where the stress produces dewetting. Only over the pores, the LSMO film is thick enough to connect the LSMO grains. The electrical conductivity of the tracks is in the range of $M\Omega$.

Different trials of printing devices on polycrystalline alumina, quartz and pyrex glass were performed and shown in next Fig. 6.35, Fig. 6.36 and Fig. 6.37.

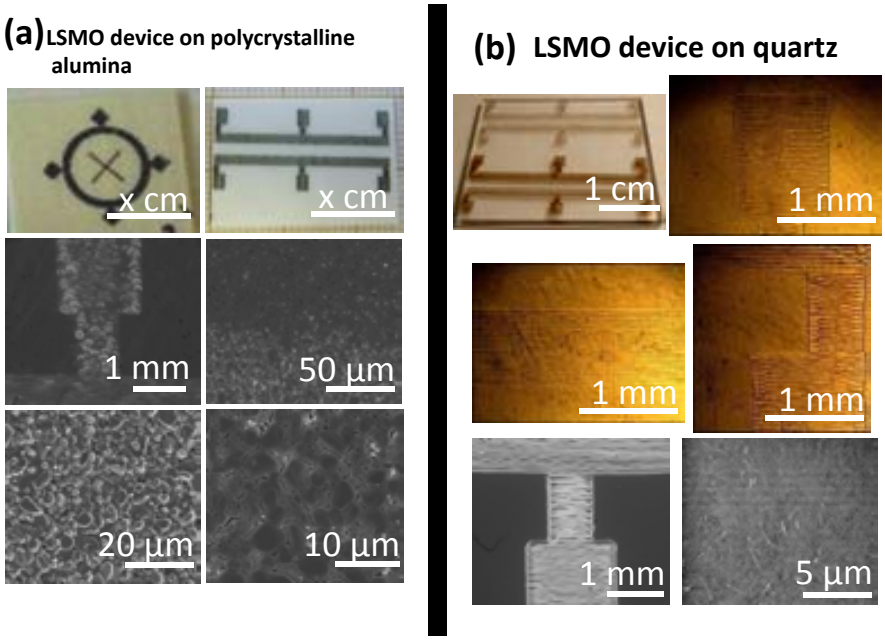


**Figure 6.35.:** LSMO devices on different polycrystalline (non-textured) substrates. Micrographs of LSMO devices (a) over polycrystalline alumina and (b) over quartz.

Next figure presents some SEM micrographs of what could be the gate of an electronic

LSMO device on polycrystalline alumina (Fig. 6.36a) and over pyrex glass (Fig. 6.36b). The patterns so obtained were connected.

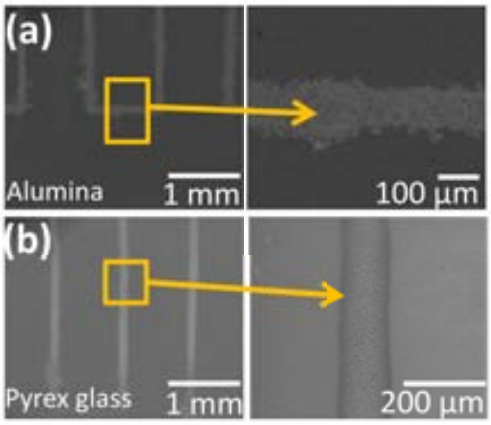


**Figure 6.36.:** Microestructural characterization by SEM of a LSMO device on (a) polycrystalline alumina and (b) pyrex glass. In both cases, the wettability is controlled and tracks around $120\mu m$ are achieved. Drop pitch was set at $25\mu m$ in the transversal and longitudinal directions for the two cases.

In much the same way, printing of magnetoresistive devices based on squared wave shaped lines with a period of $2mm$ was also tested over polycrystalline substrates. In Fig. 6.37, it is shown a set of three printouts over alumina, pyrex and quartz glass after inkjet deposition.

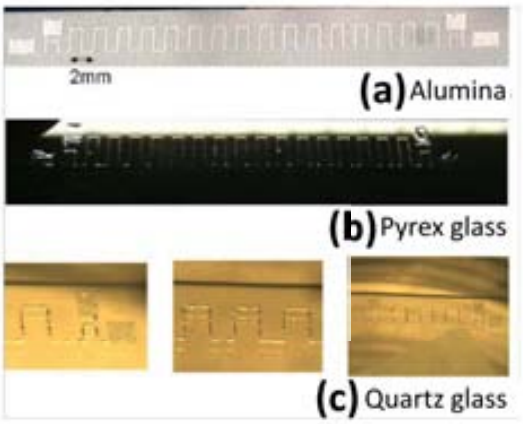


**Figure 6.37.:** LSMO magnetoresistive squared devices printed over several polycrystalline substrates. (a) polycrystalline alumina (b) pyrex glass (c) quartz glass before LSMO growth treatment. Beats are clear in the quartz glass substrate thus indicating therefore that surface tension of the ink should be accordingly decreased or, on the other hand, ink viscosity increased.

In this case, drop volume and surface tension have been modified to minimize the spreading in order to achieve thin tracks. The hydrophilic character of alumina and pyrex

glass allows good adherence of drops, while the high surface tension of the ink tends to decrease drop spreading. Track width obtained in both cases was around $120\mu m$.

Nevertheless, in the example of the less hydrophilic quartz glass, the track width is smaller (80 $\mu m$ in contrast to 120 $\mu m$), which suggests that the track width can be regulated by controlling the surface tension of the ink thus minimizing the ink spreading. In addition, in the quartz glass substrate, beats can be observed (Fig. 6.37c). As previously mentioned, these particular ink behaviour could be avoided by decreasing drop volume or increasing ink viscosity reducing in this last case the mobility of the solution. Work is currently ongoing in order to address the problem but it is important to remark that ink wettability should be adjusted for each substrate.

Apparently, the continuity of the device is noticed but conductive measurements show values of resistance about $20M\Omega$, which is quite a large value for practical applications. Thus, further optimization of the deposition and LSMO growth processes over polycrystalline substrates are underway in order to decrease those resistance values. Multideposition processes to increase the number of drops per unit area (up to 20 depositions) have been performed obtaining a decrease of the resistance until $5M\Omega$. However, previous experiments done with serigraphic pastes show that non-textured polycrystalline agreggates introduce a very high resistance trough the grain boundaries. They affect the magetoresistance and the resistivity of the material revealing so the improvement achieved by inkjet printing driven CSD processing.

### 6.6.6. Printing the LSMO magnetoresistive device on metallic tapes

The metallic substrates developed for CC's technology constitute a great opportunity to strongly reduce the cost of the LSMO devices. Getting profit about that substrate availability, our preliminary investigations were performed over commercial ferromagnetic Ni-W RABIT tape $10mm$ wide previously coated with an epitaxial LZO coating (Fig. 6.38). Fig. 6.38 displays some examples of LSMO devices on metallic Ni tape. Laboratory scale cost including both manufacturing and substrate entail a global reduction from ∼12 €/device for single crystals through ∼2 €/device for polycrystalline alumina to nearly 0.2 €/device on Ni-W metallic tape. Furthermore, metallic tapes offer the added value to constitute a true reel to reel manufacturing process.

**Figure 6.38.:** Series of LSMO printed device onto 10 mm Ni ferromagentic metallic tape. An epitaxial LZO buffer layer is commercially available on top of this metallic substrate.

As the structural characterization of a LSMO device on metallic tape shows the partial oxidation of the metallic substrate (Fig. 6.39), additional optimization of the LSMO

growth process on top of those pre-coated metallic substrates is still required. The high temperature of the thermal processing requires specific buffer layers able to stop oxygen diffusion. Although the texturing ability of the commercial LZO buffer layer is proved, protection against metallic substrate oxidation should be improved. Therefore, more research should be done in order to improve this promising option for this very low cost technique.

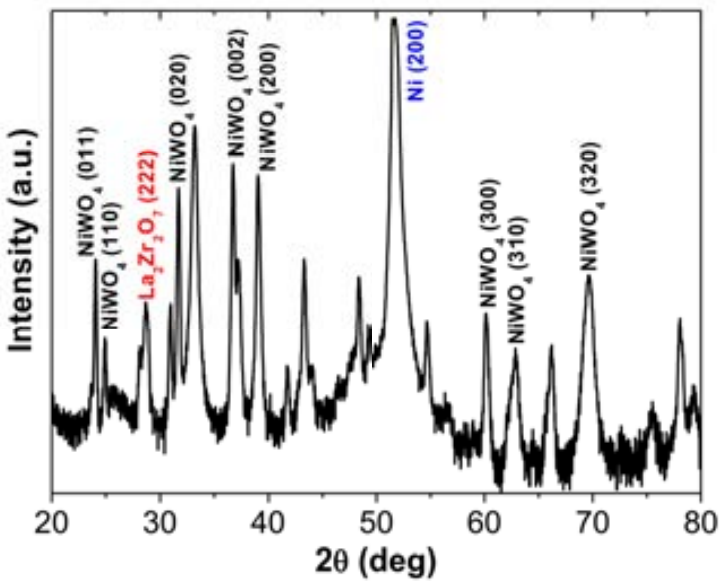


**Figure 6.39.:** Structural characterization of a LSMO round magnetoresistive device by conventional XRD. It may be observed in this XRD pattern, the complete oxidation of the buffered Ni-tape.

## 6.6.7. Upscaling of the LSMO magnetoresistive device

The LSMO device manufacturing has been systematically considered in the scope for industrial transferring. Stability and simplicity in the production of greener solutions and the use of specific properties of functional ceramic oxides for electronic operative devices have been items which we have devoted an important struggle along the EFECTS project.

The efficiency of the transferring process, however, requires an industrial scaling that should be preferably developed in a manufacturing environment. The established OXOLUTIA S.L. company, dedicated to the development of coating procedures based on CSD, acted as an endorser of the technique.

First experiments for medium scale LSMO device production were carried out using a 512 multinozzle piezo printhead with nominal drop volumes of $14pL$ (Fig. 6.40) mounted in a proprietary system. The system has been tested for scaling up achieving a resolution of 720x1440$dpi$ which is large enough to obtain reliable fusion of drops and line fidelity. Fig. 6.40b shows a serie of LSMO devices printed on SS tape in a reel to reel system from Brüker (GmbH) company. The substrate moved at a speed of $7.2m/h$ and the LSMO precursor ink employed was the one presented in Tab. 6.6.

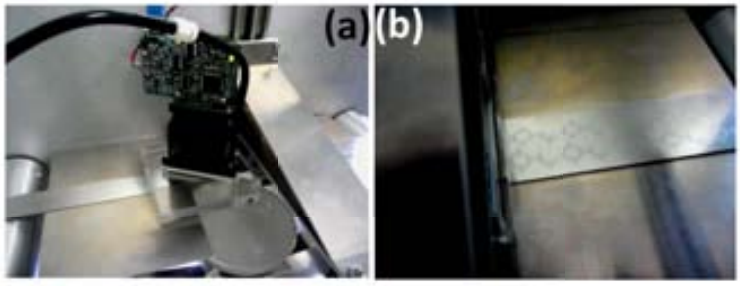


**Figure 6.40.:** (a) Detail of the reel to reel continuous printer for scaling demonstration. In the picture, a 512 nozzles Konika-Minolta printhead with 14pL of nominal drop volume mounted in a proprietary system is presented. (b) LSMO devices produced at a speed of $7.2m/h$. The substrate in this case was SS tape and the LSMO precursor solution was the same 0.05M (in Mn) water based ink with isopropanol and propionic acid treated in all this section.

The breakthrough in LSMO patterning without the need to use masks encourage the realization of magnetoresistive devices by combining the ferromagnetic and magnetoresistive LSMO phase with a shell of magnetically assisted deposited ferrite nanoparticles. As initial approach, we expected that those soft ferromagnetic ferrite nanoparticles [301] accurately positioned over the previous LSMO paths act as magnetic concentrators, enhancing the magnetic flux density over the printed LSMO paths, and therefore increasing the magnetoresistive ratio of LSMO based devices. Then, this composite system is expected to have higher sensitivity to magnetic fields than without the magnetic nanoparticle shell.

#### 6.6.7.1. Printing the magnetic nanoparticle shell: Preliminary results

Preliminar calculations (Fig. 6.41) show that the deposition of a magnetic shell over the LSMO increase the mean flux density over the magnetoresistive element in 16%. This increment supposes increasing the magnetoresistance from 0.3 to 0.4, a 33% respect the initial value.

In this regards, magnetic $Fe_3O_4$ nanorods [301] has been inkjetted on top of the magnetoresistive LSMO path under a magnetic field. Next Fig. 6.42 shows by SEM these magnetic $Fe_3O_4$ nanoparticles on top of the LSMO phase. No extra improvements in the magnetoresistance were observed, probably due to the low density of deposited nanoparticles. Further work increasing the type and density of these printed nanoparticles is underway in order to improve the magnetotransport properties of such inkjetted devices.

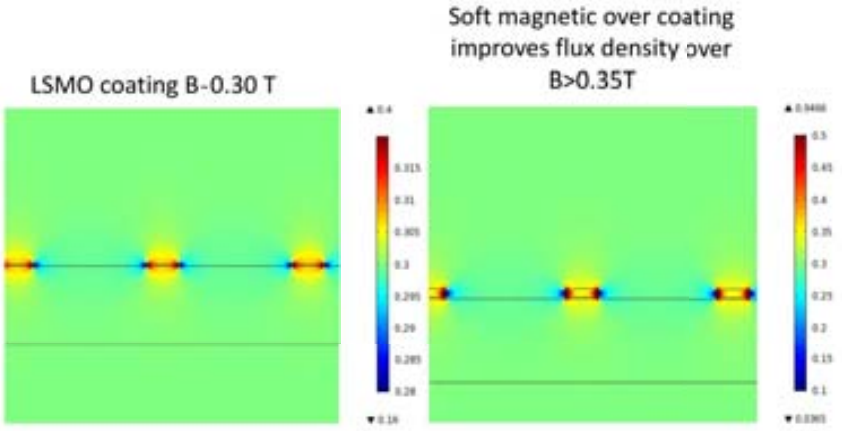


**Figure 6.41.:** Detail of the field calculations based on the magnetic properties. (a) without the nanoparticle shell. (b) with the nanoparticle shell.

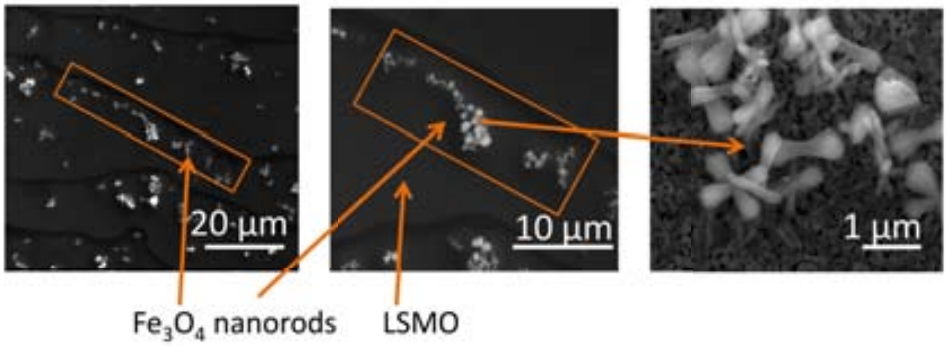


**Figure 6.42.:** SEM micrographs displaying the magnetic $Fe_3O_4$ nanoparticles on top of the LSMO phase.

## 6.7. Summary and conclusions

The development of adequate LSMO precursors in combination with the inkjet deposition and the corresponding thermal processing allow us to obtain LSMO tracks and more sophisticated magnetoresistive devices. For LSMO patterning purposes, it was developed a new LSMO ink formulation which combines the most interesting features of both acetate and propionate based LSMO precursor inks reported for films. Particularly, the printing optimization of a LSMO magnetoresistive device for position sensing was performed and the complete characterization displayed. Magnetoresistance values of about 0.35% at RT and zero applied magnetic field were achieved. Different attempts were made to improve the liquid management in order to obtain connected and continuous LSMO devices.

First, the interlaced approach was tested, however, as the drops which constitute the underlying layer were not dried when the posterior film is printed, they were not pinned on the substrate and ink displacements took place along it, obtaining disordered patterns with irregular liquid distributions. So as to enhance the liquid distribution over the substrate to improve the connectivity of the whole pattern, the second attempt was to increase the

wettability of the as-prepared ink with the substrate. In this regards, a solution with 5% by weight of polyethyleneimine (PEI) in methanol was used to impregnate the surface of the substrate in a first approach in order to increase the surface energy of the substrate. In parallel, this 5% by weight of PEI was introduced into the ink formulation with the same successful results. By means of this second approach, LSMO devices with acceptable homogeneity have been achieved on single crystal substrates. Although good performances are obtained on single crystal substrates, further optimization of inkjet deposition on top of them is ongoing in order to increase the pattern homogeneity.

In the quest to reduce the manufacturing costs and due to electrical and magnetic properties of the LSMO system are also appreciable on polycrystalline substrates, preliminary results on those substrates have been also outlined. Continuous optimization of the ink wetting behaviour on those polycrystalline substrates is required to enhance the LSMO pattern performances. The LSMO device manufacturing has been also considered in the scope for industrial transferring. First experiments for a medium scale were carried out and briefly described using the 512 multinozzle piezoelectric printhead.

Moreover, the most interesting aspect of the device upscaling tested in this work is the implementation of the metallic substrates developed for coated conductors technology as substrates for LSMO patterning. Although the optimization of the LSMO growth process on top of these buffered metallic tapes is absolutely required in order to prevent the metal oxidation, the availability in long lengths make their use in combination with the inkjet printing technology, a promising and flexible route for functional device manufacturing.

Finally, as a general observation, it is worth to remark that inkjet deposition is developed at an scale that can compete with the conventional methods in terms of pattern development and throughput. Similar device performances comparable to those fabricated by screen printing with pastes are achieved by CSD-inkjet technology. We may conclude that cost-effective materials options, high-throughput deposition techniques reviewed in this chapter offer the potential of low cost solution-processed functional devices.

# 7. Proposal of upscaling

As a final task, the technology implemented throughout this work is being up-scaled in order to produce YBCO coatings and CZO buffer layers by Chemical Solution Deposition (CSD) by OXOLUTIA SL. In this context of technology transferring from EFECTS project to real manufacturing companies, a new system which basically consists of a feed reel which holds the substrate, the printing module containing the 512 nozzle Konika Minolta piezoelectric printhead and finally the thermal treatment furnaces to obtain the ceramic oxide in the desired phase (see Fig. 7.1) was built.

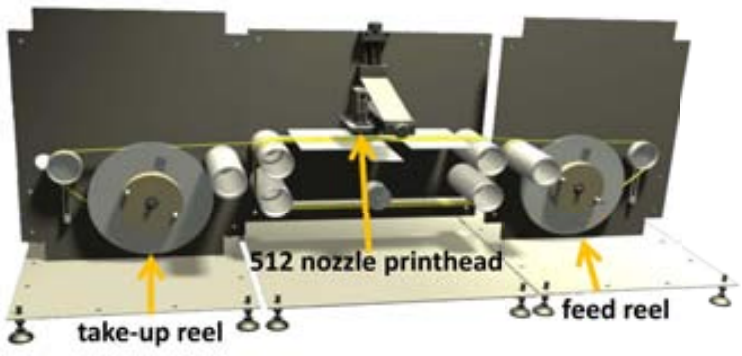


**Figure 7.1.:** Proposal of a continuous printing system in a standard reel to reel configuration.

Preliminary results regarding the manufacturing of $Ce_{0.9}Zr_{0.1}O_{2-x}$ films obtained by means of the previous system displayed in Fig. 7.1 are presented on commercial metallic tapes.

On top of this metallic substrate, it was deposited a CZO precursor solution (see sec. 3.1.3.1). Afterwards, the sample was heat-treated at 900°C in air during 1h. One meter has already been prepared with a $2m/h$ tape speed.

The quality of the buffer layer and, in particular, its surface is known to substantially affect the properties of the subsequent YBCO layer. In this sense, surface morphology and topography of as-grown CZO samples were studied through optical microscopy and atomic force microscopy (AFM). In Fig. 7.2a, it may be noticed that no cracks are detected and the sample displays an acceptable surface homogeneity. Previous works demonstrate [28,105] that an atomically flat terraced surface is strongly required for high performance epitaxial YBCO films. In this understanding, these CZO samples are being tested for the posterior YBCO growth (Fig. 7.2b). 2D and $\theta - 2\theta$ XRD diffraction patterns (Fig. 7.2c and d) show that CZO grows with a cube-on-cube type epitaxial relationship revealing a CZO single phase alhough further optimization of the inkjet deposition and growth processes is ongoing in order to increase the quality of these buffer layers.

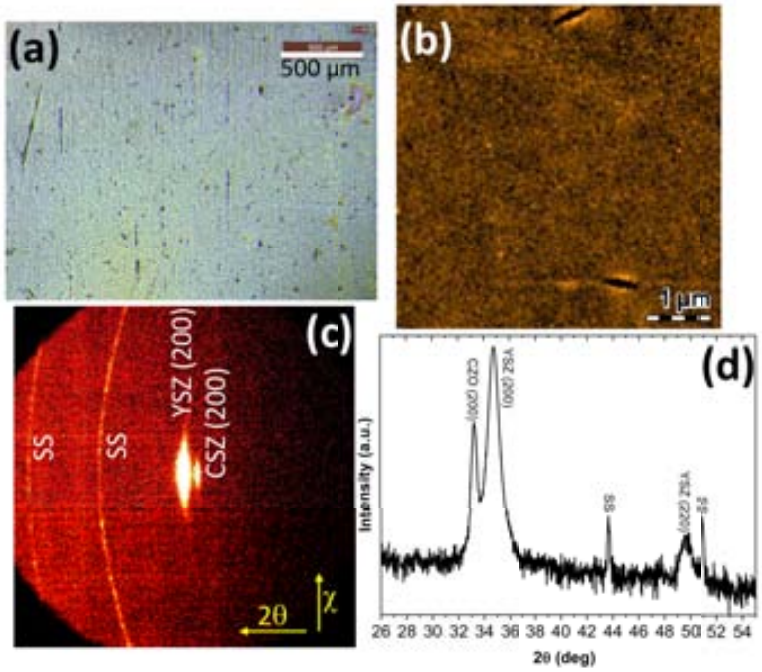


**Figure 7.2.:** Morphological, topographical and structural characterization of a CZO film obtained by means of a reel to reel continuous system. (a) OM microscopy of the CZO film. (b) AFM topographical analysis of the surface of the CZO film. Structural characterization of this CZO film by (c) 2D-GADDS and (d) $\theta - 2\theta$ XRD diagram of the CZO film displayed in (a).

We may conclude, then, that the development of high-quality and flat interfaces should constitute an essential practice for the preparation of all-chemical coated conductors constraint by the in-plane alignment of the underneath layers. Regarding this, the selection of the optimum deposition, growth and processing thermal treatments is a crucial step in the development of 2G coated conductors in long lengths.

## 7.1. Future work

So far, we have devoted a lot of effort to understand the basics of inkjet printing technology to obtain functional ceramic oxide layers and coatings at a laboratoy scale. Understanding better the factors and parameters which affect the drop formation and the fluid dynamics onto the substrate, together with the great relevance of the solution drying phenomenon in order to control the ink distribution has been proved to be crucial to improve the quality of those films and patterns. On other hand, while the feasibility of the implementation of inkjet printing technology with CSD methodology has been demonstrated, further knowledge of fluid dynamics and the required drying processes need to be acquired in order to scale such coatings in long lengths by high throughput methodologies. Furthermore, other aspects like ink compatibility with the materials of the printhead are also important issues to consider when chemical agressive inks are going to be printed.

# General conclusions

In this work, we have explored various functional ceramic oxide systems grown by combining the inkjet printing technology with the Chemical Solution Deposition (CSD) methodology, which allow the upscaling of the manufacture of low cost and high performance functional ceramic coatings. This manufacturing route has been assessed in novel applications. In particular, the present work shows the feasibility of using CSD based inks for the manufacturing of $YBa_2Cu_3O_{7-x}$, $La_{0.7}Sr_{0.3}MnO_3$ and $Ce_{0.9}Zr_{0.1}O_{2-x}$ ceramic oxides layers and patterns onto different substrates, which include $LaAlO_3$ and $SrTiO_3$ single crystals and metallic tapes, by proper adjustments of the rheological, wetting and drying characteristics of the inks. As a general rule, the control of the ink physicochemical properties such as density, surface tension, as well as viscosity and vapour pressure has been shown to be fundamental to control the drop formation and jettability, the ink-substrate interaction and solution dynamics onto the substrate, which at the end constrain the final morphology and performance of the deposit.

We have carried out a thoughtful analysis of drop formation dynamics dependence on the ink rheological and the drive parameters of the piezoelectric actuation waveform. This study allows tuning the rheology, surface tension, and driving signal in order to:

- obtain a unique single drop without satellites, cause they are detrimental for pattern resolution and accuracy.
- get adequate drop volumes accordingly to the printing application and the surface that is going to be covered.
- adjust drop speed to control spreading process and avoid singular effects such as splashing phenomena and/or re-bouncing processes.
- properly control the length and rupture times of the liquid thread, cause they determine the minimum working distance between the nozzle and the substrate, limiting therefore the maximum drop rate and so, the positioning error and printing speed.

An interesting application to modulate at a real time drop size is also described, which opens the possibility to combine in situ different layer thickness depending on the desired function, allowing to find and perform as well, a trade-off between dot quality and productivity. Such drop volume modulation was accomplished by modifying the total pulse width of the drive waveform of the piezoelectric element.

Furthermore, it has been demonstrated that stable single drops with the inverse of the Ohnesorge number Z, significantly larger than 14, may be obtained by tuning the excitation conditions of the driving signal, are obtained by tuning the excitation on harmonics.

Once a single drop with adjusted speed and volume is generated, the experimental sequences to obtain continuous, homogeneous and high-performance coatings and patterns

have been developed for, basically, two various functional oxides systems, $YBa_2Cu_3O_{7-x}$ and $La_{0.7}Sr_{0.3}MnO_3$. The control of the ejected volume from the printhead and the adaptation of the ink rheology and wetting parameters by selecting the appropriate solvent and additives have been shown to be essential for a full and homogeneous coverage of the surface.

Two printhead devices, electromagnetically driven valves and piezoelectric dispensers have been employed and also compared. The larger drop volumes, in the $nL$-$\mu L$ range, provided by the electromagnetic printhead, made more difficult to manage the deposited volume onto the substrate. Thus, the switching to the piezoelectric heads due to their smaller drops (in the $pL$ range), together with the simultaneous optimization of the ink formulation, favoured to obtain continuous and homogeneous coatings as well as more precise patterns like multifilamentary structures and more extended devices.

Besides, a model for track formation has been proposed. It has been demonstrated that is crucial to choose systems with pinned contact line for homogeneous track formation. Also, a proper tuning of the ink formulation and, therefore, ink vapour pressure, among other variables such as drop pitch and platform speed, are absolutely required to control in order to avoid particular bead morphologies such as bulging, film retraction or coffee staining.

By using a single nozzle piezoelectric printhead with a nozzle diameter of $60\mu m$, highly homogeneous and epitaxial tracks onto $LaAlO_3$ single crystal with average thickness of $250nm$ and ~$150\mu m$ wide were obtained showing a maximum critical current density $J_c$ at self field and $77K$ of $1.1MA/cm^2$. Further optimization of the ink composition by using 1,3-propanediol enables to obtain thinner structures. Moreover, it has been exhibited that by tuning the ejected volume either using smaller nozzle diameters or smaller drop volumes, thinner features may be achieved. It has also been demonstrated that the track thickness may be modulate by controlling the number of consecutive depositions on top of each other.

High-quality, continuous and well textured YBCO layers have been prepared from printing optimal TFA precursor inks by using the single nozzle piezoelectric printhead with $60\mu m$ of nozzle diameter. Critical current densities $J_c$ up to $3MA/cm^2$ at $77K$ and self field with thickness up to $400nm$ has been achieved, while in films of about $600nm$, $J_c$ decreases to $1.2MA/cm^2$ at $77K$ and self field, thus displaying that there is some room for improvement in the inkjet deposition and YBCO growth processes of those thicker films. In further work, based in the dissertation here presented, thinner YBCO full coatings of about $150nm$ with $J_c$ as high as $4.8MA/cm^2$ at $77K$ and self field have been recently reached by means of a multinozzle piezoelectric printhead. It demonstrates that the superconducting performances obtained by inkjetted CSD based coatings are comparable with those achieved by the conventional spin-coating technique. It opens the possibility to explore how to build up YBCO films, tracks and more complex devices which could contribute to the development of low AC HTS devices.

In addition, our work stresses that by modifying the number of drops per unit area, film thickness may be controlled, as the thickness varies linearly with the number of drops per unit area. As well, compacting rates along the thermal steps may be determined by calculating the slope of the thickness versus the number of drops per unit area dependence.

Preliminary results of YBCO layers onto buffered metallic tapes are ongoing. Further work in this field is absolutely necessary in order to optimize the corresponding YBCO growth process and the quality of the underlying buffer layers.

Regarding the LSMO ceramic system, different metallorganic precursor inks have been developed for coating and patterning. For LSMO coating, an acetate and propionate based LSMO precursor solutions were prepared. However, for LSMO patterning purposes, it was developed a new LSMO ink formulation which combines the most interesting features of both solutions obtained for LSMO coating. Epitaxial LSMO growth has been achieved in both full and patterned coatings onto LAO and STO single crystal substrates by means of piezoelectric and electromagnetic printheads. Magnetic properties of these solution-derived LSMO coatings show evidence of Curie temperature values around $360K$, i.e. close to the reported bulk values and the typical ferromagnetic behaviour at room temperature.

In particular, a LSMO magnetoresistive device was obtained after the corresponding printing and wetting behaviour optimizations. The liquid management onto the substrate was controlled by increasing the surface energy of the substrate when its surface is impregnated with a solution that contains a donor atom, which increases the wettability of the ink on the substrate by means of supramolecular long range interactions. Those LSMO inkjetted devices display a magnetoresistance coefficient of about 0.35% at room temperature and at zero applied magnetic field, which make those differential functional devices very appealing from the applications point of view.

Since acceptable device performances were reached on single crystal substrates and due to electrical and magnetic properties are also observable in cheaper polycrystalline substrates, effort has been done in order to reproduce in a medium scale the manufacturing of these magnetoresistive devices. Non-textured polycrystalline substrates were used as a first attempt in order to reduce the overall costs of the manufacturing process. However, the most relevant aspect on LSMO device upscaling is the preliminary tests performed onto metallic buffered tapes. Taking benefit about the developed substrate technology behind the coated conductors technology and their availability in long lengths, the combination of the inkjet printing technology with the existing CSD methodology show an enormous potential in the low cost manufacturing of functional ceramic devices.

Although there are still questions to be asked and answered about droplet generation process and wetting behaviour as each new system to be printed requires their own optimization, the versatility that offers the combination of CSD, in turn, with the inkjet printing technology, is evidenced in the ability to produce full coatings with controlled thickness and multifilamentary coatings, as well as arbitrary patterns by acting upon the ink formulation, drop pitch, drop volume and drop speed. The reported results contribute to illustrate and open a flexible way for the manufacturing of new products and applications. In this regards, nowadays, this approach has been transferred to industry for the medium scaling of a number of processes like the scale-up of 2G CC's, the deposition of $Ce_{0.9}Zr_{0.1}O_{2-x}$ buffer layers or the inkjet printing of functional devices.

In conclusion, this report has allowed exploring the enormous potentiality of CSD methodology implemented with the inkjet printing technology and the huge and complex chances related to ink formulation for various functional ceramic oxide systems. Furthermore, we would like to emphasize as well that our work shows that the combination of

the know-how on the CSD methodologies with the inkjet printing technology contributes to open a simple and flexible way to low cost manufacturing of electronic, magnetic and superconducting functional devices based on ceramics.

# A. Glossary in fluid dynamics

This appendix will review the relevant fluid properties of interest in inkjet printing. It includes the most relevant parameters that affect the working window of the printhead itself, the ejection of the ink through the printhead and the impact of the ink onto the substrate. This will be followed by a brief description of the main procedures that can be found for the measurement of those properties.

In addition to precursor properties, the decision of which solvent(s) should be selected for the ink must be take into account not only for the particular precursor system, also for other important properties, such as evaporation rate, which control the gel formation. The ink viscosity, surface tension and contact angle which makes the ink with the substrate are also crucial properties that must be evaluated cause they will dictate the wetting behaviour onto the substrate, among others.

## A.1. Density

The density ($\rho$) of a fluid is defined as the ratio of the mass of the fluid ($m$) to its volume ($V$). That is,

$$\rho = \frac{m}{V}$$

The SI unit for the density is [kg/m$^3$]. For liquids, it is not a strong function of temperature and pressure. The density of different liquids may achieve such diverse values as 999 kg/m$^3$ for water at 16°C or 13550 kg/m$^3$ for the mercury at 20°C.

## A.2. Viscosity

Another important fluid property will be introduced in this section: the viscosity. To illustrate the concept, the simplest conceptual configuration is employed in Fig. A.1, which consists of a fluid being sheared between two infinite and parallel plates separated by a distance $h$. The top plate moves at a constant velocity $v$ and the lower one is fixed ($v = 0$). This is known as Couette flow. In that understanding, the fluid speed drops down to 0 through the gap size $h$ and the shear flow created between the plates has the velocity profile given by the following equation: $v_x = v \cdot \frac{y}{h}$.

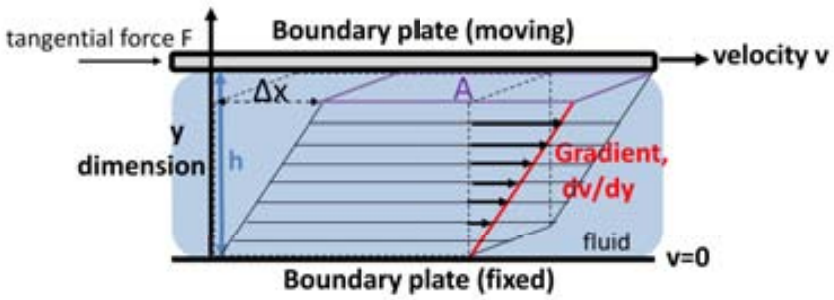


**Figure A.1.:** Laminar flow between two-parallel plates. Friction between the fluid and the moving boundaries causes the fluid to shear. The force required for this action is a mesure of the fluid viscosity.

If the difference between the moving plate and the stationary one is not too large, then the fluid flows in smooth and parallel layers with different speeds; that is, the flow of the fluid is laminar. In this case, the fluid speed varies linearly from the maximum value $v$ at the upper plate to 0 at the bottom boundary. Each layer of fluid moves faster than the one below it, and the friction between them gives rise to a force opposite to their relative motion. Specifically, the fluid applies on the upper plate an opposite force to the motion, and a force on the bottom boundary of the same magnitude but in the other sense. Therefore, an external force $F$ is required in order to keep the top plate moving at a constant velocity $v$. When an external force $F$ is applied to the fluid, it suffers a deformation $D = \frac{x}{h}$ . The magnitude of this tangential force $F$ is found to be proportional to the speed $v$ and the area $A$ of each plate and inversely proportional to the separation $h$ between layers. That is,

$$F = C \cdot \mathrm{A} \cdot \frac{v}{y}$$

The ratio of the tangential force $F$ to the plate area $A$ is the **shear stress**, $\tau$ (**sec. A.2.1**), $\tau = \frac{F}{A}$. The parameter C in this formula is a factor mainly linked to the physicochemical nature of the fluid involved and is called **viscosity**, $\eta$. The ratio $\frac{v}{y}$ is called **shear rate** $\dot{\gamma}$ (sec. A.2.2) and is the derivative of the fluid speed in the direction perpendicular to the motion plate (in the $y$ direction).

## A.2.1. Shear stress

A force $F$ applied tangentially to an area, $A$, being the interface between the upper plate and the liquid underneath, leads to a flow in the fluid. The speed of flow that can be maintained for a given force, i.e for a given *shear stress* $\tau$, is controlled by the internal resistance of the liquid, i.e. the viscosity of the ink, $\eta$.

$$F = \tau = \frac{force\ F}{area\ A}$$

### A.2.2. Shear rate

The shear stress $\tau$ causes the liquid to flow in a certain pattern. The speed differential across the gap size or the change of deformation per unit time is termed "*shear rate* $\dot{\gamma}$" and mathematically is defined as:

$$\dot{\gamma} = \frac{dv}{dy}$$

In 1687, Isaac Newton was the first to express the basic law of viscosimetry describing the flow behaviour of an ideal liquid:

$$\tau = \eta \cdot \frac{dv}{dy} = \eta \cdot \dot{\gamma} \tag{A.1}$$

The above equation is referred to as Newton's law of viscosity. This equation can also be applied in cases where the gradient velocity does not vary linearly. The proportionality constant $\eta$ is called the coefficient of viscosity or simply the ***viscosity*** $\eta$ and measures the resistance of the fluid against deformation. It has units of $[N \cdot s/m^2]$ in SI units. Sometimes, it is also expressed in the CGS system as $[dyn \cdot s/cm^2]$ and this unit is called a poise $(P)$.

### A.2.3. Viscosity

Solving equation A.1 for the viscosity $\eta$ gives $\eta =$ –. The SI unit for the viscosity is the $[Pa \cdot s]$. The unit $[mPa \cdot s]$ is also often used. Typical viscosity values at 20°C in $[mPa \cdot s]$ are shown in next table:

| **Substance** | **Viscosity (mPa · s)** |
|---|---|
| Petrol | 0.65 |
| Water | 1 |
| Ethanol | 1.2 |
| Mercury | 1.5 |
| Grape juice | 2-5 |
| Coffee cream | ∼10 |
| Honey | $\sim 10^4$ |
| Polymer melts | $\sim 10^3$-$10^6$ |
| Bitumen | $\sim 10^8$ |
| Glass | $\sim 10^{23}$ |

**Table A.1.:** Typical viscosity values at 20°C in mPa · s.

## A.2.4. Flow and viscosity curves

The correlation between the shear stress $\tau$ and the shear rate $\dot{\gamma}$, called the *flow curve*, defines the flow behaviour of a liquid and is graphically displayed in a diagram of shear stress versus shear rate. Another diagram very commom is the *viscosity curve*: in this graph it is represented the viscosity $\eta$ versus the shear rate $\dot{\gamma}$. Next Fig. A.2 shows both classical representations for the parameters which are involved in flow.

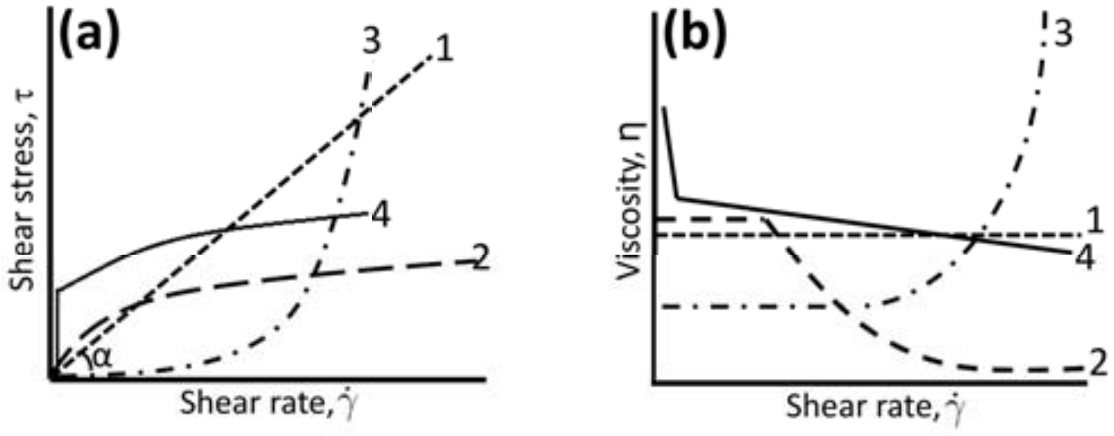


**Figure A.2.:** Various types of common flow behaviours. (a) Different flow curves depending the physicochemical nature of the liquid. (b) Viscosity curves corresponding to the flow curves of Fig. A.2a. (1) Newtonian fluid (2) Shear thinning fluid (pseudoplastic fluid) (3) Shear thickening fluid (dilatant fluid) (4) Bingham plastic fluid (pseudoplastic fluid with yield point). Fluids numbered as 2, 3 and 4 are considered Non-Newtonian fluids.

## A.2.5. Flow properties regarding viscosity behaviour

**Newtonian inks** Newtonian liquids exhibit a "Newtonian flow behaviour" under certain conditions of stress or shear rate. Newton assumed that the graphic equivalent of his equation (equation A.1) is a linear straight starting at the origin with a certain slope $\alpha$ (Fig. A.2a). Any point on this straight line define pairs of values for $\tau$ and $\dot{\gamma}$ with a constant ratio. Dividing $\tau$ by $\dot{\gamma}$ give the value of the viscosity of the fluid $\eta$. Then, this means that in this case (in curves numbered as 1 in Fig. A.2), the viscosity $\eta$ is not affected by changes in the shear rate $\dot{\gamma}$. By definition, the viscosity of a newtonian fluid depends on the temperature, pressure and chemical nature of the fluid but not on the forces acting upon it. Water, milk, mineral oils, bitumen are Newtonian inks.

**Non-Newtonian inks** For non-Newtonian fluids, the shear stress is not a linear function of the shear rate. Their viscosity changes with the applied strain rate and depends not only on the temperature but also on the shear rate. Some common types of non-Newtonian fluids are shear thinning fluids (pseudoplastic fluids), shear thickening fluids (also called dilatant fluids) and Bingham plastic fluids (pseudoplastic fluids with a yield point). For shear thinning fluids (number 2 in Fig. A.2), the viscosity decreases with shear rate, which means that for a given force, more mass can be made to flow. An example of a shear

thinning fluid is the latex paint. When brushing paint on a wall, it is noted that the larger the applied shear rate, the less resistance is found. Other examples are emulsions, suspensions, polymer solutions, milk, blood or jelly. With increasing shear rates, molecules and/or particles are turned in the direction of the flow, re-oriented and/or re-shaped in the same direction that the stress, being possible reasons for the shear thinning of materials. It should be mentioned that the shear thinning or pseudoplastic flow behaviour of these inks is not constant over the range of low to high shear rates. At low shear rates this type of inks behave as Newtonian fluids, molecules and/or particles move randomly in spite of the shear stress applied. When shear rate increases, it induces the orientation, extension, deformation and remodelling of the entities in the same direction that the flow and therefore viscosity drops drastically. Going to higher shear rates the viscosity does not increase more because the maximum shear orientation has been reached.

Shear thickening fluids (number 3 in Fig. A.2), named also dilatant fluids, show a dilatant fluid behaviour under certain conditions of shear stress or rate, which means that their viscosity increases when shear rate increases. Examples of shear thickening fluids are quicksand, water-corn flour mixtures and highly concentrated aqueous solutions of sugar. If we try to mix water with corn starch, the larger the applied shear rate, more resistance will be encountered. At low shear rates, the solute molecules can flow without assemble them and the fluid behaves as a Newtonian liquid. When the shear rate increases, solute particles collapse and agglomerate producing an increase of the viscosity. Since this fluid behaviour complicates production conditions is not convenient to work with this type of inks and usually an ink reformulation to avoid such viscosity increase is advisable.

Another non-Newtonian fluid is the Bingham plastic (number 4 in Fig. A.2). It describes pseudoplastic liquids with a characteristic yield point. The yield point of the material divides the elastic from the viscous flow behaviour. Bingham plastics only start flowing after being subjected to a certain force (shear stress), i.e. after a certain yield point, which strongly depends on external parameters like temperature and change rate of the acting force. They are mostly dispersions, such as toothpastes, greases, natural rubber polymers which at rest are subjected to binding forces such as hydrogen bonds, van der Waals forces, etc. These forces limit the volume change that can suffer the substance and define a certain value of viscosity. External forces, if smaller than the ones required to break the binding forces, will deform the substance elastically and the solid will recover its shape when the applied stresses are removed. Only when external forces are strong enough to overcome these binding forces, that is, only when the applied external forces overcome the yield point of the material, the substance begins to deform plastically and in a non-reversible way behaving as a viscous fluid.

There are other examples of fluid behaviours. For instance, in some fluids, the viscosity is a function of the time upon shearing. In the thixotropic fluids, the viscosity decreases with the duration of the applied shear stress. The application of the shear stress destroys the structure within the material which is totally recovered when the shear stress is removed. Honey and ketchup are some examples of thixotropic fluids. On the other hand, in the case of fluids which show a rheopectic behaviour, viscosity increases under shear deformation as a function of time. Some lubricants are examples of rheopectic fluids but this flow behaviour is quite rare.

Since the viscosity of those non-Newtonian fluids is a function of the applied shear

rate, more convenient studies, such as oscillatory shear or extensional flow tests could be more adequate to characterize these type of fluids.

## A.3. Wetting

In next sections, fundamental concepts of wetting [302, 303] will be introduced. The versatility of wetting problems such as interpretation of contact angles, hysteretic effects on the contact angle and their associated interfacial phenomena [189, 304], dewetting of films, spreading on a substrate, etc. are crucial processes which have a great importance in inkjet printing.

Wetting phenomena include important aspects of practical surface chemistry and many examples can be observed every day. For instance, when it rains, raindrops do not spread over the car window due to the hydrophobic characteristics of the surface. In a similar way, hydrophobic objects (i.e. spiders, beetles...) may walk on water even if their density exceeds that of the water. Also, rain cloths and tarp's tent should preferably be water repellent. Other examples are the selective wetting of mixtures in minerals, used as a basis of separation in the process known as flotation or the controlled extent of wetting on the substrate.

In next sections we first provide an introduction to the concept of the contact angle. This is followed by an explanation of the relationship between the contact angle and the surface energy of the solid upon which the individual methods for calculating the surface energy are based. In addition, various methods of measuring contact angles are briefly described and an introduction is given to the theoretical background of the methods used in the DSA program for calculating these contact angles from the video images of sessile drops or the surface tension from pendant drops. Further sections deal with a description of the surface tension concept with briefly comments about the common techniques used for surface tension measurements.

### A.3.1. Contact angle

When a drop of liquid is placed on a solid surface, the liquid will spread to a limited extent remaining as a dicrete drop on the solid when an equilibrium state is achieved. Equilibrium means that no net force acts on the system, so it can be derived, mechanically, from the balance of surface tensions of the three interfaces and, thermodynamically, from the minimization of the Helmholtz energy at a given volume and temperature. The quantitative measure of the wetting process is taken to be the ***contact angle*** $\theta$ that the drop makes with the solid at the "three-phase contact line" (see Fig. A.3) [189]. The contact angle is a suitable macroscopic characteristic and appears as a powerful tool to characterize the wettability of a liquid on a solid surface if it is measured under specified conditions of equilibrium, time, temperature, cleanliness of the surface, topography and homogeneity, etc [188].

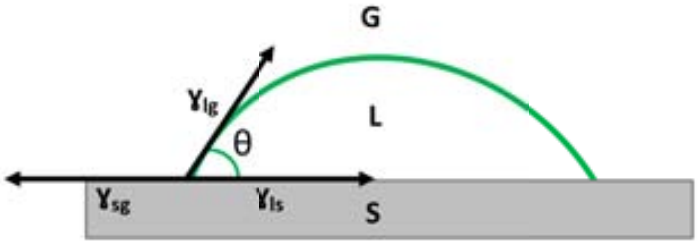


**Figure A.3.:** Contact angle $\theta$ that makes the liquid with the solid and components of surface tensions. The wetting of a solid by a liquid in the presence of a second fluid phase will be controlled by the surface tensions among the three phases: $\gamma_{lv}$ is the liquid-vapour surface tension, $\gamma_{sv}$ is the solid-vapour surface tension and $\gamma_{sl}$ is the solid-liquid surface tension.

However, next figure illustrates a real drop profile. It can be distinguished two regions: the macroscopic drop and a precursor film of the order of few $nm$ in thickness beyond the macroscopic drop. Flow in the bulk of the drop and close to the three-phase contact perimeter behaves differently due to the different liquid dimensions involved and, therefore, they should be mathematically treated in a different way. Mention that the most part of the techniques from literature which measure drop profiles [190] cannot detect the deviations from the macroscopic behaviour and the measured contact angle is extrapolated from the liquid-gas interface.

The outward pull on the perimeter by the unbalanced capillary forces tend to draw a precursor film out of the droplet. The precise profile depends on the system: on the molecular friction of the precursor film, on the viscous friction in the macroscopic part of the droplet, etc. These precursor films have been experimentally observed by scanning microscopy, ellipsometry as described in [305].

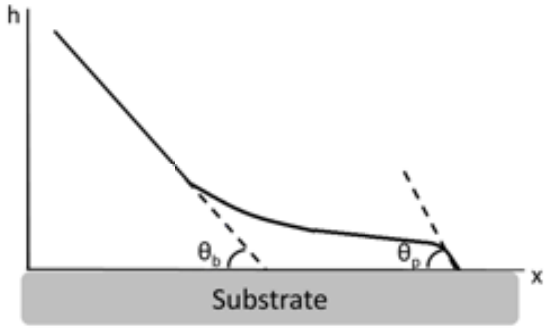


**Figure A.4.:** Schematic picture of a precursor film. The contact angle $\theta_b$ refers to the bulk contact angle and $\theta_p$ refers to the contact angle of the precursor film.

## A.3.2. Thermodynamics of wetting: Young's equation

The basic scope for the application of contact angles and wetting phenomena has been set in the field of thermodynamics.

As mentioned before, when a drop of liquid is placed on an ideal solid surface, it forms an angle $\theta$ with the surface, called contact angle. Assuming that these solid and

liquid phases are in equilibrium with the surrounding vapour phase, this contact angle is defined by the mechanical equilibrium of the drop under the action of three surface tensions involved (Fig. A.3): $\gamma_{lv}$, the liquid-vapour surface tension, $\gamma_{sv}$ is the solid-vapour surface tension and $\gamma_{sl}$ is the solid-liquid surface tension. In this regard, is possible to write an equation which describes the balance of forces in the horizontal direction:

$$\Delta G = \gamma_{sv}\Delta A_{sv} + \gamma_{sl}\Delta A_{sl} + \gamma_{lv}\Delta A_{lv} = 0$$

and,

$$\gamma_{sv} = \gamma_{sl+}\gamma_{lv}cos\theta \tag{A.2}$$

The previous equation was proposed by Young in 1805 and is generally known as ***Young s equation*** [302]. This relationship could provide a rapid insight about the wettability of the liquid on the solid and the ability to alter one or several of those surface energy components makes possible to direct the system towards the desired wetting properties.

Although Young's equation has been used since the 19th century, is still controversial and as its simplicity allows us to extract powerful information about wettability, important considerations should be taken into account. Equation A.2 assumes that the solid surface is smooth, rigid and homogeneous which might be only an ideal situation. Both roughness and chemical heterogeneity can be introduced in the equation A.2 in form of empirical corrections. Also, Young's equation is valid only for mechanical equilibrium, so it does not apply when spreading takes place. So, we consider that when the contact angle measurement is performed, the liquid drop has been allowed to come to its true state of thermodynamic equilibrium. Important issues are how fast and what is the final equilibrium situation. This equation allows us to determine the macroscopic contact angle and it seems not so easy to translate this value to the molecular scale. Until these days, how this thermodynamic contact angle relates to the one that is physically measurable remains an important issue to solve.

Between the four variables $\gamma_{sl}$, $\gamma_{sv}$,$\gamma_{lv}$ and $\theta$; only $\gamma_{lv}$ and $\theta$ are directly measurable. There are various methods which allow the determination of the surface energy of solids from contact angle data. They are mainly based on combining various starting equations for $\gamma_{sl}$ with the equation from Young to obtain equations of state in which $cos\theta$ represents a function of the phase surface tensions and, if applicable, the surface tensions components [306]. According to Owens, Wendt, Rabel and Kaelble, the surface tension of each phase can be split up into a polar and a disperse fraction [307]. In the Owens method, the equation system for the surface tension $\gamma_{sl}$ is solved using the contact angles of two liquids with known disperse and polar fractions of the surface tension. Kaelble solved the equation for combinations of two liquids and calculated the mean values of the resulting values for the surface energy. Rabel made it possible to calculate the polar and disperse

fractions of the surface energy with the aid of a single linear regression from the contact angle data of various liquids. Wu also started with the polar and disperse fractions of the surface energy of the participating phases. However, in contrast to Fowkes and Owens, Wendt, Rabel and Kaelble, who used the geometric mean of the surface tensions in their calculations, Wu used the harmonic mean. Oss and Good [308] also differentiate between polar and a disperse fraction of the surface energy. However, in contrast to the previously mentioned authors, they describe the polar fraction with the help of the acid-base model according to Lewis. The equation of state [306] only provides useful results when only disperse interactions are present or when these are in the majority. But, there are blibliography proving that surface tension component approaches fails and do not reflect physical reality [200]. A more complete thermodynamic analysis contemplate the effect of line tensions leading to the modified Young's equation. Neumann [253] proposed that line tensions are of the order of magnitude of $10^{-6} J/m$ for many solid-liquid systems, suggesting that the effect of line tension is negligible in contact angle measurements with drop diameters in the order of few $mm$.

Ideally, according to Young's equation, a unique contact angle is expected for a certain solid-liquid-gas system. However, in a real system, a range of contact angles is obtained. The upper limit is the advancing contact angle, $\theta_a$, while the lower limit is the receding contact angle, $\theta_r$. The difference between those angles is known as the contact angle hysteresis [309, 310]. Practically, because all solid surfaces exhibit contact angle hysteresis, the interpretation of contact angle in terms of Young's equation exhibits important restrictions. Even though, it is a good starting point for the determination of surface tensions [199, 311].

### A.3.3. Contact angle hysteresis

Contact angle hysteresis is a phenomenon in which the advancing contact angle, $\theta_{adv}$ differs from the receding contact angle value, $\theta_{rec}$ [309, 310]. It means that advancing and receding fronts pass through a serie of metaestable intermediate states, where at these positions, thermodynamics can also be applied. "Advancing" refers to the change in which the contact line moves in such a way that the surface of the substrate that originally is not covered, becomes wetted. The term "receding" refers to the inverse. The contact line recedes leaving part of the initially wetted substrate uncovered. Those contact angles are static quantities although one needs a dynamic step even if only extremely short in order to define a static entity. Therefore, we shall define these contact angles as the contact angles just before the wetting line starts to advance or starts to recede. The advancing contact angle always exceeds the receding one ($\theta_{adv} > \theta_{rec}$) [312].

Contact angle hysteresis is not completely understood, and there are many suggestions to possible factors involved [313]. It has been attributed to *surface roughness, chemical heterogeneity*, specific *geometric details*, molecular rearrangements, interdiffusion, adsorption, surface deformation and interactions between the liquid and the solid but the real causes of contact angle hysteresis are difficult to ascribe due to the lack of information on the submicroscopic properties of solid surfaces [310].

## A.3.4. Surface tension

If we consider any liquid surface in the absence of other external forces, they tend to reduce to the minimum surface area. If we want to extend the surface area, then we need to carry out work against the cohesive forces. This indicates that this surface has a free energy higher than the liquid bulk. This extra energy, which acts parallely to the surface, is thermed ***surface tension*** (Fig. A.5) [189, 314].

The existence of the surface tension is expected from the difference in energies and reactivities between the molecules at the surface and the molecules in the bulk phase of the material, which represents an excess of energy of the system relative to the bulk [315]. Basically, the surface tension is given by the number of bonds per unit area and the bond strength. This asymetrical environment between the interface and the core of the substance implies that work must be done in creating a new surface. This work $\delta w$ is proportional to the number of molecules brought from the bulk to the surface, and hence to the area $\delta A$ of the new surface: $\delta w \propto \delta A$ or $\delta w = \gamma \delta A$, where $\gamma$, the constant of proportionality is the surface tension. Note that it has dimensions of energy per unit area ($J/m^2$) or force per unit length ($mN/m$). To relate these two concepts, consider an arbitrary surface with perimeter $l$ that is extended $\delta x$. The increase in area $\delta A$ is given by: $\delta w = \gamma \delta x$. The work done $\delta w$ in increasing the area is: $\delta w = \gamma \delta A = \gamma l \delta x$. If that work is done by a force $F$, which is applied to the perimeter, then: $\delta w = F \delta x$, and so, $\gamma = F/l$. Surface tension $\gamma$ acts like a force per unit length of the perimeter opposing any attempt to increase the area [316].

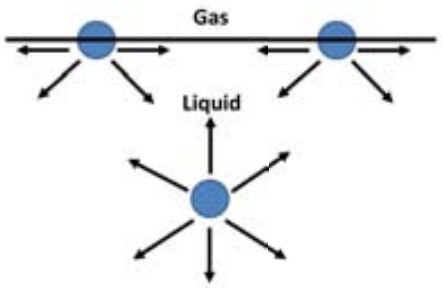


**Figure A.5.:** Definition of surface tension $\gamma$. Surface tension tends to reduce the area of the interface. Due to the different energetic and chemical environment, the molecules in the bulk possess different energy from those at the interface.

Surface tension is a force that operates along the surface and acts perpendicular and inward from the surface. Although the force acting on each individual unit at the surface is directed inward, the resultant force on all the surface units gives rise to the apparent existence of a tangential tension along the surface. Therefore, we see that two possible interpretations of $\gamma$ are possible: force per unit length of boundary of the surface and energy per unit area of the surface.

In next table are presented typical values of surface tension for a variety of liquids and solids in air at room temperature. The previous definitions and concepts should be applied also for solids. However, the lack of mobility of the atoms in a solid cannot be rearranged rapidly and a true equilibrium state can not be obtained.

| **Liquid** | **Surface tension $\gamma$ at 20°C** $(mN/m)$ |
|---|---|
| n-hexane | 18.4 |
| methanol | 22.5 |
| ethanol | 22.4 |
| chloroform | 28.5 |
| carbon disulfide | 32.3 |
| water | 72.8 |
| mercury | 484 |
| PTFE | 19.1 |
| Polyethylene | 33.1 |
| Glass | 95 |

**Table A.2.:** Representative values of $\gamma$ at 20°C of different liquid/air and solid/air interfaces. Source: D.H. Kaelbe, *Physical Chemistry of Adhesion*, Wiley, New York, 1971.

Regarding surface tensions of solids; silica, glass, metals, metal oxides, metal sulfides, and inorganic salts are examples of high-energy surfaces. Most solid organic compounds, such as polymers, have low-energy surfaces.

### A.3.5. Effects of curved interfaces: the Young-Laplace equation

When a curved surface exists, a pressure difference $\Delta p$ operates across a curved interface. The equation that relates this pressure difference with the curvature of the surface is known as the Young-Laplace equation [189] and was derived in 1805:

$$\Delta p = \gamma \quad \frac{1}{R_1} + \frac{1}{R_2} \tag{A.3}$$

where $\gamma$ is again the surface tension, and $R_1$ and $R_2$ are the radii of curvature of the two normal sections of the surface perpendicular one to another.

The force provided by the pressure difference $\triangle p$ between both sides of the curved surface balances the downward surface tension force. Since the pressure is the driving force for capillary action, then, the liquid will flow from high to low pressure until the differential pressure is decreased and finally eliminated.

There are several special cases of equation A.3:

1. For a spherical surface; $R_1 = R_2 = R_s$; therefore: $\Delta p = 2\gamma/R_s$; the greater pressure inside the spherical surface causes the surface curvature.
2. For a cylindrical surface; $R_1$ ; then: $\triangle p = \gamma/R_2$.

3. For a planar surface; $R_1 = R_2$ ; therefore: $\Delta p = 0$.

Essentially, the shape of a drop is determined by a combination of surface tension and gravity effects. Surface forces tend to make drops spherical, while gravity tends to elongate a pendant drop or flatten a sessile drop.

#### A.3.5.1. Work of adhesion and cohesion

Two important thermodynamic relationships are the work of adhesion $W_{AB}$ [317] and the work of cohesion $W_{AA}$ [202,312]. Suppose two substances A and B: the reversible work necessary to separate two phases is the sum of works: the one to eliminate the A-B interface and the work to create the interfaces A-air and B-air. In this way, $W_{AB} = \gamma_A + \gamma_B - \gamma_{AB}$ is the work of adhesion, which measures the attraction between the liquid and the solid. When A=B, we talk about work of cohesion and is defined as $W_{AA} = 2\gamma_A$. This would be the reversible isothermal work to break a column of liquid or solid of the same material. There is an interesting equation which relates the contact angle that makes a liquid onto a solid with the surface tension of the liquid by the work of adhesion, $W_{AB}$, which measures the attraction between the liquid and the solid. It is defined as follows:

$$W_{AB} = \gamma_{lv} \cdot (1 + cos\theta)$$

# Bibliography


[1] L.W. Martin and D.G. Schlom. Advanced synthesis techniques and routes to new single-phase multiferroics. *Solid State and Materials Science*, **16**: 199, (2012).

[2] D.P Norton. Synthesis and properties of epitaxial electronic oxide thin-film materials. *Materials Science and Engineering*, **R43**: 139, (2004).

[3] R.W. Schwartz, T. Schneller, and R. Waser. Chemical solution deposition of electronic oxide films. *Comptes Rendus Chimie*, **7**: 433, (2004).

[4] X. Obradors, T. Puig, A. Pomar, F. Sandiumenge, N. Mestres, M. Coll, A. Cavallaro, N. Roma, J. Gazquez, J.C. Gonzalez, O. Castano, J. Gutierrez, A. Palau, K. Zalamova, S. Morlens, A. Hassini, M. Gibert, S. Ricart, J.M. Moreto, S. Pinol, D. Isfort, and J. Bock. Progress towards all-chemical superconducting $YBa_2Cu_3O_7$ -coated conductors. *Superconductor Science and Technology*, **19**: S13, (2006).

[5] T. Puig, J.C. Gonzalez, A. Pomar, N. Mestres, O. Castano, M. Coll, J. Gazquez, F. Sandiumenge, S. Pinol, and X. Obradors. The influence of growth conditions on the microstructure and critical currents of TFA-MOD $YBa_2Cu_3O_7$ films. *Superconductor Science and Technology*, **18**: 1141, (2005).

[6] A. Hardy, D. Mondelaers, M.K. Van Bael, J. Mullens, L.C. Van Poucke, G. Vanhoyland, and J. D'Haen. Synthesis of $(Bi, La)_4Ti_3O_{12}$ by a new aqueous solution-gel route. *Journal of the European Ceramic Society*, **24**: 905, (2004).

[7] A. Carretero-Genevrier, N. Mestres, T. Puig, A. Hassini, J. Oro, A. Pomar, F. Sandiumenge, X. Obradors, and E. Ferain. Single-crystalline $La_{0.7}Sr_{0.3}MnO_3$ nanowires by polymer-template-directed chemical solution synthesis. *Advanced Materials*, **20**: 3672, (2008).

[8] J.G. Wan, X.W. Wang, Y.J. Wu, M. Zeng, Y. Wang, H. Jiang, W.Q. Zhou, G.H. Wang, and J.M. Liu. Magnetoelectric $CoFe_2O_4$-$Pb(Zr,Ti)O_3$ composite thin films derived by a sol-gel process. *Applied Physics Letters*, **86**: 122501, (2005).

[9] M. Gibert, T. Puig, X. Obradors, A. Benedetti, F. Sandiumenge, and R. Huhn. Self-organization of heteroepitaxial $CeO_2$ nanodots grown from chemical solutions. *Advanced Materials*, **19**: 3937, (2007).

[10] B. Derby. Inkjet printing of functional and structural materials: fluid property requirements, feature stability and resolution. *Annual Review of Materials Research*, **40**: 395, (2010).

[11] D.B. Bogy and F.E. Talke. Experimental and theoretical study of wave propagation phenomena in drop-on-demand ink jet devices. *IBM Journal of Research and Development*, **28**: 3, (1984).

[12] H. Wijshoff. The dynamics of the piezo inkjet printhead operation. *Physics Reports*, **491**: 77, (2010).

[13] J. Heinzl and C. Hertz. Ink-jet printing. *Advances in Electronics and Electron Physics*, **65**: 91, (1985).

[14] H. Dong, W.W. Carr, and J.F. Morris. An experimental study of drop-on-demand drop formation. *Physics of Fluids*, **18**: 072102, (2006).

[15] N. Reis, C. Ainsley, and B. Derby. Ink-jet delivery of particle suspensions by piezoelectric droplet ejectors. *Journal of Applied Physics*, **97**: 094903, (2005).

[16] B.J. De Gans and U.S. Schubert. Inkjet printing of well-defined polymer dots and arrays. *Langmuir*, **20**: 7789, (2004).

[17] J.E. Fromm. Numerical calculation of the fluid dynamics of drop-on-demand jets. *IBM Journal of Research and Development*, **28**: 322, (1984).

[18] D. Jang, D. Kim, and J. Moon. Influence of fluid physical properties on ink-jet printability. *Langmuir*, **25**: 2629, (2009).

[19] S.D. Hoath, I.M. Hutchings, G.D. Martin, T.R. Tuladhar, M.R. Mackley, and D. Vadillo. Links between ink rheology, drop-on-demand jet formation, and printability. *Journal of Imaging Science and Technology*, **53**: 041208, (2009).

[20] D. Bonn, J. Eggers, J. Indekeu, J. Meunier, and E. Rolley. Wetting and spreading. *Review of Modern Physics*, **81**: 739, (2009).

[21] A.L. Yarin. Drop impact dynamics: splashing, spreading, receding, bouncing. *Annual Review of Fluid Mechanics*, **38**: 159, (2006).

[22] P. Calvert. Inkjet printing for materials and devices. *Chemistry of Materials*, **13**: 3299, (2001).

[23] M. Vilardell, X. Granados, S. Ricart, I. Van Driessche, A. Palau, T. Puig, and X. Obradors. Flexible manufacturing of functional ceramic coatings by inkjet printing. *Thin Solid Films*, **548**: 489, (2013).

[24] H. Sirringhaus and T. Shimoda. Inkjet printing of functional materials. *Materials Research Society Newsletter*, **28**: 802, (2003).

[25] J. Feys, P. Vermeir, P. Lommens, S.C. Hopkins, X. Granados, B.A. Glowacki, M. Baecker, E. Reich, S. Ricard, B. Holzapfel, P. Van Der Voort, and I. Van Driessche. Ink-jet printing of $YBa_2Cu_3O_7$ superconducting coatings and patterns from aqueous solutions. *Journal of Materials Chemistry*, **22**: 3717, (2012).

[26] H. Rogalla and P.H. Kes. *100 Years of Superconductivity*. CRC Press, 2011.

[27] M. Salamon. The physics of manganites: structure and transport. *Reviews of Modern Physics*, **73**: 583, (2001).

[28] M. Coll. *Chemical solution deposition of oxide buffer and superconducting layers for $YBa_2Cu_3O_7$ coated conductors*. PhD thesis, Universitat Autonoma de Barcelona, (2010).

[29] X. Obradors, T. Puig, S. Ricart, M. Coll, J. Gazquez, A. Palau, and X. Granados. Growth, nanostructure and vortex pinning in superconducting $YBa_2Cu_3O_7$ thin

films based on trifluoroacetate solutions. *Superconductor Science and Technology*, **25**: 123001, (2012).

[30] M Ziese. Colossal magnetoresistance, half metallicity and spin electronics. *The Royal Society*, **358**: 137, (2000).

[31] D. Nassyrov, C. Muller, A. Roige, I. Burgues-Ceballos, O. Osso, D.B. Amabilino, M. Garriga, M.I. Alonso, A.R. Goni, and M. Campoy-Quiles. Vapour printing: pattering of the optical and electrical properties of organic semiconductors in one simple step. *Journal of Materials Chemistry*, **22**: 4519, (2012).

[32] S.E. Habas, A.S. Heather, M.F. Platt, and D.S. van Hest, A.M. Ginley. Low-cost inorganic solar cells: from ink to printed device. *Chemical reviews*, **110**: 6571, (2010).

[33] H. Sirringhaus, T. Kawase, R.H. Friend, T. Shimoda, M. Inbasekaran, W. Wu, and E.P. Woo. High-resolution inkjet printing of all-polymer transistor circuits. *Science*, **290**: 2123, (2000).

[34] L. Gonzalez-Macia, A. Morrin, M.R. Smyth, and A.J. Killard. Advanced printing and deposition methodologies for the fabrication of biosensors and biodevices. *Analyst*, **135**: 845, (2010).

[35] A. Teichler, J. Perelaer, and U.S. Schubert. Inkjet printing of organic electronics: comparison of deposition techniques and state of the art developments. *Journal of Materials Chemistry C*, **1**: 1910, (2013).

[36] L. Zhang, H. Liu, Y. Zhao, X. Sun, Y. Wen, Y. Guo, X. Gao, C. A. Di, G. Yu, and Y. Liu. Inkjet printing high-resolution, large-area graphene patterns by coffee-ring lithography. *Advanced Materials*, **24**: 436, (2012).

[37] W.J. Gallagher and S.S.P. Parkin. Development of the magnetic tunel junction MRAM at IBM: From first junctions to a 16-Mb MRAM demonstrator chip. *IBM Journal of Research and Development*, **50**: 5, (2006).

[38] J.M. De Teresa, A. Barthelemy, A. Fert, J.P. Contour, F. Montaigne, and P. Seneor. Role of metal-oxide-interface in determining the spin polarization of magnetic tunel junctions. *Science*, **286**: 507, (1999).

[39] F.F. Lange. Chemical solution routes to single-crystal thin films. *Science*, **273**: 903, (1996).

[40] H. Le. Progress and trends in ink-jet printing technology. *Society for Imaging Science and Technology*, (2008).

[41] Y. Tokura and Y. Tomioka. Colossal magnetoresistive manganites. *Journal of Magnetism and Magnetic Materials*, **200**: 1.

[42] M. Bode. Spin-polarized scanning tunneling microscopy. *Reports on Progress in Physics*, **66**: 523, (2003).

[43] A. Schwarz and R. Wiesendanger. Magnetic sensitive force microscopy. *Nano Today*, **3**: 28, (2008).

[44] A. Gupta, R. Jagannathan, E.I. Cooper, E.A. Giess, J.I. Landman, and B.W. Hussey. Superconducting oxide-films with high transition-temperature prepared from metal trifluoroacetate precursors. *Applied Physics Letters*, **52**: 2077, (1988).

[45] J. Yang, J. Kin, and Y. Kang. Effects of piezoelectric constants and thickness of lead-zirconate-titanate ceramics on the performances of inkjet printheads. *The Journal of the Korean Society*, **59**: 3008, (2011).

[46] C.E. Romano and L.J. Shaw-Klein. Inkjet recording element. (U.S.Patent 0123675 A1), (2009).

[47] E. Solano. *Synthesis and characterisation of ferrite nanoparticles for* $YBa_2Cu_3O_{7-x}$ *- nanocomposite superconducting layers: a neutron and synchrotron study.* PhD thesis, Universitat Autonoma de Barcelona, (2013).

[48] A. de Luca, M.T. Cole, A. Fasoli, S.Z. Ali, F. Udrea, and W.I. Milne. Enhanced infra-red emission from sub-millimeter microelectromechanical system micro hotplates via inkjet deposited carbon nanoparticles and fullerenes. *Applied Physics*, **113**: 214907, (2013).

[49] S. Wenfeng, Z. Xianpeng, and H. Qijin. Preparation of solid silver nanoparticles for inkjet printed flexible electronics with high conductivity. *Nanoscale*, **6**: 1622, (2014).

[50] R. Ahmad, M. Vaseen, N. Tripathy, and Y.B. Hahn. Wide linear-range detecting nonenzymatic glucose biosensor based on CuO nanoparticles inkjet-printed on electrodes. *Analytical Chemistry*, **85**: 10448, (2013).

[51] M. Neophytou, F. Hermerschmidt, A. Savva, E. Georgiou, and S.A. Choulis. Highly efficient indium tin oxide-free organic photovoltaics using inkjet-printed silver nanoparticles current collecting grids. *Applied Physics Letters*, **101**: 193302, (2012).

[52] M. Arin, P. Lommens, S.C. Hopkins, G. Pollefeyt, J. Van der Eycken, S. Ricart, X. Granados, B.A. Glowacki, and I. Van Driessche. Deposition of photocatalytically active $TiO_2$ films by inkjet printing of nanoparticle $TiO_2$ suspensions obtained from microwave-assisted hydrothermal synthesis. *Nanotechnology*, **23**: 165603, (2012).

[53] M. Abulikemu, E.H. Daas, H. Haverinen, D. Cha, M.A. Malik, and G.E. Jabbour. In situ synthesis of self-assembled gold nanoparticles on glass or silicon substrates through reactive inkjet printing. *Angewandte*, **53**: 420, (2014).

[54] E. Butovsky, I. Perelshtein, I. Nissan, and A. Gedanken. Fabrication, characterization, and printing of conductive ink based on multi core-shell nanoparticles synthesized by RAPET. *Advanced Functional Materials*, **23**: 5794, (2013).

[55] M.F.A.M van Hest and D.S. Ginley. *In solution processing of inorganic materials.* John Wiley and Sons, (2009).

[56] C. Brinker and G.W. Scherer. *The physics and chemistry of sol-gel processing.* Academic Press, (1990).

[57] B.J. de Gans, P.C. Duineveld, and U.S. Schubert. Inkjet printing of polymers: State of the art and future developments. *Advanced Materials*, **16**: 203, (2004).

[58] E. Tekin, P.J. Smith, and U.S. Schubert. Inkjet printing as a deposition and patterning tool for polymers and inorganic particles. *Soft Matter*, **4**: 703, (2008).

[59] A. Cavallaro, F. Sandiumenge, J. Gazquez, T. Puig, X. Obradors, J. Arbiol, and H.C. Freyhardt. Growth mechanism, microestructure and surface modification of nanoestructured $CeO_2$ films by chemical solution deposition. *Advanced Functional Materials*, **16**: 1363, (2006).

[60] J.R. Waldram. *Superconductivity of Metals and Cuprates*. Institute of Physics Publishing, London, (1996).

[61] M.K. Wu, J.R. Ashburn, C.J. Torng, P.H. Hor, R.L. Meng, L. Gao, Y.Q. Huang, Z.J.and Wang, and C.W. Chu. Superconductivity at 93K in a new mixed-phase Y-Ba-Cu-O compound system at ambient pressure. *Physical Review Letters*, **58**: 908, (1987).

[62] M. Tinkham. *Introduction to Superconductivity*. McGraw-Hill, Singapore, (1996).

[63] A. Llordes, A. Palau, J. Gazquez, M. Coll, R. Vlad, A. Pomar, J. Arbiol, R. Guzman, s. Ye, V. Rouco, F. Sandiumenge, S. Ricart, T. Puig, M. Varela, D. Chateigner, J. Vanacken, J. Gutierrez, V. Moschchalkov, G. Deutscher, C. Magen, and X. Obradors. Nanoscale strain-induced pair suppression as a vortex-pinning mechanism in high-temperature superconductors. *Nature Materials*, **11**: 329, (2012).

[64] M. Coll, S. Ye, V. Rouco, A. Palau, R. Guzman, J. Gazquez, J. Arbiol, H. Suo, T. Puig, and X. Obradors. Solution-derived $YBa_2Cu_3O_7$ nanocomposite films with a $Ba_2YTaO_6$ secondary phase for improved superconducting properties. *Superconductor Science and Technology*, **26**: 015001, (2013).

[65] D. Larbalestier, A. Gurevich, D.M. Feldmann, and A. Polyanskii. High $T_c$ superconducting materials for electric power applications. *Nature*, **414**: 368, (2001).

[66] N. Nucker, H. Romberg, X.X. Xi, J. Fink, B. Gegenheimer, and Z.X. Zhao. Symmetry of holes in high-$T_c$ superconductors. *Physical Review B*, **39**: 6619, (1989).

[67] N. Nucker, E. Pellegrin, P. Schweiss, J. Fink, S.L. Molodtsov, C.T. Simmons, G. Kaindl, W. Frentrup, A. Erb, and G. Mullervogt. Site-specific and doping-dependent electronic-structure of $YBa_2Cu_3O_x$ probed by O-1s and Cu-2p X-Ray-absorption spectroscopy. *Physical Review B*, **51**: 8529, (1995).

[68] F. Beech, S. Miraglia, A. Santoro, and R.S. Roth. Neutron study of the crystal structure and vacancy distribution in the superconductor $Ba_2YCu_3O_7$. *Physical Review B*, **35**: 8778, (1987).

[69] V. Breit, P. Schweiss, R. Hauff, H. Wühl, H. Claus, H. Rietschel, A. Erb, and G. Müller-Vogt. Evidence for chain superconductivity in near-stoichiometric $YBa_2Cu_3O_x$ single crystals. *Physical Review B*, **52**: R15727, (1995).

[70] A. Palau. *Critical currents and dissipation of grain boundary networks in coated conductors*. PhD thesis, Universitat Autonoma de Barcelona, (2005).

[71] D. Dimos, P. Chaudhari, J. Mannhart, and F.K. Legoues. Orientation dependence of grain-boundary critical currents in $YBa_2Cu_3O_{7-x}$ bicrystals. *Physical Review Letters*, **61**: 219, (1988).

[72] N.F. Heinig, R.D. Redwing, I.F. Tsu, A. Gurevich, J.E. Nordman, S.E. Babcock, and D.C. Larbalestier. Evidence for channel conduction in low misorientation angle [001] tilt $YBa_2Cu_3O_{7-x}$ bicrystal films. *Applied Physics Letters*, **69**: 577, (1996).

[73] M. Paranthaman and T. Izumi. High-performance YBCO-coated superconductor wires. *Materials Research Bulletin*, **8**: 533, (2004).

[74] Y. Iijima and K. Matsumoto. High-temperature-superconductor coated conductors: technical progress in Japan. *Superconductor Science and Technology*, **13**: 68, (2000).

[75] A. Goyal, M. Paranthaman, and U. Schoop. The RABITS approach: using rolling-assisted biaxially textured substrates for high-performance YBCO superconductors. *Materials Research Bulletin*, **8**: 552, (2004).

[76] Y. Iijima, K. Kakimoto, Y. Yamada, T Izumi, T. Saitoh, and Y. Shiohara. Research and development of biaxially textured IBAD-GZO templates for coated conductors. *Materials Research Bulletin*, **8**: 564, (2004).

[77] X. Obradors and T. Puig. Coated conductors for power applications: materials challenges. *Superconductor Science and Technology*, **27**: 044003, (2014).

[78] A. Goyal, D.P. Norton, J.D. Budai, M. Paranthaman, E.D. Specht, D.M. Kroeger, D.K. Christen, Q. He, B. Saffian, F.A. List, D.F. Lee, P.M. Martin, C.E. Klabunde, E. Hartfield, and V.K. Sikka. High critical current density superconducting tapes by epitaxial deposition of $YBa_2Cu_3O_{7-x}$ thick films on biaxially textured metals. *Applied Physics Letters*, **69**: 1795, (1996).

[79] Y. Iijima, N. Tanabe, O. Kohno, and Y. Ikeno. In-plane aligned $YBa_2Cu_3O_{7-x}$ thin films deposited on polycrystalline metallic substrates. *Applied Physics Letters*, **60**: 769, (1992).

[80] J.M.D. Coey, M. Viret, and S. Von Molnar. Mixed-valence manganites. *Advances in Physics*, **48**: 167, (1999).

[81] S. Jin, T.H. Tiefel, M. McCormack, R.A. Fastnacht, R. Ramesh, and L.H Chen. Thousandfold change in resistivity in magnetoresistive La-Ca-Mn-O films. *Science*, **264**: 413, (1994).

[82] E. Dagotto, T. Hotta, and A. Moreo. Colossal magnetoresistant materials: the key role of phase separation. *Physics Reports*, **334**: 1, (2007).

[83] G.H. Jonker and J.H Van Santen. Ferromagnetic compounds of manganese with perovskite structure. *Physica*, **16**: 337, (1950).

[84] C. Zener. Interaction between the d-shells in the transition metals. II. ferromagnetic compounds of manganese with perovskite structure. *Physical Review*, **82**: 403, (1951).

[85] P.W. Anderson and H. Hasegawa. Considerations on double exchange. *Physical Review*, **100**: 675, (1955).

[86] P.G. de Gennes. Effects of double exchange in magnetic crystals. *Physical Review*, **118**: 141, (1960).

[87] A.M. Haghiri-Gosnet and J.P. Renard. CMR manganites: physics, thin films and devices. *Journal of Physics D*, **36**: 127, (2003).

[88] J. H. Park, E. Vescovo, H.J. Kim, C. Kwon, R. Ramesh, and T. Venkatesan. Direct evidence for a half-metallic ferromagnet. *Nature*, **392**: 794, (1998).

[89] K. Dorr. Ferromagnetic manganites: spin-polarized conduction versus competing interactions. *Journal of Physics D*, **39**: 125, (2006).

[90] C. Adamo, X. Ke, H.Q. Wang, H.L. Xin, T. Heeg, M.E. Hawley, W. Zander, J. Schubert, P. Schiffer, D.A. Muller, L. Maritato, and D.G. Schlom. Effect of biaxial strain on the electrical and magnetic properties of (001) $La_{0.7}Sr_{0.3}MnO_3$ thin films. *Applied Physical Letters*, **95**: 112504, (2009).

[91] A. Urushibara, Y. Moritomo, T. Arima, A. Asamitsu, G. Kido, and Y. Tokura. Insulator-metal transition and giant magnetoresistance in $La_{1-x}Sr_xMnO_3$. *Physical Review B*, **51**: 14103, (1995).

[92] T. Venkatesan, M. Rajeswari, Z.W. Dong, S.B. Ogale, and R. Ramesh. Manganite-based devices: opportunities, bottlenecks and challenges. *Philosophical Transactions of the Royal Society of London Series A*, **356**: 1661, (1998).

[93] M. Ohring. *Materials science of thin films: deposition and structure*. Academic Press, (1992).

[94] F. Yang, N. Kemik, M.D. Biegalski, H.M. Christen, E. Arenholz, and Y. Takamura. Strain engineering to control the magnetic and magnetotransport properties of $La_{0.67}Sr_{0.33}MnO_3$ thin films. *Applied Physical Letters*, **97**: 092503, (2010).

[95] J.L. Maurice, F. Pailloux, A. Barthelemy, O. Durand, D. Imhoff, R. Lyonnet, A. Rocher, and J.P. Contour. Strain relaxation in the epitaxy of $La_{2\ 3}Sr_{1\ 3}MnO_3$ grown by pulsed-laser deposition on $SrTiO_3$(001). *Philosophical Magazine*, **83**: 3201, (2003).

[96] C.T. Campbell and C.H.F. Peden. Oxygen vacancies and catalysis on ceria surfaces. *Science*, **309**: 713, (2005).

[97] A. Trinchi, Y.X. Li, W. Wlodarski, S. Kaciulis, L. Pandolfi, S. Viticoli, E. Comini, and G. Sberveglieri. Investigation of sol-gel prepared $CeO_2$-$TiO_2$ thin films for oxygen gas sensing. *Sensors and Actuators B: Chemical*, **95**: 145, (2003).

[98] S. Tsunekawa, T. Fukuda, and A. Kasuya. Blue shift in ultraviolet absorption spectra of monodisperse $CeO_{2-x}$ nanoparticles. *Journal of Applied Physics*, **87**: 1318, (2000).

[99] J.A. Kilner. Defects and conductivity in ceria-based oxides. *Chemistry Letters*, **37**: 1012, (2008).

[100] V.D. Kosynkin, A.A. Arzgatkina, E.N. Ivanov, M.G. Chtoutsa, A.I. Grabko, A.V. Kardapolov, and N.A. Sysina. The study of process production of polishing powder based on cerium dioxide. *Journal of Alloys and Compounds*, **303**: 421, (2000).

[101] A. Pignolet, C. Curran, M. Alexe, S. Senz, and D. Hesse. Epitaxial and large area PLD ferroelectric thin film heterostructures on silicon substrates. *Integrated Ferroelectrics*, **21**: 485, (1998).

[102] K.B Sundaram, P.F. Wahid, and P.J. Sisk. Characterization and optimization of cerium dioxide films deposited by RF magnetron sputtering. *Thin Solid Films*, **221**: 13, (1992).

[103] E. Stewart, M.S. Bhuiyan, S. Sathyamurhy, and M. Paranthaman. Studies of solution deposited cerium oxide thin films on textured Ni-alloy substrates for YBCO superconductor. *Materials Research Bulletin*, **41**: 1063, (2006).

[104] V.R. Vlad, K. Zalamova, M. Coll, A. Pomar, A. Palau, J. Gutierrez, T. Puig, X. Obradors, and A. Usoskin. Growth of chemical solution deposited YBCO/(Ce,Zr)$O_2$/YSZ/SS Coated Conductors. *IEEE Transactions on Applied Superconductivity*, **19**: 3212, (2009).

[105] M. Coll, J. Gazquez, F. Sandiumenge, T. Puig, X. Obradors, J.P. Espinos, and R. Huhne. Nanostructural control in solution-derived epitaxial $Ce_{1-x}Gd_xO_{2-y}$ films. *Nanotechnology*, **19**: 395601, (2008).

[106] M. Coll, J. Gazquez, R. Huhne, B. Holzapfel, Y. Morilla, J. Garcia-Lopez, A. Pomar, F. Sandiumenge, T. Puig, and X. Obradors. All chemical $YBa_2Cu_3O_7$ superconducting multilayers: Critical role of $CeO_2$ cap layer flatness. *Journal of Materials Research*, **24**: 1446, (2009).

[107] M. Singh, H.M. Haverinen, P. Dhagat, and G.E. Jabbour. Improved flux pinning in $YBa_2Cu_3O_7$ with nanorods of the double perovskite $Ba_2YNbO_6$. *Advanced Materials*, **22**: 673, (2010).

[108] J.C. Owens. A tutorial on printing. *Society for Imaging Science and Technology*, (2008).

[109] M. Wang, G.Z. Yang, M. Wang, and T. Liu. Effect of film thickness controlled by ink-jet printing method on the optical properties of an electroluminescent polymer. *Polymers for Advanced Technologies*, **21**: 381, (2010).

[110] K. Murata. Super-fine ink-jet printing for nanotechnology. *Proceedings of the International Conference on MEMS, NANO and Smart Systems*, **110**: 346, (2003).

[111] R.G. Self and D.B. Wallace. Method of drop size modulation with extended transition time waveform. (U.S.Patent 6,029,896), (2000).

[112] B.V. Antohe and D.B. Wallace. Acoustic phenomena in a demand mode piezoelectric ink jet printer. *Journal of Imaging Science and Technology*, **46**: 409, (2002).

[113] D.B. van Dam and C. Le Clerc. Experimental study of the impact of an ink-jet printed droplet on a solid substrate. *Physics of Fluids*, **16**: 3403, (2004).

[114] Y. Son, C. Kim, D.H. Yang, and D.J Ahn. Spreading of an inkjet droplet on a solid surface with a controlled contact angle at low Weber and Reynolds number. *Langmuir*, **24**: 2900, (2008).

[115] B. Derby. Inkjet printing ceramics: From drops to solid. *Journal of the European Ceramic Society*, **31**: 2543, (2011).

[116] P.J. Smith and S. Magdassi. *The Chemistry of Inkjet inks*. Singapore: World Scientific, (2010).

[117] O. Basaran, H. Gao, and P. Bhat. Nonstandard inkjets. *Annual Review of Fluid Mechanics*, **45**: 85, (2013).

[118] G.D. Martin, S.D. Hoath, and I.M. Hutchings. Inkjet printing - the physics of manipulating liquid jets and drops. *Engineering and Physics*, **105**: 012001, (2008).

[119] http://www.microfab.com/images/pdfs/technote99-01.pdf, 2013.

[120] W.G. Hawkins and I. Rezanka. Thermal ink jet printing. *Imaging Science and Technology Report*, **7**: 1, (1992).

[121] A.S. Yang, C.H. Cheng, and F.S. Hsu. PZT actuator applied to a femto-liter droplet ejector. *Journal of Mechanical Science and Technology*, **21**: 1732, (2007).

[122] T. Takahashi. Adaptability of piezoelectric inkjet head. *International Conference on Digital Printing Technologies 17*, **17**: 323, (2001).

[123] http://www.domino-printing.com/global/en/home.aspx, 2013.

[124] F. Savart. Memoires sur la constitution des veines liquides lancees par des orifices circulaires en mince paroi. *Annales de Chimie et de Physique*, **53**: 337, (1833).

[125] Lord Rayleigh. On the instability of jets. *Proceedings of the London Mathematical Society*, **10**: 4, (1878).

[126] Lord Rayleigh. On the capillary phenomena of jets. *Proceedings of the Royal Society of London*, **10**:4, (1849).

[127] Lord Rayleigh. On the instability of a cylinder of viscous liquid under capillary force. *Philosophical Magazine*, **34**: 145, (1892).

[128] W. Thomson. Improvements in telegraphic receiving and recording instruments. (U.K.Patent 2,147), (1867).

[129] F. Kamphoefner. Ink jet printing. *IEEE Transactions on Electron Devices*, **19**: 584, (1972).

[130] E. Rune. Measuring instrument of the recording type. (U.S.Patent 2,566,443 A), (1951).

[131] C. Bardeau, D. Fressard, P. Atten, and B. Barbet. Formation of isolated drops in a continuous jet. *10th International Congress on Advances in Non-Impact Printing Technologies*, (1994).

[132] A. Atkinson, J. Doorbar, A. Hudd, D.L. Segal, and P.J White. Continuous ink-jet printing using sol-gel "ceramic" inks. *Journal of Sol-Gel Science and Technology*, **8**: 1093, (1997).

[133] W.Li. Method for encoding and decoding images. (U.S.Patent 5,592,569), (1997).

[134] J.M. Schneider, N.R. Lindblad, C.D. Hendricks, and J.M. Crowley. Stability of an electrified liquid jet. *Journal of Applied Physics*, **38**: 2599, (1967).

[135] K.C. Chaudhary and T. Maxworthy. The non-linear capillary instability of a liquid jet. Part 2: Experiments on jet behaviour before droplet formation. *Journal of Fluid Mechanics*, **96**: 275, (1980).

[136] W. T. Pimbley. Drop formation from a liquid jet: a linear one-dimensional analysis considered as a boundary value problem. *IBM Journal of Research and Development*, **20**: 148, (1976).

[137] P.H. Chen, W.C. Chen, and S.H. Chang. Bubble growth and ink ejection process of a thermal ink jet printhead. *International Journal of Mechanical Sciences*, **39**: 683, (1997).

[138] L. Setti, C. Piana, S. Bonazzi, D. Ballarin, D. Frascaro, A. Fraleoni-Morgera, and S. Giuliani. Thermal inkjet technology for the microdeposition of biological molecules as a viable route for the realization of biosensors. *Analytical Letters*, **37**: 1559, (2004).

[139] R. Parashkov, E. Becker, T. Riedl, H.H. Johannes, and W. Kowalsky. Large area electronics using printing methods. *Proceedings of the IEEE*, **93**: 1321, (2005).

[140] http://www.memjet.com/, 2014.

[141] J. F. Dijksman. Hydrodynamics of small tubular pumps. *Journal of Fluid Mechanics*, **139**: 173, (1984).

[142] D. Zhai, T. Zhang, J. Guo, X. Fang, and J. Wei. Water-based ultraviolet curable conductive inkjet ink containing silver nano-colloids for flexible electronics. *Colloids and Surfaces A: Physicochemical and Engineering Aspects*, **424**: 1, (2013).

[143] http://www.microfab.com/images/pdfs/technote99-02.pdf, 2013.

[144] J. Eggers and E. Villermaux. Physics of liquid jets. *Reports on Progress in Physics*, **71**: 036601, (2008).

[145] W.T. Pimbley and H.C. Lee. Satellite droplet formation in a liquid jet. *IBM Journal of Research and Development*, **21**: 21, (1977).

[146] A. Famili, S.A. Palkar, and W.J. Baldy. First drop dissimilarity in drop-demand inkjet devices. *Physics of Fluids*, **23**: 012109, (2011).

[147] H. Kang, D. Soltman, and V. Subramanian. Hydrostatic optimization of inkjet-printed films. *Langmuir*, **26**: 11568, (2010).

[148] A.M. Worthington. *A study of splahes*. Longmans, Green, and Co, (1908).

[149] S. Schiaffino and A. Sonin. Molten dropet deposition and solidification at low Weber numbers. *Physics of Fluids*, **9**: 3172, (1997).

[150] M. Pasandideh-Fard, Y.M. Qiao, S. Chandra, and J. Mostaghini. Capillary effects during droplet impact on a solid surface. *Physics of Fluids*, **8**: 650, (1996).

[151] A.L. Biance, C. Clanet, and D. Quere. First steps in the spreading of a liquid droplet. *Physical Review E*, **69**: 016301, (2004).

[152] I.M. Hutchings, G.D. Martin, and S.D. Hoath. High speed imaging and analysis of jet and drop formation. *Journal of Imaging Science and Technology*, **51**: 438, (2007).

[153] H. Park, W. Carr, J. Zhu, and J. Morris. Single drop impaction on a solid surface. *Fluid Mechanics and Transport Phenomena*, **49**: 2461, (2003).

[154] J. Stringer and B. Derby. Limits to feature size and resolution in ink jet printing. *Journal of the European Ceramic Society*, **29**: 913, (2009).

[155] I.V. Roisman, R. Rioboo, and C. Tropea. Normal impact of a liquid drop on a dry surface: model for spreading and receding. *Proceedings of the Royal Society A*, **458**: 1411, (2002).

[156] M. Passandideh-Fard, Y. M. Qiao, S. Chandra, and J. Mostaghimi. Capillary effects during droplet impact on a solid surface. *Physics of fluids*, **8**: 650, (1996).

[157] J. Fukai, Y. Shiiba, T. Yamamoto, O. Miyatake, D. Poulikakos, C.M. Megaridis, and Z. Zhao. Wetting effects on the spreading of a liquid droplet colliding with a flat surface: Experiment and modelling. *Physics of Fluids*, **7**: 236, (1995).

[158] R.E. Ford and C.G.L. Furmidge. Impact and spreading of spray drops on foliar surfaces. *Society of Chemical Industry*, **25**: 417, (1967).

[159] S. Sikalo, C. Tropea, and E.N. Ganic. Impact of droplets onto inclined surfaces. *Journal of Colloid and Interface Science*, **286**: 661, (2005).

[160] S. Chandra and C.T. Avedisian. On the collision of a droplet with a solid surface. *Proceedings of the Royal Society A*, **432**: 13, (1991).

[161] E.W. Collings, J.K. Markworth, J.K. McCoy, and J.H. Saunders. Splat-quench solidification of freely falling liquid-metal drops by impact on a planar substrate. *Journal of Materials Science*, **25**: 3677, (1990).

[162] T. Mao, D.C.S. Kuhn, and H. Tran. Spread and rebound of liquid droplets upon impact on flat surfaces. *Journal of American Institute of Chemical Engineers*, **43**: 2169, (1997).

[163] O.H. Engel. Water drop collisions with solid surfaces. *Journal of Research of the National Bureau of Standards*, **54**: 281, (1955).

[164] M. Strobel, C.S. Lyons, and K.L. Mittal. *Plasma surface modification of polymers: relevance to adhesion*. VSP BV, (1994).

[165] T.R. Hebner, C.C. Wu, D. Marcy, M.H. Lu, and J.C. Sturm. Ink-jet printing of doped polymers for organic light emitting devices. *Applied Physics Letters*, **72**: 519, (1998).

[166] F.C. Krebs, S.A. Gevorgyan, and J. Alstrup. A roll-to-roll process to flexible polymer solar cells: model studies, manufacture and operational stability studies. *Journal of Materials Chemistry*, **19**: 5442, (2009).

[167] S. Allard, M. Forster, B. Souharce, H. Thiem, and U. Scherf. Organic semiconductors for solution-processable field-effect transistors (OFETs). *Angewandte Chemie International Edition*, **47**: 4070, (2008).

[168] J. Perelaer, B.J. De Gans, and U.S. Schubert. Ink-jet printing and microwave sintering of conductive silver tracks. *Advanced Materials*, **18**: 2101, (2006).

[169] H.J. van Osch, J. Perelaer, A.W.M. de Laat, and U.S Schubert. Inkjet printing of narrow conductive tracks on untreated polymeric substrates. *Advanced Materials*, **20**: 343, (2008).

[170] C.M. Andres and N.A. Kotov. Inkjet deposition of layer-by-layer assembled films. *Journal of the American Chemical Society*, **132**: 14496, (2010).

[171] E. Tekin, B.J. De Gans, and U.S. Schubert. Ink-jet printing of polymers - from single dots to thin film libraries. *Journal of Materials Chemistry*, **14**: 2627, (2004).

[172] B.J. De Gans, E. Kazancioglu, W. Meyer, and U.S. Schubert. Ink-jet printing polymers and polymer libraries using micropipettes. *Macromolecular Rapid Communications*, **25**: 292, (2004).

[173] E. Sachs, M. J. Cima, P. Williams, D. Brancazio, and J. Cornie. Three dimensional printing: rapid tooling and prototypes directly from a CAD model. *Journal of Engineering for Industry*, **114**: 481, (1992).

[174] A. van den Berg, P. Smith, J. Perelaer, W. Schrof, S. Koltzenburgc, and U. Schubert. Inkjet printing of polyurethane colloidal suspensions. *Soft Matter*, **3**: 238, (2007).

[175] W.E. Katstra, R.D. Palazzolo, C.W. Rowe, B. Giritlioglu, P. Teung, and M.J. Cima. Oral dosage forms fabricated by three dimensional printing. *Journal of Controlled Release*, **66**: 1, (2000).

[176] K.A.M. Seerden, N. Reis, J.R.G. Evans, P.S. Grat, J.W. Halloran, and B. Derby. Ink-jet printing of wax-based alumina suspensions. *Journal of American Ceramic Society*, **84**: 2514, (2001).

[177] W.D. Teng and M.J. Edirisinghe. Development of ceramic inks for direct continuous jet printing. *Journal American Ceramic Society*, **81**: 1033, (1998).

[178] H. Minemawari, T. Yamada, H. Matsui, J. Tsutsumi, S. Haas, R. Chiba, R. Kumai, and T. Hasegawa. Inkjet printing of single-crystal films. *Nature*, **475**: 364, (2011).

[179] M. Vilardell, X. Granados, S. Ricart, R. Cobas, M. Arjona, T. Puig, X. Obradors, S.C. Hopkins, B.A. Glowacki, J. Bennewitz, M. Falter, and M. Backer. Ink jet printing for functional ceramic coatings. *Journal of Imaging Science and Technology*, **55**: 040304, (2011).

[180] I. Van Driessche, J. Feys, S. C. Hopkins, P. Lommens, X. Granados, B.A. Glowacki, S. Ricart, B. Holzapfel, M. Vilardell, A. Kirchner, and M. Backer. Chemical solution deposition using ink-jet printing for YBCO coated conductors. *Superconductor Science and Technology*, **25**: 065017, (2012).

[181] T. Mouganie and B.A. Glowacki. Chemical synthesis and microstructural analysis of superconducting $YBa_2Cu_3O_{7-x}$ ink deposited by drop-on-demand ink-jet printing on silver substrates. *Journal of Materials Science*, **41**: 8257, (2006).

[182] P.C. McIntyre, M.J. Cima, M.F. Ng, R.C. Chiu, and W.E. Rhine. Texture development in $YBa_2Cu_3O_{7-x}$ films from trifluoroacetate precursors. *Journal of Materials Research*, **5**: 2771, (1990).

[183] J.Z Wang. Texture development in $YBa_2Cu_3O_{7-x}$ films from trifluoroacetate precursors. *Journal of Materials Research*, **5**: 2771, (1990).

[184] N. Roma, S. Morlens, S. Ricart, K. Zalamova, J.M. Moreto, A. Pomar, T. Puig, and X. Obradors. Acid anhydrides: a simple route to highly pure organometallic solutions for superconducting films. *Superconductor Science and Technology*, **19**: 521, (2006).

[185] A. Calleja, S. Ricart, X. Palmer, R.F. Luccas, T. Puig, and X. Obradors. Water determination of precursor solutions with oxidant cations by the Karl Fischer method: the YBCO-TFA case. *Journal of Sol-Gel Science and Technology*, **53**: 347, (2009).

[186] J. Drelich, C. Fang, and C.L. White. *Measurement of interfacial tension in fluid-fluid systems*. Marcel Dekker, (2002).

[187] R. Miller, V.B. Fainerman, A.V. Makievski, M. Ferrari, and G. Loglio. *Handbook of Applied Surface and Colloid Chemistry: Measuring dynamic surface tensions.* Wiley, (2001).

[188] A.W. Adamson. *Physical Chemistry of Surfaces.* Wiley, (1990).

[189] P.C. Hiemenz and R. Rajagopalan. *Principles of Colloid and Surface Chemistry.* Marcel Dekker, (1997).

[190] Y. Rotenberg, L. Boruvka, and A.W. Neumann. Determination of surface tension and contact angles from the shapes of axisymmetric fluid interfaces. *Journal of Colloid and Interface Science*, **93**: 169, (1983).

[191] H.H.J. Girault, D.J. Schiffrin, and B.D.V. Smith. The measurement of surface and interfacial tension by the axisymmetric drop technique. *Journal of Colloid and Interface Science*, **101**: 257, (1984).

[192] S.H. Anastasiadis, J.K. Chen, J.T. Koberstein, A.F. Siegel, J.E. Sohn, and J.A. Emerson. The determination of interfacial tension by video image processing of pendant fluid drops. *Journal of Colloid and Interface Science*, **119**: 55, (1987).

[193] J.F. Boyce, S. Schurch, Y. Rotenberg, and A.W. Neumann. The measurement of surface and interfacial tension by the axisymmetric drop technique. *Colloid Surfaces*, **9**: 307, (1984).

[194] F.K. Hansen and J. Rodsrud. Surface tension by pendant drop. *Journal of Colloid and Interface Science*, **141**: 1, (1991).

[195] Z. Xu and J.H. Masliyah. *Encyclopedia of surface and colloid science: Contact angle measurements on oxide and related surfaces.* Marcel Dekker, (2002).

[196] Dataphysics. *Interfacial Chemistry: Introduction into the operating OCA20, Measurements after the sessile drop method.* Dataphysics, (2000).

[197] J.G. Eagle and S. Pennell. Contact angle calculations from the contact/maximum diameter of sessile drops. *International Journal for Numerical Methods in Fluids*, **32**: 851, (2000).

[198] Y. Gu. *Encyclopedia of Surface and Colloid Science: Contact angle measurement techniques for determination of wettability.* Marcel Dekker, (2002).

[199] C.N. Catherine Lam, J.J. Lu, and A.W. Neumann. *Handbook of Applied Surface and Colloid Chemistry: Measuring contact angle.* Wiley, (2001).

[200] D.Y. Kwok and A.W. Neumann. Contact angle interpretation in terms of solid surface tension. *Colloids and Surfaces A: Physicochemical and Engineering Aspects*, **161**: 31, (2000).

[201] Dataphysics. *Interfacial Chemistry: Introduction into methods of measuring and analyzing contact angles for the determination of surface free energies of solids.* Dataphysics, (2000).

[202] G. Strom, M. Frederikson, and P. Stenius. Contact angles, work of adhesion and interfacial tensions at a dissolving hydrocarbon surface. *Journal of Colloid and Interface Science*, **119**: 352, (1987).

[203] H. Dong, W.W. Carr, and J.F. Morris. Visualization of drop-on-demand inkjet: drop formation and deposition. *Review of Scientific Instruments*, **77**: 085101, (2006).

[204] http://www.fujifilmusa.com/products, 2013.

[205] http://www.konicaminolta.com, 2013.

[206] J.M. Philipps. Substrate selection for high temperature superconducting thin films. *Journal of Applied Physics*, **79**: 1829, (1996).

[207] S. Bueble, K. Knorr, E. Brecht, and W.W. Schmahl. Influence of the ferroelastic twin domain structure on the (100) surface morphology of $LaAlO_3$ HTSC substrates. *Surface Science*, **400**: 345, (1998).

[208] H. Schneidewind, M. Manze, G. Bruchlos, and K. Kirsch. TlBaCaCuO-(2212) thin films on lanthanum aluminate and sapphire substrates for microwave filters. *Superconductor Science and Technology*, **14**: 200, (2001).

[209] J.M. Huijbregtse and J.H. Rector. Effect of the two (100) $SrTiO_3$ substrate terminations on the nucleation and growth of YBCO thin films. *Physica B*, **351**: 183, (2001).

[210] B. Dam, J.M. Huijbregtse, and J.H. Rector. Strong pinning linear defects formed at the coherent growth transition of Pulsed-Laser-Deposited $YBa_2Cu_3O_{7-x}$ films. *Physical Review B*, **65**: 064528, (2002).

[211] K. Zalamova, N. Roma, S. Morlens, T. Puig, J. Gazquez, A.E. Carrillo, F. Sandiumenge, S. Ricart, N. Mestres, and X. Obradors. Smooth stress relief of trifluoroacetate metal-organic solutions for $YBa_2Cu_3O_{7-x}$ film growth. *Chemistry of materials*, **18**: 5897, (2006).

[212] P.C. McIntyre, R.C. Chiu, M.J. Cima, and W.E. Rhine. Metal-organic decomposition and microstructure development in $Ba_2YCu_3O_{7-x}$ films from metal trifluoroacetate precursors. *High-Temperature Superconductors: Fundamental properties and novel materials processing*, **169**: 743, (1990).

[213] B.B. He. *Two-dimensional X-Ray diffraction*. Wiley, (2009).

[214] P.C Bean. Magnetization of hard superconductors. *Physical Review Letters*, **8**: 250, (1962).

[215] J. Eggers. Drop formation -an overview. *Journal of Applied Mathematics and Mechanics*, **85**: 400, (2005).

[216] T. Young. An essay on the cohesion of fluids. *Philosophical Transactions of the Royal Society of London*, **95**: 65, (1805).

[217] P.S Laplace. *Mecanique Celeste Supplement*. Courier, (1805).

[218] J. Plateau. Sur les figures d'equilibre d'une masse liquide sans pesanteur. *Acad. Sci. Bruxelles*, **23**:5, (1849).

[219] L. Eotvos. An experimental investigation of fluid-flow resulting from the impact of a water drop with an unyielding dry surface. *Annals of Physics*, **27**: 448, (1886).

[220] G.H. Quincke. *Wiedemann s Annalen*, **2**: 145, (1877).

[221] N. Bohr. *Philosophical Transactions of the Royal Society A*, **209**: 281, 1909.

[222] P. Lenard. *Annual Physics*, **30**: 209, (1887).

[223] D.H. Peregrine, G. Shokes, and A. Symon. The bifurcation of liquid bridges. *Journal of Fluid Mechanics*, **212**: 25, (1990).

[224] J. Eggers. Universal pinching of 3D axisymmetric free-surface flow. *Physical Review Letters*, **71**: 3458, (1993).

[225] B. Ambravaneswaran, E.D. Wilkes, and O.A. Basaran. Drop formation from a capillary tub: comparison of one-dimensional and two-dimensional analyses and occurence of satellite drops. *Physics of Fluids*, **14**: 2606, (2002).

[226] X.D Shi, M.P Brenner, and S.R. Nagel. A cascade of structure in a drop falling from a faucet. *Science*, **65**: 219, (1994).

[227] E.D. Wilkes, S.D. Philipps, and O.A Basaran. Computational and experimental analysis of dynamics of drop formation. *Physical Review Letters*, **88**: 174501, (2002).

[228] D.Y. Shin, P. Grassia, and B. Derby. Numerical and experimental comparisons of mass transport rate in a piezoelectric drop-on-demand inkjet printhead. *International Journal of Mechanical Sciences*, **46**: 181, (2004).

[229] F.H. Harlow and J.E. Welch. Numerical calculation of time-dependent viscous incompressible flow of fluid with free surface. *Physics of Fluids*, **8**: 2182, (1965).

[230] Y.S Yoo, C.S. Kim, and Y.S. Park. Numerical and experimental evaluation of picoliter inkjet head for micropatterning of printed electronics. *Japanese Journal of Applied Physics*, **49**: 5, (2010).

[231] J.H. Hilbing and S.D. Heister. Droplet size control in liquid jet breakup. *Physics of Fluids*, **8**: 1574, (1996).

[232] D.F. Zhang and H.A. Stone. Drop formation in viscous flows at a vertical capillary tube. *Physics of Fluids*, **9**: 2234, (1997).

[233] Q. Xu and O.A. Basaran. Computational analysis of drop-on-demand drop formation. *Physics of Fluids*, **19**: 102111, (2007).

[234] J.R. Castrejon-Pita, G.D. Martin, S.D. Hoath, and I.M. Hutchings. A simple large-scale droplet generator for studies of inkjet printing. *Review of Scientific Instruments*, **79**: 075108, (2008).

[235] H.C. Wu, H.J. Lin, and W.S. Hwang. A numerical study of the effect of operating parameters on drop formation in a squeeze mode inkjet device. *Modelling and Simulation in Materials Science and Engineering*, **13**: 17, (2005).

[236] X. Zhang and O.A. Basaran. An experimental study of dynamics of drop formation. *Physics of Fluids*, **7**: 1884, (1995).

[237] R.M. Verkouteren and J.R. Verkouteren. Inkjet metrology II: Resolved effects of ejection frequency, fluidic pressure, and droplet number on reproducible drop-on-demand dispensing. *Langmuir*, **27**: 9644, (2011).

[238] D. Henderson, H. Segur, L.B. Smolka, and M. Wadati. The motion of a falling liquid filament. *Physics of Fluids*, **12**: 3, (2000).

[239] P. Shin, J. Sung, and M.H. Lee. Control of droplet formation for low viscosity fluid by double waveforms applied to a piezoelectric inkjet nozzle. *Microelectronics Reliability*, **51**: 797, (2011).

[240] R. Li, N. Ashgriz, and S. Chandra. Droplet generation from pulsed micro-jets. *Experimental Thermal and Fluid Science*, **32**: 1679, (2008).

[241] Y.S. Chen, Y.L. Huang, C.H. Kuo, and S.H. Chang. Investigation of design parameters for droplet generators driven by piezoelectric actuators. *International Journal of Mechanical Sciences*, **49**: 733, (2007).

[242] M.H. Tsai, W.S. Hwang, H.H. Chou, and P.H. Hsieh. Effects of pulse voltage on inkjet printing of a silver nanopowder suspension. *Nanotechnology*, **19**: 335304, (2008).

[243] http://www.microfab.com/images/pdfs/technote99-05.pdf, 2013.

[244] J. Kimura, Y. Kawana, and T. Kuriyama. An immobilized enzyme membrane fabrication method using an ink jet nozzle. *Biosensors*, **4**: 41, (1988).

[245] G.L. Bernardini, B.A. Rampy, G.A. Howell, D.J. Hayes, and C.J. Frederickson. Applications of piezoelectric fluid jetting devices to neuroscience research. *Journal of Neuroscience Methods*, **38**: 81, (1991).

[246] G. Percin, A. Atalar, F.L. Degertekin, and B.T. Khuri-Yakub. Micromachined two-dimensional array piezoelectrically actuated transducers. *Applied Physics Letters*, **72**: 1397, (1998).

[247] D. Sziele, O. Bruggeman, M. Doring, R. Freitag, and K. Schugerl. Adaptation of a microdrop injector to sampling in capillary electrophoresis. *Journal of Chromatography A*, **669**: 254, (1994).

[248] F.C. Lee, R.N. Mills, and F.E. Talke. Drop-on-demand method and apparatus using converging nozzles and high viscosity fluids. (U.S.Patent 4,475,113), (1984).

[249] O.A. Basaran and D.W. DePaoli. Nonlinear oscillations of pendant drops. *Physics of Fluids*, **6**: 2923, (1994).

[250] H.Y. Gan, X. Shan, T. Eriksson, B.K. Lok, and Y.C. Lam. Reduction of droplet volume by controlling actuating waveforms in inkjet printing for micro-pattern formation. *Journal of Micromechanics and Microengineering*, **19**: 055010, (2009).

[251] A.U. Chen and O. A. Basaran. A new method for significantly reducing drop radius without reducing nozzle radius in drop-on-demand drop production. *Physics of Fluids*, **14**: L1, (2002).

[252] S. Sakai. Recording method by ink jet recording apparatus and recording head adapted for said recording method. (U.S.Patent 5,933,168), (1999).

[253] A.U. Chen and O.A. Basaran. Method and apparatus for producing drops using a drop-on-demand dispenser. (U.S.Patent 6,513,894), (2003).

[254] C. Rensch. *Creation of small microdrops*. MicroFab Technologies, Inc, (2006).

[255] R.F. Burr, D.A. Tence, H.P. Le, R.L. Adams, and J.C. Mutton. Method and apparatus for producing dot size modulated ink jet printing. (U.S.Patent 5,495,270), (1996).

[256] S. Schiaffino and A. A. Sonin. Formation and stability of liquid and molten beads on a solid surface. *Journal of Fluid Mechanics*, **343**: 95, (1997).

[257] C.W Visser, Y. Tagawa, C. Sun, and D. Lohse. Microdroplet impact at very high velocity. *Soft matter*, **8**: 10732, (2012).

[258] R. Rioboo, M. Marengo, and C. Tropea. Time evolution of liquid drop impact onto solid, dry surfaces. *Experiments in Fluids*, **33**: 112, (2002).

[259] C.D. Stow and M.G. Hadfield. An experimental investigation of fluid-flow resulting from the impact of a water drop with an unyielding dry surface. *Proceedings of the Royal Society of London: Series A*, **373**: 419, (1981).

[260] J. Stringer and B. Derby. Formation and stability of lines produced by inkjet printing. *Langmuir*, **26**: 10365, (2010).

[261] P.J. Smith, D.Y. Shin, J.E. Stringer, and B. Derby. Direct ink-jet printing and low temperature conversion of conductive silver patterns. *Journal of Materials Science*, **41**: 4153, (2006).

[262] S.H. Davis. Moving contact lines and rivulet instabilities. Part 1: The static rivulet. *Journal of Fluid Mechanics*, **98**: 225, (1980).

[263] F. Gao and A. A. Sonin. Precise deposition of molten microdrops: The physics of digital microfabrication. *Proceedings Royal Society of London*, **A 444**: 533, (1994).

[264] P.G. de Gennes, F. Brochard-Wyart, and D. Quere. *Capillarity and wetting phenomena: drops, bubbles, pearls, waves*. Springer Science, (2004).

[265] P.G. de Gennes. Wetting: statics and dynamics. *Reviews of modern physics*, **57**: 827, (1985).

[266] R.D. Deegan. Pattern formation in drying drops. *Physical Review E*, **61**: 475, (2000).

[267] S. Srinivasan, G.H. McKinley, and R.E. Cohen. Assessing the accuracy of contact angle measurements for sessile drops on liquid repellent surfaces. *IBM Journal of Research and Development*, **27**: 13582, (2011).

[268] P.C. Duineveld. The stability of ink-jet printed lines of liquid with zero receding contact angle on a homogeneous substrate. *Journal of Fluid Mechanics*, **477**: 175, (2003).

[269] R.D. Deegan, O. Bakajin, T.F. Dupont, G. Huber, S.R. Nagel, and T.A. Witten. Capillary flow as the cause of ring stains from dried liquid drops. *Nature*, **389**: 827, (1997).

[270] R.D. Deegan, O. Bakajin, T.F. Dupont, G. Huber, S.R. Nagel, and T.A Witten. Contact line deposits in an evaporating drop. *Physical Review E*, **62**: 756, (2000).

[271] D. Soltman, B. Smith, H. Kang, S.J.S. Morris, and V. Subramanian. Methodology for inkjet printing of partially wetting films. *Langmuir*, **26**: 15686, (2010).

[272] B.A. Glowacki and M. Makoros. Superconducting-magnetic heterostructures: a method of decreasing AC losses and improving critical current density in multifilamentary conductors. *Journal of Physics: Condensed Matter*, **21**: 254206, (2009).

[273] N. Amemiya, S. Kasai, K. Yoda, Z. Jiang, G.A. Levin, P.N. Barnes, and C.E. Oberly. AC loss reduction of YBCO coated conductors by multifilamentary structure. *Superconductor Science and Technology*, **17**: 1464, (2004).

[274] J.Z. Wang, J. Gu, F. Zenhausern, and H. Sirringhaus. Low-cost fabrication of submicron all polymers field effect transistors. *Applied Physics Letters*, **88**: 133502, (2006).

[275] X. Granados, S. Illiescu, B. Bozzo, E. Bartolome, T. Puig, X. Obradors, J. Amoros, and M. Carrera. Magnetic mapping, a way to test and understand current flows in thin and bulk superconductors. *Advances in Science and Technology*, **47**: 1, (2006).

[276] M. Carrera, X. Granados, J. Amoros, R. Maynou, T. Puig, and X. Obradors. Detection of current distribution in bulk samples with artificial defects from inversion of hall magnetic maps. *IEEE Transactions of Applied Superconductivity*, **19**: 3553, (2009).

[277] D. Soltman, B. Smith, H. Kang, S.J.S. Morris, and V. Subramanian. Methodology for inkjet printing of partially wetting films. *Langmuir*, **26**: 15686, (2010).

[278] S. Morlens, N. Roma, S. Ricart, A. Pomar, T. Puig, and X. Obradors. Thickness control of solution deposited YBCO superconducting films by use of organic polymeric additives. *Journal of Materials Research*, **22**: 2330, (2007).

[279] J. Gazquez, F. Sandiumenge, M. Coll, A. Pomar, N. Mestres, T. Puig, X. Obradors, Y. Kihn, M.J. Casanove, and C. Ballesteros. Precursor evolution and nucleation mechanism of $YBa_2Cu_3O_7$ films by TFA metalorganic decomposition. *Chemistry of Materials*, **18**: 6211, (2006).

[280] W. Wong, Z. Yang, L.P. Cook, Q. Huang, J.A. Kaduk, and J. Frank. Chemical interaction between $Ba_2YCu_3O_{6+x}$.

[281] Y.A. Boikov, T. Claeson, D. Erts, F Bridges, and Z. Zvitky. $CeO_2$ compatibility with $YBa_2Cu_3O_{7-x}$ in superconducting-film multilayers. *Solid State Sciences*, **7**: 1333, (2005).

[282] T.G. Holesinger, S.R. Foltyn, P.N. Arendt, Q.X. Jia, P.C. Dowden, R.F. DePaula, and J.R. Groves. A comparison of buffer layer architectures on continuously processed YBCO coated conductors based on the IBAD YSZ process. *IEEE Transaction on Applied Superconductivity*, **11**: 3359, (2001).

[283] A.M. El-Toni, T. Yamaguchi, S. Shimizu, Y. Fujishiro, and M. Awano. Development of a dense electrolyte thin film by the ink-jet printing technique for a process LSM substrate. *Journal of the American Ceramic Society*, **91**: 346, (2008).

[284] C. Moreno. *New features in solution derived $La_{0.7}Sr_{0.3}MnO_3$ thin films: spontaneous outcropping and nanoscale reversible resistive switching.* PhD thesis, Universitat Autonoma de Barcelona, (2010).

[285] U. Hasenkox, C. Mitze, and R. Waser. Metal propionate synthesis of magnetoresistive $La_{1-x}(Ca,Sr)_xMnO_3$ thin films. *Journal of American Ceramic Society*, **80**: 2709, (1997).

[286] S. Daengsakul, C. Mongkolkachit, S. Thomas, S. Siri, I. Thomas, V. Amornkitbamrung, and S. Maensiri. A simple thermal decomposition synthesis, magnetic properties, and cytotoxicity of $La_{0.7}Sr_{0.3}O_3$ nanoparticles. *Applied Physics A*, **96**: 691, (2009).

[287] M. Nasui, T. Petrisor Jr, R.B. Mos, M.S. Gabor, T. Ristoiu, A. Rufoloni, L. Ciontea, and T. Petrisor. Precursor chemistry for the solution deposition of epitaxial of $La_{0.66}Sr_{0.33}O_3$ (LSMO) thin films. *Thin Solid Films*, **518**: 4753, (2010).

[288] J. Zabaleta. *Growth and advanced characterization of solution-derived nanoscale $La_{0.7}Sr_{0.3}MnO_3$ heteroepitaxial systems.* PhD thesis, Universitat Autonoma de Barcelona, (2012).

[289] Z. Yan, S. Wu, Q. Pan, R. Geng, B. Gu, and J. Wang. Interactions of dipeptides with triton X-100 in aqueous solution: a volumetric and spectroscopic study. *Journal of Chemical Thermodynamics*, **71**: 112, (2014).

[290] H. Luo, H. Yang, S.A. Baily, O. Ugurlu, M. Jain, M.E. Hawley, T.M. McCleskey, A.K. Burrell, E. Bauer, L. Civale, T.G. Holesinger, and Q. Jia. Self-assembled epitaxial nanocomposite $BaTiO_3$-$NiFe_2O_4$ films prepared by Polymer Assisted Deposition. *Journal of the American Ceramic Society*, **129**: 14132, (2007).

[291] A.P. Ramirez. Colossal magnetoresistance. *Journal of Physics-Condensed Matter*, **9**: 8171, (1997).

[292] C. Moreno, P. Abellan, A. Hassini, A. Ruyter, A.P. del Pino, F. Sandiumenge, M.J. Casanove, J. Santiso, T. Puig, and X. Obradors. Spontaneous outcropping of self-assembled insulating nanodots in solution-derived metallic ferromagnetic $La_{0.7}Sr_{0.3}MnO_3$ films. *Advanced Functional Materials*, **19**: 2139, (2009).

[293] J.B. Szczech, C.M. Megaridis, D.R. Gamota, and J. Zhang. Fine-line conductor manufacturing using drop-on demand PZT printing technology. *IEEE Transactions on Electronics Packaging Manufacturing*, **25**: 26, (2002).

[294] S.B. Fuller, E.J. Wilhelm, and J.M. Jacobson. Ink-jet printed nanoparticle microelectromechanical systems. *Journal of Microelectromechanical Systems*, **11**: 55, (2002).

[295] K. Woo, C. Bae, Y. Jeong, D. Kim, and J. Moon. Ink-jet printed Cu source/drain electrodes for solution-deposited thin film transistors. *Journal of Materials Chemistry*, **20**: 3877, (2010).

[296] Y. Yoshioka, P.D. Calvert, and G.E. Jabbour. Simple modification of sheet resistivity of conducting polymeric anodes via combinatorial ink-jet printing techniques. *Macromolecular Rapid Communciations*, **26**: 238, (2005).

[297] A.R. Liberski, J.T. Delaney, A. Liberska, J. Perelaer, M. Schwarz, T. Schuler, R. Moller, and U.S. Schubert. Printed conductive features for DNA chip applications prepared on PET without sintering. *RSC Advances*, **2**: 2308, (2011).

[298] http://www.efects.ugent.be/, 2010.

[299] Z. Wu, C.U. Pittman, and S.D. Gardner. Nitric acid oxidation of carbon fibers and the effects of subsequent treatment in refluxing aqueous NaOH. *Carbon*, **33**: 597, (1995).

[300] J.B. Brzoska, I.B. Azouz, and F. Rondelez. Silanization of solid substrates: a step toward reproducibility. *Langmuir*, **10**: 4367, (1994).

[301] E. Solano, L. Perez-Mirabet, F. Martinez-Julian, R. Guzman, J. Arbiol, T. Puig, X. Obradors, R. Yanez, A. Pomar, S. Ricart, and J. Ros. Facile and efficient one-pot solvothermal and microwave-assisted synthesis of stable colloidal solutions of $MFe_2O_4$ spinel magnetic nanoparticles. *Journal of Nanoparticle Research*, **14**: 1034, (2012).

[302] J. Lyklema. *Fundamentals of Interface and Colloid Science: Liquid Fluid Interfaces*. Academic Press, (2005).

[303] J.F. Padday. *Wetting, spreading and adhesion*. Academic Press, London, (1978).

[304] A. Marmur. Solid-surface characterization by wetting. *Annual Review of Materials Research*, **39**: 473, (2009).

[305] T. Stoebe, Z. Lin, R.M. Hill, M.D. Ward, and H.T. Davis. Surfactant-enhanced spreading. *Langmuir*, **12**: 337, (1996).

[306] J.K. Spelt and A.W. Neumann. Solid surface tension: the equation of state approach and the theory of surface tension components. Theoretical and conceptual considerations. *Langmuir*, **3**: 588, (1987).

[307] http://www.kruss.de/services/education-theory/glossary/owens-wendt-rabel-and-kaelble-owrk-method/, 2012.

[308] R.G. Good and L.A. Girifalco. A theory for estimation of surface and interfacial energies, III. Estimation of surface energies of solids from contact angle data. *The Journal of Physical Chemistry*, **64**: 561, (1960).

[309] X.D. Wang, X.F. Peng, J.F. Lu, T. Liu, and B.X. Wang. *Contact angle hsyteresis on rough solid surfaces*. Wiley Periodicals, (2004).

[310] C.W. Extrand. An experimental study of contact angle hysteresis. *Journal of Colloid and Interface Science*, **191**: 378, (1999).

[311] M. Mulqueen and P.D.T. Huibers. *Handbook of Applied Surface and Colloid Chemistry: Measuring equilibrium surface tensions*. Wiley, (2002).

[312] E. Chibowski. On some relations between advancing, receding and Young contact angles. *Advances in Colloid and Interface Science*, **133**: 51, (2007).

[313] G.D. Nadkarni and S. Garoff. An investigation of microscopic aspects of contact angle hysteresis: pinning of the contact line on a single defect. *Europhysics Letters*, **20**: 523, (1992).

[314] R.J. Hunter. *Foundations of Colloid Science*. Oxford University Press, (2001).

[315] S. Stolen and T. Grande. *Chemical Thermodynamics of Materials: Macroscopic and microscopic aspects*. Wiley, (2004).

[316] D. Myers. *Surfaces, interfaces and colloids: Principles and applications*. Wiley, (1999).

[317] W.A. Zisman. Relation of the equilibrium contact angle to liquid and solid constitution. *Advances in Chemistry*, **43**: 1, (1964).

# Nomenclature

| | |
|---|---|
| $\dot{\gamma}$ | Shear rate |
| $\epsilon$ | Lattice mismatch |
| $\eta$ | Viscosity |
| $\gamma$ | Surface tension air-liquid |
| $\nu$ | Number of drops per unit area |
| $\rho$ | Density |
| $\tau$ | Shear stress |
| $\theta_a$ | Advancing contact angle |
| $\theta_r$ | Receding contact angle |
| 2a | Drop diameter on the flight |
| 2b | Drop diameter after impact process |
| 2D | Two-dimensions |
| ADSA-P | Axisymmetric Drop Shape Analysis Profile |
| AE | Alkaline Earth |
| B | Magnetic induction |
| b | Maximum spreading diameter |
| Bo | Bond number |
| c | Total metal concentration |
| CC's | Coated Conductors |
| CIJ | Continuous Inkjet printing |
| CMR | Colossal Magnetoresistance |

| | |
|---|---|
| CSD | Chemical Solution Deposition |
| CVD | Chemical Vapour Deposition |
| CZO | $Ce_{0.9}Zr_{0.1}O_2$ Zirconium-doped cerium oxide |
| DE | Double Exchange Model |
| DoD | Drop on Demand |
| EG | Ethyleneglycol |
| EM | Electromagnetic |
| EtOH | Ethanol |
| $F_L$ | Lorentz force |
| $F_P$ | Pinning force |
| FWHM | Full Width at Half Maximum |
| GADDS | General Area Detector Diffraction System |
| H | Applied magnetic field |
| $H_{c1}$ | Lower critical magnetic field |
| $H_{c2}$ | Higher critical magnetic field |
| HTS | High Temperature Superconductors |
| IBAD | Ion Beam Assited Deposition |
| ICMAB | Institut de Ciència de Materials de Barcelona |
| J | Electrical current density |
| $J_c$ | Critical current density |
| l | Nozzle diameter |
| LAO | $LaAlO_3$ Lanthanum Aluminate |
| LED | Light Emitting Diode |
| LSMO | $La_{0.7}Sr_{0.3}MnO_3$ Strontium-Doped Lanthanum Manganite |
| LTS | Low Temperature Superconductors |
| MAGLEVS | Magnetic Levitation Systems |
| MEMS | Microelectromechanical system |

| | |
|---|---|
| MeOH | Methanol |
| MOCVD | Metalorganic Chemical Vapour Deposition |
| MOD | Metalorganic Decomposition Route |
| MR | Magnetoresistance coefficient |
| MRI | Magnetic Ressonance Imaging |
| Oh | Ohnesorge number |
| OM | Optical Microscopy |
| PEG | Polyethyleneglycol |
| PEI | Polyethyleneimine |
| PLD | Pulsed Laser Deposition |
| PPMS | Physical Properties Measurement System |
| PTFE | Polytetrafluoroethylene |
| PW | Pulse width |
| PZT | Piezoelectric element |
| RABiTS | Rolling Assisted Biaxial Textured Substrates |
| RE | Rare Earth |
| Re | Reynolds number |
| RT | Room Temperature |
| SEM | Scanning Electron Microscopy |
| sf | Self field |
| SQUID | Superconducting Quantum Interference Device |
| SS | Stainless Steel |
| STO | $SrTiO_3$ Strontium Titanate |
| T | Temperature |
| $T_C$ | Curie Temperature |
| $T_c$ | Critical Temperature |
| TEA | Triethanolamine |

| | |
|---|---|
| TFA | Trifluoroacetates |
| V | Pulse Voltage |
| v | Drop velocity |
| $V_d$ | Drop volume |
| v/v | volume/volume |
| w/w | weight/weight |
| We | Weber number |
| WV | Waveform |
| XRD | X-Ray Diffraction |
| $XRD^2$ | 2D X-Ray difraction |
| YBCO | $YBa_2Cu_3O_{7-x}$ |
| YSZ | Yttria Stabilized Zirconia |
| Z | Inverse of the Ohnesorge number |
| ZFC | Zero Field Cool |